

The Pennsylvania State University
The Graduate School
Department of Materials Science and Engineering

**TAILORING DEFECT FREE FUSION WELDS BASED ON
PHENOMENOLOGICAL MODELING**

A Thesis in
Materials Science and Engineering

by
Amit Kumar

Submitted in Partial Fulfillment
of the Requirements
for the Degree of

Doctor of Philosophy

August 2006

The thesis of Amit Kumar was reviewed and approved* by the following:

Tarasankar DebRoy
Professor of Materials Science and Engineering
Thesis Advisor
Chair of Committee

Kwadwo Osseo-Asare
Distinguished Professor of Materials Science and Engineering

Long-Qing Chen
Professor of Materials Science and Engineering

Kenneth K. Kuo
Distinguished Professor of Mechanical Engineering

John W. Elmer
Adjunct Professor of Materials Science and Engineering
Group Leader Materials Joining
Chemistry and Materials Science Department
Lawrence Livermore National Laboratory
Special Member

Gary L. Messing
Professor of Ceramic Science and Engineering
Head of the Department of Materials Science and Engineering

*Signatures are on file in the Graduate School

ABSTRACT

In the last few decades, phenomenological models of fusion welding have provided important understanding and information about the welding processes and welded materials. For example, numerical calculations of heat transfer and fluid flow in welding have enabled accurate quantitative calculations of thermal cycles and fusion zone geometry in fusion welding. In many simple systems such as gas tungsten arc (GTA) butt welding, the computed thermal cycles have been used to quantitatively understand weld metal phase compositions, grain sizes and inclusion structure. However, fabrication of defect free welds with prescribed attributes based on scientific principles still remains to be achieved. In addition, higher fabrication speeds are often limited by the occurrence of humping defects which are characterized by periodic bead-like appearance. Furthermore, phenomenological models have not been applied to tailor welds with given attributes. The goal of the present work is to apply the principles of heat transfer and fluid flow to attain defects free welds with prescribed attributes.

Since there are a large number of process variables in welding, the desired weld attributes such as the weld geometry and structure are commonly produced by empirically adjusting the welding variables. However, this approach does not always produce optimum welds and inappropriate choice of variables can lead to poor welds. The existing transport phenomena based models of welding can only predict weld characteristics for a given set of input welding variables. What is needed, and not currently available, is a capability to systematically determine multiple paths to tailor weld geometry and assess robustness of each individual solution to achieve safe, defect free welds. Therefore, these heat transfer and fluid flow based models are restructured to predict the welding conditions to achieve the defect free welds with desired attributes. Systematic tailoring of weld attributes based on scientific principles still remains an important milestone in changing welding from almost an empirical art to a mainstream science-based technology. The ability to determine multiple welding variable sets to achieve desired weld attributes, based on scientific principles, would be an important step to achieve this goal. Furthermore, no comprehensive unified theoretical model exists

today that can predict the formation of commonly occurring humping defects considering the effects of important welding variables such as the arc current, voltage, welding speed, nature of the shielding gas, electrode geometry, torch angle and ambient pressure. In this research work, a model is developed to achieve desired weld attributes and avoid high speed weld defects like humping.

Three main requirements are desirable in a model for systematic tailoring of weld attributes. First, the procedure should embody an adequate phenomenological description of the complex physical processes in welding. Although the heat transfer and fluid flow models use time-dependent equations of conservation of mass, momentum and energy, the predictions of temperature fields and thermal cycles do not always agree with experimental results because the models require many input variables all of which cannot be prescribed with certainty. For example, the reported values of arc efficiency vary significantly for minor differences in the surface characteristics that are difficult to characterize for every welding process. Second, the models are designed to calculate the temperature and velocity fields for a given set of welding variables. However, very often what is needed is to determine the welding variables required to achieve a given weld attribute such as the weld geometry, cooling rate and the microstructure. The current generation of unidirectional heat transfer and fluid flow models are designed to calculate temperature and velocity fields from welding conditions and are incapable of determining welding conditions. Finally, the welding system is highly complex and involves non-linear interaction of several welding variables. As a result, a particular weld attribute such as the geometry can be obtained via multiple paths, i.e., through the use of various sets of welding variables. The current generation of numerical heat transfer and fluid flow models cannot determine alternative pathways to achieve a target weld attribute.

In this thesis, a new structure of the phenomenological models is developed by combining numerical heat transfer and fluid flow models with a suitable optimization algorithm in the form of genetic algorithm. The combined model has new capabilities for bi-directional simulation where either the traditional input or the output variables can be specified. The new formulation also allows determination of multiple solutions to attain a specified weld attribute. Genetic algorithms (GA) can systematically search for multiple

combinations of welding variable sets that comply with the phenomenological laws of welding physics and obtain a population of solutions following certain rules of evolution. This research represents the very first effort to adapt transport phenomena based models along with genetic algorithm based optimization model to attain defects free welds with desired attributes during gas metal arc fillet welding. Through uncommon synthesis of appropriate concepts from transport phenomena, optimization and data mining, this research work outlines a completely new direction of exceptional promise.

TABLE OF CONTENTS

LIST OF FIGURES	x
LIST OF TABLES	xx
ACKNOWLEDGEMENTS	xxii
Chapter 1 INTRODUCTION.....	1
1.1 General Background	1
1.2 Research Objectives.....	5
1.3 Tasks Undertaken for this Thesis	5
1.4 Significance of this Research Work	7
1.5 Thesis Structure	8
1.6 References.....	10
Chapter 2 BACKGROUND.....	13
2.1 Gas Metal Arc (GMA) Fusion Welding	15
2.1.1 Metal Transfer Mechanisms during GMA Welding	17
2.1.2 Process Variables.....	18
2.1.2.1 Welding current.....	19
2.1.2.2 Polarity	19
2.1.2.3 Arc voltage (or, arc length)	19
2.1.2.4 Travel speed (or, welding speed)	20
2.1.2.5 Weld joint position	20
2.1.2.6 Shielding gas	21
2.1.2.7 Weld joint configurations.....	23
2.2 Transport Processes during Fusion Welding	26
2.2.1 Energy absorption efficiency.....	27
2.2.2 Energy flux at top surface.....	28
2.2.3 Quasi-stationary state and non-stationary state	30
2.2.4 Development of transport phenomena based models to calculate weld bead geometry, thermal cycles and cooling rates	31
2.2.4.1 Electromagnetic force or Lorentz force.....	32
2.2.4.2 Marangoni force or surface tension gradient force	35
2.2.4.3 Buoyancy force	38
2.2.4.4 Shear stress induced by plasma jet.....	38
2.2.5 Convection versus conduction on weld pool heat transfer	40
2.2.6 Turbulence in weld pool.....	40
2.2.7 Weld pool free surface calculation	45
2.3 Estimation of Uncertain Input Parameters.....	47
2.4 Neural Networks.....	50
2.4.1 The Backpropagation Algorithm.....	53

2.4.2 Example showing the application of back-propagation algorithm to find the optimal weights in the neural network.....	56
2.4.3 Modeling issues.....	59
2.4.3.1 Finding optimal weights.....	59
2.4.3.2 Gradient versus stochastic optimization techniques.....	60
2.4.3.3 Selection of hidden layers.....	63
2.5 Weld Defects.....	67
2.5.1 Porosity.....	67
2.5.2 Hydrogen porosity.....	68
2.5.3 Slag inclusions.....	69
2.5.4 Incomplete fusion.....	71
2.5.5 Undercut.....	72
2.5.6 Cracks.....	72
2.5.6.1 Hot cracking.....	72
2.5.6.2 Cold cracks.....	73
2.5.7 Weld distortion or warping defects.....	74
2.5.8 Humping.....	76
2.6 Important Unanswered Questions.....	78
2.7 References.....	79

Chapter 3 HEAT AND FLUID FLOW IN COMPLEX JOINTS DURING GAS METAL ARC FILLET WELDING.....	89
3.1 Mathematical Formulation.....	91
3.1.1 Assumptions and salient features.....	91
3.1.2 Governing equations.....	91
3.1.3 Coordinate transformation.....	94
3.1.4 Boundary conditions.....	100
3.1.5 Calculation of effective viscosity and thermal conductivity using mixing length hypothesis.....	101
3.1.6 Grid system and discretization of the governing equations.....	102
3.1.7 Heat transfer from metal droplets.....	103
3.1.8 Calculation of the weld pool top surface profile.....	106
3.1.9 Overall solution procedure.....	112
3.2 Results and Discussion.....	112
3.2.1 Selection of optimal number of grids to make the results independent of their size.....	112
3.2.2 Temperature distribution, velocity field and free surface profile of weld bead.....	113
3.2.3 Dimensionless analysis to calculate the relative importance of various driving forces.....	120
3.2.4 Effect of workpiece orientations on temperature distribution, velocity fields and free surface profile.....	122
3.2.5 Effect of arc current and orientation angles on the weld pool geometry.....	133

3.2.6 Weld thermal cycles	133
3.3 Summary and Conclusions	139
3.4 References.....	143
 Chapter 4 IMPROVING RELIABILITY OF MODELING HEAT TRANSFER AND FLUID FLOW IN COMPLEX GAS METAL ARC FILLET WELDS	 147
4.1 Mathematical Model.....	150
4.1.1 Modeling of heat transfer and fluid flow during GMA fillet welding.....	150
4.1.2 Optimization of uncertain variables	151
4.1.2.1 The uncertain variables	151
4.1.2.2 The optimization problem	153
4.1.3 Optimization techniques.....	155
4.1.3.1 Levenberg-Marquardt method.....	155
4.1.3.2 Conjugate gradient method	158
4.2 Results and Discussion	160
4.2.1 Validation of the model.....	164
4.2.2 Optimized values of effective thermal conductivity, viscosity and arc efficiency.....	167
4.3 Summary and Conclusions	175
4.4 References.....	177
 Chapter 5 A NEURAL NETWORK MODEL OF HEAT AND FLUID FLOW IN GAS METAL ARC FILLET WELDING	 180
5.1 Mathematical Model.....	182
5.1.1 Heat Transfer and Fluid Flow Model of GMA Fillet Welding to Generate Database.....	182
5.1.2 Neural Network Model.....	182
5.1.3 Modified Backpropagation Algorithm	190
5.2 Database Generation Based on Design of Experiments	196
5.3 Results and Discussion	201
5.4 Summary and Conclusions	214
5.5 References.....	214
 Chapter 6 TAILORING FILLET WELD GEOMETRY USING GENETIC ALGORITHM AND A NEURAL NETWORK.....	 217
6.1 Mathematical Model.....	219
6.1.1 Genetic algorithm	221
6.1.2 PCX operator based genetic algorithm.....	222
6.2 Results and Discussion	227
6.2.1 Sensitivity analysis to study the dependency of welding variables	227

6.2.2 Combinations of welding variables obtained by using bi-directional model to achieve desired weld geometry	230
6.3 Summary and Conclusions	238
6.4 References.....	239
Chapter 7 A UNIFIED MODEL TO PREVENT HUMPING DEFECTS IN GAS TUNGSTEN ARC WELDING	241
7.1 Mathematical Model.....	243
7.1.1 Humping model based on Kelvin-Helmholtz hydrodynamic instability	243
7.1.2 Three-dimensional heat transfer and fluid flow model	251
7.1.3 Average velocity and other arc parameters	253
7.2 Results and Discussion	254
7.2.1 Sensitivity of different variables on humping	254
7.2.2 Effect of arc current and welding speed	257
7.2.3 Effect of shielding gas	263
7.2.4 Effect of the electrode tip angle.....	264
7.2.5 Effect of the electrode shape	267
7.2.6 Effect of external magnetic field	267
7.2.7 Effect of the ambient pressure	271
7.2.8 Effect of torch angle	272
7.3 Summary and Conclusions	280
7.4 References.....	281
Chapter 8 CONCLUDING REMARKS	284
8.1 Summary.....	284
8.2 Conclusions.....	286
8.3 Future Work.....	289
Appendix A NEURAL NET MODEL OF GAS METAL ARC FILLET WELDING.....	291

LIST OF FIGURES

<p>Figure 1-1: Humping defects in (a) in GMAW [32] and (b) in GTAW [26]. These defects are characterized by periodic undulation or bead-like appearance. Figure (c) shows the transverse cross-sections of the weld bead along sections AA and BB (marked in figure (b)), respectively [26]. Section AA has extra mass deposition while section BB does not have any metal in that region which reduces the strength of the joint.....</p>	4
<p>Figure 1-2: Flow chart of the thesis work.....</p>	6
<p>Figure 2-1: Schematic of gas-metal-arc welding process [7].....</p>	16
<p>Figure 2-2: Effect of workpiece inclination on the weld bead geometry (a) downhill welding, i.e. workpiece is lifted from behind the moving welding torch; (b) uphill welding, i.e. workpiece is lifted from ahead of the moving welding torch [9].....</p>	22
<p>Figure 2-3: (a) Bead contour and penetration profiles for various shielding gases; and (b) Relative effect of oxygen versus carbon dioxide additions to the argon shielding gas [8].....</p>	24
<p>Figure 2-4: Parts of a fillet weld. Weld A is concave and the weld size is smaller than weld B, which is a convex weld. Notice that the leg-sizes in weld A and B are the same, but the weld size is larger with a straight or slightly convex bead.....</p>	25
<p>Figure 2-5: Measured arc efficiency for different fusion welding processes [18].</p>	29
<p>Figure 2-6: Driving force for weld pool convection: (a, b) buoyancy force; (c, d) Lorentz or electromagnetic force; (e, f) shear stress caused by surface tension gradient; (g, h) shear stress caused by arc plasma.....</p>	33
<p>Figure 2-7: (a, b) Marangoni convection with an outward flow in a NaNO_3 molten pool; (c,d) Marangoni convection with an inward flow in a NaNO_3 pool containing 2 mol % of $\text{C}_2\text{H}_5\text{COOK}$ as a surface active agent. Adapted from Limmaneevichitr and Kou [63, 64].....</p>	37
<p>Figure 2-8: Weld pool shapes and isotherms in a 304 stainless steel with 50 ppm sulfur calculated based on (a) laminar flow and (b) turbulent flow. Adapted from [40].....</p>	44
<p>Figure 2-9: Schematic plot depicting the GMA fillet welding process: (a) interaction between the heat source and the base material; and (b) the transverse section showing the physical processes occurring in the weld pool. ...</p>	46

Figure 2-10: (a) Common paradigm; (b) New paradigm of inverse modeling [80]	48
Figure 2-11: A basic neuron structure	52
Figure 2-12: Neural network with input layer, single hidden layer and an output layer.	55
Figure 2-13: Example showing the application of back-propagation algorithm to find the optimal weights in the neural network. The red colored numbers in the figure represent the current weights while blue colored numbers represent the updated values of the weights. The orange boxes show the summed input to a neuron while green boxes show the output of the neuron. In the network, the values of the inputs are 0.3 and 0.6 and the desired output value is 0.8. This example shows how the weights are updated in the network. The error in the network reduces to 0.617 at second iteration compared to 0.681 at first iteration.	58
Figure 2-14: (a) Simple smooth variation of objective function with variables; (b) Complex variation of objective function with variables.....	61
Figure 2-15: Flowchart of a basic genetic algorithm process.....	64
Figure 2-16: General neural network structures and their corresponding decision regions based on Kolmogorov theorem [127-129].....	65
Figure 2-17: Effect of GMA and SAW welding processes and aluminum content in the workpiece on inclusions size, their distribution on Si-Mn-Al-Ti deoxidized steel welds. (a) Effect of aluminum content on average inclusion diameter; (b) Relation between average inclusion diameter and their number density; (c) Variation of average inclusion diameter with the average spacing between them. The data is taken from references [135] and [136].	70
Figure 3-1: Schematic illustration of fillet joint in various orientations. Figures (a), (b) (c) and (d) show the transverse section of the fillet joint perpendicular to the welding direction while figures (e), (f) and (g) show the central longitudinal section of the fillet joint parallel to the welding direction. (a) Symmetric V-shape joint; (b) L-shape joint; (c) fillet joint with tilt angle θ ; (d) fillet joint with tilt angle $-\theta$; (e) welding in flat position; (f) downhill welding with lift angle = φ ; and (g) uphill welding with lift angle = $-\varphi$	95
Figure 3-2: Transformation of physical domain to computational domain.	96
Figure 3-3: Schematic plot showing the coordinate transformation from the physical (x, y, z) to the computational domain (ξ , η , ζ). Symbols \vec{n}_t , \vec{t}_ξ and	

\vec{t}_η are normal and tangential vectors to the top surface. The shadowed area, A_{FW} , is equal to the amount of fed wire per unit length. Adapted from [1, 3]. 98

- Figure 3-4: Schematic diagram of droplet volumetric heat source where d is the effective height of the volumetric heat source, h_v is the height of the cylindrical heat source, r_d is the droplet radius, f_d is the ratio of the radii of droplet volumetric cylindrical heat source and the droplet and x_v is the distance traveled by the center of the slug between the impingement of two successive droplets. The height of the volumetric heat source is calculated based on conservation of energy. It involved equating the kinetic energy transported by the droplets to the work done required for depressing the weld pool surface and the surface energy. The various parameters defining the volumetric heat source depend on the surface tension of the molten feed wire and size, frequency, velocity and acceleration of the droplets. 104
- Figure 3-5: (a) Definition of the coordinate system; and (b) Surface deformation in weld pool. 107
- Figure 3-6: Projected view of top surface..... 111
- Figure 3-7: Calculated temperature field and velocity fields during GMA welding of (a) V-shaped fillet joint in flat position; (b) L-shaped fillet joint in flat position; (c) V-shaped fillet joint in downhill position at an angle of 10° and (d) V-shaped fillet joint in uphill position at an angle of -10° . For clarity, only a portion of the plate marked as 1, is shown in these figures. Welding conditions used in the calculation are given in case # 1 (table 3-3). 116
- Figure 3-8: Calculated enhancement factor in viscosity using mixing-length hypothesis on various planes perpendicular to the welding direction during horizontal GMA welding of V-shape fillet joint: (a, b) Enhancement factor in viscosity directly under the arc and 5 mm behind the arc location; and (c, d) Corresponding temperature and velocity field in the weld pool. Welding conditions are the same as those in case # 1 (table 3-3). 119
- Figure 3-9: Calculated temperature field, velocity fields and solidified bead geometry during horizontal welding of symmetrical V-shape joint as shown in inset. Welding conditions are same as those given in case # 1 (table 3-3). The temperature and velocity fields at different cross sections planes perpendicular to the welding direction are shown in figures (a), (b) and (c). These figures represent the following regions: (a) directly under the arc, (b) 2.5 mm rear of the arc location, (c) 5 mm rear of the arc location and (d) the solidified reinforced weld bead geometry. 123
- Figure 3-10: Calculated temperature field, velocity fields and solidified bead geometry during horizontal welding of L-shape joint. Welding conditions are

same as those given in case # 1 (table 3-3). The temperature and velocity fields at different cross sections planes perpendicular to the welding direction are shown in figures (a), (b) and (c). These figures represent the following regions: (a) directly under the arc, (b) 2.5 mm rear of the arc location, (c) 5 mm rear of the arc location and (d) the solidified reinforced weld bead geometry. 124

Figure 3-11: Calculated temperature field, velocity fields and solidified bead geometry during downhill welding of V-shape joint. The workpiece is lifted from behind the electrode at an angle of 10°. Welding conditions are same as those given in case # 1 (table 3-3). The temperature and velocity fields at different cross sections planes perpendicular to the welding direction are shown in figures (a), (b) and (c). These figures represent the following regions: (a) directly under the arc, (b) 2.5 mm rear of the arc location, (c) 5 mm rear of the arc location and (d) the solidified reinforced weld bead geometry. 125

Figure 3-12: Calculated temperature field, velocity fields and solidified bead geometry during uphill welding of V-shape joint. The workpiece is lifted from ahead of the electrode at an angle of 10°. Welding conditions are same as those given in case # 1 (table 3-3). The temperature and velocity fields at different cross sections planes perpendicular to the welding direction are shown in figures (a), (b) and (c). These figures represent the following regions: (a) directly under the arc, (b) 2.5 mm rear of the arc location, (c) 5 mm rear of the arc location and (d) the solidified reinforced weld bead geometry. 126

Figure 3-13: Calculated reinforced weld bead profile during (a) horizontal welding of V-shape; (b) horizontal welding of L-shape joints and (c) downhill welding of V-shape joint. During downhill welding, the workpiece was lifted from behind the electrode at an angle of 30°. Welding conditions are same as those given in case # 4 (table 3-3). 128

Figure 3-14: Nomenclature of weld bead geometry used to define (a) V-shape joints and (b) L-shape joints. 129

Figure 3-15: Calculated temperature and velocity vectors (shown by arrows) along central vertical longitudinal plane i.e. plane AB as shown in the inset. (a) Horizontal welding of V-shaped joint; (b) Horizontal welding of L-shaped joint; (c) Downhill welding of V-shaped joint at an angle of 10°; and (d) Uphill welding of V-shaped joint at an angle of 10°. The weld pool boundary is represented by the 1745 K isothermal line. Electrode is located at X =2.5 cm. Welding conditions are the same as those in case #1 in table 3-3. 132

- Figure **3-16**: Effect of arc current and the workpiece tilt angle on (a) Horizontal leg-length; (b) Vertical leg-length; and (c) throat of the weld bead. Tilt angle = 0° refers to the V-shaped joint and 45° refers L-shape joint. 134
- Figure **3-17**: Calculated thermal cycles in the fillet weld at four different locations during horizontal welding of (a) V-shape joint; and (b) L-shape joint. Symbol δ represents the distance from the joint root to the monitoring locations as shown in the insat..... 135
- Figure **3-18**: Calculated average cooling rate $\dot{T}_{8/5}$ at different monitoring locations in the fillet weld for (a) different orientations of workpiece; and (b) during downhill and uphill welding of V-shape geometry. The solid triangles represent the cooling rate estimated using the nomograph available in the literature [42]. 137
- Figure **3-19**: Effect of the (a) lift angle; and (b) tilt angle on the avergae cooling rates ($\dot{T}_{8/5}$) from 1073K to 773K at different monitoring locations during GMA fillet welding..... 140
- Figure **3-20**: Comparison between the calculated and experimental weld geometry during GMA welding of (a) V-shape symmetric fillet joint; (b) L-shape symmetric fillet joint; (c) downhill welding at lift angle = 6° and (d) uphill welding at lift angle = -4° . The experimental micrograph in figure (b) is taken from reference [21]. Since the wire feed rate was not mentioned in the experimental conditions for this micrograph, a value of 150.0 mm/s is chosen in the simulation based on the arc current value. The inner isotherm (blue line) in all these figures represents the calculated weld pool boundary based on solidus temperature of 1745K, while outer isotherm (blue line) represents the 1073 K temperature. 141
- Figure **4-1**: Contour plot of (a) non-dimensional leg-length, (b) non-dimensional penetration (c) and non-dimensional throat for various values of arc efficiency (η) and effective thermal conductivity (k_e) for case #1 listed in table **4-1**. 161
- Figure **4-2**: Computed values of non-dimensional actual throat, penetration and leg-length using $\eta = 0.59$, $k_e = 209.0 \text{ J m}^{-1} \text{ s}^{-1} \text{ K}^{-1}$ and $\mu_e = 0.12 \text{ kg m}^{-1} \text{ s}^{-1}$ for 1 to 8 measurement cases listed in table **4-1**. The non-dimensional values of penetration, actual throat and leg-length are obtained by dividing their computed values with the corresponding experimentally measured values. 163
- Figure **4-3**: Computed values of the objective function, $O(\mathbf{f})$, using LM method and the two versions of CG method as a function of iteration number. 168

Figure 4-4: Optimized values of (a) arc efficiency (represented on left side vertical axis) and non-dimensional weld dimensions (represented on right side vertical axis) (b) enhancement factor of thermal conductivity (i.e. $f_k^e = \frac{k_e}{k_L}$) and viscosity (i.e. $f_\mu^e = \frac{\mu_e}{\mu_L}$); by using Fletcher-Reeves CG method for case #2 of table 4-1. 169

Figure 4-5: Computed values of arc efficiency using estimated values of unknown parameters for different welding conditions listed in table 4-1. 172

Figure 4-6: Computed values of enhancement factor for thermal conductivity and viscosity using estimated values of unknown parameters by using proposed model and vorticity based turbulence model for different welding conditions listed in table 4-1. 173

Figure 4-7: Comparison between the computed and the experimental values of (a) penetration (b) actual throat and (c) leg-length obtained using the optimized value of arc efficiency, effective thermal conductivity and effective viscosity for all the conditions listed in table 4-1. 176

Figure 5-1: The architecture of the neural net model used in this work. The input layer comprises of 22 variables, which is connected to a hidden layer. The output of the network is either penetration, leg-length, throat, weld pool length, cooling time between 800 °C to 500 °C, maximum velocity or peak temperature in the weld pool. 185

Figure 5-2: The working principle of the genetic algorithm based on Generalized Generation Gap (G3) model and using parent centric recombination (PCX) operator. 195

Figure 5-3: Linear graphs of the $L_{81} (3^{40})$ orthogonal array for columns (a) 6, 18, 28 and 35, (b) 1, 8, 9 and 10, (c) 2, 14, 17 and 20, (d) 3, 23, 27 and 31, (e) 4, 32, 37 and 39, (f) 5, 15, 24 and 33, to capture the interaction among variables. The numbers in these figures represents the column numbers of the original $L_{81} (3^{40})$ orthogonal array. The columns of the orthogonal array correspond to the different variables whose effects are being analyzed. 197

Figure 5-4: The range of input variables in the database used for training, validation and testing of the network. The normalized value of the variables was obtained using eq. 5.4 and corresponding minimum and maximum value listed in table 5-1. Various combinations of these 22 input variables were generated using the modified $L_{81} (9^6 \times 3^{16})$ array in the database. 200

- Figure 5-5: Flow chart of the modified backpropagation algorithm using hybrid optimization model after coupling of generalized generation gap (G3) genetic algorithm with the conjugate gradient method. 202
- Figure 5-6: Variation of log(MSE) for (a) penetration; and (b) leg-length with number of hidden nodes for training data by using the CG optimization method after 50000 iterations. The box whisker plot shows the variation and the mean of the log(MSE) for different number of hidden nodes. In the box plot, the shaded region shows the lower quartile, median and upper quartile. The dots represent the log(MSE) obtained in ten different runs which were taken to examine the effect of initial weights on the final converged solution. 75% of the data lies inside the shaded box. 203
- Figure 5-7: Variation of log(MSE) for penetration training data with number of iterations for 19 hidden nodes by using the CG optimization method. 205
- Figure 5-8: Variation of log of mean square error (MSE) in (a) penetration and (b) leg-length for training, validation and testing data by using the hybrid optimization scheme after 50,000 iterations. Figure shows that the 19 nodes in the hidden layer provide less error on all the three datasets. 206
- Figure 5-9: Variation of averaged log of mean square error (MSE) in penetration and leg-length for all the 100 individual members in the population by using the hybrid optimization method for 19 nodes in the hidden layer. The calculation was stopped when the error on the validation data started increasing. 208
- Figure 5-10: Frequency plot showing the number of training datasets of penetration lying in different ranges of relative % error. This plots shows that the relative % error follows the Gaussian distribution with center around zero. Also, more than 90% of data has error with in -0.8 % to 0.8 % on training dataset. 210
- Figure 5-11: Comparison of relative % error in penetration for (a) training data, (b) validation data, (c) testing data, calculated by taking ten different runs of CG method, GA method and the hybrid optimization method. These box-whisker plots show that the hybrid optimization method always produced less error than the CG method or GA method alone. The dots represent the relative % error in the data and 75% of the data points lie inside the shaded box. 211
- Figure 5-12: Comparison of output variables, i.e. (a) penetration, (b) leg-length, (c) throat, (d) length of weld pool, (e) peak temperature in the weld pool, (f) cooling time between 800°C to 500°C, (g) maximum velocity (U_{max}) in the weld pool, calculated by heat transfer and fluid flow model (x-axis) with corresponding values predicted by neural network model of GMA fillet weld.

The diagonal lines in each plot show that ideally all the points should lie on this line. The training data, validation data and test data comprises of 486, 50 and 25 datasets, respectively.....	213
Figure 6-1: Flow chart of the proposed model after coupling of generalized generation gap (G3) genetic algorithm with neural network model.....	225
Figure 6-2: Weld bead geometric parameters as a function of input power: (a) penetration, (b) throat, and (c) leg-length. The values indicated in the legends represent the welding speed and wire feed rate, respectively.....	229
Figure 6-3: Initial values of individual welding variable sets and their objective functions. (a) A large space of variables was searched to find optimum solutions as shown by two hundred randomly selected initial welding variable sets. (b) The low values of the objective functions of several individuals in the initial population indicate the possibility of existence of multiple optimal solutions.....	232
Figure 6-4: Variation of the minimum value and the average value of the objective function in whole population with iterations for 5 different randomly selected initial populations. The low value of the objective function shows that the converged solution is independent on initial selection of values of individuals in the population.....	233
Figure 6-5: Several fairly diverse welding variable sets could produce low values of the objective function indicating the existence of alternate paths to obtain the target weld geometry. The plots show the welding variable sets that produced low values of the objective function, $O(f)$ with iterations. (a) individuals after 1000 iterations with $O(f)$ less than 1×10^{-2} , (b) individuals after 3000 iterations with $O(f)$ less than 1×10^{-4} , and (c) individuals after 6000 iterations with $O(f)$ less than 1×10^{-5}	234
Figure 6-6: Comparisons between the calculated and the desired weld bead geometry for different optimum combinations of welding parameters. The results show that a target geometry can be obtained via multiple paths. The blue line represents the calculated weld pool boundary.....	237
Figure 7-1: The waves generated at the interface of shielding gas layer and liquid metal in the weld pool due to shear across the interface.....	246
Figure 7-2: Segment of a free surface under the action of surface tension.....	248
Figure 7-3: Effects of gravity and surface tension forces on the (B^2-4AC) term calculated by using eqs. 7.23.a, 7.23.b, 7.23.c, 7.23.d and 7.24. The negative value of (B^2-4AC) term signifies the instability of surface wave or the initiation of humping in the weld pool. Values of different variables used in	

- the calculation are: $h_l = 1.5$ mm, $h_g = 7.5$ mm, $U_l = 0.7$ m/s, $U_g = 210.0$ m/s, $\rho_l = 7200$ kg/m³, $\rho_g = 0.018$ kg/m³ and $\gamma = 1.8$ N/m. These values are selected because they represent the same order of the values in GTA welding with Ar-shielding gas at 300 A, 11 mm/s welding speed and arc length = 2.4 mm.....256
- Figure 7-4: Sensitivity of (a) U_g , ρ_g and L_p ; and (b) h_g , h_l , U_l , γ and ρ_l on (B^2-4AC) term given by eqs. 7.23.a, 7.23.b, 7.23.c and 7.23.d. The negative value of (B^2-4AC) term signifies the instability of surface wave or the initiation of humping in the weld pool.258
- Figure 7-5: The variation of critical welding speed with arc current for argon and helium as shielding gases. The welding conditions used in the calculation are: 2.4 mm arc length, 90⁰ electrode tip angle, 3.2 mm thick tungsten electrode and the 1 atm ambient pressure. The welding speed higher than the critical speed will produce humping.260
- Figure 7-6: Variations of (a) relative velocity (i.e. the difference between arc velocity and liquid velocity); (b) weld pool depth; (c) length and (d) the surface tension of liquid metal with arc current. The welding speed has more prominent effect on relative velocity and weld pool depth compared to weld pool length and surface tension of the liquid metal.262
- Figure 7-7: Dynamic viscosity of the helium, argon and their mixture at 1 atm. pressure [25, 33].265
- Figure 7-8: Variation of Richardson number with arc current and welding speed for (a) argon and (b) helium shielding gases. If Richardson number (Ri) is less than 0.8, then there are chances of humping defects to occur.266
- Figure 7-9: The effect of the electrode tip angle on humping. The welding conditions used in the calculations are: 2.4 mm arc length, 3.2 mm diameter tungsten electrode, argon shielding gas and 1 atm. ambient pressure. The results show that the electrodes with smaller tip angle produces humping at lower welding speed than those with larger tip angles.268
- Figure 7-10: The effect of the hollow and solid electrodes on the critical welding speed to initiate humping. The welding conditions used in the calculation are: 2.4 mm arc length, 90⁰ electrode tip angle, argon shielding gas and 1 atm. ambient pressure. The results show that solid electrodes produce humping at lower welding speed than hollow electrodes.269
- Figure 7-11: The effect of the externally applied transverse magnetic field on arc deflection based on Fleming's left hand rule. The arc is deflected in the welding direction when the north pole is on the left side of the moving electrode. If the north and south poles are interchanged, the arc will be deflected in the reverse direction.270

- Figure 7-12:** The effect of the externally applied transverse magnetic field on the critical welding speed to initiate humping in the weld. The welding conditions used in the calculation are: 2.4 mm arc length, 90° electrode tip angle, argon shielding gas and 1 atm. ambient pressure. The results show that the critical welding speed increases with the increase in externally applied transverse magnetic field.273
- Figure 7-13:** The variation of critical welding speed with externally applied transverse magnetic field for different arc lengths. The welding conditions used in the calculation are: 300 A arc current, 90° electrode tip angle, argon shielding gas and the 1 atm. ambient pressure. The results show that the critical welding speed increases with the increase in externally applied transverse magnetic field and the arc length.....274
- Figure 7-14:** The variation of critical welding speed with arc current at low pressure for vertical torch position. The welding conditions used in the calculation are 2.4 mm arc length, 25° electrode tip angle, 3.2 mm diameter tungsten electrode, argon shielding gas and 32 mm of Hg ambient pressure. Higher values of critical welding speed were achieved at low ambient pressures.275
- Figure 7-15:** The effect of torch inclination on the effective arc length. Figure (a) shows the welding torch in push position while figure (b) shows the pull position.276
- Figure 7-16:** The variation of weld pool depth with inclination of torch for 67.0 A arc current, 9.0 V arc voltage and 4.0 mm/s welding speed. The positive torch angle means that the welding torch is in push position while the negative angle means that torch is used in pull position.278
- Figure 7-17:** The variation of critical welding speed with arc current for the initiation of humping defects in the weld for different torch angles at (a) atmospheric pressure and (b) at 32 mm Hg pressure. Higher values of critical welding speed were achieved when the welding torch was in the push configuration i.e., when the arc strikes ahead of the torch axis.279
- Figure A-1:** “Welcome window” obtained on clicking the MS-DOS batch file.292
- Figure A-2:** The “material window” obtained after clicking the start button. The welding process parameters and other welding conditions along with material properties need to be typed at appropriate places in the applet.293
- Figure A-3:** This screen shows the calculated values of the penetration, leg-length, actual throat, peak temperature, maximum velocity and the cooling time for 800°C to 500°C along the weld center line for given welding conditions.295

LIST OF TABLES

Table 3-1 : Effect of the grid size on the results and the computation time. The $n_x \times n_y \times n_z$ represents the grids distribution in x, y and z-directions, respectively.....	113
Table 3-2 : Physical properties of the A-36 steel [1, 40] and the other data used in the calculation.....	114
Table 3-3 : Welding conditions used in the GMA fillet welding experiments [1, 3].....	117
Table 3-4 : Effect of different orientations of workpiece on the weld pool characteristics. Symbol u_{\max} , v_{\max} and w_{\max} represent the maximum velocity (magnitude) in x, y and z directions, respectively. The welding conditions used in calculations are listed in case # 1 in table 3-3	131
Table 4-1 : Welding conditions used in the experiments.	152
Table 4-2 : Estimates of the exact parameters (i.e. $\eta = 0.6$, $k_e = 80.0$ J/m-s-K, $\mu_e = 0.064$ kg/m-s) during validation of model by using Levenberg-Marquardt (LM) and two versions of conjugate gradient method (CG), i.e., Fletcher-Reeves and Polak- Ribiere using initial assumed values of $\eta = 0.75$, $k_e = 63.0$ J/m-s-K and $\mu_e = 0.0512$ kg/m-s.....	165
Table 4-3 : Comparison of optimized values of arc efficiency, η , effective thermal conductivity, k_e , and effective viscosity, μ_e , obtained using Fletcher and Reeves CG method for the first eight welds listed in table 4-1	174
Table 5-1 : The range of input variables used in the generation of training, validation and testing datasets.	184
Table 5-2 : Root mean square error for different output variables.....	186
Table 5-3 : Terminology used in genetic algorithm.....	194
Table 5-4 : Columns of L_{81} (3^{40}) orthogonal array selected based on linear graph shown in figure 4(a).....	198
Table 5-5 : First nine rows of the modified multi-level L_{81} ($9^6 \times 3^{16}$) orthogonal array.....	198
Table 6-1 : Terminology used in genetic algorithm.....	222

Table 6-2: The coefficients of correlation matrix obtained using eqs. 6.8 and 6.9. The magnitude and the sign of the coefficients provide information about the inter-dependency of the estimated welding variables values.	228
Table 6-3: The various combinations of welding parameters, i.e., arc current (I), arc voltage (V), welding speed (U) and wire feed rate (w_f) obtained using neural network model to achieve the following target weld dimensions: penetration = 1.6 mm, leg-length = 10.5 mm and throat = 7.2 mm. The target weld geometry was obtained experimentally using the following welding variables: I = 286.8 A, V= 33.0 V, U = 4.2 mm/s and w_f = 169.3 mm/s.....	235
Table 6-4: The various combinations of welding parameters, i.e., arc current (I), arc voltage (V), welding speed (U) and wire feed rate (w_f) obtained using neural network model to achieve the following target weld dimensions: penetration = 3.7 mm, leg-length = 12.0 mm and throat = 10.0 mm. The target weld geometry was obtained using the welding conditions listed in (a)....	236
Table 7-1: Data used for the calculation of weld pool geometry and the velocity of the liquid metal by three dimensional heat transfer and fluid flow model [14, 18].....	252
Table 7-2: Constants for arc characteristic used in the calculation of arc voltage [25, 26].....	252
Table 7-3: Effect of various welding variables on the parameters required to predict the humping defects.....	255
Table 7-4: Values of effective arc radius, r_j for current density distribution, and effective arc radius for heat flux distribution, r_q , in mm for different welding conditions [25, 27, 31-35] used in the heat transfer and fluid flow calculations and arc velocity calculation [22]. The variables I and l_a in the table represent arc current (A) and arc length (m), respectively.....	259
Table 7-5: Properties of shielding gas [22, 25, 33, 35] required for arc velocity calculation using the expression proposed by Chang et al. [22].....	259
Table 7-6: Welding conditions of Mendez and Eager [8] used for the prediction of humping by the proposed model.	263

ACKNOWLEDGEMENTS

This thesis is the result of four years of work at Penn State whereby I have been accompanied and supported by many people. I would first like to express my deep appreciation and sincere gratitude to my advisor, Dr. Tarasankar DebRoy. He gave me many opportunities to advance my research as well as my professional development. His enthusiasm and integral view on research and his mission for providing 'only high-quality work and never compromise', has made a deep impression on me. I owe him lots of gratitude for having shown me this way of research.

I would like to acknowledge Drs. Long-Qing Chen, Kwadwo Osseo-Asare, John W. Elmer and Kenneth K. Kuo for their valuable advice and suggestions on my work while serving on my thesis committee. I am very appreciative to them for giving their time to review and comment on this thesis.

I would also like to express my thanks to Dr. John W. Elmer at Lawrence Livermore National Laboratory, Dr. Sudarsanam S. Babu at Edison Welding Institute, Dr. Stan A. David at Oak Ridge National Laboratory and Dr. Harshad K. D. H. Bhadeshia at Cambridge University for their helpful discussions on various topics during the progress of my research work.

Many thanks to my colleagues, Dr. Amitava De, Dr. Cheolhee Kim, Dr. Gour G. Roy, Dr. Wei Zhang, Dr. Xiuli He, Dr. Saurabh Mishra, Mr. Rohit Rai, Mr. Rituraj Nandan and Mr. Brandon Ribic, for the help and informative discussion during my study at Penn State.

I am grateful to my parents and parents-in-law for their love and support. Especially, I would like to give my special thanks to my wife Nidhi whose patient love and encouragement enabled me to complete this work.

Finally, I would like to acknowledge a grant from the U.S. Department of Energy, Office of Basic Energy Sciences, Division of Materials Sciences, for supporting this research work, under grant number DE-FGO2-01ER45900. I am also grateful to the American Welding Society Foundation, which provided me with a graduate fellowship to support my research at Penn State.

Chapter 1

INTRODUCTION

1.1 General Background

Recent applications of transport phenomena have resulted in improved understanding of complex fusion welding processes and welded materials. Fluid flow and heat transfer in the weld pool strongly affect the shape, size, structure and the properties of the welded joints [1-18]. The computed temperature profiles have been used to understand microstructure, grain size distribution, inclusion structure and chemical composition of the welded materials. In reality, the numerical heat transfer and fluid flow codes for fusion welding have so far been used mostly as a research tool rather than by the industrial welding community. There are several reasons for the restricted use of these models. An important difficulty is the need for several input parameters that cannot be easily specified [1, 2]. Values of these input parameters are important, since they allow accurate modeling of the transport of heat and mass in the welding systems. Furthermore, the existing phenomenological models only provide the weld characteristics for a given set of input welding variables whereas in industry welding engineers need values of operating variables to produce welds with desired attributes like weld geometry, cooling rate and the microstructure. The mismatch between model capabilities and welding engineers need has restricted the use of these models in industry [19]. A potential solution for this problem is to formulate models based on an entirely new approach.

The proposed approach is based on coupling an optimization model with a phenomenological model for heat transfer and fluid flow and a limited volume of experimental data. The optimization algorithm minimizes the objective function (i.e. squared error between the predicted and the experimentally observed weld geometry) during fusion welding. The genetic algorithm based optimization model [20-25] will be

used in the proposed work due to its unique capability to generate a population of optimized solutions which clearly delineate different combinations of welding variables parameters to achieve desired attributes. Genetic algorithm (GA) is the perfect algorithm for finding the global solution [20-25] which is based on natural evolution process. Since a population of solutions is obtained in each iteration, the outcomes of GA are combinations of operating welding variables.

During gas metal arc (GMA) fillet welding, the evolution of weld pool involves complex physical processes such as application of welding arc, metal droplet transfer, heat transfer through conduction and convection, free surface deformation and the fluid flow inside the weld pool [4, 5]. To simulate these simultaneous processes in the numerical heat transfer and fluid flow analysis, several combinations of welding variables are possible to obtain desired weld attributes like weld bead geometry and the microstructure. In order to obtain alternative combinations of welding variables to attain desired attributes, the existing models need to be coupled with a genetic algorithm (GA) based optimization model. However, the proposed model structure is computationally very intensive since it requires multiple runs of the numerical heat transfer and fluid flow model, which takes about 30 minutes of computation time for each run. It is expected that the proposed model will take more than 100 hours of computation time if the heat transfer and fluid flow model is used as the main computational engine to calculate the weld geometry. To reduce the computational time, the genetic algorithm based optimization model will be parallelized to run on multiple processors simultaneously. Although, parallelization of the model will reduce the computation time somewhat, the model will still remain computationally very intensive. For this model to be practically applicable, further reduction of computational time will be required.

A reasonable solution to this problem is to substitute the information produced by the heat transfer and fluid flow model through pre-calculated results of temperature and velocity fields for various welding conditions embodied in the form of a neural network model. This neural network model [26-28] will be trained and tested by using the data obtained from heat transfer and fluid flow model. Therefore the results of the heat and fluid flow calculations will be made available to the GA in the form of a easy to

calculate, rapid computer program that includes all welding variables as input and provides weld dimensions, peak temperatures, maximum velocities and the cooling rates between 800 to 500 °C in the form of a neural network program. The neural network will take only few seconds for predicting the weld bead geometry compared to the heat transfer and fluid flow model which requires around 30 minutes. The incorporation of the neural network in place of a heat transfer and fluid flow model in the proposed model will reduce the computation time since it does not require solution of non-linear partial differential equations. By combining this neural network model with the genetic algorithm, a useful phenomenological framework can be created for welding engineers to systematically tailor a weld attribute via multiple paths in a reasonable time. Furthermore, a new comprehensive computational model will be developed that can predict and prevent the formation of commonly occurring defects like humping at high welding speeds [29-36] by considering the values of arc current, welding speed, nature of the shielding gas, electrode geometry, ambient pressure, torch angle and external magnetic field during gas tungsten arc (GTA) welding. These humping defects are characterized by periodic undulation or bead-like appearance as shown in figure 1-1. It reduces the static, fatigue and fracture strength of the welded assembly. These defects are generally observed during welding at high speed to increase the productivity. Furthermore, the available experimental data showed that its occurrence is also affected by the type of shielding gas used, the electrode geometry, torch angle and ambient pressure etc. The computational model will consider the stability of the waves on the weld pool surface due to relative motion between the shielding gas and the liquid metal based on the Kelvin-Helmholtz instability theory [37-39]. The model predictions of humping will be verified with the independent experimental results from various sources available in the literature. Based on the results, the recommendations of alternate combinations of welding conditions will be provided to welding engineers to increase the manufacturing productivity without any humping defects in the weld.

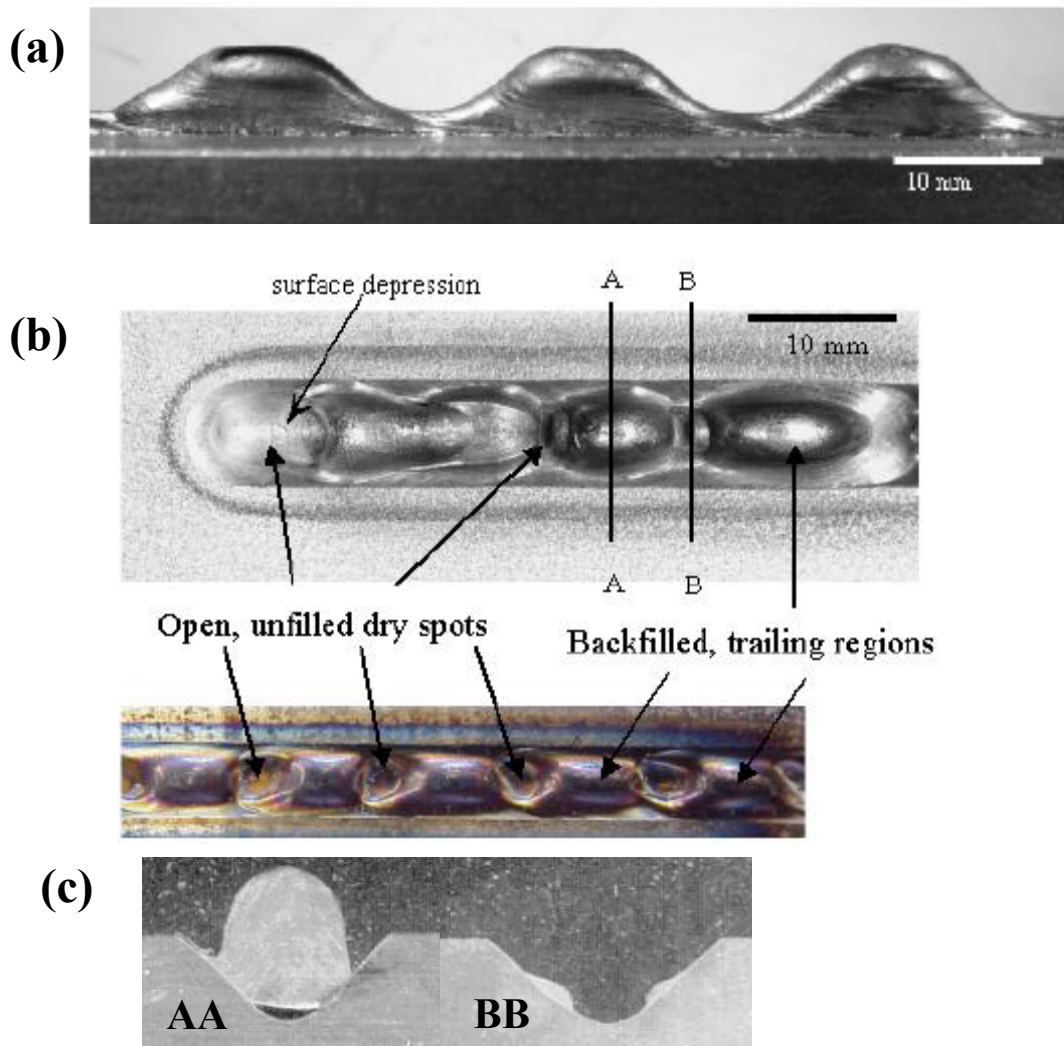


Figure 1-1: Humping defects in (a) in GMAW [32] and (b) in GTAW [26]. These defects are characterized by periodic undulation or bead-like appearance. Figure (c) shows the transverse cross-sections of the weld bead along sections AA and BB (marked in figure (b)), respectively [26]. Section AA has extra mass deposition while section BB does not have any metal in that region which reduces the strength of the joint.

1.2 Research Objectives

This doctoral research seeks to develop a reliable model that can predict alternate combinations of input welding conditions to achieve defect free welds with desired attributes. The reliability of the outputs of this model will be improved by determining uncertain welding process parameters from a limited number of experimental data of molten zone shape and size. The proposed new approach is based on coupling an optimization model with phenomenological model for heat transfer and fluid flow. Furthermore, a mathematical model based on fluid flow instability on the surface of the weld pool will be developed to predict the welding conditions that result in commonly occurring humping defects.

The methodology used in the present thesis research is depicted in figure 1-2. As shown in this figure, first the existing heat transfer and fluid flow model of gas-metal-arc (GMA) fillet welding of symmetric V-shape joint [4, 5] was modified to take any geometrical configuration. This model was then combined with limited volume of experimental data and optimization subroutine to find the values of uncertain input parameters like arc efficiency. Then the neural network models were developed which are capable of relating input variables like welding process parameters and material properties with weld characteristics such as the weld geometry, cooling rate, liquid velocities and peak temperature in the weld pool. These neural net models provided significant computational economy compared to complex heat transfer and fluid flow model of fusion welding. Later, these neural network models were coupled with the genetic algorithm to systematically tailor a weld attribute via multiple paths. Finally, a comprehensive numerical model was developed to predict and prevent the formation of humping defects.

1.3 Tasks Undertaken for this Thesis

The following tasks were performed in this doctoral thesis work:

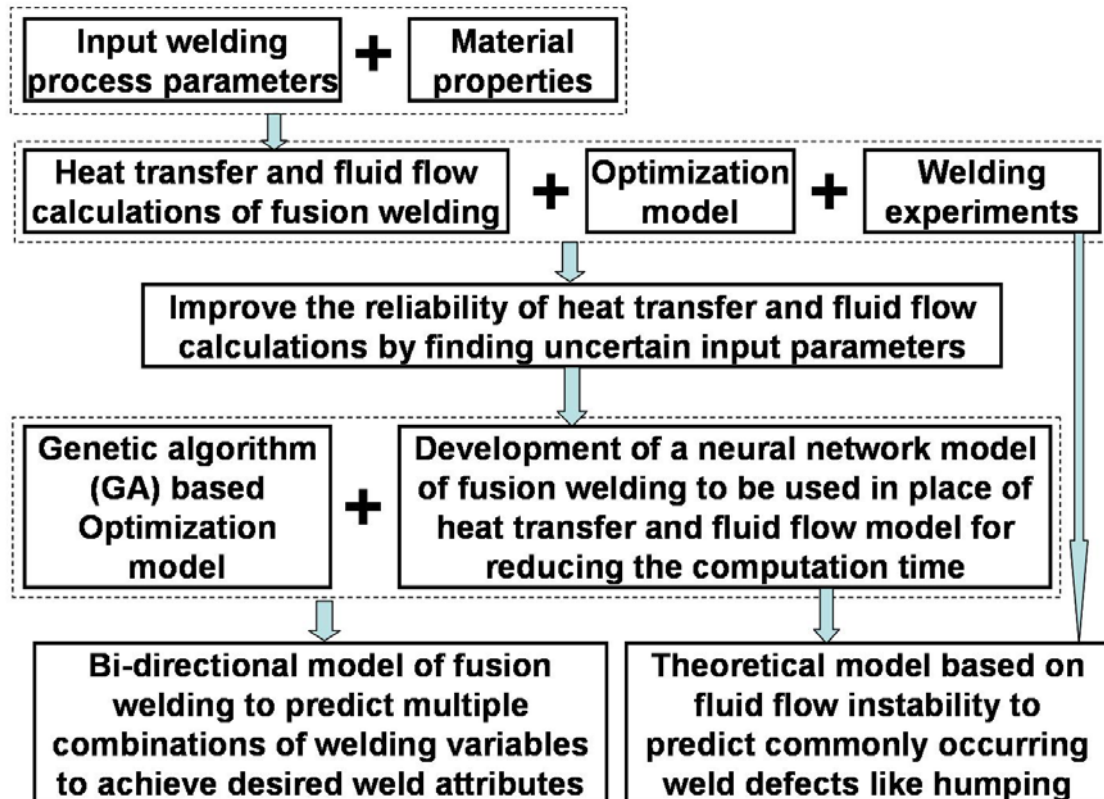


Figure 1-2: Flow chart of the thesis work

Task 1: The heat transfer and fluid flow during welding of workpiece of different fillet geometry was studied. The effect of welding variables and orientation of workpiece on the weld geometric features, free surface profile, solidified bead geometry and thermal cycles were quantitatively understood for GMA fillet welding.

Task 2: The reliability of heat transfer and fluid flow calculations was improved by finding the uncertain input parameters such as arc efficiency.

Task 3: Neural network models to predict the weld geometry in gas-metal-arc (GMA) fillet welding were developed using hybrid optimization scheme which involves combination of a derivative based conjugate gradient method and stochastic optimization technique in the form of genetic algorithm.

Task 4: A bi-directional model was developed by coupling the neural network with real coded genetic algorithm (GA) based optimization model to find different combinations of welding parameters to achieve the desired attribute such as weld geometry.

Task 5: A computational model to predict the welding conditions for preventing commonly occurring weld defects like humping was developed.

1.4 Significance of this Research Work

Through synthesis of appropriate concepts from transport phenomena, optimization and data mining, this doctoral thesis work outlines a completely new direction of exceptional promise. The ability of the model to correctly predict multiple welding variable sets that can lead to the target weld dimensions proves that by combining the principles of evolutionary biology with welding physics, a useful phenomenological framework can be created to systematically tailor a weld attribute via multiple paths. This kind of work for tailoring the weld geometry has not been done outside our research group. Recent research along similar thoughts was conducted by Dr. Mishra [40] at PennState for simplified butt weld systems. In the present doctoral work, a model for tailoring the geometry of more complex fillet joints during GMA welding is developed. Although the work reported here focuses on tailoring of weld geometry, these results

provide hope that by using the proposed approach, welding engineers will be able to tailor the structure and properties of weldments in the future.

1.5 Thesis Structure

The thesis consists of eight chapters. Chapter 1 describes the subject matter, the research objectives and the thesis contents.

In chapter 2, the transport phenomena based models, neural network models and the optimization techniques are critically reviewed. Initially, the current understanding of various transport processes occurring during welding are examined. Then the current status of heat transfer and fluid flow models and neural network models to predict the weld geometry during fusion welding are discussed. Finally, various theories to predict the weld defects such as humping are evaluated.

In chapter 3, the heat transfer and fluid flow during welding of workpiece of different fillet geometry are studied. The heat transfer and fluid flow model of GMA fillet weld available in our research group was capable of calculating bead profile for V-shape fillet joints only. However, L-shape fillet joints are more commonly manufactured in the industry. The difference in arrangements of plates affects the weld pool convective flow and hence the weld bead profile. Therefore, to study the effect of various welding variables on thermal cycles and cooling rates for any fillet geometry, the existing heat transfer and fluid flow model was modified.

In chapter 4, a comprehensive model was developed to improve the reliability of heat transfer and fluid flow calculations that extract values of uncertain input parameters from a limited volume of experimental data based on inverse modeling approach. In this approach, an optimization algorithm was coupled with a heat transfer and fluid flow model to find the uncertain input parameters based on the phenomenological governing equations.

Chapter 5 seeks to document the problems, issues and lessons learnt in the development of a neural net model from the results of a heat transfer and fluid flow

model that considers all the major input variables including all important process variables and material properties and correlate them with output variables. The number of neurons in the hidden layer and weights connecting them was found by using a hybrid scheme based on conjugate gradient and genetic algorithm optimization techniques. These neural net models provided significant computational economy compared to complex heat transfer and fluid flow model of fusion welding. The ability of neural network to learn from the training data i.e. the outputs of heat transfer and fluid flow model made it a good choice to be used in place of heat transfer and fluid flow model in this work.

Chapter 6 explains the development of a bi-directional model by coupling the neural network with real coded genetic algorithm (GA) based optimization model to find different combinations of welding parameters to achieve the desired attribute such as weld geometry. Genetic algorithm (GA) [10-14] is the perfect technique to systematically search the multiple combinations of welding variable sets that comply with the phenomenological laws of welding physics and improve with iterations following certain rules of evolution. Therefore, the GA, when combined with neural network models [15-17], has the potential to produce multiple sets of welding variables that can result in a particular weld attribute. The results obtained in this thesis indicate that multiple sets of welding variables that are capable of producing a target weld geometry can be calculated in reasonable time.

In Chapter 7, a comprehensive mathematical model is described to quantitatively understand the welding conditions that result in humping defects [19-26]. The model is based on Kelvin-Helmholtz hydrodynamic instability of waves [27-29] on the surface of the weld pool. The model predicted humping when the elevation of the surface wave increases with time. Since the original Kelvin-Helmholtz model uses semi-infinite thickness of both the layers, a modified version was used in this research work to take into account the finite depths of weld pools and specific thicknesses of the shielding gas layer depending on welding conditions. This model considered the effect of arc current, welding speed, electrode tip angle, electrode type, nature of the shielding gas, ambient pressure, inclination of the torch and the external magnetic field on humping formation in GTA steel welds.

The conclusions of this research are presented in chapter 8. The suggestions for future work are also documented in this chapter.

A brief documentation of the developed Java applet of the neural network model of GMA fillet welding is appended as an Appendix.

1.6 References

1. A. De and T. DebRoy, *J. Appl. Phys.* **95**(9), 5230 (2004).
2. S. Mishra and T. DebRoy, *J. Phys.D: Appl. Phys.* **38**, 1977 (2005).
3. H. B. Smartt and C. J. Einerson, *Welding J.* **72**(5), 217 (1993).
4. W. Zhang, C. H. Kim and T. DebRoy, *J. Appl. Phys.* **95**, 5210 (2004).
5. W. Zhang, C. H. Kim and T. DebRoy, *J. Appl. Phys.* **95**, 5220 (2004).
6. R. T. C. Choo, J. Szekely and R. C. Westhoff, *Weld. J.*, **69**, 360s (1990).
7. G. M. Oreper, J. Szekely, *J. Fluid. Mech.*, **147**, 53 (1984).
8. C. S. Wu and L. Dorn, *Comput. Mater. Sci.*, **2**, 341 (1994).
9. N. S. Tsai and T. W. Eagar, *Metall. Trans. B*, **16B**, 841 (1985).
10. M. L. Lin and T. W. Eagar, *Welding J.*, **64**, 163s (1985).
11. M. C. Tsai and S. Kou, *Numer. Heat Transfer A*, **17**, 73 (1990).
12. S. Kou and D. K. Sun, *Metall. Trans. A*, **16A**, 203 (1985).
13. K. Hong, D. D. Weckman, A. B. Strong and W. Zheng, *Sci. Technol. Weld. Joining*, **3**, 125 (2002).
14. K. Hong, D. C. Weckmann, A. B. Strong and W. Zheng, *Sci. Technol. Weld. Joining* **8**, 313 (2003).
15. T. Zacharia, S. A. David, J. M. Vitek and T. DebRoy, *Weld. J.*, **68**, 499s (1989).
16. J. W. Kim and S. J. Na, *Weld. J.*, **74**, 141s (1995).
17. Y. M. Zhang, Z. N. Cao and R. Kovacevic, *J. Mech. Engg. Sci.*, **210**, 187 (1996).
18. A. Matsunawa and Y. Shinichiro, in *International Trends in Welding Science and Technology*, edited by S. A. David et al., ASM International, Materials Park, OH, p. 3 (1993).

19. V. R. Dave, J. H. Cowles, Jr., D. S. Lindland, G. C. Shubert, W. Lin and D. A. Hartman, *Welding J.* **82**, 24 (2003).
20. D.E. Goldberg, *Genetic Algorithm in Search, Optimization and Machine Learning*, Addison-Wesley, MA (1989).
21. T. Back, D.B. Fogel, Z. Michalewicz, Eds., *Handbook of Evolutionary Computations*, IOP Publishing Ltd., Oxford University Press (2000).
22. K. Deb, *Multi-objective Optimization Using Evolutionary Algorithms*, Wiley, NY (2001).
23. E. Zitzler, K. Deb and L. Thiele, *Evol. Comp. J.* **8**, 173 (2000).
24. E. Cantú-Paz, *Efficient and Parallel Genetic Algorithms*, Kluwer Academic Publishers, Boston (2000).
25. K. Deb, A. Anand and D. Joshi, *Evol. Comp. J.* **10**, 371 (2002).
26. Simon Haykin, *Neural Networks: A Comprehensive Foundation*, Prentice-Hall, NJ (1999).
27. A. Kumar and T. DebRoy, *Sci. Technol. Weld. Joining* **11**, 106 (2006).
28. I. S. Kim, S. H. Lee and P. K. D. V. Yarlagadda, *Sci. Technol. Weld. Joining*, **8** (5), 347 (2003).
29. B. J. Bradstreet, *Welding J.* **47**(7), 314 (1968).
30. W. F. Savage, E. F. Nippes and K. Agusa, *Welding J.* **58** (7), 212 (1979).
31. T. Yamamoto and W. Shimada, *International Symposium in Welding*, Osaka, Japan (1975).
32. T. C. Nguyen, D. C. Weckman, D. A. Johnson and H. W. Kerr, *Sci. Tech. Weld. Joining*, **10**(4), 447 (2005).
33. K. C. Mills and B. J. Keene, *Int. Mater. Rev.* **35**(4), 185 (1990).
34. U. Gratzke, P. D. Kapadia, J. Dowden, J. Kroos and G. Simon, *J. Phys. D: Appl. Phys.* **25**, 1640 (1997).
35. N. Yamauchi and T. Taka, *International Institute of Welding*, document no.: 212-437-78 (1978).
36. P. F. Mendez and T. W. Eagar, *Welding J.* **82**(10), 296 (2003).

37. P. K. Kundu and I. M. Cohen, *Fluid Mechanics*, Elsevier Academic Press, San Diego (2004).
38. L. M. Thomson, *Theoretical Hydrodynamics*, Macmillan, New York (1968).
39. P. G. Drazin and W. H. Reid, *Hydrodynamic Stability*, Cambridge University Press, Cambridge (2004).
40. S. Mishra, *Tailoring Weld Geometry and Composition in Fusion Welding Through Convective Mass Transfer Calculations*, Doctoral thesis, The Pennsylvania State University, PA (2006).

Chapter 2

BACKGROUND

The objective of the present thesis research is to predict the input welding parameters to achieve a target weld geometry during gas-metal-arc welding of various fillet weld geometries based on the fundamental principles of transport phenomena. In particular, the research work seeks to predict the welding conditions such as arc current, arc voltage, wire feed rate and welding speed to achieve defect free welds with desired weld bead geometry during complex gas-metal-arc fillet welding. Initially, the reliability of the outputs of the numerical transport phenomena based model was improved by finding the values of uncertain input parameters using inverse modeling technique and a limited volume of experimental data. Later, a neural network was developed in order to obtain the results within a second compared to 30 minutes taken by the heat transfer and fluid flow model. This network was trained by data generated from the numerical heat transfer and fluid flow model of fusion welding. Finally, the neural network model was combined with a genetic algorithm to go backwards, i.e., to find alternate combinations of input welding variables to obtain a specific weld geometry. The model is also capable of quantitatively predicting the liquid convection in the weld pool, temperature distribution in the weldment, thermal cycles, weld bead shape and size, weld defects such as humping for given welding conditions.

Since the subject of heat transfer, fluid flow and weld defects covers a wide range of topics, only the important problems and issues pertinent to the subject of this study are selected to be reviewed here. The purpose of this chapter is to examine and critically review the current status of transport phenomena based models of fusion welding, inverse modeling technique and various theories used in the literature to predict and prevent humping defects. The following topics are covered in this chapter.

(1) This chapter first describes the gas-metal-arc welding processes and the importance of various welding process parameters that can be controlled to achieve

desired weld attributes. The current understanding of heat transfer, fluid flow and free surface flow modeling during gas metal arc (GMA) welding of complex joint geometry is also reviewed in this chapter.

(2) Although, the existing transport phenomena based models use time-tested fundamental equations of conservation of mass, momentum and energy with appropriate boundary conditions, their predictions are affected by the uncertainty in the values of various input parameters used in the modeling. This section explains the application of inverse modeling technique to find the values of uncertain input parameters using limited volume of experimental data for improving the reliability of outputs by restructuring the model. A brief discussion on various inverse modeling techniques and their applications in modeling of welding processes is presented in this chapter.

(3) The transport phenomena based models are coupled with optimization techniques in this work to systematically determine multiple paths or alternate combinations of welding variables to achieve desired weld geometry. However, the resulting model is computationally very intensive and requires several days of computational time. The large amount of time is needed for multiple runs of the numerical heat transfer and fluid flow model. For this model to be useful to welding engineers, a neural network model is developed to replace the heat transfer and fluid flow calculations. The neural network model takes only fraction of a second for predicting the weld bead geometry compared to the heat transfer and fluid flow model which requires about 30 minutes. Furthermore, it takes same inputs as heat transfer and fluid flow model and provides the outputs in the weld pool geometry, peak temperature, cooling rate and maximum velocity. This chapter reviews the previous work done in this regard, and the problems and issues involved in developing a neural network for a complex problem like fusion welding.

(4) The defects generated in the workpiece during welding affect the quality, chemical behavior and strength of the joints. The weld defects usually encountered during fusion welding include incomplete penetration, incomplete fusion, undercutting, porosity, longitudinal cracking and humping. In this thesis, a numerical model for predicting and preventing the humping defects is developed. These humping defects

reduce the static, fatigue and fracture strength of the welded assembly. These defects are commonly observed during high speed welding and are characterized by periodic undulation of the weld bead profile. The occurrence of humping limits the range of usable welding speeds in most fusion welding processes and prevents further increases in productivity in a welding operation. This chapter discusses the merits, demerits and the limitations of various theories used in the literature to predict humping defects. These existing theories are not able to explain the physical mechanisms responsible for humping. The objectives of this research are to identify and validate the physical mechanisms using experimental results responsible for the humping phenomenon during high speed welding of plain carbon steel.

At the end of this chapter, a selection of important unanswered questions in the field of heat transfer, fluid flow and weld defects during gas-metal-arc welding are identified. Solving these unanswered questions is an important goal of the present thesis study, and details of the solution are presented in subsequent chapters.

2.1 Gas Metal Arc (GMA) Fusion Welding

In gas metal arc (GMA) fusion welding, a source of energy is necessary to cause the required melting of materials to be joined [1-7]. The transfer of energy from a source to a workpiece is a complex process in which the true energy density of the welding heat source cannot be expressed precisely. Even after the net energy from the source is transferred to workpiece as heat, not all of heat contributes to cause melting to produce the weld. Some is conducted away from the point of deposition, raising the temperature of the material surrounding the zone of fusion and causing metallurgical and geometrical changes [1-7]. This surrounding region is called heat affected zone. The gas-metal arc welding (GMAW) process employs a continuous consumable solid wire electrode and an externally supplied inert shielding gas [1, 5, 7, 8]. A schematic diagram of this process is shown in figure 2-1. The consumable wire electrode produces an arc with a workpiece made part of the electric circuit and provides filler to the weld joint.

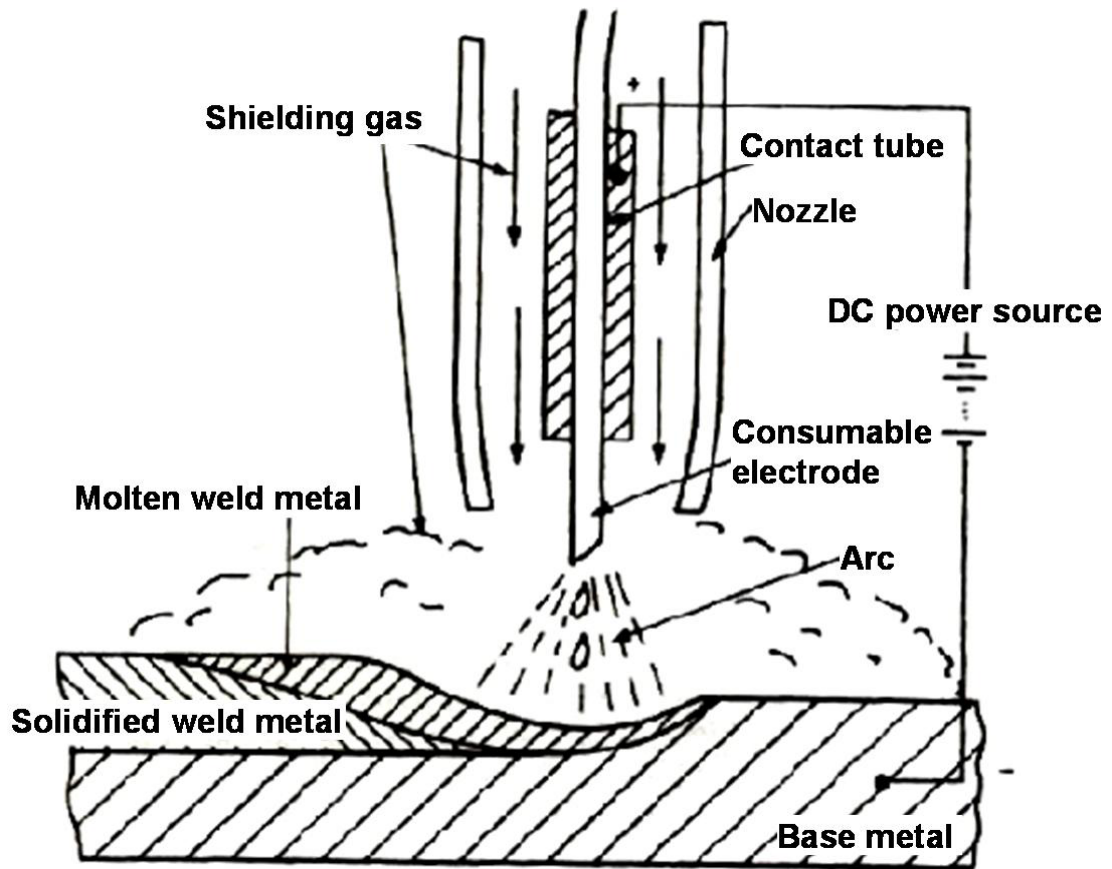


Figure 2-1: Schematic of gas-metal-arc welding process [7].

2.1.1 Metal Transfer Mechanisms during GMA Welding

The characteristics of the GMAW process are described in terms of three basic means by which metal is transferred from the electrode to the workpiece [1, 5, 7, 8]:

1. Short circuiting transfer
2. Globular transfer
3. Spray transfer

Short circuiting encompasses the lowest range of welding current and electrode diameters associated with GMAW [1, 5, 7, 8]. This type of transfer produces a small, fast freezing weld pool that is generally suited for joining thin sections, for out of position welding and for bridging large root openings. Metal is transferred from the electrode to the work only during a period when electrode is in contact with the weld pool. No metal is transferred across the arc gap. Even though metal transfer occurs only during short circuiting, shielding gas composition has dramatic effect on molten metal surface tension [7, 8]. Changes in the shielding gas composition may dramatically affect the drop size, the operating characteristics of the arc and the base metal penetration. In the literature [1, 5, 7, 8], it is observed during experiments that CO₂ generally produces higher spatter levels and promotes deeper penetration compared to inert gases. This behavior can be explained based on the fact that the surface tension of the liquid droplet metal decreases due to presence of oxygen in the shielding gas which is a surface active element. The low surface tension of the liquid droplet reduces the surface energy of the droplets and supports the formation of larger droplets with no spattering. Furthermore, the high specific heat and low thermal conductivity of CO₂ may also be other contributing factors in increasing the penetration. The higher value of specific heat of CO₂ compared to other shielding gases like Ar and He helps in carrying more heat to the workpiece from the electrode. While the low thermal conductivity of CO₂ leads to non-uniform distribution of heat in the arc with more heat along the central axis which increases the penetration.

Globular transfer is characterized by drop size with a radius greater than that of electrode. It is formed at the tip of a consumable electrode and carried to the workpiece predominantly by gravity and to a lesser extent by arc forces including Lorentz pinching

and frictional force [1, 7]. With a positive electrode (DCEP), globular transfer takes place when the arc current is relatively low, regardless of shielding gas [1, 5, 7, 8]. However, with CO₂ and helium shielding gases, this type of transfer takes place at all levels of welding current. It is due to effect of electrode polarity on the anode spot which forms more or less symmetrical around the electrode tip if the electrode is positive. When the electrode is negative, a mobile cathode tip forms on the molten tip. This leads to generation of a reaction force at electrodes and in consequence, the drop may be repelled asymmetrically [1].

The spray transfer mode is characterized by an axial transfer of fine, discrete droplets from the consumable electrode to the workpiece at rates of several hundred per second [1, 5, 7, 8]. The metal transfer is very stable, directional and free of spatter. Spray transfer is produced by welding in the direct current electrode positive (i.e. DC +) mode at high voltages and current levels above some critical value called the transition current [8]. Below this transition current, the transfer occurs in the globular mode at the rate of few drops per second. The transition current, which is dependent on the liquid metal surface tension, is inversely proportional to the electrode diameter [1, 8]. It varies with the filler metal melting temperature and the shielding gas composition which affects the pinch stability of the molten electrode metal [1].

2.1.2 Process Variables

Knowledge and control of the welding variables are essential to consistently produce defect free welds with desired attributes. The main variables that affect weld penetration, bead geometry and weld quality are welding current, wire feed speed, arc voltage (or arc length), travel speed, electrode extension, contact tube to workpiece distance (CTWD), electrode orientation, electrode diameter and shielding gas composition [1, 5, 7, 8]. These variables are not completely independent, and changing one generally requires changing of one or more of others to produce the desired attributes in the weldment. Thus there is no single set of parameters that gives optimum results in every situation.

2.1.2.1 Welding current

When all other variables are kept constant, the arc current varies with wire feed rate or melting rate in non-linear fashion. At the low arc current (approx. 200 A) for each electrode size, the variation is almost linear with wire feed rate. However, at higher current levels (approx. 350A), particularly with small diameter electrodes, the variation of arc current with wire feed rate becomes nonlinear. This is attributed to resistance heating of the electrode extension beyond the contact tube [8]. The increase in welding current generally results in increase in depth and width of weld bead and increase in deposition rate.

2.1.2.2 Polarity

Polarity describes the electrical connection of welding torch with terminals of a DC power source. When the welding torch is connected to the positive terminal, the polarity is designated as direct current electrode positive (DCEP). DCEP yields a stable arc, smooth metal transfer, low spatter, good weld bead characteristics and large penetration [1, 5, 7, 8]. It is due to the formation of symmetrical anode spot around the electrode tip which lead to axi-symmetric drop formation [1]. The alternating current can not be used satisfactorily in GMAW since the cyclic wave form creates arc instability due to the tendency of the arc to extinguish as the current passes through the zero point [8].

2.1.2.3 Arc voltage (or, arc length)

Arc voltage depends on the arc length as well as many other variables, such as electrode composition and dimensions, the shielding gas and the welding technique. With all variables held constant, arc voltage is directly related to arc length. In GMAW, arc length is a critical variable to control the arc and droplet transfer characteristics [1, 5, 7, 8]. For example, in the spray mode with Ar shielding gas, an arc that is too short

experiences momentary short circuits. This causes pressure fluctuations which pump shielding gas and air into the arc stream and produces porosity. An increase in arc voltage tends to flatten the weld bead and increase the width of fusion zone. Excessive arc voltage may cause porosity, spatter, undercut and humping defects in the welded material [7, 8].

2.1.2.4 Travel speed (or, welding speed)

It is the linear rate at which the arc is moved along the weld joint. The safe welding speed during GMA linear welding is generally below 20 mm/s in argon shielding gas. At very slow speeds (i.e. below 5 mm/s), the welding arc impinges on the molten weld pool, rather than the base metal, thereby reducing the effective penetration. As the travel speed is increased, the thermal energy per unit length of weld transmitted to the base metal from the arc is at first increased, because the arc interacts with the base metal directly. With further increase in travel speed, less thermal energy per unit length of weld is imparted to the base metal which reduces the weld bead dimensions. As travel speed is increased further, there is a tendency toward undercutting along the edges of the weld bead and formation of humping defects due to insufficient deposition of filler metal [1, 7, 8, 9].

2.1.2.5 Weld joint position

Spray type GMAW is done in the flat or horizontal positions; while at low energy levels, pulsed and short circuiting GMAW can be used in all positions. Fillet welds made in the flat position with spray transfer are usually more uniform, less likely to have unequal legs and convex profiles, and are less susceptible to undercutting than similar fillet welds made in horizontal position [8, 9]. To overcome the pull of gravity on the weld metal in the vertical or overhead positions of welding, small diameter electrodes are

usually used, with either short circuiting metal transfer or spray transfer with pulsed direct current [8, 9]. The low heat input allows the molten metal to freeze quickly.

Downhill welding affects the weld contour and penetration, as shown in figure 2-2(a). The weld puddle tends to flow toward the electrode and preheats the base metal, particularly at the surface. As the angle of declination increases, the middle surface of the weld is depressed, penetration decreases and the width of weld increases [9].

Uphill welding affects the fusion zone and the weld surface as shown in figure 2-2(b). The force of gravity causes the liquid metal to flow back and lag behind the electrode. The edges of the weld lose metal, which flows to the center. As the angle of inclination increases, reinforcement and penetration increases, and the width of the weld pool decreases. When higher welding currents are used, the maximum usable angle decreases [9].

2.1.2.6 Shielding gas

The primary function of the shielding gas is to exclude the atmosphere from contact with the molten weld metal. This is important because the molten metal exhibit a strong tendency to form oxides and to a lesser extent, nitrides. These reaction products may result in weld defects such as trapped slag, porosity and weld metal embrittlement [1, 7-9]. In addition to providing a protective environment, the shielding gas and its flow rate also affect arc characteristics, mode of metal transfer, weld bead profile, undercutting tendency and weld metal mechanical properties [1, 5, 7-9].

Argon, Helium and their mixtures are generally used as shielding gas to weld non-ferrous metals and stainless, carbon and low alloy steels. The physical differences between argon and helium are density, thermal conductivity and arc characteristics. Helium has a higher thermal conductivity than argon and produces arc plasma in which the arc energy is more uniformly distributed [1]. The argon arc plasma on the other hand is characterized by a high energy inner core and outer zone of less energy. This difference strongly affects the weld bead profile. A welding arc shielded by helium produces a deep, broad, parabolic weld bead.

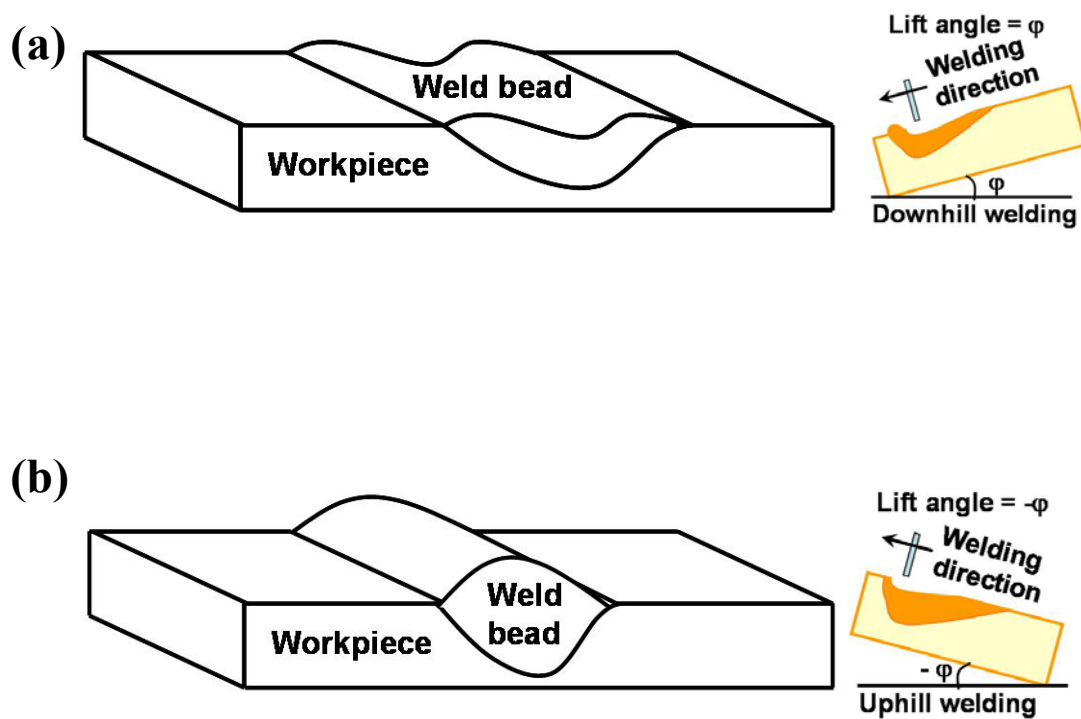


Figure 2-2: Effect of workpiece inclination on the weld bead geometry (a) downhill welding, i.e. workpiece is lifted from behind the moving welding torch; (b) uphill welding, i.e. workpiece is lifted from ahead of the moving welding torch [9].

An arc shielded by argon produces a bead profile characterized by a “finger” type penetration due to generation of higher arc pressure around the axi-symmetric axis [1, 8]. However, pure argon shielding on ferrous alloys causes an erratic arc and a tendency for undercut to occur. Addition of small amount of oxygen or carbon dioxide in the shielding gas produces a noticeable improvement in arc stability and freedom from undercut by eliminating the arc wander caused by cathode sputtering. Since oxygen is a surface active element, its presence in the shielding gas lowers down the surface tension of the liquid metal. The low surface tension of the liquid droplet reduces the surface energy of the droplets and supports the formation of larger droplets with no spattering. Furthermore, the presence of surface active elements near the weld pool surface makes the surface tension gradient with temperature positive. This leads to the inward flow from the periphery towards the center of the weld pool which increases the depth of the weld pool as explained later in section **2.2.6.2**. Typical bead profiles for argon, argon-helium mixtures and carbon dioxide are shown in figure **2-3**.

2.1.2.7 Weld joint configurations

The size, shape and the configuration of the weld joint affects the heat distribution and deposition rate inside the workpiece. The type of joint or the joint geometry is predominantly determined by the geometric requirements or restrictions of the structure and the type of loading [8, 9]. Fillet weld, which joins two pieces of metals approximately at right angle to each other in a lap joint, T-joint, or corner joint, is one of the most important joint types used in shipbuilding and other heavy industries. GMA welding is particularly well suited for welding of fillet joints due to its high productivity and amiability to automation [8, 9]. The various dimensions used to define the size of a fillet weld are shown in figure **2-4**. This figure also shows that two fillet welds with same leg dimensions can be of different sizes. The size of the weld with a concave bead, figure **2-4(a)**, is smaller than the size of the weld with a convex bead, figure **2-4(b)**.

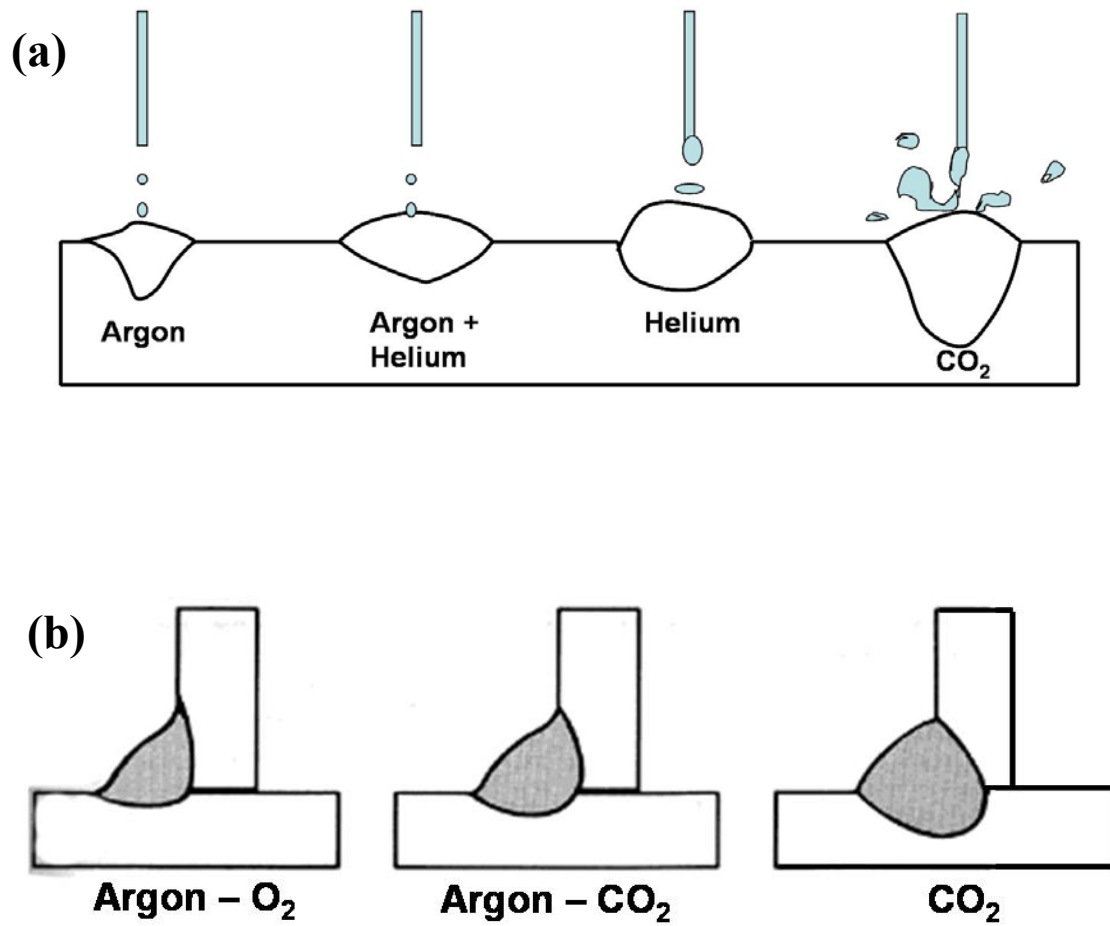


Figure 2-3: (a) Bead contour and penetration profiles for various shielding gases; and (b) Relative effect of oxygen versus carbon dioxide additions to the argon shielding gas [8].

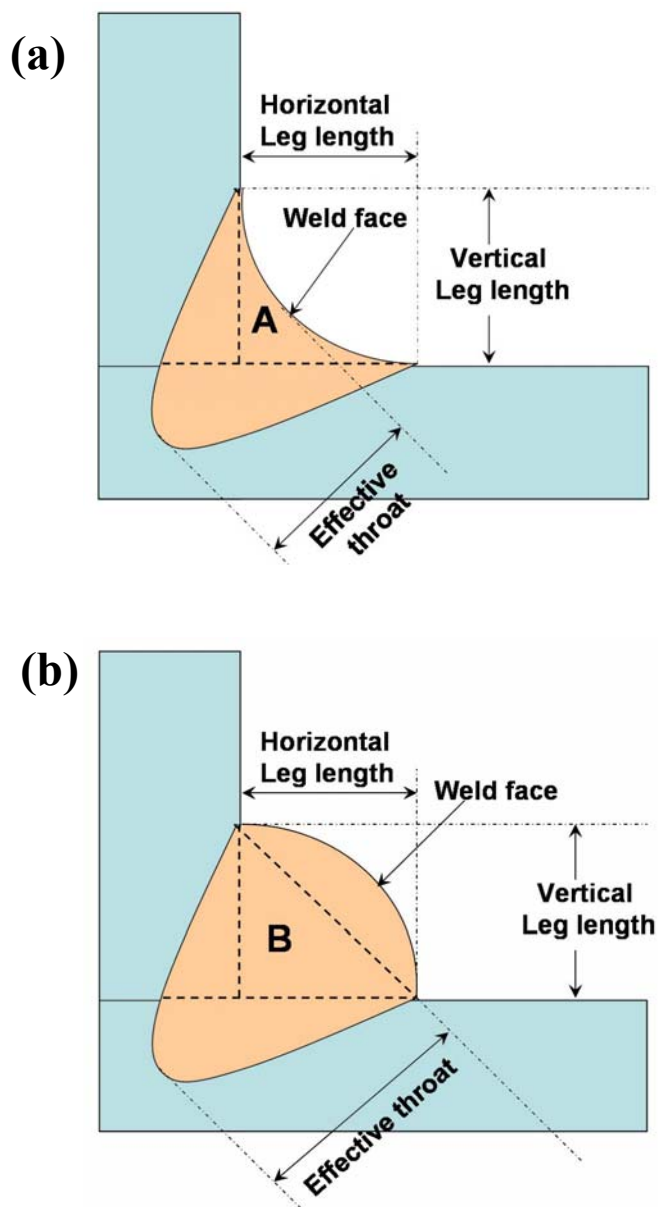


Figure 2-4: Parts of a fillet weld. Weld A is concave and the weld size is smaller than weld B, which is a convex weld. Notice that the leg-sizes in weld A and B are the same, but the weld size is larger with a straight or slightly convex bead.

A fillet weld with a convex bead is stronger than one with a concave bead because of additional filler metal [9]. Performance of structurally sound fillet welds is determined by the geometrical features of the weld bead [8-10]. Various factors such as the weld pool convective flow, arc pressure, droplet transfer, weldment thermal history and physical properties of the weld metal affect the weld bead profile [3, 4, 6, 11-14]. At present, the control of weld bead shape is often achieved through trial and error. This approach has three main disadvantages. First, the trial and error procedure is inherently expensive because of the large number of welding variables. Second, the chosen ranges of variables do not always produce optimum results. Finally, the trial and error approach does not utilize the advanced scientific tools that can provide better fundamental understanding of welding science.

2.2 Transport Processes during Fusion Welding

The thermal cycles in and near the fusion zone of a fusion weld must be maintained within specific limits to control metallurgical structure, residual stresses and distortions and chemical reactions that result from welding operation [10, 13]. Of specific interests are (1) fusion zone geometry, (2) the cooling rates in the fusion and heat-affected zones, (3) the peak temperature and its distribution in the work piece, (4) solidification rate of weld metal, and (5) the distribution of heat between the fusion zone and the heat affected zone [8, 10, 13, 15]. Since the number of processes occurring simultaneously during welding is rather large, it is often necessary to divide the complex welding process into a number of simple constituent parts. These parts include the interaction of the heat source and the weld pool, the heat transfer and fluid flow in the weld pool, the evolution of microstructure of the FZ and HAZ, and the development of residual stress and distortion in the weldment [10]. The transfer of heat in the workpiece is governed primarily by the time-dependent conduction of heat, which is expressed by following general energy flow equation [5, 7]:

$$\rho C \frac{\partial T}{\partial t} = \frac{\partial}{\partial x} \left[k \frac{\partial T}{\partial x} \right] + \frac{\partial}{\partial y} \left[k \frac{\partial T}{\partial y} \right] + \frac{\partial}{\partial z} \left[k \frac{\partial T}{\partial z} \right] - \rho C \left(V_x \frac{\partial T}{\partial x} + V_y \frac{\partial T}{\partial y} + V_z \frac{\partial T}{\partial z} \right) + Q \quad 2.1$$

where, x, y and z represent the Cartesian co-ordinate system; T is the temperature; k is thermal conductivity; ρ is the density of the workpiece; C is specific heat of the workpiece; V_x , V_y , and V_z are the components of velocity and Q is the rate of any internal heat generation. During welding, the heat generation rate, i.e. Q, is a function of distance from the heat source (or the electrode), arc characteristics and the welding speed. The arc characteristics are generally represented by two variables viz. arc radius and arc distribution factor assuming that arc is Gaussian in nature. For most of the welding processes, energy from the heat source is deposited on the surface of the workpiece. The net amount of heat transferred to the workpiece depends on the absorption efficiency which is explained in the next section.

2.2.1 Energy absorption efficiency

During welding, only a fraction of energy is transferred from the heat source to the workpiece. Rest of the energy is consumed in heating/melting the electrode and lost in the form of radiation to the surrounding atmosphere [1, 8]. The amount of energy transferred is importance since it directly affects the shape and size of the weld pool and the temperature distribution in the HAZ. The physical phenomena that influence the energy absorption are unique to each welding process [1, 8, 13]. When a consumable electrode is used, such as in GMA welding, q_e is also transferred to the workpiece and therefore the arc efficiency is thus given as [1]:

$$\eta = 1 - \frac{q_e + (1-n)q_p + mq_w}{VI} \quad 2.2$$

where q_p is the rate of heat radiated and convected from the arc column, n is the proportion of heat output form the arc column that is transferred into the workpiece, q_w is the rate of heat absorbed by the workpiece, m is the fraction of absorbed energy that is radiated away and lost, and V and I are welding voltage and current, respectively. It

should be noted that although eq. 2.2 are useful in explaining the manner in which various types of heat loss affect arc efficiency. However, evaluation of the values of q_e , q_p , q_w , n and m from theoretical considerations is very difficult. Therefore, a common practice is to experimentally determine the arc efficiency under various welding conditions.

Various researchers have measured energy absorption efficiency using calorimetric technique during various welding processes [1, 5, 8, 16-19]. Kou and Le [16] and Tsai and Eagar [19] experimentally measured the arc efficiency for a gas tungsten arc on a water-cooled copper anode as a function of various welding parameters. Malmuth et al. [17] used the dry calorimetric technique to measure the arc efficiency. Figure 2-5 shows the values of arc efficiency obtained experimentally [18] during various welding processes. The arc efficiency is usually higher for GMAW than for GTAW, since a fraction of energy lost to the electrode is transferred into the workpiece in the form of superheating metal droplets [1]. The droplet transfer is a unique feature in GMAW where a consumable electrode is used, and it is often responsible for the finger penetration observed in the GMA welds.

2.2.2 Energy flux at top surface

According to the local effect principle of heat conduction theory, the heat distribution pattern of a heat source affects the temperature distribution substantially only in the region adjacent to the source [10]. Therefore, it is important to know how the heat energy is distributed over the weld top surface to calculate the weld pool geometry accurately. For GTA welding, the following Gaussian distribution has been widely used to account for the heat flux at the weld top surface [20-28].

$$q(r) = \frac{f_d VI \eta}{\pi r_b^2} \exp\left(-f_d \frac{r^2}{r_b^2}\right) \quad 2.3$$

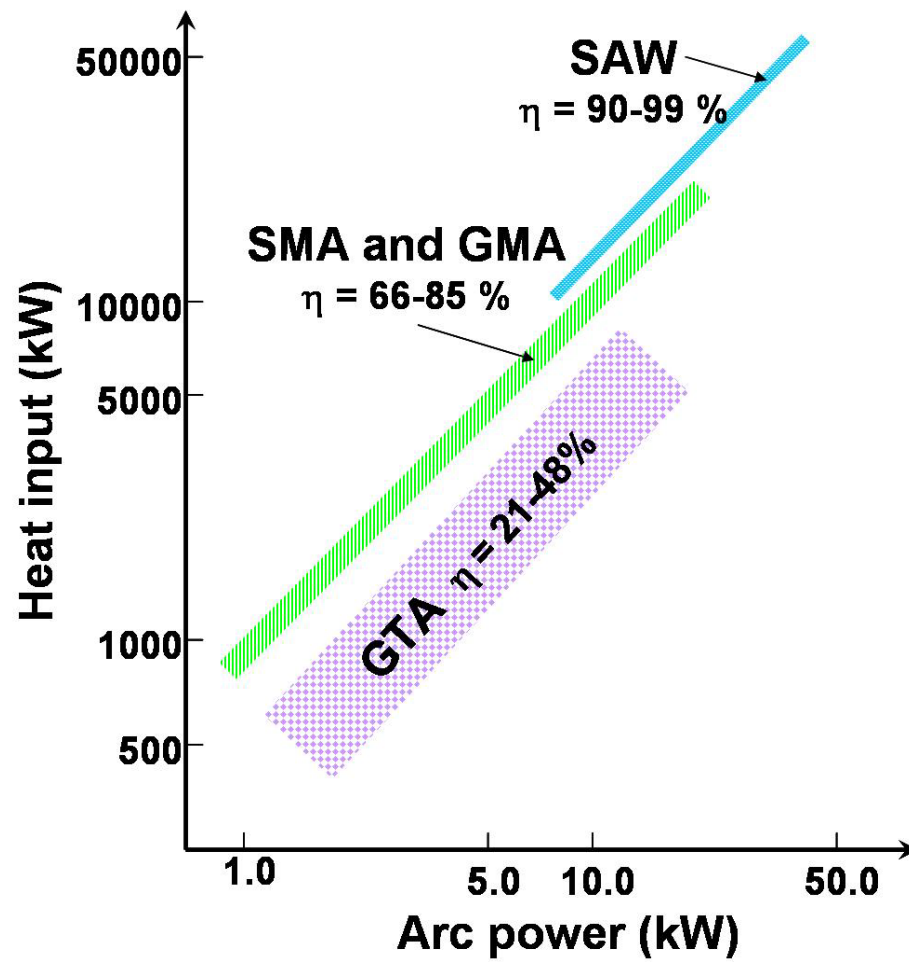


Figure 2-5: Measured arc efficiency for different fusion welding processes [18].

where q is the heat flux at a given location at the weld top surface, r is the distance between the specific location and the heat source, f_d is a distribution factor, V and I are welding voltage and current, respectively, η is the arc efficiency and r_b is the arc radius. Eq. 2.3 indicates that to calculate the heat flux at the weld top surface, the values of f_d , η and r_b are required. In the literature, two typical values of f_d have been reported: 3 and 0.5. Based on experimental measurements, Tsai et al. [19] and Smartt et al. [26] proposed the value of f_d as 0.5. On the other hand, various researchers used the f_d value of 3 in their calculations [20-23]. The value of the arc radius (r_b) depends on the electrode tip angle, arc length and welding current [1,19]. Various researchers [27-30] have calculated the energy distribution for different welding conditions by solving the Navier-Stokes equations with appropriate boundary conditions. The knowledge of heat input flux is a prerequisite to calculate the heat dissipation in the weldment. It should be noted that although eq. 2.3 was originally proposed for GTA welding, similar expressions have also been used to describe the heat flux at the weld top surface for GMA welding [31-35].

2.2.3 Quasi-stationary state and non-stationary state

Heat flow in arc welding primarily involves three stages [10]:

- (1) The initial starting period during which the temperature around the heat source is rising.
- (2) Quasi-stationary state in which the temperature distribution is stationary in a coordinate system which moves with the heat source
- (3) Final period or the leveling off stage in which the temperature evens out after the welding arc is extinguished.

Various researchers [23-25, 31-45] have modeled the fusion welding process using quasi-stationary system by treating the system as a steady state problem for a moving coordinate system. The quasi-stationary state occurs in a small area close to workpiece during long weld cycles. During linear fusion welding, the quasi-stationary state

assumption is valid. However, this assumption is not realistic in spot welding where the start (stage 1) and the extinguishing the arc (stage 3) affect the heat flow in the weld.

2.2.4 Development of transport phenomena based models to calculate weld bead geometry, thermal cycles and cooling rates

The first significant work in the field of modeling of welding was done by Rosenthal [46]. His study was essentially an analysis of heat conduction in a solid with moving point heat source. In the late 1940s and the early 1950s, Nippes et al. [47, 48] studied the cooling rates of heat affected zones. They used the Rosenthal equations in analyzing experimental data and found large discrepancies between analytical and experimental results. Because of this, they simply graphed their experimental data. Later modifications in Rosenthal solution were made by various researchers [49-52]. All of these analytical models had several restrictive assumptions that are often hard to justify on the basis of the known physics of the welding process. Due to the unrealistic assumptions, these analytical models could not accurately calculate the heat flow and solidification rate in and immediately outside the weld pool (i.e. at the fusion zone boundary). Neglecting the convective heat transfer in the weld pool and considering the conductive transfer only, caused the size of the weld pool to be under-predicted. In last few decades, various researchers [36-45, 53-62] have developed the heat transfer and fluid flow models of GTA welding of butt joints. They reported that the properties of the weld metal are strongly affected by the fluid flow and heat transfer in the weld pool.

Since the calculation of convective heat transfer involves the solution of the equations of conservations of mass, momentum and heat and is highly complicated, numerical solution is often utilized. The effect of various driving forces must be properly incorporated into the momentum equation in order to accurately predict the convective heat transfer in the weld pool. The flow in the weld pool during arc welding is driven by surface tension, buoyancy and electromagnetic forces [1, 3-5]. Figure 2-6 is a schematic plot showing the various driving forces in the weld pool and the resulting liquid flow pattern. Buoyancy effects originate from the spatial variation of the liquid metal density,

mainly because of temperature variations, and to a lesser extent, from local composition variations [3-5]. The density of the liquid metal decreases with increase in temperature. As shown in figure 2-6(a), gravity causes the heavier liquid metal at point b to sink since the liquid metal is higher near the center of pool ((i.e. point a in figure 2-6(a)). Consequently, the liquid metal falls along the pool boundary and rises along the pool axis as shown in figure 2-6(b). Electromagnetic effects are a consequence of the interaction between the divergent current path in the workpiece and the magnetic field that it generates [1, 3-5, 57]. The electric current in the workpiece converges towards the electrode and hence near the center of weld pool surface. This converging current field together with the magnetic field it induces, causes a downward and inward Lorentz force as shown in figure 2-6(c). As such, the liquid metal is pushed downward along the pool axis and rises along the pool boundary as shown in figure 2-6(d). The shear stress or surface tension gradient tries to pull liquid from low surface tension regions to regions of higher surface tension as shown in figures 2-6(e) and 2-6(f). In arc welding, a high velocity plasma stream impinges on the weld pool surface. The friction of the impinging jet on the weld pool surface can cause significant fluid motion. The plasma moving outwards at high speeds along a pool surface can exert an outward shear stress at the pool surface which causes the liquid metal to flow from the center of the pool surface to the pool edge, as shown in figures 2-6(g) and 2-6(h). The fluid flow and convective heat transfer are very important in determining the weld pool geometry, thermal cycles, cooling rates, microstructures, grain size and the residual stress in the weldment [3-5].

2.2.4.1 Electromagnetic force or Lorentz force

Depending on the welding condition, the electromagnetic force can have a strong influence in determining the temperature and velocity fields and the resulting weld pool geometry and thermal cycles [3-5]. The electromagnetic force, \mathbf{F}_{emf} , results from the interaction between the current flow and the induced magnetic field in the weldment, and is equal to the vector product of current density, \mathbf{J} , and the self-induced magnetic flux, \mathbf{B} :

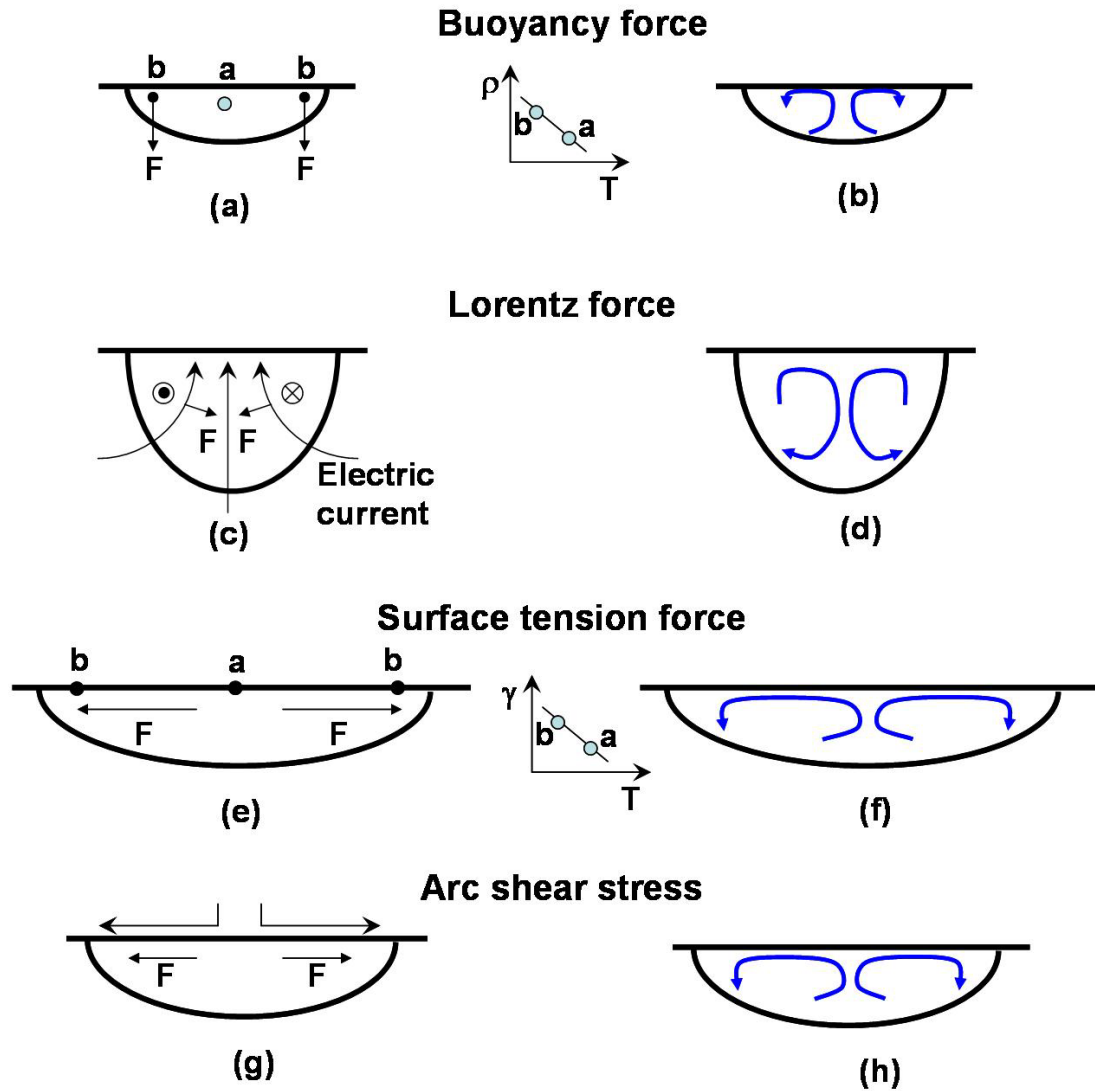


Figure 2-6: Driving force for weld pool convection: (a, b) buoyancy force; (c, d) Lorentz or electromagnetic force; (e, f) shear stress caused by surface tension gradient; (g, h) shear stress caused by arc plasma.

$$\mathbf{F}_{\text{emf}} = \mathbf{J} \times \mathbf{B} \quad 2.4$$

Comprehensive three-dimensional calculations of \mathbf{J} and \mathbf{B} fields are needed for accurate determination of the electromagnetic body force. Since such calculations are fairly complex and time consuming, simplifications have been made to obtain analytical expressions for the electromagnetic body force. Kou and Sun [41] developed an expression for the electromagnetic force in the weld pool by solving Maxwell's equations with several simplifications. Their calculations were based on the following main assumptions: (1) the electromagnetic properties of the workpiece are temperature independent, so that the electrical conductivity and the magnetic permeability remain constant, and the problem is axi-symmetric; (2) Magneto-hydrodynamics (MHD) approximation is valid in the weld pool; (3) the current density on the weld pool surface obeys a Gaussian distribution and can be described by following function:

$$J_z = \frac{3I}{\pi\sigma_j^2} \exp\left(-\frac{3r^2}{\sigma_j^2}\right) \quad 2.5$$

where J_z is the vertical component of the current density, I is the current, r is the radial distance from the arc location and σ_j is the effective radius of the arc; and (4) the radial and the axial components of the magnetic flux, B_r and B_z , are zero. Their expressions of electromagnetic force are valid only for the current density distribution expressed by eq. 2.5 and when the radial and axial components of the magnetic field (i.e. B_r and B_z) are both zero. Tsao and Wu [42] also proposed a set of analytical expressions for the electromagnetic force field that have been widely used in the literature [24, 25, 33-40, 54-56]. In addition to the four assumptions used by Kou and Sun [41], Tsao and Wu [42] further assumed the following two simplifications: (5) the r -component of the current density in workpiece is taken as an average value through the thickness L and (6) B_θ and J_z decrease linearly with z and become zero at the bottom of the workpiece. These analytical expressions of calculating electromagnetic force assumed the axi-symmetric condition, which is valid for the welding of a circular disk or cylinder with the torch placed at the axis. In practice, the three components of current density induce significant

magnetic flux in all three dimensions. Furthermore, these simplified analytical expressions for calculating electromagnetic force distribution [41, 42] do not consider the effects of work piece size on the electromagnetic force distribution.

Recently, Kumar and DebRoy [57] developed a numerical model to accurately calculate the \mathbf{J} and \mathbf{B} fields and the resulting electromagnetic force field in three dimensions in the entire weldment. Contributions of the electrode current, arc plasma and current distribution inside the three-dimensional workpiece to the magnetic field and the electromagnetic force field were determined. They evaluated the effects of different arc locations and work piece geometry on the electromagnetic force field. They concluded that the accuracy of the computed electromagnetic force field can be significantly improved by considering the contributions of electrode current, arc plasma and the current distribution within the workpiece.

2.2.6.2 Marangoni force or surface tension gradient force

The spatial gradient of surface tension is known as Marangoni stress. The spatial variation of the surface tension at the weld pool surface may arise due to variations of both temperature and composition in the weld pool. This stress arises due to spatial variation of temperature and composition, which can be expressed as:

$$\tau = \frac{\partial \gamma}{\partial T} \frac{\partial T}{\partial r} + \frac{\partial \gamma}{\partial C} \frac{\partial C}{\partial r} \quad 2.6$$

where τ is the shear stress due to surface tension, T is the temperature, r is the distance along the surface from the heat source, and C is the concentration of surface active element. The spatial variation of the surface tension (i.e. the gradient) present on the weld pool surface can cause the molten metal to be drawn along the surface from the region of low surface tension to the region of higher surface tension. As temperature increases for a liquid of fixed composition, the surface tension decreases. However, the composition gradients act to complicate the temperature effects, depending on how a change in

composition of any particular component affects the surface tension. Impurities in the weld metal often alter the surface tension of the molten metal through surface activity.

Limmaneevichitr and Kou [63, 64] observed the Marangoni stress driven flow in the weld pool experimentally. In their experiments, the Marangoni convection was introduced in a transparent pool of NaNO₃ with a defocused CO₂ laser beam. Figures 2-7 (a) and (b) show the Marangoni convection with an outward surface flow in the NaNO₃ molten pool, which has a $\partial\gamma/\partial T$ value of $5.6 \times 10^{-5} \text{ N m}^{-1} \text{ K}^{-1}$. They observed that the outward surface flow is much faster than the inward return flow due to Marangoni shear stress. The liquid mass continuity indicates that the amount of liquid flowing in outward and inward directions should be the same. Hence, the return inward flow, which occupies a much larger area than the surface outward flow, has a lower velocity than the outward flow.

To study the effect of surface active elements on the liquid convection, Limmaneevichitr and Kou [63, 64] added C₂H₅COOK into the NaNO₃ molten pool, and they found the direction of Marangoni convection was reversed. Figures 2-7(c) and (d) show the inward surface flow when 2 mol% of C₂H₅COOK was added into the pool. This inward flow is due to the presence of C₂H₅COOK which is a surface active compound.

Sahoo et al. [65] determined the $\partial\gamma/\partial T$ as a function of both temperature and composition, which is expressed as:

$$\frac{\partial\gamma}{\partial T} = A - R\Gamma_s \ln(1 + Ka_i) - \frac{Ka_i}{(1 + Ka_i)} \frac{\Gamma_s (\Delta H^\circ - \Delta \bar{H}_i^M)}{T} \quad 2.7$$

where A is the $\partial\gamma/\partial T$ value for pure metal, Γ_s is the surface excess at saturation, K is the adsorption coefficient, a_i is the activity of species i in the solution, ΔH° is the standard heat of adsorption, and $\Delta \bar{H}_i^M$ is the partial molar enthalpy of mixing of species i in the solution. Mundra and DebRoy [66] calculated fusion zone profiles for pure iron and an iron with 0.03 wt. % O alloys and found that oxygen concentration significantly affects the weld pool shape and the aspect ratio. Pitscheneder et al. [67] applied eq. 2.7 and a thermo-fluid model to study the effect of sulfur content and heat input on the weld pool geometry.

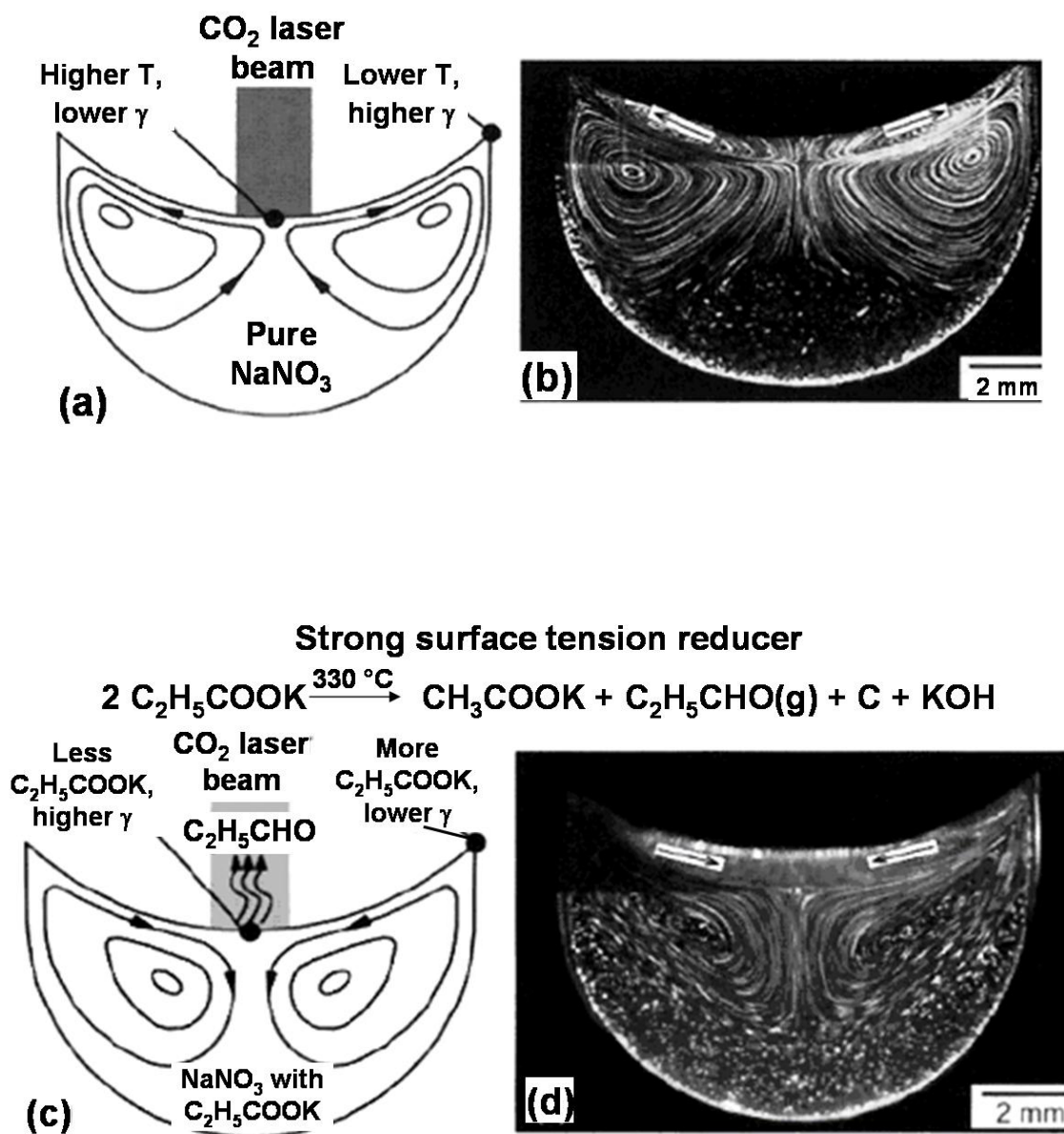


Figure 2-7: (a, b) Marangoni convection with an outward flow in a NaNO_3 molten pool; (c,d) Marangoni convection with an inward flow in a NaNO_3 pool containing 2 mol % of $\text{C}_2\text{H}_5\text{COOK}$ as a surface active agent. Adapted from Limmaneevichitr and Kou [63, 64].

They found that the Peclet number was greater than 200 for laser power of 5.2 kW. Such high Peclet number indicated that convection was dominant in transporting the heat in the weld pool. As a result, the weld pool geometry was largely determined by the direction of the liquid flow.

2.2.4.3 Buoyancy force

The buoyancy force (F_b) in weld pools arises from gravity. It is defined as [36]:

$$F_b = \rho g \beta (T - T_{ref}) \quad 2.8$$

where ρ is the density of liquid metal, g is the acceleration due to gravity, β is the thermal expansion coefficient, T is the temperature of the liquid metal, and T_{ref} is an arbitrarily selected reference temperature. It can be seen from the above equation that this force has its origin in gravity due to differences in densities. The density difference in the molten weld pool can, in turn, have two origins: (1) the local temperature and (2) the local composition. The Boussinesq approximation [68] was used in the calculation of buoyancy force driven flow. In other words, the variation in the density of the liquid metal is ignored, except insofar as it gives rise to a buoyancy force, which is also termed as the gravitational force [3-5, 36].

2.2.4.4 Shear stress induced by plasma jet

When an electric arc is used during welding, the arc plasma moves outward at high speeds along the weld pool surface, which can exert an outward shear stress at the pool surface, as shown in figure 2-6(e). The direction of the shear stress is similar to that resulting from the surface tension gradient with negative $\partial\gamma/\partial T$ value. The liquid metal flows from the center of the pool surface to the pool periphery, and then returns below the pool surface in the middle of the molten pool. Matsunawa and Shinichiro [69, 70] experimentally studied the importance of the plasma shear stress during GTA welding.

They found that the surface tension gradient force dominates at low arc current levels while the plasma shear stress was dominant at very high arc current, generally above 450 Amp.

As shown in the above discussion, the different driving forces play important role in dissipating the heat in the weld pool and determine the temperature distribution in both the weld pool and the heat affected zone. In short, the convective heat transfer and fluid flow in the weld pool need to be incorporated in the model to capture the following effects:

- (a) Surface active element content:** The conduction based heat transfer models are not able to capture the effect of surface active elements like sulfur, phosphorus and oxygen in the workpiece. Various researchers [80-82] have shown that the content of these elements in the workpiece significantly affects the weld pool dimensions. For example, Heiple and Roper [81] observed experimentally that the aspect (i.e. depth-to-width) ratios of the weld pool changes from 0.25 to 1.05 by changing the weight % oxygen in the weld pool from 0.0 % to 0.075%. A similar behavior was also observed by Zacharia et al. [82] for the GTAW fusion welding of 304 stainless steel containing sulfur. The effect of these elements can be easily captured by including the convection calculations because they take into account the effect of these elements on the surface tension of the liquid metal
- (b) Effect of welding process parameters:** The convective heat transfer and fluid flow models can easily differentiate the effect of various welding process parameters on the weld pool geometry which is not possible with conduction based models.
- (c) Differentiate between welding processes geometry:** The conduction based heat transfer models can not differentiate between arc welding or laser welding. The inclusion of convection in the model provides the capability to capture the effect of electromagnetic force on the weld pool during arc welding. This leads to different weld pool shape and size even for similar heat inputs.

In short, ignoring the effect of convection during simulation will lead to inaccurate weld pool shape, size, thermal cycles and cooling rates. Therefore, to

accurately simulate the weld heat transfer and fluid flow, the various driving forces need to be incorporated in the governing conservation equations and corresponding boundary conditions.

2.2.5 Convection versus conduction on weld pool heat transfer

In the weld pool, heat is transported by a combination of convection and conduction. The relative importance of convection versus conduction in transferring heat in the molten pool can be evaluated using the Peclet number (Pe), which is given by [4, 68]:

$$Pe = \frac{\text{heat}_{\text{convection}}}{\text{heat}_{\text{conduction}}} = \frac{u_R \rho C_{pl} L_R}{k_l} \quad 2.9$$

where u_R and L_R are the characteristic velocity and length in the weld pool, respectively, ρ is the density, and C_{pl} and k_l are the specific heat and thermal conductivity of liquid metal, respectively. When Pe is large, which in physical terms means large liquid metal velocity, large weld pool, and poor thermal diffusivity (i.e. $k_l / (\rho C_{pl})$), the liquid metal convection significantly affects the heat transfer in the weld pool. In contrast, when Pe is small, say much less than unity, the conduction plays an important role in the heat dissipation in the weld pool [3-5]. Various researchers have calculated the Peclet number for various welding processes and found that Pe is more much higher than unity. Therefore, the models which take into account only the conduction heat transfer in the pool, is not able to accurately describe the heat transport process in the GTA weld pool.

2.2.6 Turbulence in weld pool

During linear welding, the temperature and velocity fields in the weld pool often do not change appreciably except at the beginning and the end of the welding. In these quasi-steady weld pools, local velocities typically have two components, a time-

independent or steady mean velocity and a time-dependent or fluctuating velocity. The instantaneous velocity in x, y and z directions can be represented by u_x , u_y and u_z , respectively, in the following form:

$$u_x = \bar{u}_x + u'_x, \quad u_y = \bar{u}_y + u'_y, \quad u_z = \bar{u}_z + u'_z \quad \mathbf{2.10}$$

where \bar{u}_x , \bar{u}_y and \bar{u}_z are the mean velocity components and u'_x , u'_y , u'_z are the fluctuating velocity components. The time-smoothed value of the cross products of the fluctuating components of the velocity and the density, i.e. $\overline{\rho u'_x u'_z}$, $\overline{\rho u'_y u'_z}$ and $\overline{\rho u'_x u'_y}$ have the dimension of stress and are called the Reynold stress. These Reynold stresses designate the momentum transfer in the system due to the turbulent fluctuations.

For modeling the turbulence behavior during material processing, three different kinds of models are generally used. These are mixing length models, one-equation models and two-equations (or, k- ϵ) models. The mixing length models are very simple in nature. These models calculate the turbulent viscosity using the velocity gradient and the mixing length which is generally obtained based on experiments. Prandtl proposed the following expression for defining the turbulent viscosity, μ_t [68]:

$$\mu_t = \rho l_m^2 \frac{\partial \bar{u}_x}{\partial y} \quad \mathbf{2.11}$$

where, l_m is the mixing length. For the three-dimensional flow, Badwin-Lomax suggested the following expression for calculating the turbulent viscosity [68]:

$$\mu_T = \rho l_{\text{mix}}^2 |\omega|$$

where, $|\omega|$ is the magnitude of the vorticity vector. This mixing length is model is very attractive because it enables us to calculate the unidirectional flows quite accurately without recourse to excessive computational labor [68].

The one-equation models are less common in use and require the solution of one more equation along with the Navier-Stokes and the energy equation. In this kind of model, the turbulent viscosity, μ_t , is calculated as a product of mixing length and turbulent energy as follows [68]:

$$\mu_t = \rho l_m K^{1/2} \quad 2.12$$

where, l_m is the previously defined mixing length and K is the kinetic energy, due to turbulent fluctuations in the velocity and is defined as [68]:

$$K = \frac{1}{2} [u_x'^2 + u_y'^2 + u_z'^2] \quad 2.13$$

i.e. half the sum of the time-smoothed values of the square of fluctuating velocity components. In using the one equation models for calculating turbulence, the information on mixing length and boundary conditions for turbulence energy equation are required. To calculate the value of turbulent viscosity, the kinetic energy, K need to be computed by solving one more differential equation which includes the information on fluctuating velocity components. This makes the computational task complex because the equations to be solved are simultaneous and non-linear partial differential equations.

In two equation models (i.e. k - ϵ model), the turbulent viscosity is determined as the product of two factors: a characteristic energy and the reciprocal of characteristic frequency- both of which need to be evaluated as a solution of differential equations. The principle postulates of two-equation models can be summarized as follows:

$$\mu_t = \rho KW^{-1/2} \quad 2.14$$

where,

$$l_m = (KW)^{1/2} \quad 2.15$$

and W is the mean square of the frequency of the turbulent eddies or the gradient of acceleration of the turbulent field. The K and W are calculated in this model by solving the appropriate conservation equations. The calculation procedure is quite complex because several non-linear partial differential equations have to be solved simultaneously. Furthermore, the conservation equations used to define K and W , have various empirical constant parameters. The values of these parameters depend on the type of flow and may affect the final calculation. The empirical constants in these models have been determined using experimental data from large scale parabolic flows. In contrast, the

fluid flow in the weld pool is elliptic in nature. The difference in nature of the flow in the weld pool has limited the use of $k-\varepsilon$ model for modeling the turbulence in the weld pool.

The convective heat and mass transport in the weld pool is affected by both the mean as well as the fairly significant fluctuating velocities that are present in the weld pool. In order to accurately simulate the heat transfer and fluid flow in the weld pool, it is important to understand the turbulent behavior of the liquid metal. It is not yet completely clear whether the flow in the weld pool is turbulent in nature. However, there are evidences that suggest the existence of turbulence in the weld pool. Malinowski-Brodnicka et al. [71] measured the flow velocity in AISI 310 stainless steel weld pools and found that the Reynolds number was about 3000. Comparing this value to the classical critical Reynolds number of 2100, they concluded that the flow in the weld pool was most likely turbulent.

Choo and Szekely [72] first considered turbulence in the GTA weld pool using a $K-\varepsilon$ turbulence model. They showed that the turbulence can affect the weld pool depth significantly. Hong et al. [39, 40, 62] also developed a $K-\varepsilon$ turbulence thermo-fluid model, where the free surface of the weld pool and the wall function boundary for the solid-liquid interface were considered by using a dynamic grid-remapping technique. They demonstrated that a fluid flow model based on laminar flow can over-predict the pool depth, as shown in figure 2-8 for a GTA weld in 304 stainless steel. More recently, Yang and DebRoy [53] studied the turbulent heat transfer and fluid flow during GMA welding of HSLA-100 steels. Hong et al. [62] analyzed the spatial variation of turbulent viscosity and turbulent thermal conductivity in the weld pool based on vorticity based mixing-length turbulence model. Their model was algebraic in form and, therefore, significantly less computationally intensive than the $k-\varepsilon$ turbulence model. They [62] showed that vorticity based mixing-length approach can satisfactorily describe enhancement of transport properties and convective heat transport in hemispherical GTA weld pools. Due to the difficulties in applying the $K-\varepsilon$ turbulence model, a more widely used approach is to use an effective viscosity and an effective thermal conductivity in the weld pool [33-39, 54, 73, 74].

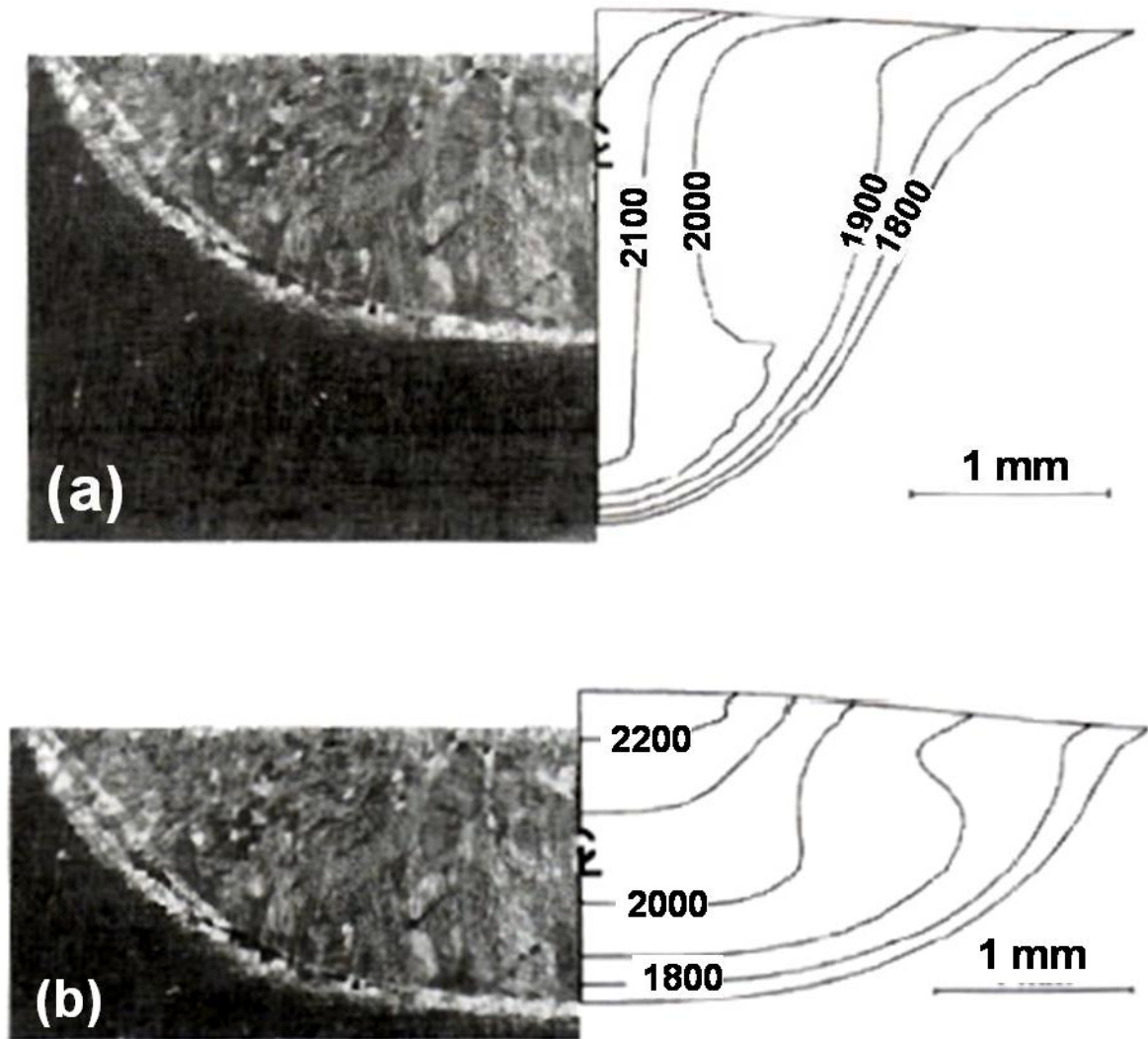


Figure 2-8: Weld pool shapes and isotherms in a 304 stainless steel with 50 ppm sulfur calculated based on (a) laminar flow and (b) turbulent flow. Adapted from [40].

Recently, De and DebRoy [59, 60] and Mishra and DebRoy [61] proposed a procedure combining a heat transfer and fluid flow model and an optimization algorithm to estimate the effective viscosity and thermal conductivity in GTA welding. Their model could determine the effective viscosity and thermal conductivity as a function of power input from a limited volume of experimental data, and the computed weld pool geometry were in good agreement with the experimental results.

2.2.7 Weld pool free surface calculation

It should be noted that the weld pool top surface, i.e., the liquid/gas interface, is a free surface. Accurate calculation of heat transfer and fluid flow in a deformable weld pool requires the knowledge of the free surface profile. Lin and Eagar [75] experimentally measured the depression of the pool top surface during GTA stationary welding of 304 stainless steel and found that the surface depression can be as high as 4.5 mm in the stainless steel weld pools when arc current is about 300 A. Such deformed pool surface may affect the heat transfer and fluid flow in the weld pool, the weld pool geometry and the temperature distribution in the HAZ [72]. In the worst case, the severely deformed surface may result in the formation of several weld defects such as humped bead and undercutting [27, 76]. Hence, understanding the weld pool top surface profile and its effect on the heat transfer and fluid flow is very important.

Previous computer simulation efforts to understand welding processes and welded materials through numerical heat transfer and fluid flow calculations have focused mainly on simple systems [23-33, 36, 38-45, 53-62]. Most of these studies considered butt welding of rectangular workpiece and ignored any deformation of the weld pool top surface. However, such simple systems may not be readily applicable to more complicated and useful welding processes such as the GMA fillet welding process. The various physical process occurring during gas-metal-arc welding of fillet joints are shown in figure 2-9. Previous efforts to model GMA fillet weld were limited either to conduction heat transfer models or symmetric V-shape fillet joint [32, 77, 78].

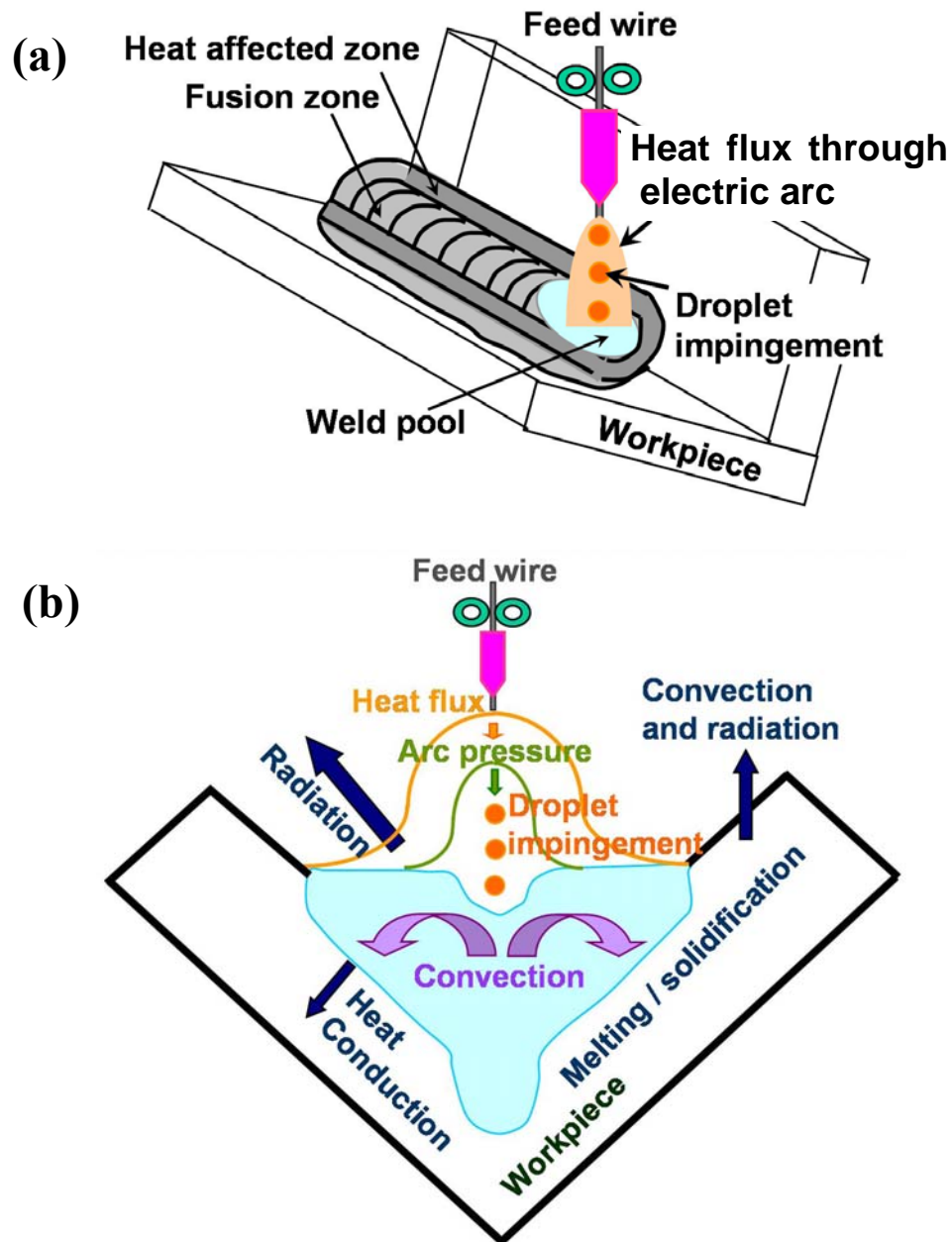


Figure 2-9: Schematic plot depicting the GMA fillet welding process: (a) interaction between the heat source and the base material; and (b) the transverse section showing the physical processes occurring in the weld pool.

For example, Jeong and Cho [79] analytically calculated transient temperature distribution in the fillet welds assuming a flat bead surface. Cho and Kim [78] studied the thermal history using a two-dimensional finite element analysis considering the bead shape for the horizontal fillet joints. Cho and Kim [78] calculated the temperature distribution during GMA fillet weld by ignoring the effect of convective heat transfer. Recently, Zhang et al. [34, 35] developed a three dimensional heat transfer and fluid flow of GMA fillet welding. Their model used a boundary fitted coordinate system to accurately calculate temperature and velocity fields. They showed that the liquid metal convection plays a dominant role in dissipating the heat in the weld. However, their model is only applicable to simulate the temperature and velocity distribution in symmetric flat linear welding of V-shape joints. In practice, the welding engineers come across various kinds of joints such as L-joint, uphill and downhill welding of fillet joints. Therefore, we need a transport phenomena based model which can predict the temperature field and weld bead geometry during GMA fillet welding in various different positions.

2.3 Estimation of Uncertain Input Parameters

Although numerical heat transfer and fluid flow models have provided significant insight about fusion welding processes and welded materials, several model input parameters cannot be easily prescribed from fundamental principles. As a result, the calculated outputs of these models do not always agree with the experimental results. In order to address this problem, the inverse modeling technique is generally used to find the value of uncertain process variables using a limited volume of experimental data.

Inverse modeling is a new research paradigm which is an interactive combination of limited amount of experiments and numerical analysis to find uncertain input parameters [83-91]. Figure 2-10 shows the difference between commonly used numerical models and this approach. This inverse modeling approach provides more reliable results due to accurate values of input parameters.

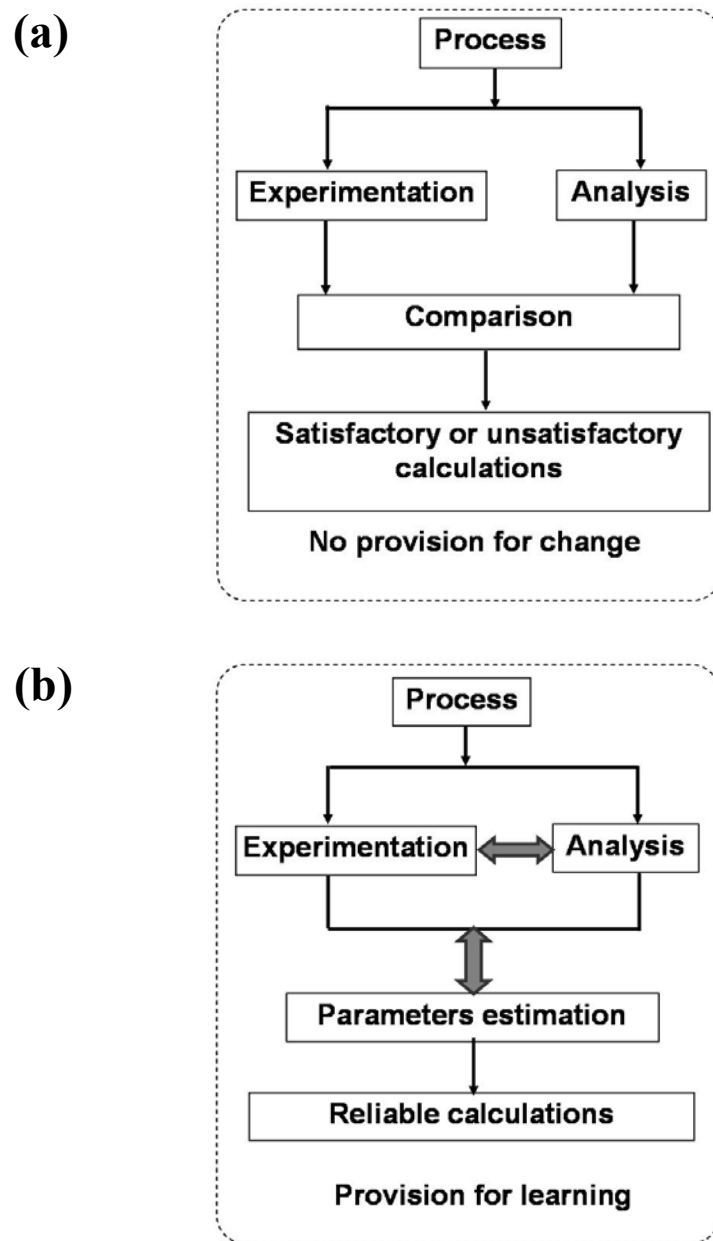


Figure 2-10: (a) Common paradigm; (b) New paradigm of inverse modeling [80]

To estimate the values of uncertain input parameters, both measured values and corresponding calculated quantities are required. Experiments are needed to determine the unknown parameters or uncertain quantities. The purpose of inverse methods is to provide analytical tools to learn quantitatively more about the uncertain parameters. This is in contrast of visual comparison of the experimental and computational results which existed implicitly in commonly-used research paradigm in last two-three decades. Since most inverse problems cannot be solved analytically, computational methods play a fundamental role in finding the values of the input parameters [83-86].

In this technique, the phenomenological models which govern the physics of the problem are generally referred as forward models. These models are then coupled with optimization algorithms to minimize an objective function which represents the error between calculated outputs and the desired or experimentally obtained outputs. It is an iterative process, where the optimization algorithm first starts the calculation by running the phenomenological model using the initial guessed values of uncertain input parameters. The calculation is repeated till the objective function reaches the prescribed tolerable value.

The optimization schemes are computationally very intensive since they require multiple runs of the forward model or the phenomenological model. In the literature of inverse modeling application in welding process, models were extremely simplified for the convenience of the computation. As a result, the inverse modeling applications in welding process reported [92, 93] so far have been based on rather simple heat conduction equations, often utilizing Rosenthal's analytical solution of heat conduction equation that completely ignores convection in the weld pool. Furthermore, the primary focus of these works was to determine the distribution of heat flux at the work-piece surface exposed to an arc or a laser beam from measured temperatures at several monitoring locations in the solid region. It seems that the adaptation of the simplified heat conduction equation in the previous work [92, 93] was mandated, at least to a large extent, because of the lack of advanced software necessary to rigorously analyze heat and fluid flow in the weldment. With the advances in the computational hardware and software in recent years, it is now possible to undertake computationally intensive

optimization schemes that embody realistic three dimensional numerical heat transfer and fluid flow calculations. De and DebRoy [59, 60] and Mishra and DebRoy [61] recently developed inverse models to calculate various unknown input parameters such as the arc efficiency, effective thermal conductivity and effective viscosity for numerical transport phenomena based modeling of the welding processes. However, they implemented this technique to find uncertain input parameters in Gas-Tungsten-Arc welding which is much easier than GMA fillet welding process because of the relative simplicity of the process and geometric configurations. In this thesis work, the uncertain welding variables such as the arc efficiency, effective thermal conductivity and effective viscosity are calculated using derivative base optimization techniques. Various alternative techniques are explored in this research work to find better optimal values of these uncertain input variables.

2.4 Neural Networks

For predicting the alternate combinations of welding variables to achieve desired geometry, the bi-directional model requires multiple runs of phenomenological model. The use of heat transfer and fluid flow model as the phenomenological model in the bi-directional model increases the computation time. The use of neural network in place of heat transfer and fluid flow model provide significant computational economy since it takes about a second to produce outputs compared to heat transfer and fluid flow model of GMA fillet welding takes approx. 40 minutes. The neural network are also capable of relating input variables like welding process parameters and material properties with weld characteristics such as the weld geometry, cooling rate, liquid velocities and peak temperature in the weld pool. The ability of neural network to learn from the training data i.e. the outputs of heat transfer and fluid flow model makes it a good choice to be used in place of heat transfer and fluid flow model in this work.

Neural Networks (NNs) are computational systems whose architecture and operation are inspired from our knowledge about biological neural cells (neurons) in the

brain. NNs can be described either as mathematical and computational models for non-linear function approximation, data classification, clustering and non-parametric regression or as simulations of the behavior of collections of model biological neurons [94-97]. The NNs are analogous to biological neural structures. The starting point for any kind of neural network analysis is a model neuron whose behavior follows closely our understanding of how real neurons work. This model neuron is shown in figure 2-11. The neuron has N input lines which represent various welding variables such as arc current, voltage and material properties and a single output which can be any weld geometry parameter, peak temperature or cooling rate. Each input signal is weighted, that is, it is multiplied with the weight value of the corresponding input line (by analogy to the synaptic strength of the connections of real neurons). The neuron will combine these weighted inputs by forming their sum and, with reference to a threshold value and activation function; it will determine its output.

Neural network models are powerful non-linear regression analysis methods that can relate input variables like welding process parameters and material properties with weld characteristics such as weld pool geometry, cooling rates and mechanical properties [98-123]. In mathematical terms, we may describe the neuron by writing the following pair of equations [94-96]:

$$y = f \left(\sum_{i=0}^N w_i x_i \right) \quad 2.16$$

where $x_1, x_2, x_3, \dots, x_N$ are the input signals which represent various welding variables such as arc current, voltage and material properties, $w_1, w_2, w_3, \dots, w_N$ are the synaptic weights to include the non-linear behavior of these input variables on the output, y is the output signal of the neuron, and $f(.)$ is the *activation function*. The combination of a fixed input, $x_0 = 1$, and of an extra input weight, w_0 , accounts for the *bias* input [94-96]. The activation function, denoted by $f(.)$, defines the output of the neuron in terms of the activity level at its input and is essential to capture the non-linear interaction of various welding variables like arc current, voltage, wire feed rate, welding speed and material properties on the weld geometry, cooling rate and peak temperature in the weld pool.

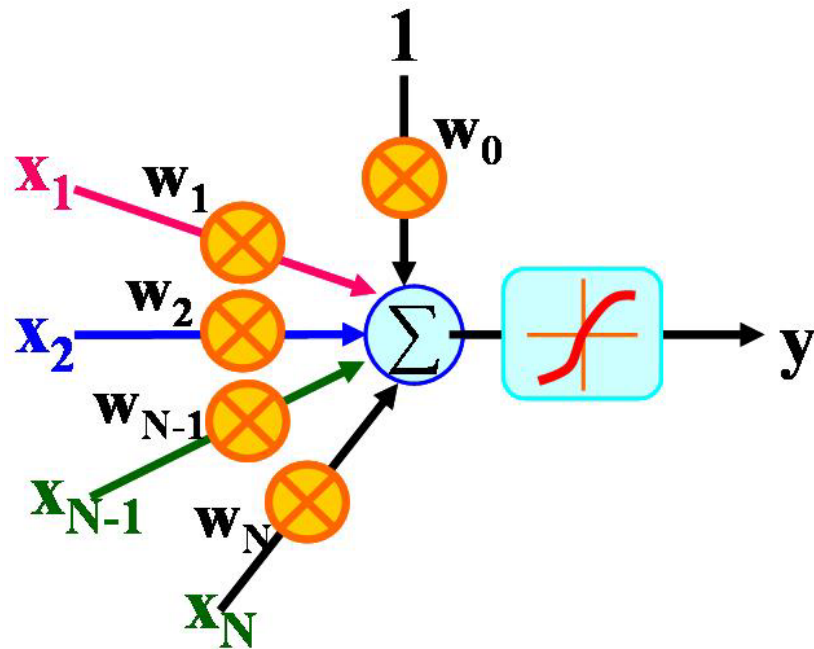


Figure 2-11: A basic neuron structure

The most common form of activation function used in the construction of NNs is the symmetric *sigmoid* function or hyperbolic tan function [94-96]. It is defined by:

$$f(u) = \tanh(au) \quad 2.17$$

where a is the *slope parameter* of the sigmoid function. By varying the parameter a , we can obtain sigmoid functions of different slopes. The nice feature of hyperbolic tangent function is that their derivatives are easy to compute.

2.4.1 The Backpropagation Algorithm

The Error-Backpropagation (or simply, backpropagation) algorithm is the most important algorithm for the training of multilayer feed-forward NNs [94-97]. It derives its name from the fact that error signals are propagated backward through the network on a layer-by-layer basis. The backpropagation algorithm is based on the selection of a suitable error function or objective function which is actually the error between testing output data like weld geometry, cooling rate, peak temperature and the corresponding predicted data from neural network. The desired outputs of the network such as weld penetration, leg-length, throat, cooling rate and peak temperature is dependent on input welding conditions, material properties and the network parameters such as the weights and the thresholds. The basic idea is that the objective function has a particular surface over the weight space and therefore an iterative process such as the gradient descent method can be used for its minimization. The method of gradient descent is based on the fact that, since the gradient of a function always points in the direction of maximum increase of the function then, by moving to the direction of the negative gradient induces a maximal "downhill" movement that will eventually reach the minimum of the function surface over its parameter space. This is a rigorous and well established technique for minimization of functions and has probably been the main factor behind the success of backpropagation. However, as we shall see in the next section the method does not guarantee that it will always converge to the minimum of the error surface as the network can be trapped in various types of minima [94-97].

A typical multilayer feed-forward NN is shown in figure 2-12. The units (or nodes) of the network are nonlinear threshold units described by eq. 2.16 and their activation function is given by eq. 2.17. The inputs of this network in nodes k represent set of welding variables and their effects propagate through the layer j to output layer which is actually a set of outputs such as weld geometry parameters like penetration, throat, leg-length, peak temperature, root-mean square velocity in the weld pool and the cooling time from 800 °C to 500 °C.

The units are arranged in layers and each unit in a layer has all its inputs connected to the units of a preceding layer (or to the inputs from the external world in the case of the units in the first layer), but it does not have any connections to units of the same layer to which it belongs [94-101]. The layers are arrayed one succeeding the other so that there is an input layer, multiple intermediate layers and finally an output layer. Intermediate layers, that have no inputs or outputs to the external world, are called hidden layers. Figure 2-12 shows a multilayer network with only one hidden layer. Back-propagation neural networks are usually fully connected. This means that each unit is connected to every output from the preceding layer (or to every input from the external world if the unit is in the first layer) as well as to a bias signal which is common to all the units. Correspondingly, each unit has its output connected to every unit in the succeeding layer. Generally, the input layer is considered as the distributor of the information contained in welding variables and is not therefore counted as a layer. Therefore, in figure 2-12, the hidden layer is the first layer of the network.

The backpropagation training consists of two passes of computation: a forward pass and a backward pass [94-96]. In the forward pass an input pattern vector an input vector (i.e. set of welding variables) is applied to the sensory nodes of the network that is, to the units in the input layer. The signals from the input layer propagate to the units in the first layer and each unit produces an output according to eq. 2.16. The outputs of these units are propagated to units in subsequent layers and this process continuous until the signals reach the output layer where the actual response of the network (i.e. weld geometry parameters) to the input vector is obtained.

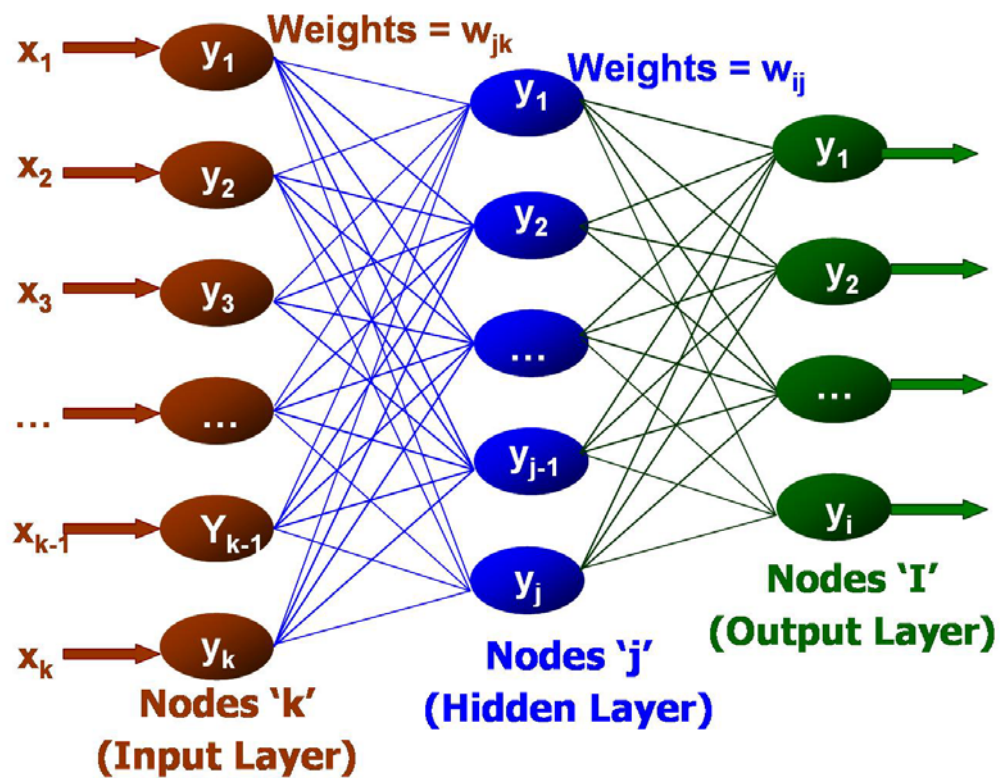


Figure 2-12: Neural network with input layer, single hidden layer and an output layer.

During the forward pass the synaptic weights of the network are fixed. During the backward pass, on the other hand, the synaptic weights are all adjusted in accordance with an error signal which is propagated backward through the network against the direction of synaptic connections.

The backpropagation algorithm can be implemented in two different modes: on-line mode and batch mode [94-96]. In the on-line mode the error function or the objective function is calculated after the presentation of each input pattern (i.e. set of welding conditions) and the error signal is propagated back through the network modifying the weights before the presentation of the next pattern or set of welding conditions. This error function is usually the Mean Square Error (MSE) of the difference between the desired and the actual outputs of the network. Then the new weights remain fixed and a new set of welding conditions is presented to the network and this process continuous until all the set of welding conditions have been presented to the network. The presentation of all the set of welding conditions is usually called one epoch or one iteration. In practice many epochs are needed before the error or objective function becomes acceptably small. In the batch mode the error signal or objective function is again calculated for each input set of welding conditions but the weights are modified only when all input set of welding conditions have been presented.

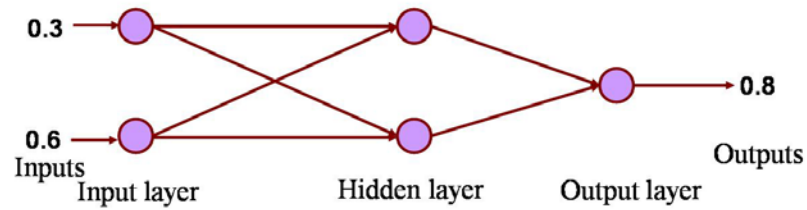
2.4.2 Example showing the application of back-propagation algorithm to find the optimal weights in the neural network

The working of neural network is explained below using a simple example. There are two inputs and one output in the network. The values of the inputs are 0.3 and 0.6 and the desired output value is 0.8. The steps involved in the calculation are as follows:

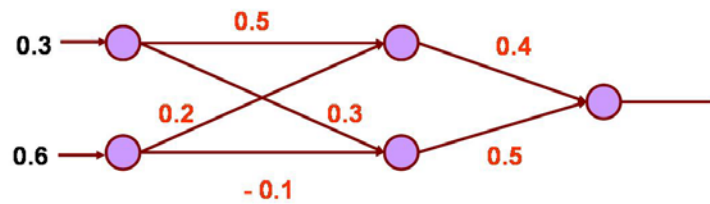
Step 1: Initially, the network architecture is decided by selecting the number of hidden nodes in the hidden layer. In the example shown in figure 2-13, two nodes are selected in the hidden layer for simplifying the calculation.

Step 2: The weights are assigned randomly in the range of $[-0.5, 0.5]$ to each link.

Step 1: Selection of the network architecture

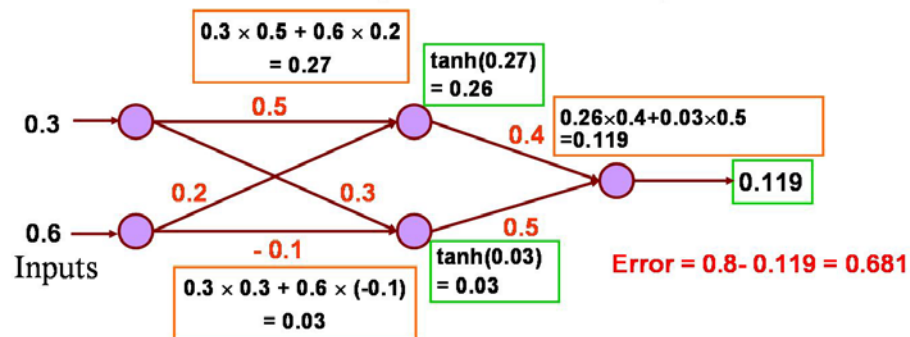


Step 2: Initialization of the weights



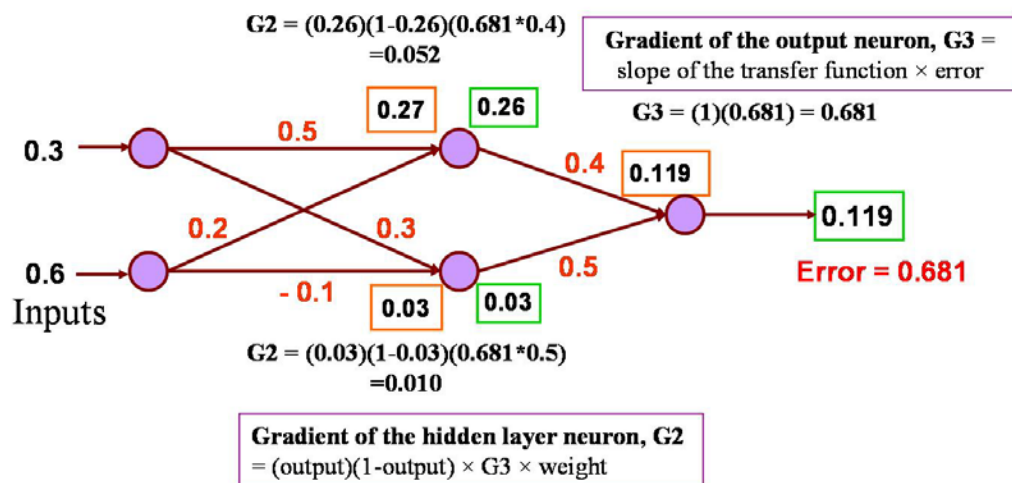
Step 3: Forward pass

Calculation of the outputs and error in the prediction



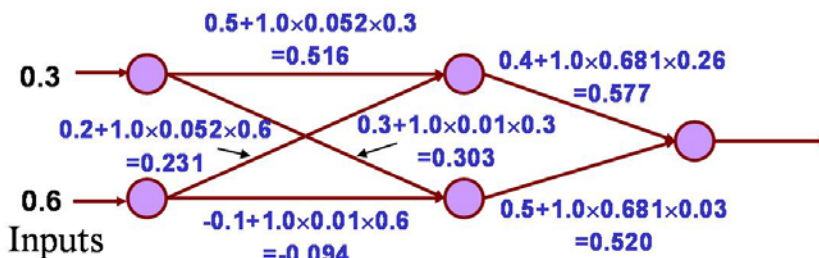
Step 4: Backward pass

(a) Gradient calculation at each node



(b) Update of weights

New Weight = Old Weight + {(learning rate) × (gradient) × (prior output)}
Assuming learning rate = 1.0



Step 5: Repeat step 3 and step 4 till convergence

The error in the network at second iteration using modified weights

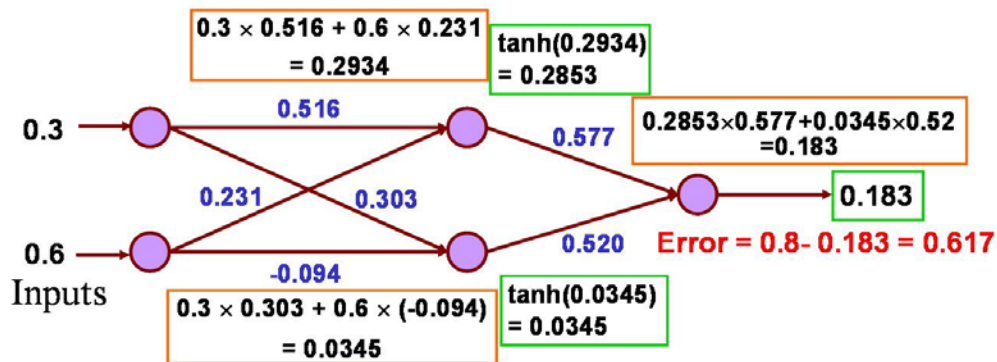


Figure 2-13: Example showing the application of back-propagation algorithm to find the optimal weights in the neural network. The red colored numbers in the figure represent the current weights while blue colored numbers represent the updated values of the weights. The orange boxes show the summed input to a neuron while green boxes show the output of the neuron. In the network, the values of the inputs are 0.3 and 0.6 and the desired output value is 0.8. This example shows how the weights are updated in the network. The error in the network reduces to 0.617 at second iteration compared to 0.681 at first iteration.

Step 3: The outputs at each nodes are calculated using the assigned weights and the inputs to the neuron as shown in step 3 in figure 2-13. The following activation functions were used in the calculation for simplifying the demonstration of calculation procedure.

$$y = \tanh\left(\sum_{i=1}^2 w_i x_i\right); \quad \text{for hidden nodes}$$

$$y = \left(\sum_{i=1}^2 w_i x_i\right); \quad \text{for output nodes}$$
2.18

where w_i and x_i are the weights and the inputs to a node, respectively. This step is known as forward pass since the information about the inputs is traveling in the forward direction. The aim of the network is to obtain the desired output value by prescribing the input value. To achieve the desired output value, the error in the output value should be zero. Therefore, the error in the network is calculated in this step for the assigned weights. The next step is to modify the weights so that the error in the network reduces.

Step 4: In this step, the weights are modified using the back-propagation algorithm by transferring the error value in the backward direction. This step is termed as backward pass. The steepest gradient algorithm is used in this demonstration to modify the weights. Initially, the gradient was calculated at each node in the network as shown in step 4(a) figure 2-13. Later, the gradient information was used to modify the weights in the network.

Step 5: Steps 3 and 4 are repeated till the error in the network reaches an acceptable value. Figure 2-13 shows that the error in second iteration has reduced to 0.617 from 0.681.

2.4.3 Modeling issues

2.4.3.1 Finding optimal weights

Since back-propagation uses a gradient-descent procedure, the network follows the contour of an error surface (or, objective function) with weight updates moving it in

the direction of steepest descent [94-96]. The back-propagation algorithm calculates the direction of steepest descent on the surface, and jumps down the surface a distance proportional to the learning rate and the slope, picking up momentum as it maintains the steepest descent direction. The more advanced or modified back-propagation algorithm uses conjugate gradient method in place of steepest descent method to find the optimal weights. In the conjugate gradient method, once the algorithm has minimized along a particular direction, the second derivative along that direction is kept at zero. Conjugate directions are selected to maintain this zero second derivative on the assumption that the surface is parabolic. In reality, on a complex error surface the conjugacy deteriorates, but the algorithm still typically requires far less iterations than back propagation, and also converges to a better minimum (to settle down thoroughly, back propagation must be run with an extremely low learning rate). Levenberg-Marquardt is typically the fastest of the training algorithms, although unfortunately it has some important limitations, specifically, it can only be used on single output networks and has large memory requirements [94-96]. It makes this algorithm impractical for reasonably big networks with large number of weights and outputs. Conjugate gradient algorithm is nearly as good, and doesn't suffer from these restrictions. The conjugate gradient algorithms require only a little more storage than the simpler algorithms, so they are often a good choice for networks with a large number of weights. It is the recommended technique for any network with a large number of weights (more than a few hundred) and multiple output units.

2.4.3.2 Gradient versus stochastic optimization techniques

In gradient descent algorithms we start at some point on the error function defined over the weights, and attempt to move to the global minimum of the function. In the simplified function of figure 2-14(a) the situation is simple. Any step in a downward direction will take us closer to the global minimum. For real problems, however, error surfaces are typically complex, and may more resemble the situation shown in figure 2-14(b).

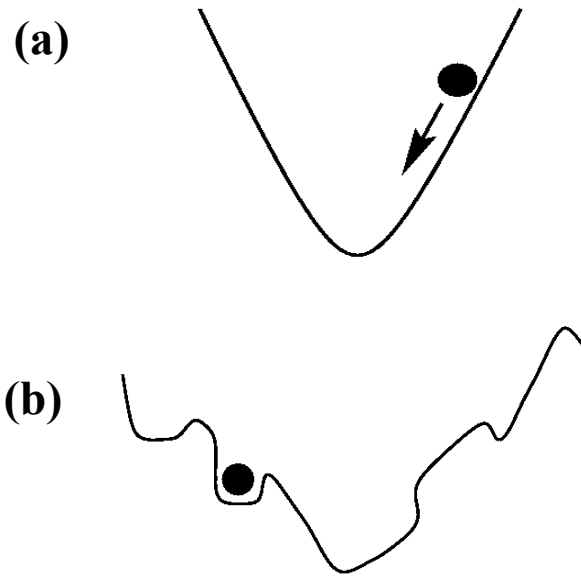


Figure 2-14: (a) Simple smooth variation of objective function with variables; (b) Complex variation of objective function with variables

Here there are numerous local minima, and the ball shown is trapped in one such minimum. Progress here is only possible by climbing higher before descending to the global minimum. Gradient based methods get easily trapped in such local minima. Generally, stochastic optimization techniques are capable of finding the global minima and coming out of these local traps.

Genetic algorithm (GA) is a stochastic, population based optimization technique that can find the global optimal solution independent of the initial guessed values [124-126]. Genetic algorithms work with a set of "individuals" - a population, where each individual is a solution of a given problem [124]. The initial population defines the possible solutions of the optimization problem, i.e., sets of variables that need to be optimized. There are two popular ways of representing the variables in the population in GA: binary and real numbers.

In binary genetic algorithm, each individual is a binary string consisting of combinations of zeroes and ones. The binary string format allows modification and manipulation of the set of unknown welding variables. A set of coded variables is like a chromosome in genetics, in other words a modifiable carrier of information. The aim of genetic algorithm is to find the solutions having least error between the calculated and experimentally obtained weld pool geometry. To achieve this aim a fitness function is defined as the squared error between the predicted and the experimentally obtained weld pool geometry. Fitness evaluation is a procedure necessary to decide the survival of each individual. Individuals with small fitness values represent better values of the unknown welding parameters.

The least fitted individuals will be assigned a lower probability so that their features are excluded from the solution sets over time. Thus, good features spread over the whole population. The next step is to use each individual's fitness and genetic operations, i.e., crossover/mating, selection and mutation to produce the next generation of population. Crossover of the most fitting individuals leads to exploration of the most promising solution space. In the long run the population will converge to a set of optimal solutions. The selection (reproduction) operator selects chromosomes according to their fitness function values. In this procedure, the well-fitted individuals have higher chance

of getting selected. Mutation increases the algorithm's search space for the optimized solutions outside the current region of parameter space. The flowchart and the details about these operations are presented in figure 2-15. Generally binary representation of variables converges slowly compared to the real representations [124, 125]. In addition, since the binary genetic algorithm has its precision limited by the binary representation of variables, using real numbers allows representation to the machine precision in continuous search space [124, 125]. The real coded genetic algorithm also has the advantage of requiring less storage than the binary GA because a single floating point number represents a variable instead of many integers having values 0 and 1 [124, 125].

A number of real parameter genetic algorithms have been developed recently with an aim to solve real-world optimization problems. Deb et al. [127] developed an efficient real coded GA, called the generalized generation gap (G3) model using parent centric recombination (PCX) operator. The generic G3 model using the PCX operator is an elite-preserving, scalable, and computationally fast population-alteration model [127]. Deb et al. [127] showed that this model converged at a much faster rate on standard test functions as compared to other real-parameter GAs as well as classical optimization algorithms. Also, this model required the least number of calculations of the test function in finding the global optimal solution [127]. Keeping the number of function evaluations to a minimum is very important in an optimization problem involving repeated runs of numerical transport phenomena based models, because these models are complex and consume a large amount of computer time.

2.4.3.3 Selection of hidden layers

Number of hidden layers in neural network depends on the type of the problem and behavior of the decision space [127-129]. Theoretically, any convex shaped decision space can be represented by using a single hidden layer. Addition of more nodes in this hidden layer allows us to define more and more edges in our decision space. Therefore, more complex convex regions can be represented by adding more nodes in the hidden layer as shown in figure 2-16.

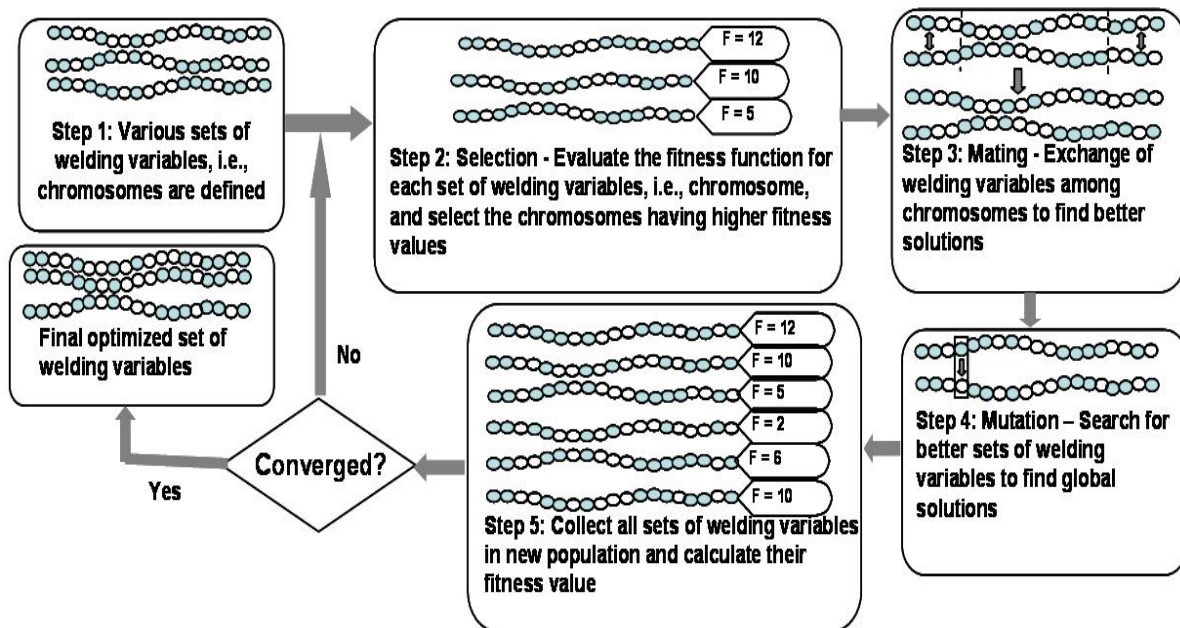


Figure 2-15: Flowchart of a basic genetic algorithm process.

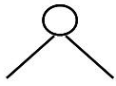
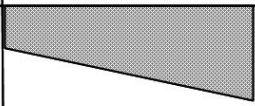
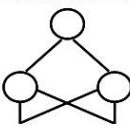
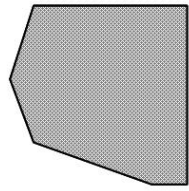
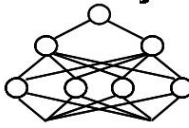
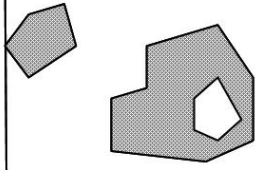
Structure	Types of Decision Regions	Most General Region Shapes
Single-Layer <i>(i.e. no hidden layer)</i> 	Half Plane Bounded By Hyperplane	
Two-Layer <i>(i.e. 1 hidden layer)</i> 	Convex Open Or Closed Regions	
Three-Layer <i>(i.e. 2 hidden layers)</i> 	Arbitrary (Complexity Limited by No. of Nodes)	

Figure 2-16: General neural network structures and their corresponding decision regions based on Kolmogorov theorem [127-129].

If the search space or decision space is discontinuous, then 2 hidden layers are required to capture the interaction among variables. The units or nodes in second hidden layer receive convex regions generated by first hidden layer. This hidden layer then produces combinations of convex regions as outputs which may intersect, overlap or be separate from each other, producing arbitrary shapes. In short, three layered neural net is capable of representing any arbitrary complex shapes. The complexity of the shapes is limited by the number of nodes in the network, since these define the number of edges that we can have. This statement is also referred as Kolmogorov theorem [127-129]. We should never use more than optimal number of hidden layers in the network as it may result in overfitting of the data.

In recent years, many researchers have attempted to develop systematic correlations between various welding variables and weld geometry using neural networks [97-123]. The previous efforts to model the fusion welding process using neural network were based on training the network with very limited volume of experimental data. Since the volume of experimental data required to train a neural network depends on the number of input and output variables, most previous efforts considered only few input parameters to keep the necessary volume of experimental data tractable. For example, Tarng et al. [115], Andersen et al. [117], Juang et al. [120] and Eguchi et al. [121] developed neural network models of GTA welding process, which considered the effects of input process parameters like welding speed, arc current and voltage on the weld pool geometry. These neural network models were developed using a limited volume of experimental data, and they could not determine the effect of material properties on weld pool geometry. Furthermore, the existing neural network models [114-122] do not provide any information about some of the other important output parameters such as the cooling rate and peak temperature. A neural network can only be used as a substitute for numerical transport phenomena based models if it can incorporate the effects of the important input welding process parameters and material properties on the weld pool geometry, cooling rate and peak temperature. Such a neural network can be produced by training and testing it with the results of a well tested numerical transport phenomena based model providing reliable output.

2.5 Weld Defects

Welds often contain various types of defects such as porosity, slag inclusions, tungsten inclusions, incomplete fusion, inadequate joint penetration, undercut, cracks, arc strikes and humping. Several factors that influence these defects can be categorized into design-related and process-related variables. The important design-related variables include configuration details of weld joint, workpiece thickness and mechanical restraint conditions etc. On the other hand, the process-related variables are welding technique, electrode quality, process variables like arc current, voltage, arc length, travel speed, wire feed rate and welding sequence. The following section briefly describes the above mentioned weld defects.

2.5.1 Porosity

Porosity refers to the gas pockets or voids free of any solid material, frequently found in welds. Porosity is caused when gas is released as weld metal cools and its solubility is reduced, and from gases formed by chemical reactions in the weld [5, 7, 8]. Porosity may be scattered uniformly throughout the weld, isolated in small areas, or concentrated at the root. Though in many cases, porosity is spherical, in some it is worm shaped, and elongated in the solidification direction of the weld metal. Porosity is caused by excessive welding temperatures or incorrect manipulation.

Beyond the solubility limit, every molten metal is unable to dissolve any more of a particular gas. The solubility limit in the molten metal usually decreases with decreasing temperature, until at the melting point, upon solidification, the solubility drops precipitously [5, 7]. As the solubility for a gas decreases in a liquid metal upon cooling, it comes out of solution in the form of bubbles. These bubbles form near the boundaries of the weld pool where the molten weld metal is coolest. Once formed in the liquid, these bubbles attempt to rise in the weld pool since they are buoyant. However, because of this buoyancy, they are also subject to convection, and, so, are swept through the liquid in a direction that depends on the direction of convective flow. This direction, in turn,

depends on the particular force that dominates the convection- buoyancy (or, gravity force), surface tension gradient force or the electromagnetic force [5]. If, for example, the surface tension gradient force dominates, molten metal in the weld pool will move outward from the center and downward near the pool edges, sweeping any gas bubbles back down into the weld pool. If, on the other hand, electromagnetic forces dominate, molten metal will move from the pool edges to the weld center, at which point, upon colliding with fluid flowing in the opposite direction from the other side of the weld pool, it will turn downward, strike the bottom of the pool, and turn outward and upward along the pool edges. This action will sweep any gas bubbles forming near the pool edges up to the pool surface to escape. Systematic work on porosity has been less extensive than that on gas absorption, but Uda et. al. [130-132] have addressed this defect in detail.

Unfortunately, these gas bubbles never get to escape, regardless of the convection flow pattern. The reason is that solidification occurs first, trapping the bubbles to produce pores. Gas porosity, whether from nitrogen, oxygen or hydrogen, is always problematic. First, it indicates that the shielding gas was less than adequate, and that unwanted gas-metal reactions are occurring. Second, pores can easily act as stress risers, thereby promoting brittle fracture and aggravating susceptibility to cyclic loading (fatigue). However, the pores can be beneficial for arresting a propagating crack by blunting it, and, thereby, reducing the stress at its tip. During GTAW and GMAW, the average size of the pores is very small compared to other welding processes like SAW due to low heat input per unit length used during these processes.

2.5.2 Hydrogen porosity

Another form of weld defect attributed to excessive hydrogen is hydrogen porosity. The solubility of hydrogen in liquid metallic iron based alloys at the melting point is nearly four times that in solid δ -iron at the melting point [7, 133]. Thus, during intervals of rapid growth at an advancing solid-liquid interface, the liquid at the interface can become supersaturated and nucleate tiny bubbles of gaseous hydrogen. These bubbles

often become entrapped in the spaces between dendrites and grow as a result of rejection of additional hydrogen from the surroundings. Upon further cooling, more hydrogen is rejected by the solid as a result of the solubility of hydrogen decreasing with reduction in temperature, enters the small voids, and builds up high hydrostatic pressures within these voids. Even if the bubbles do not grow to visible size, the fracture surface of the failed weld will often exhibit shiny circular patches which are indicator of excessive hydrogen. If the amount of hydrogen dissolves in the liquid is very high then the spherical voids which are shiny on their interior surface are formed and are known as hydrogen porosity [5, 7, 8]. This type of defect is avoided during practice by using dried electrodes with low moisture content and using proper shielding gas atmosphere near the weld.

2.5.3 Slag inclusions

Slag inclusions term is used to describe the oxides and other non-metallic solids that become entrapped in the weld metal or between the weld metal and the base metal [7, 8]. They generally come from the electrode covering material or from fluxes employed in the welding operations. In multilayer welding operations, failure to remove the slag between layers will result in slag inclusions in these zones.

Figure 2-17(a) shows the relationship between the average inclusion diameter, d and the weld metal aluminum content for submerged arc welding (SAW) and gas metal arc welding (GMAW) [134-136]. As shown in these figures, the average inclusion diameter increases with the weld metal aluminum content. The increase in inclusion diameter is accompanied by reduction in the total number of inclusions as shown in figure 2-17(b), which suggests that the inclusion coarsening is mainly caused by coagulation of smaller inclusions. As a result, the average spacing between the inclusions also increases with increase in inclusion size as shown in figure 2-17(c). Furthermore, the average inclusion size and their numbers were smaller for GMAW compared to SAW [134-136]. This difference was probably due to high heat input i.e. 4.9 kJ/mm used in SAW compared to 1.6 kJ/mm used in GMAW.

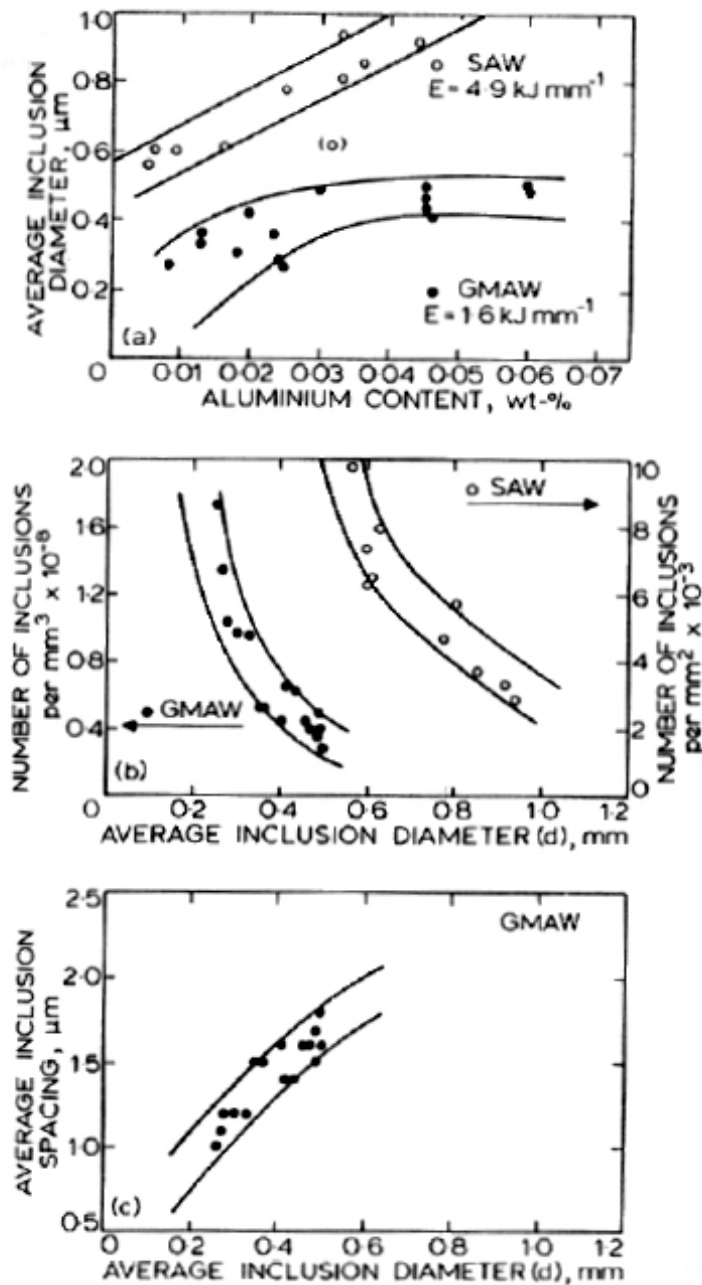


Figure 2-17: Effect of GMA and SAW welding processes and aluminum content in the workpiece on inclusions size, their distribution on Si-Mn-Al-Ti deoxidized steel welds. (a) Effect of aluminum content on average inclusion diameter; (b) Relation between average inclusion diameter and their number density; (c) Variation of average inclusion diameter with the average spacing between them. The data is taken from references [135] and [136].

Grong and Matlock [134] suggested that the high input per unit length tries to promote the growth of inclusions by extending the weld pool retention time. Widgery [135], Terashima and Hart [136] observed that the variations in heat input significantly affect the inclusion size and their distribution inside the weldment, even for similar workpiece chemical composition.

Many researchers have studied the composition, size and spatial distribution of inclusion experimentally. Klucken and Grong [137] studied mechanisms of inclusion formation in Al-Ti-Si-Mn steel weld metals and precipitate stability in weld metals. They calculated the volume fraction, size and chemical composition of inclusions in low alloy steel welds as a function of weld metal chemistry with stoichiometric relations and a fixed oxidation sequence based on the standard free energy of oxide formation. The rate of precipitation of the oxide inclusions from a supersaturated molten metal can be determined using the rate of diffusion of elements to the reaction interface. The diffusion rate coupled with nucleation rate can provide the growth kinetics of the various types of the inclusions. Babu et al. [138, 139] have compared the transformation time for various oxides as a function of temperature. They [138, 139] considered the cooling rates and nucleation rates in different locations of the weld pool to estimate the inclusions density. Hong et al. [140, 141] showed that the final size of inclusions can be calculated by considering the growth and dissolution of inclusions considering its thermal cycle. They applied the collision and coalescence model to calculate the final size distribution and number density of inclusions. Pitscheneder et al. [142] and Hong et al. [140, 141] have developed calculation procedures to trace trajectories of inclusion particles during their transport within weld pool. The literature review on these defects shows that these defects have been studied and explored very well by various researchers.

2.5.4 Incomplete fusion

Incomplete fusion, or lack of fusion as it is frequently termed, is used to describe the failure to fuse together the adjacent layers of weld metal or adjacent weld metal and the base metal. This failure to obtain fusion may occur at any point in the welding

groove. Incomplete fusion may be caused by: failure to raise the temperature of the base metal to the melting point, or failure to remove slag, mill scale, arc shift, oxides or other foreign material present on the surfaces to which the deposited metal must fuse.

2.5.5 Undercut

This term is used to describe a groove melted into the base metal adjacent to the toe of a weld and left unfilled by the weld metal. It also describes the melting away of the sidewall of a welding groove at the edge of a layer of a bead, thus forming a sharp recess in the sidewall in the area to which the next layer or bead must fuse.

2.5.6 Cracks

Cracks result from ruptures of metals under stress. Although sometimes large, they are often very narrow separations in weld or adjacent base metal. Cracks are one of the most harmful of welding defects and can be classified as follows:

2.5.6.1 Hot cracking

Hot cracking, also known as edge-of-weld cracking, base metal cracking, liquation cracking, and heat-affected zone (HAZ) cracking, occurs in the HAZ when low melting point region, i.e., partially melted zone (PMZ), is formed during welding. Cracks form when the PMZ cannot withstand the tensile stresses generated during solidification. Cracks which form at temperatures near the bulk solidus temperature are called hot cracks. Hot cracks occur in the weld metal and in the heat affected zone immediately adjacent to fusion zone. Hot cracks are inter-granular fractures. If a hot crack is open to atmosphere, its surfaces are usually discolored by oxidation. Frequently, the surfaces at the tip of a hot crack will be smooth as result of its formation while portions of the

weldment were molten. Kammer et al. [143] has presented a generalized theory of hot cracking based on solidification process. Zener [144] suggested that wedge shaped microcracks were formed as a result of intersection of two slip planes. The concept was further developed by several investigators, including Chen and Machlin [145], McLean [146] and Gifkins [147]. Based upon these studies of creep fracture, Masubuchi and Martin [148] tried to explain the mechanisms of heat-affected zone cracking based on critical stress calculation. They suggested following formula to express the critical stress for forming an inter-granular micro-crack in the weld heta affected zone [148]:

$$\sigma_{cr} = k\sqrt{\frac{\gamma E}{d}} \quad 2.19$$

where, k is a coefficient; γ is surface free energy of grain boundary material; E is Young's modulus of grains and d is grain diameter. When liquation takes place along grain boundaries, γ decreases, resulting in intergranular cracking.

Recently, Mishra et al. [149] developed a transport phenomena based mathematical model to understand liquation cracking in weldments during fusion welding. Their model used an effective partition coefficient that considers both the local interface velocity and the undercooling to simulate solidification during welding. Their calculations showed that convection plays a dominant role in solute transport in the weld pool and diffusion calculations alone are insufficient. They were able to successfully predict liquation cracking in aluminum alloys by comparing the solid fraction in the solidifying weld metal with the corresponding value [150] in the partial melted zone (PMZ).

2.5.6.2 Cold cracks

Cold cracks are formed at much lower temperatures, generally below 200°C. Cold cracks are generally transgranular [5, 10]. Cold cracks can be divided into two general types, short time and delayed. Short time cracks are initiated during cooling to

room temperature after welding or after a short time at room temperature. Delayed cracks are initiated after some time lapse at room temperature.

Hydrogen is known to be responsible for cold cracking in steel weldments. The fact that embrittlement associated with hydrogen dissolution disappears at high strain rates and low testing temperatures is indicative that such embrittlement, as well as any subsequent cracking, involves the transport of hydrogen to the neighborhood of an advancing crack. Thus, at high strain rates and at low temperatures, the rate of diffusion of hydrogen through the crystalline lattice is too slow to cause embrittlement. Over the years, several theories have been proposed for embrittlement and cracking by hydrogen, and, indeed, the mechanism of hydrogen-induced crack formation is still being investigated and debated. Several early hypotheses involving the buildup of hydrogen gas pressure in voids are now generally discredited [151-156]. Preferred models involve the presence of preexisting defect sites in the material, including small cracks or discontinuities caused by minor phase particles or inclusions. In the presence of residual or applied stresses, such sites may develop highly localized regions of bi-axial and tri-axial stress concentration. Hydrogen diffuses preferentially to these sites because of the lattice expansion that exists. As the local hydrogen concentration increases, the cohesive energy and strength of the lattice decrease. When the cohesive strength falls below the local intensified stress level, spontaneous fracture occurs. Additional hydrogen then evolves in the crack volume, and the process is repeated. A theory by Troiano [151] suggests that certain sites act to concentrate stress to promote cracking, while a theory by Petch and Stables [152] suggests that adsorption of hydrogen lowers surface energy to promote cracking.

2.5.7 Weld distortion or warping defects

During welding, the non-uniform expansion and contraction of the weld and the surrounding base metal result in mismatched thermal strains, making welding residual stresses and permanent deformation. Out of plane distortion or warping is a common problem experienced during welding of thin-walled panel structures due to distortion.

Several factors that influence workpiece distortion may be categorized into design-related and process-related variables. The important design-related variables include configuration details of weld joint, workpiece thickness, thickness transition if the joint consists of plates of different thickness and mechanical restraint conditions. On the other hand, the process-related variables are welding technique, heat input, travel speed and welding sequence. It has been observed that better control of certain welding variables eliminates the conditions that promote distortion. For example, reducing fillet weld size and length, using high-speed welding, using a low heat input welding process and using intermittent welds reduces the distortion problem. The implementation of distortion mitigation techniques during welding counteracts the effects of shrinkage during cooling, which distorts the welded structure. Several mitigation methods, including controlled preheating, mechanical tensioning, thermal tensioning, pre-bending fillet joints, presetting butt joints and using appropriate heat sinking arrangements have been suggested in the literature. All these mitigation techniques are to balance weld shrinkage forces.

Various researchers have developed numerical models to study the effect of process parameters on workpiece distortion. Taniguchi [157] investigated angular bending of fillet welded aluminum panel structures using an integrated numerical and experimental approach. He suggested a relationship between angular changes and plate thickness for various fillet sizes and span widths. Similarly, Satoh and Terasaki [158] proposed simple formulas that correlate residual stress, angular bending and transverse shrinkage to the welding heat input for different materials, including mild steel, high-strength steel, 9% Ni steel, Al 5083-O and stainless steel.

In last few decades, researchers also studied the predictive methods for welding-induced distortions using the finite element method (FEM). More recently, Michaleris and DeBiccari [159] studied the numerical analysis technique to predict welding-induced distortion in large and complex structures. This technique combines a three-dimensional, small deformation, buckling, eigenvalue analysis with a two-dimensional thermo-elastoplastic analysis and a three-dimensional large deformation elastic analysis in a decoupled approach. They used this method to assess various distortion mitigation

techniques such as thermal tensioning to prevent buckling in the thin-walled panel structures. Vanli *et al* [160] used this approach in the prediction of welding distortions in T-beam fabrications. Hinrichsen [161] performed a finite element analysis on single-pass fillet welds using a two-step analysis. Initially, a thermo-elasto-plastic, two-dimensional model establishes the transverse shrinkage and later the longitudinal shrinkage is found from a three-dimensional, shell element model, whereby the whole length of the plate is assumed to be heated simultaneously along the weld seam—similar to a plane deformation analysis. Lindgren [162, 163] suggested that the major phenomena leading to welding distortion is a thermal, metallurgical and structural coupled process. However, Lindgren also points out that welding simulations can be broken down into simple treatments by uncoupling the thermal and elasto-plastic analysis, without losing accuracy. Radaj [164] states that the main driving factor for welding residual stresses is thermal stress. However, in ferritic steels, phase changes (e.g. austenite–pearlite transformation) will also impose a transformation strain and hence should be modeled. The review of literature related to distortion modeling indicates towards the availability of various numerical models to simulate and prevent these defects. Furthermore, in the literature, the use of high welding speed was suggested to reduce the chances of distortion. However, the use of high welding speed may lead to humping defects which affects the quality and strength of the weld joint. Furthermore, there exists no scientific theory which can properly explain the reasons and suggest methods to prevent the humping defects. This is the reason which motivated us to study the governing physics of humping defects.

2.5.8 Humping

These defects are characterized by bead-like appearance known as humping [165-174]. They usually occur due to increase in the welding speed and arc current. Several researchers have proposed theories to predict humping. Based on the experiments on gas metal arc welding (GMAW) of plain carbon steel in spray mode, Bradstreet [165] suggested that humping occurs due to capillary instability. He applied Rayleigh's theory of instability of a free liquid cylinder and suggested the following expression:

$$L_c = 2\pi R \quad 2.20$$

where L_c is the critical length of the weld pool and R is radius of the cylindrical liquid metal which was claimed to represent the weld pool width. He suggested that when the length of the weld pool exceeds this critical length, L_c , humping occurs due to breakage of the cylindrical liquid metal and its premature solidification. Savage et al. [166] experimentally determined the range of critical welding speed for humping in gas tungsten arc (GTA) welding for various welding conditions. Yamamoto and Shimada [167] studied low pressure GTA and suggested that the onset of humping was related to a transition in which the weld pool turns into a thin film under the arc and the metal velocity in the film exceeds a critical value depending on the thickness of the liquid film. Beck et al. [168] used a two dimensional finite element model for calculating fluid flow in the molten pool during laser welding neglecting thermo-capillary effects and observed that at high travel speeds, humping results from a jet created behind the keyhole. Mills and Keene [169] proposed that humping was caused by Marangoni convection. In contrast, Gratzke et al. [170] concluded that humping cannot be explained from Marangoni convection. They [170] modified the model proposed by Bradstreet [164] and calculated instability of a liquid cylinder based on Rayleigh's instability theory. The onset of humping was found to be influenced by the change in potential energy (due to capillarity) of a partially bounded liquid cylinder. The width of the weld pool was represented by the diameter of the cylinder and the weld pool length was taken as the length of the liquid cylinder.

$$L_c > 2\pi RB(\phi_0) \quad 2.21$$

$$\text{where, } B(\phi_0) = \left(1 - \left(\frac{\pi}{2(\pi - \phi_0)} \right)^2 \right)^{-0.5}$$

Eq. 2.21 differs from eq. 2.20 by a function $B(\Phi_0)$. In eq. 2.21, Φ_0 represents the half angle between the axis of the cylinder and the contact location of the cylinder with the work piece [170]. Based on the shapes of typical arc and laser weld pools, Gratzke et

al. [170] suggested values of $B(\Phi_0)$ as 1.5 and 2 for arc and laser welding, respectively. Thus, for arc welding eq. 2.21 can be simplified to the following:

$$\frac{L_c}{R} = \frac{\text{Weld pool length}}{\text{Weld pool width}} > 3\pi \quad 2.22$$

Apart from the simplification of the weld pool geometry, the gravitational and shear forces are ignored eqs. 2.20 and 2.22 and they cannot predict the conditions for the initiation of humping.

Yamauchi and Taka [171] compared the arc and the metallo-static pressures at the tail of the weld pool to explain humping. Mendez and Eagar [172] and Mendez et al. [173] explained the periodic nature of humping by finding the location of transition line between the arc gouge and the trailing region based on pressure balance. Their model was based on scaling laws, and they predicted humping at high arc currents [172, 173].

No comprehensive unified theoretical model exists today that can predict the formation of humping defects considering the effects of important welding variables such as the arc current, voltage, welding speed, nature of the shielding gas, electrode geometry, torch angle and ambient pressure.

2.6 Important Unanswered Questions

Although the transport phenomena based model have provided significant insights into the various welding processes and the properties of the welded materials, still there are many important unanswered questions. In this doctoral thesis, following important unanswered questions are addressed.

- (i) What is the effect of fillet joint orientations on the temperature distribution, velocity fields, thermal cycles and the solidified weld bead profile?
- (ii) How can the reliability of the calculated outputs of the transport phenomena based models be improved? Furthermore, can we find the values of uncertain input parameters using limited volume of experimental data?

- (iii) How can the computation time of the phenomenological models be reduced? Can we develop any statistical regression model or the neural network to relate with inputs with the outputs? Can we use same input parameters in the neural network model as used in heat transfer and fluid flow model? How should we generate the sufficient training data to train the network which can capture the effect of all the input variables on the output variables? What algorithms should we use to find the optimal weights in the network? How good is the agreement of these neural network models in comparison with the corresponding outputs from the transport phenomena based phenomenological models?
- (iv) How can the phenomenological models be made bi-directional i.e. have the ability to predict input parameters in reasonable time? Will it be possible to achieve desired weld attributes by alternate combinations of welding conditions?
- (v) Can a model predict and prevent the humping defects to increase manufacturing efficiency? Furthermore, can this model be used to quantitatively study the effect of various welding variables such as arc current, welding speed, shielding gas composition, electrode geometry, electrode tilt angle and ambient pressure on humping defects?

2.7 References

1. J. F. Lancaster, *The Physics of Welding*, 2nd Edition, Pergamon, Oxford (1986).
2. K. Easterling, *Introduction to the Physical Metallurgy of Welding*, 2nd Edition, Butterworth-Heinemann, Oxford (1992).
3. S. A. David and T. DebRoy, *Science*, **257**, 497 (1992).
4. T. DebRoy and S. A. David, *Rev. Mod. Phys.* **67**, 85 (1995).
5. S. Kou, *Welding Metallurgy*, 2nd edition, John Wiley & Sons, Hoboken, New Jersey (2003).
6. Ø. Grong, *Metallurgical Modeling of Welding*, 2nd edition, The Institute of Materials, London (1997).

7. R. W. Messler, *Principles of Welding*, 1st edition, John Wiley & Sons, New York (1993).
8. R.L. O'Brien ed., *Welding Handbook- Vol. 2*, 8th edition, American Welding Society, Miami, Florida (1991).
9. W. A. Bowditch and K. E. Bowditch, "*Welding Technology Fundamentals*", 2nd edition, The Goodheart-Willcox Company, Tinley Park, Illinois (1997).
10. K. Masubuchi, "*Analysis of Welded Structures*", 1st edition, Pergmon Press, London (1980).
11. H. G. Kraus, *Weld. J.*, **68**, 84s (1989).
12. W. Pitscheneder, R. Ebner, T. Hong, T. DebRoy, K. Mundra and R. Benes, in *Mathematical Modelling of Weld Phenomena 4*, edited by H. Cerjak, p. 4 (1998).
13. T. DebRoy and S. Kou, *Heat Flow in Welding*, Chapter 3, Welding Handbook, vol. 1, 9th Edition, American Welding Society (2001).
14. N. S. Tsai and T. W. Eager, *Metall. Trans. B*, **16B**, 841 (1985).
15. H. Zhao, D. R. White and T. DebRoy, *Int. Mater. Rev.*, **44**, 238 (1999).
16. S. Kou and Y. Le, *Metall. Trans. A*, **15A** (6), 1165 (1984)
17. N. D. Malmuth, W. F. Hall, B. I. Davis and C. D. Rosen, *Welding J.*, **53**(9), 388 (1974).
18. N. Christensen, V. De L. Davis and K. Gjermundsen, *British Welding J.*, **12** (2), 54 (1965).
19. N. S. Tsai and T. W. Eager, *Metall. Trans. B*, 16B, 841 (1985).
20. M. C. Tsai and S. Kou, *Numer. Heat Transfer A*, **17**, 73 (1990).
21. M. C. Tsai and S. Kou, *Weld. J.*, **69**, 241s (1990).
22. M. C. Tsai and S. Kou, *Int. J. Numer. Meth. Fl.*, **9**, 1503 (1989).
23. S. Kou and Y. H. Wang, *Metall. Trans. B*, **17B**, 2271 (1986).
24. T. Zacharia, S. A. David, J. M. Vitek and T. DebRoy, *Weld. J.*, **68**, 499s (1989).
25. K. Mundra, T. DebRoy, T. Zacharia and S. A. David, *Weld. J.*, **71**, 313s (1992).

26. H. B. Smartt, J. A. Stewart and C. J. Einerson, in *85 ASM International Welding Congress*, edited by E. F. Nippes et al., paper no. 8511-011, ASM International, Materials Park, OH (1985).
27. R. T. C. Choo, J. Szekely and R. C. Westhoff, *Weld. J.*, **69**, 360s (1990).
28. K. C. Hsu, K. Etemadi and E. Pfender, *J. Appl. Phys.* **54**, 1293 (1983).
29. J. McKelliget and J. Szekely, *Met. Trans. A*, **17A**, 1139 (1986).
30. P. Kovitya and J. J. Lowke, *J. Phys. D: Appl. Phys.*, **18**, 53 (1985).
31. C. S. Wu and L. Dorn, *Comput. Mater. Sci.*, **2**, 341 (1994).
32. J. W. Kim and S. J. Na, *Weld. J.*, **74**, 141s (1995).
33. W. Zhang, G. G. Roy, J. W. Elmer and T. DebRoy, *J. Appl. Phys.* **93**, 3022 (2003).
34. W. Zhang, C. H. Kim and T. DebRoy, *J. Appl. Phys.* **95**, 5210 (2004).
35. W. Zhang, C. H. Kim and T. DebRoy, *J. Appl. Phys.* **95**, 5220 (2004).
36. K. Mundra, T. DebRoy and K. Kelkar, *Numer. Heat Transfer A*, **29**, 115 (1996).
37. W. Zhang, G. G. Roy, J. W. Elmer and T. DebRoy, *J. Appl. Phys.*, **93**, 3022 (2003).
38. W. Zhang, J. W. Elmer and T. DebRoy, *Mater. Sci. Eng. A*, **333**, 320 (2002).
39. K. Hong, D. C. Weckman and A. B. Strong, in *Trends in Welding Research*, edited by H. B. Smartt et al., ASM International, Materials Park, OH, p. 399 (1996).
40. K. Hong, D. D. Weckman, A. B. Strong and W. Zheng, *Sci. Technol. Weld. Joining*, **3**, 125 (2002).
41. S. Kou and D. K. Sun, *Metall. Trans. A*, **16A**, 203 (1985).
42. C. K. Tsao and C. S. Wu, *Welding J.*, **67**(3), 70 (1988).
43. A. R. Woods and D. R. Milner, *Welding J.*, **50**(4), 163 (1971).
44. Y. M. Zhang, Z. N. Cao and R. Kovacevic, *J. Mech. Engg. Sci.*, **210**, 187 (1996).
45. G. M. Oreper, J. Szekely, *J. Fluid. Mech.*, **147**, 53 (1984).
46. D. Rosenthal, *Welding J.*, **20** (5), 220 (1941).
47. E. F. Nippes, L. L. Merrill and W. F. Savage, *Welding J.*, **28** (11), 556 (1949).

48. E. F. Nippes, W. F. Savage and R. J. Allis, *Welding J.*, **36** (12), 531 (1957).
49. A. A. Wells, *Welding J.*, **31** (5), 263 (1952).
50. D. M. Rabkin, *British Welding J.*, **6** (8), 132 (1959).
51. C. M. Adams, *Welding J.*, **37** (5), 97 (1963).
52. P. Jhaveri, W. G. Moffat and C. M. Adams, *Welding J.*, **41** (1), 12 (1962).
53. Z. Yang and T. DebRoy, *Metall. Mater. Trans. B*, **30B**, 483 (1999).
54. K. Mundra, J. M. Blackburn and T. DebRoy, *Sci. Technol. Weld. Joining*, **2**, 174 (1997).
55. T. Zacharia, S. A. David, J. M. Vitek and T. DebRoy, *Welding J.*, **68**, 510s (1989).
56. Z. Yang, J. W. Elmer, J. Wong and T. DebRoy, *Welding J.*, **79**, 97s (2000).
57. A. Kumar and T. DebRoy, *J. Appl. Phys.*, **94**, 1267 (2003).
58. M. L. Lin and T. W. Eagar, *Welding J.*, **64**, 163s (1985).
59. A. De and T. DebRoy, *J. Phys. D: Appl. Phys.* **37**, 140 (2004).
60. A. De and T. DebRoy, *J. Appl. Phys.* **95**, 5230 (2004).
61. S. Mishra and T. DebRoy, *J. Phys. Appl. Phys.* **38**, 2977 (2005).
62. K. Hong, D. C. Weckmann, A. B. Strong and W. Zheng, *Sci. Technol. Weld. Joining* **8**, 313 (2003).
63. C. Limmaneevichitr and S. Kou, *Welding J.*, **79**, 126s (2000).
64. C. Limmaneevichitr and S. Kou, *Welding J.*, **79**, 324s (2000).
65. P. Sahoo, T. DebRoy and M. J. McNallan, *Metall. Trans. B*, **19B**, 483 (1988).
66. K. Mundra and T. DebRoy, *Metall. Mater. Trans. B*, **26B**, 149 (1995).
67. W. Pitscheneder, T. DebRoy, K. Mundra and R. Ebner: *Welding J.*, **75**, 71s (1996).
68. R. B. Bird, W. E. Stewart and E. N. Lightfoot, *Transport Phenomena*, John Wiley & Sons, New York (1960)
69. A. Matsunawa and Y. Shinichiro, in *Recent Trends in Welding Science and Technology*, edited by S. A. David et al., ASM International, Materials Park, OH, p. 31 (1990)

70. A. Matsunawa and Y. Shinichiro, in *International Trends in Welding Science and Technology*, edited by S. A. David et al., ASM International, Materials Park, OH, p. 3 (1993).
71. M. Malinowski-Brodnicka, G. denOuden, and W. J. P. Vink, *Welding J.*, **69**, 52s (1990).
72. R. T. C. Choo and J. Szekely, *Welding J.*, **73**, 25s (1994).
73. X. He, P. W. Fuerschbach and T. DebRoy, *J. Phys. D: Appl. Phys.*, **36**, 1388 (2003).
74. X. He, T. DebRoy and P. W. Fuerschbach, *J. Appl. Phys.*, **94**, 6949 (2003).
75. M. L. Lin and T. W. Eagar, *Welding J.*, **64**, 163s (1985).
76. D. A. Schauer, W. H. Giedt and S. M. Shintaku, *Welding J.*, **57**, 127s (1978).
77. C.-H. Kim, W. Zhang and T. DebRoy, *J. Appl. Phys.* **94**, 2667 (2003).
78. S. -H. Cho and J. -W. Kim, *Sci. Technol. Weld. Joining* **6**(4), 220 (2001).
79. S.-K. Jeong and H.-S. Cho, *Proc. Instn. Mech. Engrs.* **211B**, 63 (1997).
80. C. R. Heiple and J. R. Roper, *Welding J.* **61**, 97 (1982).
81. C. R. Heiple and J. R. Roper, in *Trends in Welding Research*, edited by S. A. David, ASM, Mtals Park, OH (1982).
82. T. Zacharia, S. A. David, J. M. Vitek and T. DebRoy, *Welding J.* **68**, 510 (1989).
83. J. V. Beck, B. Blackwell and C. R. St. Clair, "*Inverse Heat conduction: ill-posed problems*" Wiley International, NY (1985).
84. J. V. Beck and K. J. Arnold, "*Parameter estimation in engineering and science*", John Wiley and Sons, NY (1977).
85. M. N. Ozisik and H. R. B. Orlande, "*Inverse heat transfer: fundamentals and applications*", Taylor and Francis, NY (2000)
86. Y. Bard, "*Nonlinear parameter estimation*", Academic Press, NY (1974).
87. J. Dennis and R. Schnabel, "*Numerical methods for unconstrained optimizations and non-linear equations*", Prentice Hall (1983).
88. A. N. Tikhonov, *J. Engg. Physics*, **29**(1), 816 (1975).
89. O. M. Alifanov, "*Inverse heat transfer problems*", Springer-Verlag, NY (1994).

90. O. M. Alifanov, *J. Engg. Physics*, **26** (4), 471 (1974).
91. R. Fletcher and C. M. Reeves, *Computer J.*, **7**, 149 (1964).
92. R. W. Fonda and S. G. Lambrakos, *Sci. Technol. Weld. Joining*, **7**(3), 177 (2002).
93. V. A. Karkhin, V. V. Plochikhine and H. W. Bergmann, *Sci. Technol. Weld. Joining*, **7**(4) 224 (2002).
94. S. Haykin, '*Neural Network: A Comprehensive foundation*', 2nd ed., Prentice Hall Pub., NJ.
95. M. T. Hagan, '*Neural Network Design*', 1st ed., PWS Pub., Boston.
96. T. Masters: 'Practical neural network recipes in C++', 64-127; Academic Press, Boston.
97. Barry L. Kalman and Stan C. Kwasny, *Proceedings of the International Joint Conference on Neural Networks*, 1992, **4**, 578-581.
98. J. M. Vitek, Y. S. Iskander and E. M. Oblow, *Welding J.* **79**, 33s (2000).
99. J. M. Vitek, Y. S. Iskander and E. M. Oblow, *Welding J.* **79**, 41s (2000).
100. D. E. Rumelhart, G. E. Hinton and R. J. Williams, *Nature* **323**, 533 (1986).
101. I. S. Kim, S. H. Lee, and P. K. D. V. Yarlagadda, *Sci. Technol. Weld. Joining*, **8** (5), 347 (2003).
102. H. B. Smartt and J. A. Johnson, in *Proceedings of the Artificial Neural Networks in Engineering (ANNIE'91)*, St. Louis, MO, 10 to 13 November 1991, C. H. Dagli, S. R. T. Kumara, Y. C. Shin, Eds., ASME, New York, , p.711 (1991).
103. G. E. Cook, K. Andersen, G. Karsai, and K. Ramaswamy, *IEEE Transactions on Industry Applications*, **26**, 824 (1990).
104. X. Li, S. W. Simpson, and M. Rados, *Sci. Technol. Weld. Joining*, **5** (2), 71 (200).
105. H. K. D. H. Bhadeshia, *ISIJ Int.*, **39**, 966 (1999).
106. S. H. Lalam, H. K. D. H. Bhadeshia, and D. J. C. MacKay, *Sci. Technol. Weld. Joining*, **5** (3), 135 (2000).
107. E. A. Metzbower, J. J. DeLoach, S. H. Lalam, and H. K. D. H. Bhadeshia, *Sci. Technol. Weld. Joining*, **6** (2), 116 (2001).

108. I. S. Kim, Y. J. Jeong, C. W. Lee, and P. K. D. V. Yarlagadda, *Inter. J. Adv. Manuf. Tech.*, **22** (9-10), 713 (2003).
109. D. S. Nagesh, and G. L. Datta, *J. Mater. Process. Technol*, **123** (2), 303 (2002).
110. L. Burke and J. P. Ignizio, *J. Intelligent Manufacturing* **8**, 157 (1997).
111. I. S. Kim, J. S. Son, S. H. Lee and P. K. D. V. Yarlagadda, *Robotics Computer-Integrated Manufacturing* **20**, 57 (2004).
112. I. S. Kim, J. S. Son and P. K. D. V. Yarlagadda, *Robotics Computer-Integrated Manufacturing* **19**, 567 (2003).
113. H. K. D. H. Bhadeshia, D. J. Mackay and L. E. Svensson, *Mat. Sc. Technol.* **11**, 1046 (1995).
114. P. Li, M. T. C. Fang and J. Lucas, *J. Mat. Process. Technol.* **71**, 288 (1997).
115. Y. S. Tarn, H. L. Tsai and S. S. Yeh, *Int. J. Machine Tools & Manufacture* **39**, 1427 (1999).
116. E. A. Metzbower, J. J. Deloach, S. H. Lalam and H. K. D. H. Bhadeshia, *Sc. Technol. Weld. Joining* **6**, 116 (2001).
117. K. Andersen, G. E. Cook, G. Karsai and K. Ramaswamy, *IEEE Trans. Ind. Appl.* **26**, 824 (1990).
118. H. Tsuei, D. Dunne and H. Li, *Sci. Technol. Weld. Joining* **8**, 205 (2003).
119. J. Gao and C. Wu, *Sci. Technol. Weld. Joining* **8**, 143 (2003).
120. S. C. Juang, Y. S. Tarn and H. R. Lii, *J. Mat. Process. Technol.* **75**, 54 (1998).
121. K. Eguchi, S. Yamane, H. Sugi, T. Kubota and K. Oshima, *Sci. Technol. Weld. Joining* **4**, 327 (1999).
122. X. Li, S. W. Simpson and M. Rados, *Sci. Technol. Weld. Joining* **5**, 71 (2000).
123. E. A. Metzbower, J. J. Deloach, S. H. Lalam and H. K. D. H. Bhadeshia, *Sci. Technol. Weld. Joining* **6**, 368 (2001).
124. D. E. Goldberg, "Genetic Algorithm in Search, Optimization and Machine Learning," Addison-Wesley, MA (1989).
125. K. Deb, "Multi-objective optimization using evolutionary algorithms", Wiley, New York (2001).

126. K. Deb, A. Anand and D. Joshi, *Evolut. Comp.* **10**, 371 (2002).
127. C. Charalambus, *IEE Proceedings-G*, **139**, 301 (1992).
128. R. P. Lippman, *IEEE ASAP magazine*, 4 (1987).
129. J. Makhoul, A. El-Jaroudi, and R. Schwartz, *International Joint Conference on Neural Nets*, Vol. 1, Seattle, 455 (1989).
130. M. Uda, *Transactions of the National Research Institute for Metals*, **24**, 218 (1982).
131. M. Uda and S. Ohno, *Transactions of the National Research Institute for Metals*, **17**, 71 (1975).
132. M. Uda, T. Dan and S. Ohno, *Transactions of the Iron and Steel Institute of Japan*, **16**, 664 (1976).
133. A. Bandopadhyay, A. Banerjee and T. DebRoy, *Metall. Trans.*, **23B**, 207 (1992).
134. O. Grong and D. K. Matlock, *Int. Mat. Rev.*, **31**(1), 27 (1986).
135. D. J. Widgery, *Welding J.*, **55**, 57 (1976).
136. H. Terashima and P. H. M. Hart, in *Proceedings of International Welding Conference*, The Welding Institute, London (1983).
137. O. Kluken and O. Grong, *Metall. Trans. A*, **20A**, 1335 (1981).
138. S. S. Babu, S. A. David and T. DebRoy, *Sci. Technol. Weld. Joining*, **1**, 17 (1996).
139. S. S. Babu, S. A. David, J. M. Vitek, K. Mundra and T. DebRoy, *Trends in Welding Research*, Proc. 4th Int. Conf., Gatlinburg, TN (1995).
140. T. Hong, W. Pitschender and T. DebRoy, *Sci. Technol. Weld. Joining*, **3**, 33 (1998).
141. T. Hong, T. DebRoy, S. S. Babu and S. A. David, *Metall. Mater. Trans. B*, **31B**, 161 (2000).
142. W. Pitschender, T. DebRoy, K. Mundra and R. Ebner, *Welding J.*, **75**, 71 (1996).
143. P. A. Kammer, K. Masubuchi and R. E. Monroe, *DMIC Report 197, Defense metals Information Center*, Battelle Memorial Institute, Columbus, OH (1964).
144. C. Zener, *Fracturing of Metals*, ASM Cleveland, OH, 3(1948).
145. C. W. Chen and E. S. Machin, *Acta Metallurgica*, **4**, 655 (1956).
146. D. McLean, *J. Institute Metals*, **85**, 468 (1956).

147. R. C. Gifkins, *Fracture Proceedings of the Swampscott Conference on Atomic Mechanisms of Fracture*, John Wiley and Sons, 579 (1979).
148. K. Masubuchi and D. C. Martin, *Welding J.*, **41**(8), 375 (1962).
149. S. Mishra, S. Chakarworthy and T. DebRoy, *J. Appl. Phys.* **97**(9): Art. No. 094912 (2005).
150. C. Huang and S. Kou, *Weld. J.* **83**, 50 (2004).
151. A. R. Troiano, *Trans. of ASM*, **52**, 54 (1960).
152. N. J. Petch and P. Stables, *Nature*, **169**, 842 (1952).
153. C. A. Zapffe, *Iron Age*, **166**(26), 60 (1950).
154. H. G. Vaughn and M. E. DeMorton, *British Welding J.* **4**(1), 40 (1957).
155. P. G. Bastein, *Welding Research Abroad*, **2**, 12 (1961).
156. R. Pehlke and J. F. Elliott, *Trans. Metall. Soc. AIME*, **218**, 1088 (1960).
157. C. Taniguchi, *Master's thesis*, MIT, Cambridge, MA (1972).
158. K. Satoh and T. Terasaki, *J. Japan Weld. Soc.* **45**(1), 42 (1976).
159. P. Michaleris and A. DeBiccari, *Welding J.* **76**(4), 172 (1997).
160. O. A. Vanli and P. Michaleris, *J. Ship Prod.* **17**, 226 (2001)
161. B. Hinrichsen, *Ship Technol. Res.* **46**, 153 (1999).
162. L. E. Lindgren, *J. Therm. Stresses* **24**, 141 (2001).
163. L. E. Lindgren, *J. Therm. Stresses* **24**, 195 (2001).
164. D. Radaj D, *Weld. Res. Abroad* **35**, 31 (1989).
165. B. J. Bradstreet, *Welding J.* **47**(7), 314 (1968).
166. W. F. Savage, E. F. Nippes and K. Agusa, *Welding J.* **58** (7), 212 (1979).
167. T. Yamamoto and W. Shimada, in *International Symposium in Welding*, Osaka, Japan (1975).
168. M. Beck, P. Berger, F. Dausinger and H. Hugel, in *Proceedings of 8th International Symposium on Gas Flow and Chemical Lasers*, Madrid, Spain (1991).

169. K. C. Mills, B. J. Keene, *International Materials Reviews*, **35**(4), 185 (1990).
170. U. Gratzke, P. D. Kapadia, J. Dowden, J. Kroos and G. Simon, *J. Phys. D: Appl. Phys.* **25**, 1640 (1992).
171. N. Yamauchi and T. Taka, *International Institute of Welding*, document no.: 212-437-78 (1978).
172. P. F. Mendez and T. W. Eagar, *Welding J.* **82**(10), 296 (2003).
173. P. F. Mendez, K. L. Niece and T. W. Eagar, in Proceedings of the International Conference on Joining of Advanced and Specialty Materials II, Materials Solutions '99, Cincinnati, OH, pp: 151 (2000).
174. T. C. Nguyen, D. C. Weckman, D. A. Johnson and H. W. Kerr, *Sci. Tech. Weld. Joining*, **10**(4), 447 (2005).

Chapter 3

HEAT AND FLUID FLOW IN COMPLEX JOINTS DURING GAS METAL ARC FILLET WELDING

Previous computer modeling efforts to simulate and understand various welding processes through transport phenomena based models have focused mainly on simple butt joints of rectangular workpiece [1-3] and ignored the weld pool surface deformation [4-11]. During GMA welding, many physical processes occur simultaneously. For example, heat is transported from the arc to the workpiece plates and the liquid metal droplets formed from the electrode wire also carry heat and mass into the weld pool [12]. Depending on the current and the voltage levels, the arc can exert significant pressure on the surface of the weld pool which deforms the free surface [1-3, 12-15]. The deformation of the weld pool surface affects the heat transfer, fluid flow and the solidified weld bead geometry [1, 2, 13-17]. The welding process parameters such as arc current, voltage, shielding gases etc. have complex non-linear effect on the droplet size, transfer frequency, impingement velocity and the arc characteristics [12]. All these parameters, in turn, affect the resulting temperature distribution inside the workpiece, thermal cycles, cooling rates, microstructure and the final mechanical properties of the weldment [1, 2]. The purpose of this study is to investigate how the temperature distribution, velocity fields, free surface profile and the cooling rates change with orientations of workpiece during GMA fillet welding.

In case of GMA fillet welding, the complexity in modeling the system is often augmented by the complicated joint geometry containing curved weld pool surface. Fan and Kovacevic [16] considered the metal droplet transfer during GMA welding by using a volume of fluid (VOF) method for two-dimensional spot welding. Kumar and Bhaduri [19] suggested a time-averaged volumetric heat source model to consider the heat transported by metal droplets during GMA welding. They developed a finite element model for butt welding and assumed the flat weld pool surface. Jeong and Cho [20]

suggested a simple analytical method based on heat transfer analysis to calculate the transient temperature distribution in the fillet welds. They assumed flat weld pool surface to simplify the calculations. Cho and Kim [21] developed a two-dimensional finite element model for heat transfer calculation in horizontal fillet joints. In the literature, it has been well established that convection is usually the dominant mechanism of heat transfer in the weld pool and affects the weld bead shape prominently [1-3]. Recently, Zhang et al. [1, 2] developed a three-dimensional (3D) heat transfer and fluid flow model of GMA fillet welding. They studied the temperature distribution, fluid flow inside the weld pool and free surface deformation using a boundary fitted coordinate system. They transformed the governing conservation equations and corresponding boundary conditions into the curvilinear coordinate system. However, their model was applicable only to simulate symmetric V-shaped fillet joints and could not capture the different orientations of joints [1-3]. The difference in arrangements of plates affects the weld pool convective flow and hence the weld bead profile and their strength [22]. Therefore, to study the effect of various welding variables on thermal cycles and cooling rates for any fillet geometry, the existing heat transfer and fluid flow model was modified. Such modeling of GMA fillet welding process is important because the improved understanding would lead to better welds.

The purpose of the study reported in this chapter is to modify an existing heat transfer and fluid flow model of GMA fillet welding available in our research group to capture the different orientations of fillet joints. The numerical model considers the complex joint geometry, the deformation of the weld pool free surface and the addition of the heat and mass through metal droplets. The numerical model was used to investigate the heat transfer and fluid flow during GMA fillet welding of A-36 mild steel. The calculated weld bead shape was compared with the corresponding experimental result. The effect of various welding parameters on weld bead geometry parameters was quantitatively studied using the numerical model.

3.1 Mathematical Formulation

3.1.1 Assumptions and salient features

Because of the complexity of the GMA fillet welding, the following simplifying assumptions were made to make the computational work tractable [1-3]. (a) The thermo-physical properties such as thermal diffusivity and the specific heat needed for the calculations are taken at 1745°C since the values of these variables were not readily available for the temperature range of interest. (b) The additional heat transported by the droplets into the weld pool was taken into account by using a time-averaged volumetric heat source which has been widely used in the literature [12, 19]. (d) The heat flux from the arc was assumed to have a Gaussian distribution on the top surface [1-11]. The effect of the shielding gas was considered in the model in the form of arc radius and arc distribution parameter. (e) For welding with moving heat source, it is assumed that a quasi-steady state is quickly reached after the start of welding, for a constant welding speed and long workpiece block. In such case, the problem becomes steady state using a co-ordinate system that moves with the heat source [5-7, 11].

3.1.2 Governing equations

The welding problem is assumed to be at steady state by using a coordinate system attached to the heat source. Therefore, the heat transfer and fluid flow during welding can be calculated by solving the following governing equations [1-4, 7]:

$$\frac{\partial u_i}{\partial x_i} = 0 \quad 3.1$$

$$\rho \frac{\partial(u_i u_j)}{\partial x_i} = \frac{\partial}{\partial x_i} \left(\mu \frac{\partial u_j}{\partial x_i} \right) + S_j \quad 3.2$$

$$\rho \frac{\partial(u_i h)}{\partial x_i} = \frac{\partial}{\partial x_i} \left(\alpha \frac{\partial h}{\partial x_i} \right) - \rho L \frac{\partial(u_i f_1)}{\partial x_i} - \rho U_w \frac{\partial h}{\partial x_1} - \rho U_w L \frac{\partial f_1}{\partial x_1} + S_v \quad 3.3$$

Eqs. **3.1**, **3.2** and **3.3** are the continuity, momentum conservation and energy conservation equations, respectively. In these equations, subscripts i and j indicate the coordinate direction ($i, j = 1, 2$ and 3), x is the distance, u is the liquid metal velocity, ρ is the density, μ is the viscosity, S_j is the source term for j -th momentum equation, h is the sensible heat, α is the thermal diffusion coefficient (defined as $\alpha = k/\rho C_p$, where k is the thermal conductivity and C_p is the specific heat), U_w is the material moving speed (parallel to the positive x direction, i.e., $i = 1$ direction), L is the latent heat of fusion, S_v is a source term accounting for the additional heat from metal droplets. The source term S_j used in eq. **3.2**, can be written as [1-4, 7, 23, 24]:

$$S_j = -\frac{\partial p}{\partial x_j} - \rho U_w \frac{\partial u_j}{\partial x_1} - C \left(\frac{(1-f_l)^2}{f_l^3 + B} \right) u_j + F_j^e + F_j^b + F_j^i \quad \mathbf{3.4}$$

where p represents pressure, f_l is the liquid metal fraction, and F_j^e , F_j^b and F_j^i correspond to the electromagnetic, buoyancy and inertia forces in the j -th direction, respectively. In eq. **3.4**, the third term represents the frictional dissipation in the mushy zone according to the Carman-Kozeny approximation [23, 24], where B and C are two constants. These constants (i.e. A and B) are introduced in the equation to avoid zero and for accounting the mushy zone morphology, respectively. A value of 1.6×10^4 was used for C in the present study [1, 7]. The liquid metal fraction, f_l , is assumed to vary linearly with temperature inside the mushy zone [1-4, 7]:

$$f_l = \begin{cases} 1 & T \geq T_l \\ \frac{T - T_s}{T_l - T_s} & T_s < T < T_l \\ 0 & T \leq T_s \end{cases} \quad \mathbf{3.5}$$

where T_l and T_s are the liquidus and solidus temperature of the material, respectively. Eqs. **3.1**, **3.2** and **3.3** are solved simultaneously to calculate the temperature and velocity distribution in side the entire workpiece. If the temperature in the workpice is less than solidus temperature, i.e. $f_l = 0$, then the liquid metal velocity is zero in that region. The electromagnetic force, \vec{F}^e , is given as [25, 26]:

$$\vec{F}^e = \vec{J} \times \vec{B} \quad 3.6$$

where \vec{J} and \vec{B} are the current flux and magnetic field in the workpiece, respectively. In this study, the electromagnetic force is approximated using the following equations derived for a rectangular domain [26] to simplify the calculation.

$$\vec{F}^e = B_\theta (J_r \vec{z} - J_z \vec{r}) \quad 3.7$$

where \vec{z} and \vec{r} are the unit vectors in the axial (z direction) and radial directions, respectively, J_r is the radial component of \vec{J} , J_z is the axial component of \vec{J} , and B_θ is the θ component of B. The J_r , J_z and B_θ can be calculated using the following equations [26]:

$$J_z = \frac{I}{2\pi} f_0(\lambda) = \frac{I}{2\pi} \int_0^\infty \lambda J_0(\lambda r) \exp(-\lambda z - \lambda^2 r_b^2 / 12) d\lambda \quad 3.8$$

$$J_r = \frac{I}{2\pi} f_1(\lambda) = \frac{I}{2\pi} \int_0^\infty \lambda J_1(\lambda r) \exp(-\lambda z - \lambda^2 r_b^2 / 12) d\lambda \quad 3.9$$

$$B_\theta = \frac{\mu_m I}{2\pi} f_1(\lambda) = \frac{\mu_m I}{2\pi} \int_0^\infty J_1(\lambda r) \exp(-\lambda z - \lambda^2 r_b^2 / 12) d\lambda \quad 3.10$$

where μ_m is the magnetic permeability, I is the welding current, r_b is the arc radius, J_0 and J_1 are the Bessel functions of the first kind and of the zero and first order, respectively. It should be noted the above analytical solutions are strictly valid for the electromagnetic force for current passing a semi-infinite rectangular solution domain with Gaussian current flux distribution at the top surface [25]. Accurate calculation of this driving force requires the solution of the electrical potential field and the induced-magnetic field in the fillet weld. In this work, these analytical solutions for the calculation of electromagnetic force were used for simplicity.

Using the Boussinesq approximation, the gravity (buoyancy) force, \vec{F}^b , is given as [1-3, 7]:

$$\vec{F}^b = -\rho \vec{g} \cos\left(\frac{\pi}{4} - \theta\right) \cos \varphi \beta (T - T_{ref}) \quad 3.11$$

where \bar{g} is the gravity acceleration and is in the negative z or ζ direction, θ is the tilt angle or inclination of plates from horizontal position, φ is angle of lift from horizontal plane as shown in figure 3-1, β is the thermal expansion coefficient, T and T_{ref} are the local and arbitrarily selected reference temperatures.

The inertia force, \bar{F}^i , is given as:

$$\bar{F}^i = -\rho g \sin \varphi \hat{i} + \rho g \cos \left(\frac{\pi}{4} - \theta \right) \hat{j} \quad 3.12$$

where \bar{g} is the gravity acceleration and is in the negative z direction, \hat{i} and \hat{j} are unit vectors in x and y-directions, respectively.

3.1.3 Coordinate transformation

Coordinate transformation is a widely used approach to solve problems in physical domain with complex geometry [27, 28]. The main idea is to transform the complex physical domain into a simple rectangular computational domain and then discretize and solve the transformed equations in the computational domain. This approach has two major advantages. One is that the governing equations, although in more complicated forms, can be discretized and solved easily in the computational domain following the same procedure of control volume method (or other methods). The other advantage is that the boundary is precisely defined and therefore the boundary conditions can be applied precisely [27, 28]. The Cartesian or Cylindrical grid system is generally used in the numerical solution of governing equations of conservation of mass, momentum and energy [27, 28]. This is the reason for most of the previous research was focused mainly on simple systems such as butt welds [1-3]. For fillet welding, the numerical solution of heat transfer and fluid flow with a deformable weld pool surface and complex joint geometry requires the use of non-orthogonal deformable curvilinear grid system. Therefore, in the present work, the governing equations are transformed from the Cartesian to curvilinear coordinate system.

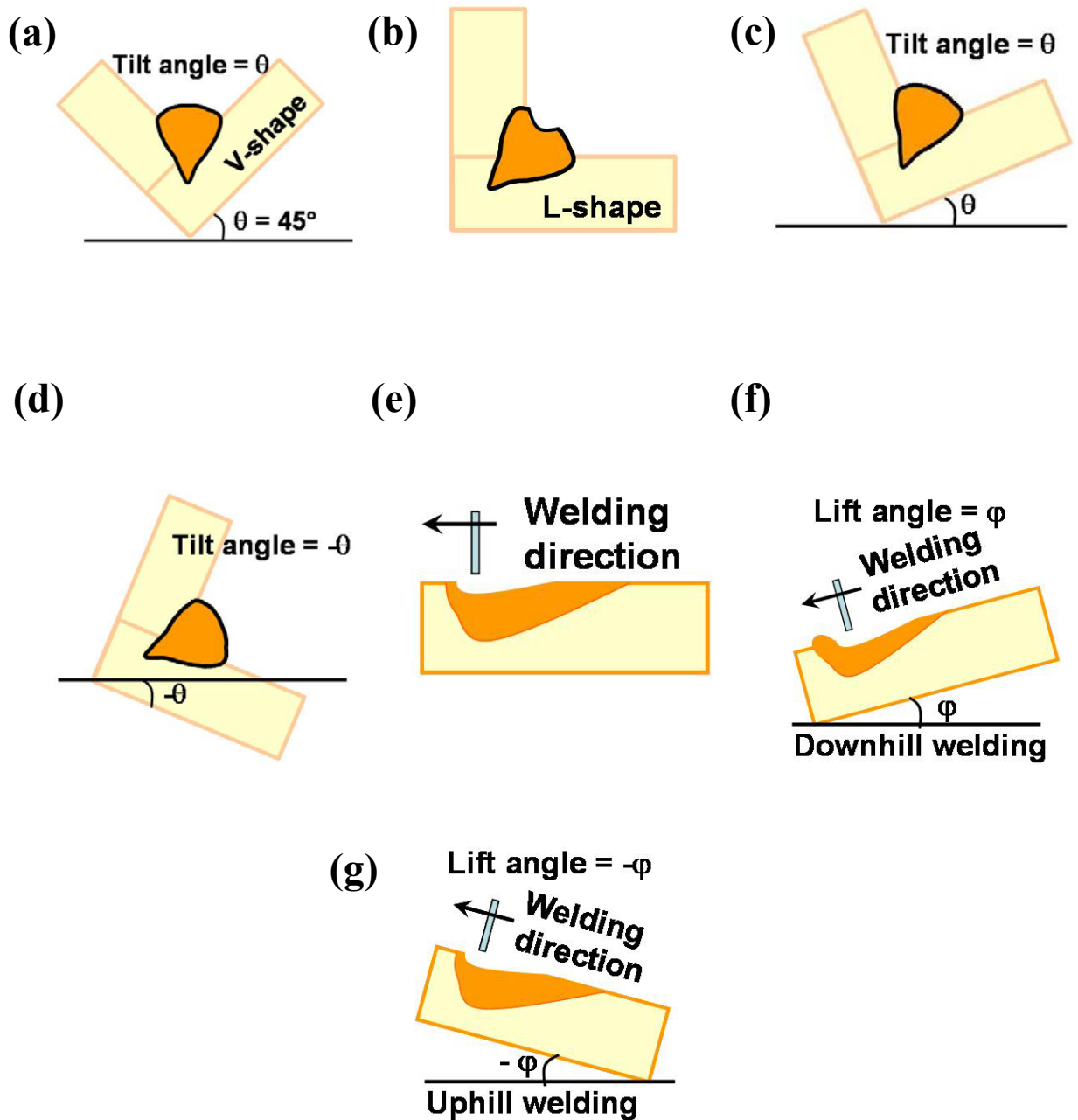


Figure 3-1: Schematic illustration of fillet joint in various orientations. Figures (a), (b) (c) and (d) show the transverse section of the fillet joint perpendicular to the welding direction while figures (e), (f) and (g) show the central longitudinal section of the fillet joint parallel to the welding direction. (a) Symmetric V-shape joint; (b) L-shape joint; (c) fillet joint with tilt angle θ ; (d) fillet joint with tilt angle $-\theta$; (e) welding in flat position; (f) downhill welding with lift angle $= \phi$; and (g) uphill welding with lift angle $= -\phi$.

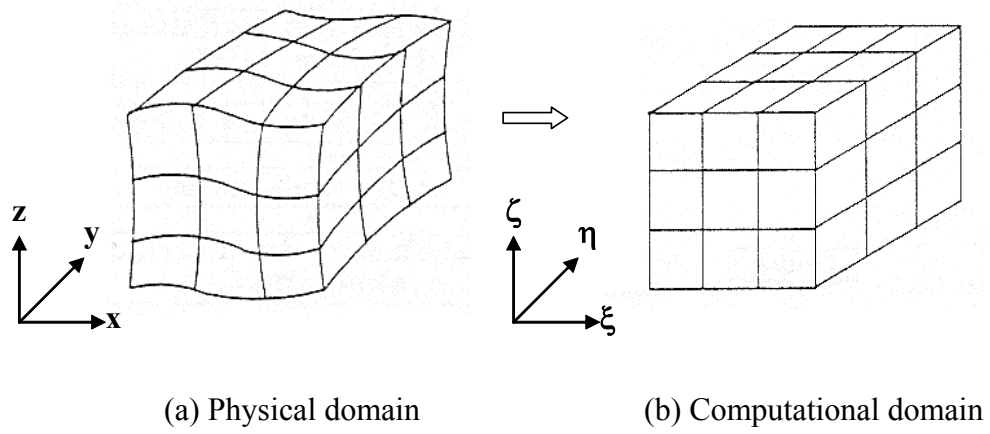


Figure 3-2: Transformation of physical domain to computational domain.

Figure 3-2 shows the transformation from a physical domain represented by (x, y, z) to the computational domain denoted by (ξ, η, ζ) . It should be noted that the governing equations presented in section 3.1.2 are derived in Cartesian coordinate or in physical domain. To solve these equations in the computational domain, they need to be transformed into forms in the curvilinear coordinate system. The following chain rule [27, 28] is used to connect the Cartesian coordinate with the curvilinear coordinate.

$$\begin{aligned}\frac{\partial}{\partial x} &= \frac{\partial}{\partial \xi} \frac{\partial \xi}{\partial x} + \frac{\partial}{\partial \eta} \frac{\partial \eta}{\partial x} + \frac{\partial}{\partial \zeta} \frac{\partial \zeta}{\partial x} \\ \frac{\partial}{\partial y} &= \frac{\partial}{\partial \xi} \frac{\partial \xi}{\partial y} + \frac{\partial}{\partial \eta} \frac{\partial \eta}{\partial y} + \frac{\partial}{\partial \zeta} \frac{\partial \zeta}{\partial y} \\ \frac{\partial}{\partial z} &= \frac{\partial}{\partial \xi} \frac{\partial \xi}{\partial z} + \frac{\partial}{\partial \eta} \frac{\partial \eta}{\partial z} + \frac{\partial}{\partial \zeta} \frac{\partial \zeta}{\partial z}\end{aligned}\tag{3.13}$$

For clarity, in the following discussion, the subscripts $x, y, z, \xi, \eta,$ and ζ are used to represent corresponding partial derivatives. For example, symbols ξ_x and η_y represent the partial derivatives $\partial \xi / \partial x$ and $\partial \eta / \partial y$. The values of ξ_x and η_y , etc. are numerically computed using the following relationship [27, 28]:

$$\begin{bmatrix} \xi_x & \xi_y & \xi_z \\ \eta_x & \eta_y & \eta_z \\ \zeta_x & \zeta_y & \zeta_z \end{bmatrix} = J \begin{bmatrix} y_\eta z_\zeta - y_\zeta z_\eta & x_\zeta z_\eta - x_\eta z_\zeta & x_\eta y_\zeta - x_\zeta y_\eta \\ y_\zeta z_\xi - y_\xi z_\zeta & x_\xi z_\zeta - x_\zeta z_\xi & x_\zeta y_\xi - x_\xi y_\zeta \\ y_\xi z_\eta - y_\eta z_\xi & x_\eta z_\xi - x_\xi z_\eta & x_\xi y_\eta - x_\eta y_\xi \end{bmatrix}\tag{3.14}$$

where J is the Jacobian of the transformation and is given as:

$$J = \frac{\partial(\xi, \eta, \zeta)}{\partial(x, y, z)} = \frac{1}{x_\xi(y_\eta z_\zeta - y_\zeta z_\eta) - x_\eta(y_\xi z_\zeta - y_\zeta z_\xi) + x_\zeta(y_\xi z_\eta - y_\eta z_\xi)}\tag{3.15}$$

Figure 3-3 shows the transformation from the V-shape physical domain denoted by (x, y, z) to a simple rectangular computational domain represented by (ξ, η, ζ) , where the transformed governing equations were discretized and numerically solved [1, 3]. As shown in this figure, only the z coordinate in the physical domain is transformed into the ζ coordinate in the computational domain, while ξ and η coordinates remain the same as x and y coordinates, respectively. For clarity, subscripts x, y, z, ξ, η and ζ are used to represent corresponding partial derivatives in the following discussion.

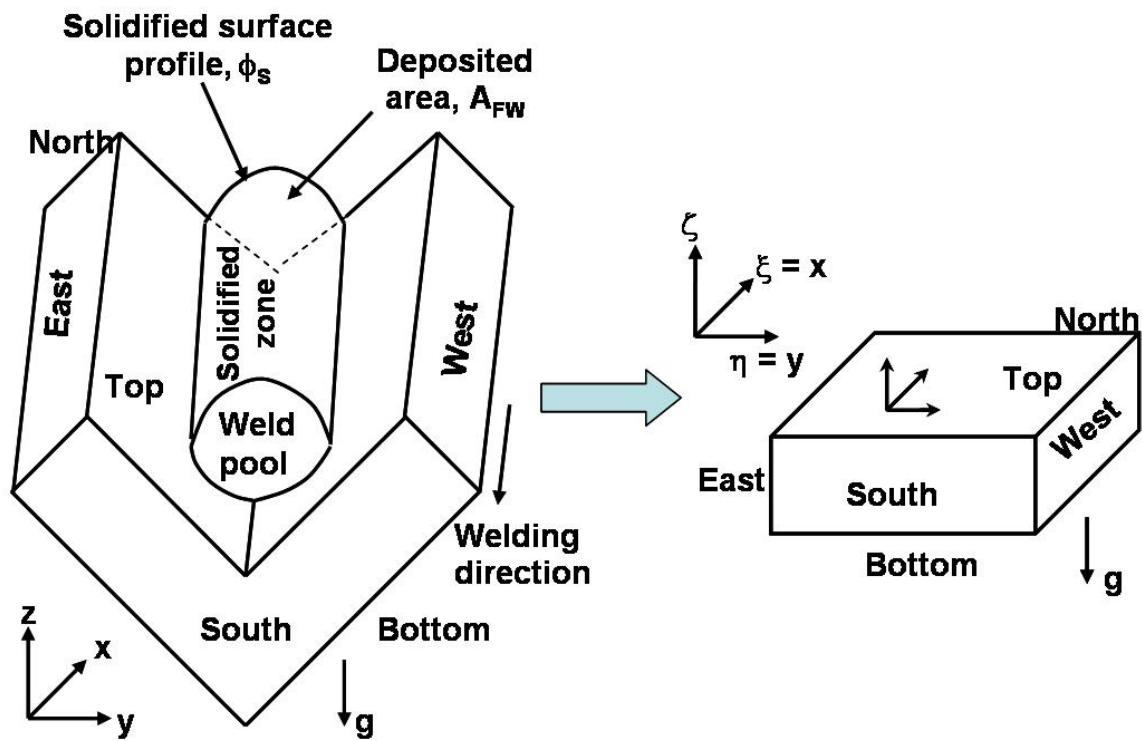


Figure 3-3: Schematic plot showing the coordinate transformation from the physical (x , y , z) to the computational domain (ξ , η , ζ). Symbols \bar{n}_t , \bar{t}_ξ and \bar{t}_η are normal and tangential vectors to the top surface. The shadowed area, A_{FW} , is equal to the amount of fed wire per unit length. Adapted from [1, 3].

For example, symbols ξ_x and h_η represent the partial derivatives $\partial\xi/\partial x$ and $\partial h/\partial\eta$, respectively. Using the Chain rule, the governing equations (i.e. eqs. **3.1**, **3.2** and **3.3**) are transformed into eqs. **3.16**, **3.17** and **3.18**, respectively, in the curvilinear coordinate [1, 3, 27].

$$\frac{\partial U}{\partial\xi} + \frac{\partial V}{\partial\eta} + \frac{\partial W}{\partial\zeta} = 0 \quad \mathbf{3.16}$$

$$\begin{aligned} \rho \left[\frac{\partial(Uu)}{\partial\xi} + \frac{\partial(Vu)}{\partial\eta} + \frac{\partial(Wu)}{\partial\zeta} \right] &= \frac{\partial}{\partial\xi} \left[\mu(z_\zeta \frac{\partial u}{\partial\xi} - z_\xi \frac{\partial u}{\partial\zeta}) \right] + \frac{\partial}{\partial\eta} \left[\mu(z_\zeta \frac{\partial u}{\partial\eta} - z_\eta \frac{\partial u}{\partial\zeta}) \right] \\ &+ \frac{\partial}{\partial\zeta} \left[\mu(-z_\xi \frac{\partial u}{\partial\xi} - z_\eta \frac{\partial u}{\partial\eta} + q_{33} \frac{\partial u}{\partial\zeta}) \right] - \left(z_\zeta \frac{\partial p}{\partial\xi} - z_\xi \frac{\partial p}{\partial\zeta} \right) \end{aligned} \quad \mathbf{3.17}$$

$$\begin{aligned} -\rho U_w \left(\frac{\partial(z_\zeta u)}{\partial\xi} - \frac{\partial(z_\xi u)}{\partial\zeta} \right) - C \left(\frac{(1-f_1)^2}{f_1^3 + B} \right) z_\zeta u + z_\zeta F_x^e + z_\zeta F_x^b \\ \rho \left[\frac{\partial(Uh)}{\partial\xi} + \frac{\partial(Vh)}{\partial\eta} + \frac{\partial(Wh)}{\partial\zeta} \right] &= \frac{\partial}{\partial\xi} \left[\alpha(z_\zeta \frac{\partial h}{\partial\xi} - z_\xi \frac{\partial h}{\partial\zeta}) \right] + \frac{\partial}{\partial\eta} \left[\alpha(z_\zeta \frac{\partial h}{\partial\eta} - z_\eta \frac{\partial h}{\partial\zeta}) \right] \\ &+ \frac{\partial}{\partial\zeta} \left[\alpha(-z_\xi \frac{\partial h}{\partial\xi} - z_\eta \frac{\partial h}{\partial\eta} + q_{33} \frac{\partial h}{\partial\zeta}) \right] - \rho U_w \left[\frac{\partial(z_\zeta h)}{\partial\xi} - \frac{\partial(z_\xi h)}{\partial\zeta} \right] \\ -\rho L \left[\frac{\partial(Uf_1)}{\partial\xi} + \frac{\partial(Vf_1)}{\partial\eta} + \frac{\partial(Wf_1)}{\partial\zeta} \right] &- \rho U_w L \left[\frac{\partial(z_\zeta f_1)}{\partial\xi} - \frac{\partial(z_\xi f_1)}{\partial\zeta} \right] + z_\zeta S_v \end{aligned} \quad \mathbf{3.18}$$

where u , v and w are Cartesian velocity components along the x , y and z directions, respectively, and U , V and W are the contravariant velocity components in the ξ , η , and ζ directions, respectively. The transformation coefficients are expressed as [1, 3, 27]:

$$\begin{bmatrix} \xi_x & \xi_y & \xi_z \\ \eta_x & \eta_y & \eta_z \\ \zeta_x & \zeta_y & \zeta_z \end{bmatrix} = \begin{bmatrix} 1 & 0 & 0 \\ 0 & 1 & 0 \\ -Jz_\xi & -Jz_\eta & J \end{bmatrix} \quad \mathbf{3.19}$$

where J is the Jacobian of the transformation and is given as $J = 1/z_\zeta$. Coefficient q_{33} is defined as $q_{33} = J(z_\xi^2 + z_\eta^2 + 1)$. The contravariant velocity components U , V and W are related to the Cartesian velocity components u , v and w by the following equation [1, 3, 27].

$$\begin{aligned}
U &= \frac{\xi_x u}{J} + \frac{\xi_y v}{J} + \frac{\xi_z w}{J} = z_\zeta u \\
V &= \frac{\eta_x u}{J} + \frac{\eta_y v}{J} + \frac{\eta_z w}{J} = z_\zeta v \\
W &= \frac{\zeta_x u}{J} + \frac{\zeta_y v}{J} + \frac{\zeta_z w}{J} = -z_\zeta u - z_\eta v + w
\end{aligned} \tag{3.20}$$

3.1.4 Boundary conditions

The velocities at the weld pool top surface are given as [1, 3]:

$$\bar{v} \cdot \bar{n}_t = 0 \tag{3.21}$$

$$\mu \nabla (\bar{v} \cdot \bar{t}_\zeta) \cdot \bar{n}_t = f_1 \left(\frac{d\gamma}{dT} \right) \nabla T \cdot \bar{t}_\zeta \tag{3.22}$$

$$\mu \nabla (\bar{v} \cdot \bar{t}_\eta) \cdot \bar{n}_t = f_1 \left(\frac{d\gamma}{dT} \right) \nabla T \cdot \bar{t}_\eta \tag{3.23}$$

where \bar{v} is the liquid metal velocity, $d\gamma/dT$ is the temperature coefficient of surface tension, \bar{n}_t is the local unit normal vector to the top surface, and \bar{t}_ζ and \bar{t}_η are local unit tangential vectors to the top surface along the ζ and η directions, respectively. Eq. 3.21 indicates that the normal velocity to the weld pool top surface is zero, while eqs. 3.22 and 3.23 represent the Marangoni shear stress at the top surface. The normal and tangential vectors to the weld pool top surface are given as [1, 3, 27]:

$$\begin{aligned}
\bar{n}_t &= \frac{\zeta_x \bar{i} + \zeta_y \bar{j} + \zeta_z \bar{k}}{\sqrt{\zeta_x^2 + \zeta_y^2 + \zeta_z^2}}, \quad \bar{t}_\zeta = \frac{x_\xi \bar{i} + y_\xi \bar{j} + z_\xi \bar{k}}{\sqrt{x_\xi^2 + y_\xi^2 + z_\xi^2}}, \\
\bar{t}_\eta &= \frac{x_\eta \bar{i} + y_\eta \bar{j} + z_\eta \bar{k}}{\sqrt{x_\eta^2 + y_\eta^2 + z_\eta^2}}
\end{aligned} \tag{3.24}$$

where \bar{i} , \bar{j} and \bar{k} are the unit vectors along x, y and z directions, respectively. The liquid metal velocity at all other surfaces, i.e., bottom, east, west, south and north surfaces, are equal to zero.

The heat flux from the arc is assumed to be a Gaussian distribution at the weld top surface. The heat flux at the top surface, F_t , is given as [1, 3]:

$$\alpha \nabla h \cdot \bar{n}_t = F_t = \frac{IV\eta}{2\pi r_b^2} \exp\left(-\frac{x_h^2 + y_h^2}{2r_b^2}\right) (\bar{k} \cdot \bar{n}_t) - \sigma \varepsilon (T^4 - T_a^4) - h_c (T - T_a) \quad 3.25$$

where I is the current, V is the voltage, η is the power efficiency, r_b is the heat distribution parameter, x_h and y_h are the x and y distances to the arc axis, respectively, σ is the Stefan-Boltzmann constant, ε is the emissivity, h_c is the convective heat transfer coefficient, and T_a is the ambient temperature (a value of 298 K is used).

For the bottom surface, the heat flux, F_b , is given as [1, 3]:

$$\alpha \nabla h \cdot \bar{n}_b = F_b = h_c (T - T_a) \quad 3.26$$

where \bar{n}_b is a unit normal vector to the bottom surface. The temperatures at other surfaces, i.e., east, west, south, and north surfaces are set to the ambient temperature. The above mentioned boundary conditions for momentum and energy conservation equations are discretized in the computational domain.

3.1.5 Calculation of effective viscosity and thermal conductivity using mixing length hypothesis

Vorticity based mixing length turbulence model has been used extensively for the calculation of effective viscosity and effective thermal conductivity. In this model, the computational effort is significantly less compared to the $k-\varepsilon$ turbulence model, since it is algebraic in nature and does not require solution of any additional partial differential equations. Hong et al. [29] implemented a vorticity based turbulence model in their thermo-fluid calculation in the weld pool using a constant value of Prandtl mixing length that was calculated by taking the ratio of the weld pool volume to its interfacial area. The constant mixing length model cannot be applied to finger type penetration characteristic of the GMA fillet welding process where the flow is constrained by the weld boundary which varies with the location. Therefore, mixing length was calculated in the present

work using Van Driest model [30, 31] which can accommodate local variation of mixing length in a weld pool of irregular geometry containing finger penetration. According to this model, mixing length at distance y from the weld pool boundary is given by:

$$l_{\text{mix}} = \kappa y [1 - e^{-y^+ / A_0^+}] \quad 3.27$$

The values of the constants κ and A_0^+ used in eq. 3.27 are 0.41 and 26.0, respectively [30, 31], whereas the non-dimensional distance, y^+ , from the weld pool boundary is calculated as follows [31]:

$$y^+ = y \sqrt{\frac{\rho}{\mu} \left(\frac{\partial u}{\partial y} \right)_w} \quad 3.28$$

The term $\left(\frac{\partial u}{\partial y} \right)_w$ in eq. 3.28 represents the velocity gradient at the weld pool boundary. For the three-dimensional flow in the weld pool, the turbulent viscosity is calculated using Badwin-Lomax model [30, 31] as follows:

$$\mu_T = \rho l_{\text{mix}}^2 |\omega| \quad 3.29$$

where, $|\omega|$ is the magnitude of the vorticity vector given by:

$$\omega = \left[\left(\frac{\partial v}{\partial x} - \frac{\partial u}{\partial y} \right)^2 + \left(\frac{\partial w}{\partial y} - \frac{\partial v}{\partial z} \right)^2 + \left(\frac{\partial u}{\partial z} - \frac{\partial w}{\partial x} \right)^2 \right]^{1/2} \quad 3.30$$

where u , v and w represent the mean component of the velocity in the weld pool in x , y and z directions, respectively.

3.1.6 Grid system and discretization of the governing equations

The transformed governing equations, i.e., 3.16, 3.17 and 3.18, were discretized using the control volume method, where the computational domain was divided into small rectangular control volumes. A scalar grid point was located at the center of each

control volume, storing the values of scalar quantities such as pressure and enthalpy. Velocity components were stored at the control volume faces, staggered with respect to scalar locations. Discretized equations for a variable were formulated by integrating the corresponding governing equation over the control volumes in the computational domain. A power-law based scheme was used to describe the convective flux at the control volume faces. A modified Semi-Implicit Algorithm for Pressure Linked Equations (SIMPLE) was used to solve the discretized equations [32]. The modification takes into account the main feature in the transformed governing equations in the curvilinear coordinate system, i.e., a mixed Cartesian-contravariant velocity components.

3.1.7 Heat transfer from metal droplets

An important feature of the GMA welding is the finger penetration which is mainly caused by the transfer of heat from the superheated metal droplets into the weld pool. In the present work, the droplet heat transfer is effectively simulated by incorporating a time-averaged volumetric heat source term (S_v) in the energy conservation equation. This volumetric heat source is characterized by its radius, height and power density. For the calculation of the heat transfer from the metal droplets, the effective height of the volumetric heat source, d , is calculated from the following equation based on energy balance [1, 3, 12, 19]:

$$d = h_v - x_v + f_d r_d \quad \mathbf{3.31}$$

The variables d , h_v , x_v and $f_d r_d$ are shown in figure 3-4. The total sensible heat input from the metal droplets, Q_d , is given as [1, 19]:

$$Q_d = \rho_w \pi r_w^2 w_f C_p (T_d - T_1) \quad \mathbf{3.32}$$

The values of h_v and x_v in eq. 3.31 are calculated based on energy balance as [1, 3, 12, 19]:

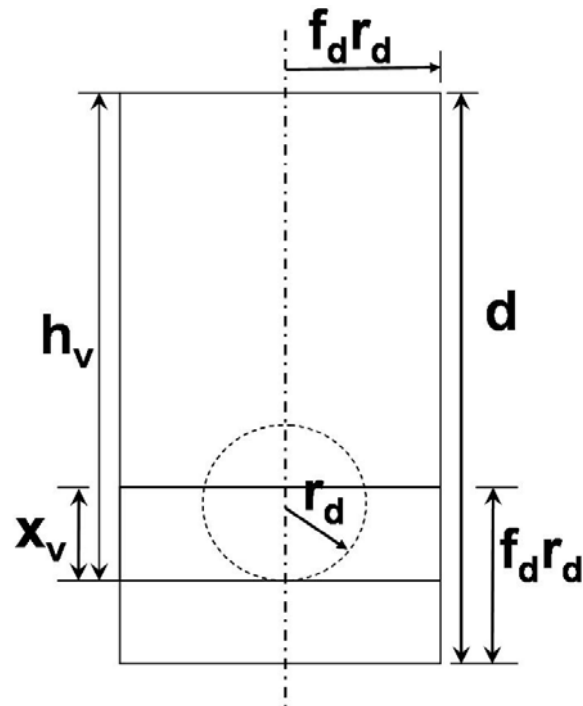


Figure 3-4: Schematic diagram of droplet volumetric heat source where d is the effective height of the volumetric heat source, h_v is the height of the cylindrical heat source, r_d is the droplet radius, f_d is the ratio of the radii of droplet volumetric cylindrical heat source and the droplet and x_v is the distance traveled by the center of the slug between the impingement of two successive droplets. The height of the volumetric heat source is calculated based on conservation of energy. It involved equating the kinetic energy transported by the droplets to the work done required for depressing the weld pool surface and the surface energy. The various parameters defining the volumetric heat source depend on the surface tension of the molten feed wire and size, frequency, velocity and acceleration of the droplets.

$$h_v = \left(-\frac{\gamma}{r_d \rho g} + \sqrt{\left[\left(\frac{\gamma}{r_d \rho g} \right)^2 + \frac{r_d v_d^2}{3g} \right]} \right) \quad 3.33$$

$$x_v = \left(h_v + \frac{\gamma}{r_d \rho g} \right) \left\{ 1 - \cos \left[\left(\frac{g}{h_v} \right)^{1/2} \Delta t \right] \right\} \quad 3.34$$

As shown in eqs. **3.33** and **3.34**, calculation of the dimensions of the volumetric heat source requires the knowledge of the droplet transfer frequency, radius and impingement velocity.

Rhee [33] and Jones [34] found that the droplet frequency was strongly affected by the welding current under the conditions of this investigation. Kim et al. [18] calculated the droplet transfer frequency by fitting their experimental results into a sigmoid function combined with a quadratic function. The resulting equation is given as [18]:

$$f = \frac{-243.44}{1 + \exp\left(\frac{I - 291.086}{6.06437}\right)} + 323.506 - 0.874 \times I + 0.0025 \times I^2 \text{ (Hz)} \quad 3.35$$

With the knowledge of the droplet transfer frequency, assuming that the droplets are spherical, the droplet radius, r_d , is given by [1, 3, 18]:

$$r_d = \sqrt[3]{\frac{3}{4} r_w^2 w_f / f} \quad 3.36$$

From the computed values of Q_d , r_d and d , the time-averaged power density of the volumetric heat source, S_v , is calculated as follows [1, 18, 19]:

$$S_v = \frac{Q_d}{\pi f_d^2 r_d^2 d} \quad 3.37$$

It should be noted that eq. **3.37** is only valid for grid points within the cylindrical heat source, and the power density is zero outside the cylinder. More details about the calculation of the volumetric heat source based on the available knowledge base of the interaction between metal droplets and the weld pool for various welding conditions are available in reference.

3.1.8 Calculation of the weld pool top surface profile

During GMA fillet welding, the weld pool top surface under the electrode is depressed by the arc force. Therefore, the pool top surface is not flat and the surface profile needs to be determined.

At steady state, the weld pool surface can be determined by using the energy minimization method. The total energy to be minimized includes the surface energy due to the change in area of the weld surface, the potential energy in the gravitational field and the work performed by the arc pressure displacing the weld pool surface, as shown below:

(Total Energy) = (the surface energy) + (the gravitational potential energy) – (the work performed by the arc pressure)

Figure 3-5(a) shows a coordinate system used in current work. The z-axis and the surface profile, ϕ , are defined as the opposite direction of gravity and arc pressure. As shown in figure 3-5(b), when the surface deviates only slightly from an original position, the deformed surface area (A_s) is given approximately as [18, 21]:

$$l_x = \sqrt{(dx)^2 + \left[\left(\frac{\partial \phi}{\partial x} \right) dx \right]^2} = dx \sqrt{1 + \left(\frac{\partial \phi}{\partial x} \right)^2} \quad 3.38$$

$$l_y = \sqrt{(dy)^2 + \left[\left(\frac{\partial \phi}{\partial y} \right) dy \right]^2} = dy \sqrt{1 + \left(\frac{\partial \phi}{\partial y} \right)^2} \quad 3.39$$

$$A_s = l_x l_y = \left[1 + \left(\frac{\partial \phi}{\partial x} \right)^2 + \left(\frac{\partial \phi}{\partial y} \right)^2 + \left(\frac{\partial \phi}{\partial x} \frac{\partial \phi}{\partial y} \right)^2 \right]^{1/2} dx dy \cong \left[1 + \left(\frac{\partial \phi}{\partial x} \right)^2 + \left(\frac{\partial \phi}{\partial y} \right)^2 \right]^{1/2} dx dy \quad 3.40$$

where l_x , l_y are the length in x and y directions, respectively. The surface energy, E_s , evaluated in the small area A_s is then given as [18, 21]:

$$E_s = \sigma \iint_s \left[1 + \left(\frac{\partial \phi}{\partial x} \right)^2 + \left(\frac{\partial \phi}{\partial y} \right)^2 \right]^{1/2} dx dy \quad 3.41$$

where σ is the surface tension of the molten metal. The potential energy, E_g , increases by the deformation of surface and can be written in the following form:

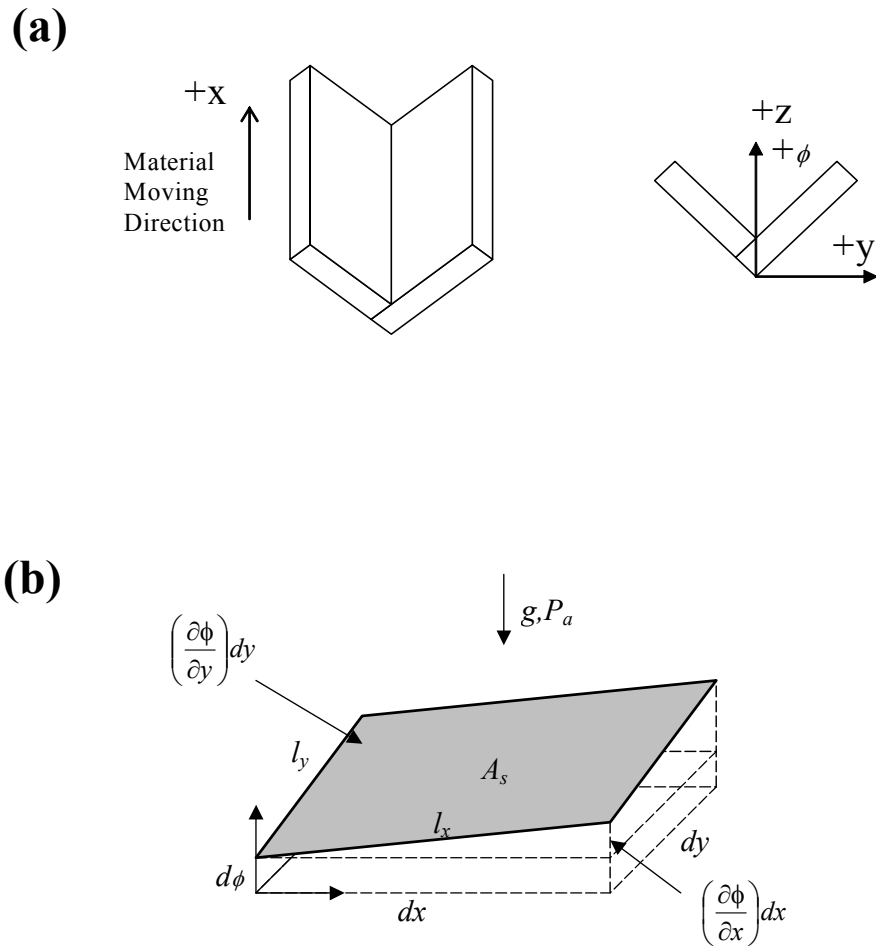


Figure 3-5: (a) Definition of the coordinate system; and (b) Surface deformation in weld pool.

$$\begin{aligned}
E_g &= \iiint \rho g \left[\phi \cos\left(\frac{\pi}{4} - \theta\right) - y \sin\left(\frac{\pi}{4} - \theta\right) - x \sin \phi \right] dx dy dz \\
&= \iint \rho g \left[\frac{\phi^2}{2} \cos\left(\frac{\pi}{4} - \theta\right) - \phi y \sin\left(\frac{\pi}{4} - \theta\right) - \phi x \sin \phi \right] dx dy
\end{aligned} \tag{3.42}$$

where θ is the titling of the workpiece from horizontal position and ϕ is angle of lift from horizontal plane as shown in figure 3-1 . Therefore, $\theta = 45^\circ$ for V-configuration and $\theta = 0^\circ$ for L-shape joints. If angle of lift, ϕ , is positive, then it is downhill welding. The surface tension, σ is assumed to vary with temperature as follows [35, 36]:

$$\sigma(T) = \sigma(T_1) + \left(\frac{d\sigma}{dT} \right) (T - T_1) \tag{3.43}$$

where T_1 is the liquidus temperature of metal.

The arc pressure energy, E_p is equal to the work done by arc pressure (W_p) but with a negative sign. In the current coordinate system, the arc energy increases by the deformation as follows [37, 38]:

$$E_p = -W_p = \iint P_a \phi dx dy \tag{3.44}$$

where P_a is the arc pressure. The arc pressure is assumed as the following Gaussian distribution [37, 38]:

$$P_a(r) = P_{\max} \exp\left(-\frac{3r^2}{r_a^2}\right) \tag{3.45}$$

where r_a is a 95% effective radius of arc pressure (i.e. $P_a(r_a) = 0.95 \times P_{\max}$). In free surface modeling, an adjustment of the maximum arc pressure is accompanied with the change of the pressure distribution parameter to conserve total arc force which can be calculated as follows:

$$F = \int 2\pi r P_a dr \tag{3.46}$$

So, if the total arc force is conserved, the following equation is preferred rather than eq. 3.45:

$$P_a = \frac{F}{2\pi\sigma_p^2} \exp\left(-\frac{x^2 + y^2}{2\sigma_p^2}\right) \quad 3.47$$

The total arc force was calculated by numerical integration of experimental results by Lin and Eagar [37]. The pressure distribution parameters are also given by the Gaussian fitting. At a specific tip angle, the total arc force and the pressure distribution parameter are linearly modeled with respect to the welding current as follows [1, 18]:

$$F = \begin{cases} -0.06049 + 0.0002808 \times I \text{ (N)} & \text{(for 30 Deg. tip angle)} \\ -0.04017 + 0.0002553 \times I \text{ (N)} & \text{(for 60 Deg. tip angle)} \\ -0.04307 + 0.0001981 \times I \text{ (N)} & \text{(for 90 Deg. tip angle)} \end{cases} \quad 3.48$$

$$\sigma_p = \begin{cases} 0.7725 + 0.00193 \times I \text{ (mm)} & \text{(for 30 Deg. tip angle)} \\ 1.4875 + 0.00123 \times I \text{ (mm)} & \text{(for 60 Deg. tip angle)} \\ 1.4043 + 0.00174 \times I \text{ (mm)} & \text{(for 90 Deg. tip angle)} \end{cases} \quad 3.49$$

The total energy, E_t was calculated by the following equation.

$$E_t = E_s + E_s + E_p \\ = \iint \left(\sigma \sqrt{1 + \phi_x^2 + \phi_y^2} + \rho g \left[\frac{\phi^2}{2} \cos\left(\frac{\pi}{4} - \theta\right) - y\phi \sin\left(\frac{\pi}{4} - \theta\right) - x\phi \sin \varphi \right] + p_a \phi \right) dx dy \quad 3.50$$

The total energy is minimized by using the variational problem, with the constraint that the deposited area, A_{FW} , at a solidified cross section of the fillet weld is equal to the amount of fed wire per unit length. The constraining mass conservation equation is given by the following equation [1, 18].

$$\int (\phi_s - z_0) dy - \frac{\pi r_w^2 w_f}{U_w} = 0 \quad 3.51$$

where ϕ_s is the solidified surface profile, z_0 is the z location of the workpiece top surface, and r_w , w_f and U_w are the wire radius, wire feeding rate and the welding speed, respectively.

From the Euler equation, the governing equation is derived as follows.

$$\sigma \left\{ \frac{(1 + \phi_y^2)\phi_{xx} - 2\phi_x\phi_y\phi_{xy} + (1 + \phi_x^2)\phi_{yy}}{(1 + \phi_x^2 + \phi_y^2)^{3/2}} \right\} = \rho g \left[\phi \cos\left(\frac{\pi}{4} - \theta\right) - y \sin\left(\frac{\pi}{4} - \theta\right) - x \sin\varphi \right] + P_a + \lambda \quad 3.52$$

where λ is the Lagrange multiplier. The front and rear solid boundaries are defined as shown in figure 3-6. The front boundary is located in front of the plane A in which the weld pool has maximum width and the rear boundary is located behind the plane A. The boundary conditions are given as following expressions [1, 18]:

$$\text{At the front solid boundary: } \phi = Z_0 \quad 3.53$$

$$\text{At the rear solid boundary : } \frac{\partial\phi}{\partial x} = 0 \quad 3.54$$

The front and rear pool boundaries can also be defined so that the temperature gradient along the x direction (dT/dx) is positive at the front pool boundary and negative at the rear boundary. The cross-sectional shape at any plane located behind the plane B is uniform and can be regarded as the shape of solidified weld bead.

The governing eq. 3.52 is solved using the Gauss-Seidel method [39]. After these calculations, the results are applied to the constraining eq. 3.51, and the calculation is repeated after modification of the Lagrange multiplier, λ to satisfy the constraining equation. The value of λ is modified by using the bisection method [39].

In this grid system, only the Z direction of the grid points is adjusted to fit the free surface profile. The top surface grid points, $z(i, j, nk)$, is expressed as:

$$z(i, j, nk) = \phi(i, j) \quad 3.55$$

where $\phi(i, j)$ is the surface profile at the (i, j)th grid point in the top plane. All other grid points are then adjusted to be proportional to the initial grid spacing [1, 18].

$$z(i, j, k) = z(i, j, 1) + \frac{z_0(i, j, k) - z_0(i, j, 1)}{z_0(i, j, nk) - z_0(i, j, 1)} \{z(i, j, nk) - z(i, j, 1)\} \quad 3.56$$

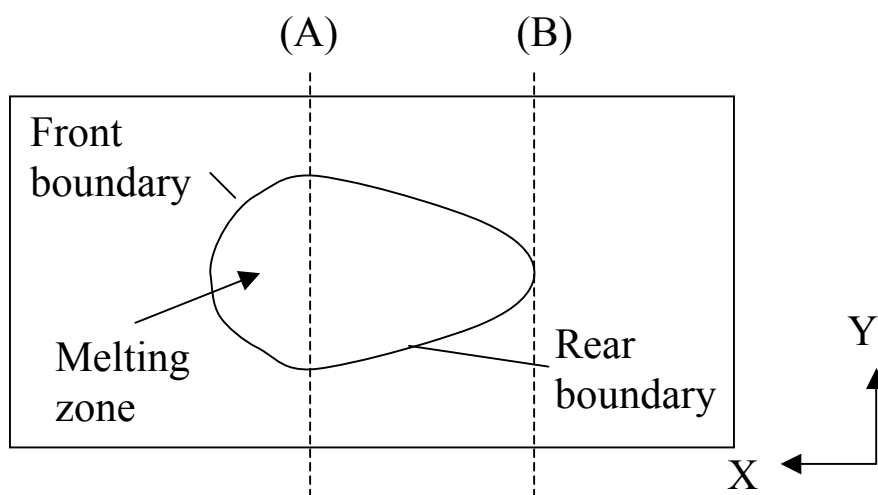


Figure 3-6: Projected view of top surface.

3.1.9 Overall solution procedure

The governing equations are solved simultaneously to obtain the temperature and velocity fields and the free surface profile. First, the modified SIMPLE algorithm is used to calculate the temperature and velocity fields. Then, the free surface profile is calculated based on the temperature field obtained in the previous step. After the solution of the free surface profile, the z locations of grids are adjusted to fit the surface profile, and the temperature and velocity fields are then re-calculated in the fitted grid system [1, 3]. The calculation procedure is repeated until converged temperature and velocity fields and free surface profile are obtained.

3.2 Results and Discussion

3.2.1 Selection of optimal number of grids to make the results independent of their size

Grid independency tests were performed to select the optimal number of grids so that the results are not affected by their size and numbers. The solution domain had dimensions of 450 mm in length, 108 mm in width and 18 mm in depth. Spatially non-uniform grids with finer grids near the heat source were used for maximum resolution of variables. Table 3-1 lists the various combinations of grids used in the calculation to find the optimal grid size. With increase in number of grids, the accuracy of the calculation increases. However, with increase in the number of grid points, the computation time increases. In the trade off between accuracy and the computation time, a $77 \times 66 \times 47$ grid system was selected for the calculation in this work since it provides the same solution as obtained with more finer grid systems and the calculations took about 20 minutes to converge in a PC with 3.2 GHz Intel P4 CPU and 2048 Mb PC2700 DDR-SDRAM memory.

Table 3-1: Effect of the grid size on the results and the computation time. The $n_x \times n_y \times n_z$ represents the grids distribution in x, y and z-directions, respectively.

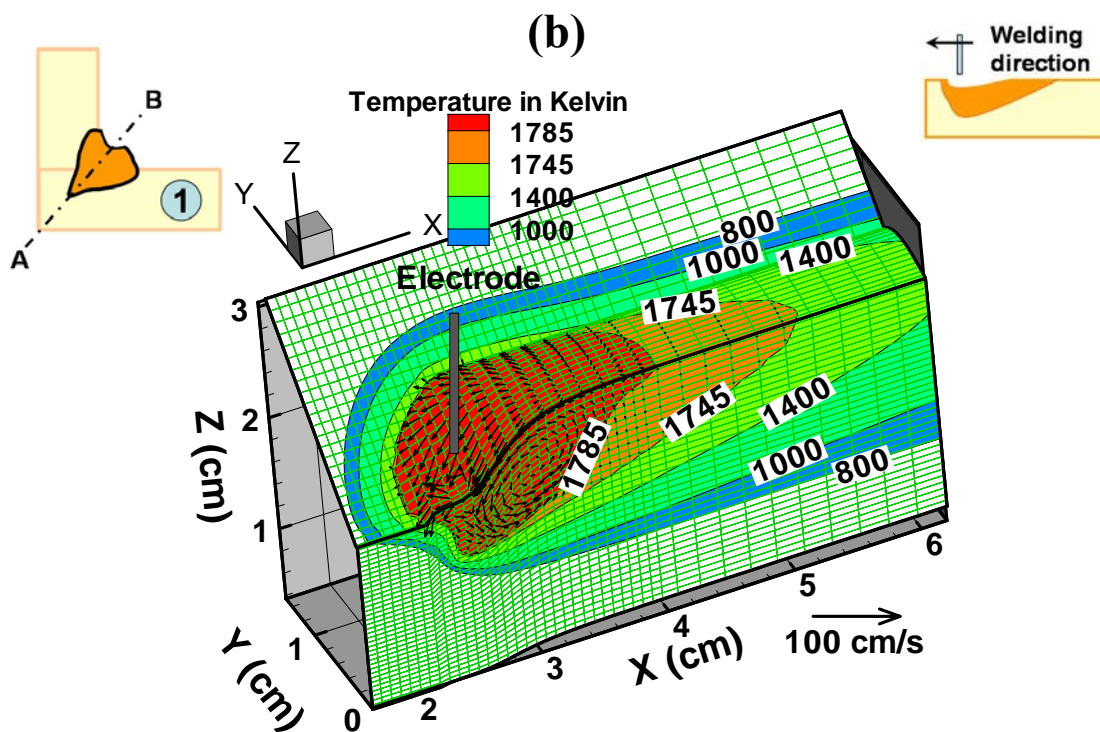
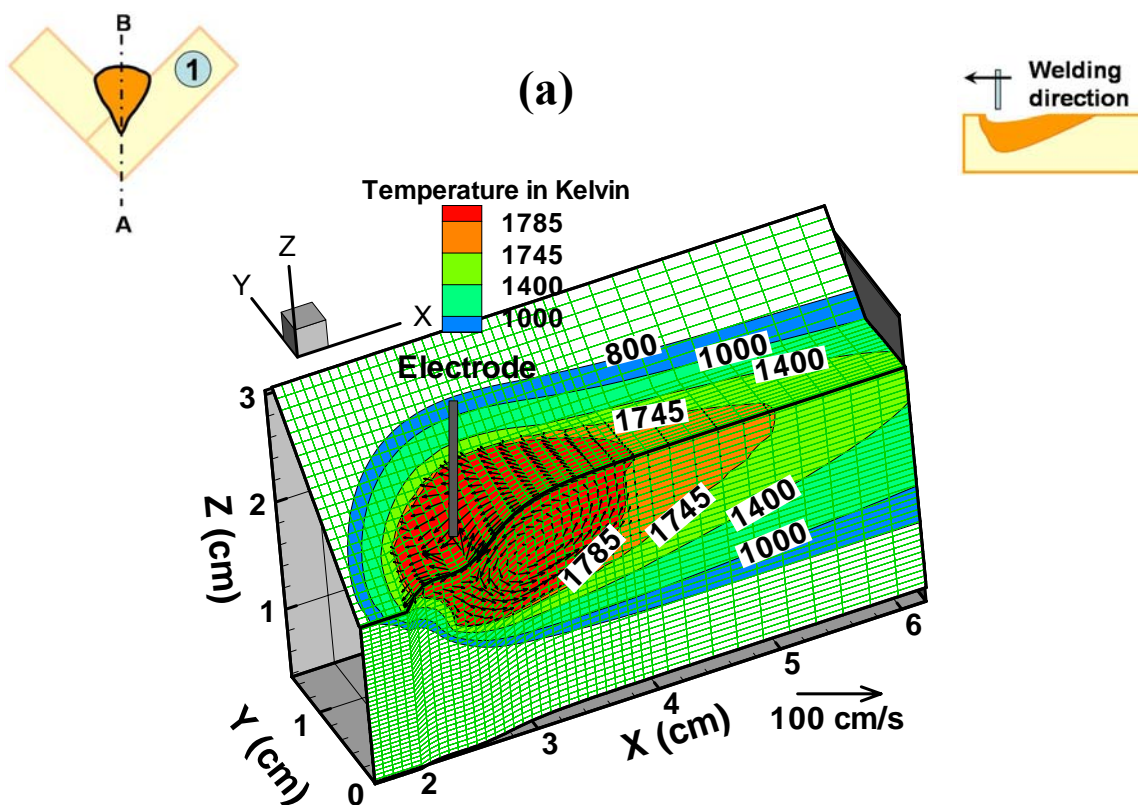
	50×40×30	60×50×40	70×56×40	77×66×47	80×70×50	100×80×60
Throat (cm)	1.07	1.05	1.06	1.06	1.06	1.06
Horizontal leg-length (cm)	0.96	0.98	0.98	0.98	0.98	0.99
Vertical leg-length (cm)	0.96	0.98	0.98	0.98	0.98	0.99
Computation time (minutes)	6	10	13	19	22	37

3.2.2 Temperature distribution, velocity field and free surface profile of weld bead

The numerical heat transfer and fluid flow model was used for the calculation of temperature and velocity fields in the weld pool for different configurations of workpiece plates. The nominal composition of A-36 steel is maximum 0.29% C, 0.80–1.2% Mn, 0.04% P, 0.05% S, 0.15–0.3% Si and remaining percentage of Fe. The material properties for the A-36 steel workpiece [1, 40] and the other data used in the calculations are presented in table 3-2. The welding conditions used in the calculation are given in case # 1 in table 3-3. Figure 3-7(a), 3-7(b), 3-7(c) and 3-7(d) show the temperature distribution, velocity fields and free surface profile of the weld bead during GMA fillet welding of V-shape symmetric joint in horizontal position, L-shape joint, downhill and uphill welding of V-shape joint at an angle of 10° , respectively. For clarity and comparison, only half of the workpiece section is shown in these cases. In these figures, the isotherms in front of the weld pool are compressed while those behind the weld pool are expanded because of the motion of the heat source.

Table 3-2: Physical properties of the A-36 steel [1, 40] and the other data used in the calculation.

Name	Value
Liquidus Temperature, T_l , (K)	1785
Solidus temperature, T_s , (K)	1745
Density of metal, ρ , (kg m^{-3})	7.2×10^3
Thermal conductivity of solid, k_s , ($\text{J m}^{-1} \cdot \text{s}^{-1} \cdot \text{K}^{-1}$)	21.0
Specific heat of solid, C_{ps} , ($\text{J kg}^{-1} \cdot \text{K}^{-1}$)	703.4
Specific heat of liquid, C_{pl} , ($\text{J kg}^{-1} \cdot \text{K}^{-1}$)	808.1
Surface tension of liquid metal at melting point, γ , (N m^{-1})	1.2
Temperature coefficient of surface tension, $d\gamma/dT$, ($\text{N m}^{-1} \cdot \text{K}^{-1}$)	-3.5×10^{-4}
Magnetic permeability, μ_m , (N A^{-2})	1.26×10^{-6}
Coefficient of thermal expansion, β , (K^{-1})	1.0×10^{-5}
Arc efficiency, η	54%
Arc radius, r_b , (mm)	5.0
Convective heat transfer coefficient, h_c , ($\text{W mm}^{-2} \text{K}^{-1}$)	42.0
Emissivity, ε	0.7
Ambient temperature, T_a , (K)	298
Constant B in the Carman-Kozeny equation	1.0×10^{-7}
Constant C in the Carman-Kozeny equation	1.6×10^4



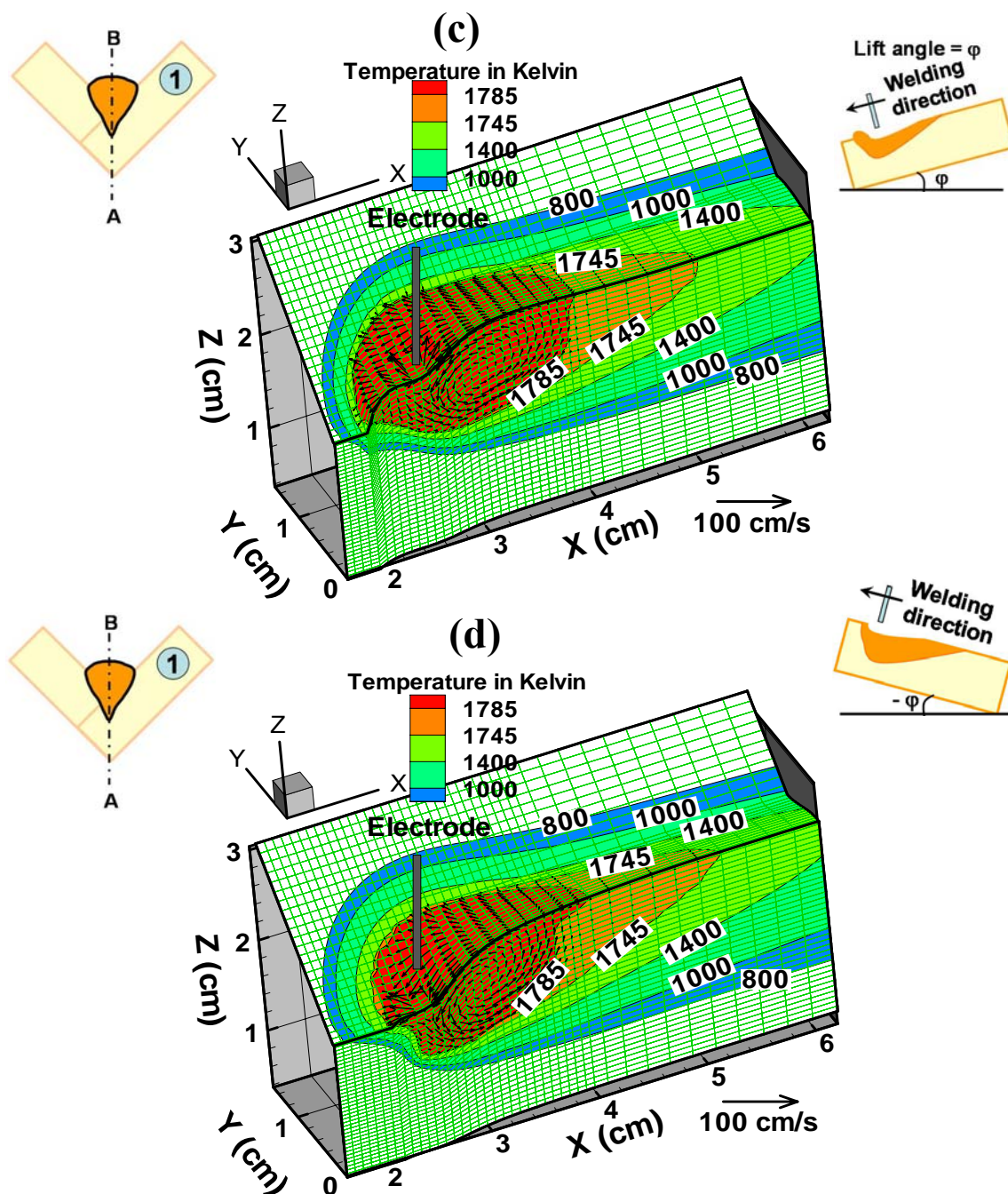


Figure 3-7: Calculated temperature field and velocity fields during GMA welding of (a) V-shaped fillet joint in flat position; (b) L-shaped fillet joint in flat position; (c) V-shaped fillet joint in downhill position at an angle of 10° and (d) V-shaped fillet joint in uphill position at an angle of -10° . For clarity, only a portion of the plate marked as 1, is shown in these figures. Welding conditions used in the calculation are given in case # 1 (table 3-3).

Table 3-3: Welding conditions used in the GMA fillet welding experiments [1, 3].

Case No.	CTWD (mm)	Wire feeding rate (mm/s)	Travel speed (mm/s)	Voltage (V)	Current (A)
1	22.2	169.3	4.2	31	312.0
2	22.2	211.7	6.4	31	362.0
3	22.2	169.3	6.4	33	312.0
4	22.2	211.7	4.2	33	362.0
5	28.6	169.3	6.4	31	286.8
6	28.6	169.3	4.2	33	286.8
7	28.6	211.7	4.2	31	331.4
8	28.6	211.7	6.4	33	331.4
Polarity:		Direct current electrode positive (DCEP)			
Joint type:		V-shape Fillet joint, horizontal welding and no root gap			
Electrode type:		AWS E70S-6, 1.32 mm (0.052 inch) diameter solid wire.			
Base metal:		ASTM A-36 mild steel			
Shielding gas:		Ar – 10% CO ₂			
Droplet transfer:		Spray transfer mode			

The figures 3-7(a), 3-7(b), 3-7(c) and 3-7(d) also indicate that the depression of the grid lines is maximum under the arc while the grids are elevated in the rear part of the weld pool. In these figures, the weld pool boundary is represented by the 1745 K solidus isotherm of A-36 steel. The maximum velocity in the weld pool was found to be 35.2 cm/s, 34.9 cm/s and 21.0 cm/s in x, y and z-directions, respectively. The presence of such high velocities affects the weld pool shape and indicates towards the presence of turbulent behavior in the weld pool. Due to presence of turbulence behavior, the viscosity and thermal conductivity of the liquid metal in the weld pool increase. Unlike the molecular values of the thermal conductivity and viscosity, the enhanced values of these transport properties are not physical properties of the fluid and depend on the welding

conditions. The calculated enhancement factor for viscosity ($f_{\mu}^e = 1 + \frac{\mu_T}{\mu_L}$) calculated using eq. 3.29 for case # 1 (table 3-3) is shown in figure 3-8. The results show that the enhanced viscosity is high under the arc while its value decreases in the rear part of the weld pool. The magnitude of enhancement factor for viscosity is high under the arc due to high spatial gradients of velocity in this region. The plane located 5 mm behind the arc shown in figure 3-8(b) is characterized by lower values of the enhanced viscosity compared with the region directly under the arc indicated in figure 3-8(a). The profiles of viscosity enhancement factor in figures 3-8(a) and 3-8(b) clearly show the finger penetration characteristic of the GMA welding. From figure 3-8(a), it can be seen that enhancement factor for viscosity is in the range of 60 to 80 directly under the arc. The region further away and behind the arc has relatively low enhanced viscosity as observed in figures 3-8(b) because of the low velocities as shown in figures 3-8(c) and 3-8(d), respectively.

The calculated average value of enhancement factor for viscosity and thermal conductivity in the weld pool is 6 and 7, respectively for welding conditions given in case #1 (table 3-3). In the literature [2, 6, 11, 29, 38], it is suggested that the effects of turbulence can be simulated by enhancing the molecular values of thermal conductivity and viscosity by 10 to 100 times. Using k- ϵ model and vorticity based model, Hong et al. [6, 29] found that the enhancement factor during GTA welding of 304 stainless steel and 6061 aluminum can be more than 20 and 100, respectively. These enhancement factors were obtained for arc current = 120 A and arc voltage = 9.2 V. They also [6] suggested an average enhancement factor between 12 to 15 for thermal conductivity and a factor more than 6 for the viscosity for GTA welding using 150 A current and 25 V based on peak temperature analysis. But there is no available experimental data to validate the simulated temperature distributions, velocity fields and turbulent viscosity in the weld pool. However, the calculated values of peak velocity and viscosity are of the same order as reported in the literature [6, 11, 29, 38].

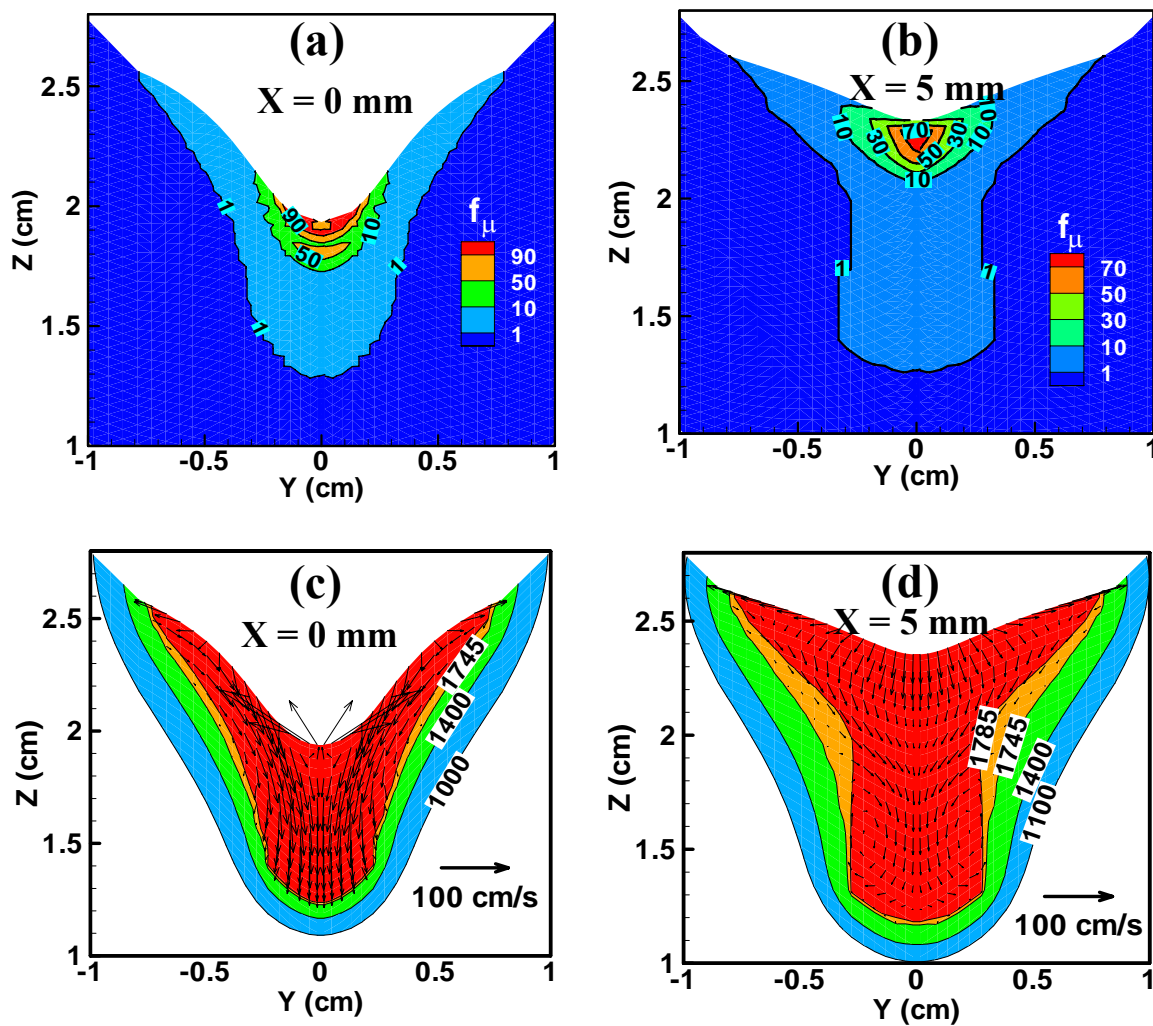


Figure 3-8: Calculated enhancement factor in viscosity using mixing-length hypothesis on various planes perpendicular to the welding direction during horizontal GMA welding of V-shape fillet joint: (a, b) Enhancement factor in viscosity directly under the arc and 5 mm behind the arc location; and (c, d) Corresponding temperature and velocity field in the weld pool. Welding conditions are the same as those in case # 1 (table 3-3).

3.2.3 Dimensionless analysis to calculate the relative importance of various driving forces

During GMA fillet welding, the energy from the arc is transported from the top surface of the weld pool to the surrounding solid region by both heat conduction and liquid metal convection. The heat transfer rate inside the workpiece determines the peak temperature, shape of the weld pool and the temperature distribution in the heat-affected zone (HAZ). Therefore, it is important to understand the effects of conduction and convection mode of heat transfer in the weld pool.

The Peclet number (Pe) can be used to assess the relative importance of convection versus conduction in transferring heat in the pool. A large value of Pe in physical terms means the liquid metal convection significantly affects the heat transfer in the weld pool due to high liquid metal velocity and larger weld pool size. In contrast, when Pe number is less than unity, the conduction mode of heat transfer plays an important role in the heat dissipation in the pool. The Peclet number was calculated using average velocity and pool width as characteristic velocity and length of the weld pool respectively. The value of Peclet number (Pe) was 120 for the case#1 listed in table 3-3. The magnitude of the Pe was in the range of 115 to 140 for other cases. Since this value is much higher than unity, the liquid metal convection plays a dominant role in dissipating the heat in the weld pool for all of these cases.

The relative importance of the electromagnetic, Marangoni and buoyancy forces in affecting fluid flow in the weld pool can be determined from the values of appropriate dimensionless numbers. The ratio of buoyancy force to viscous force is determined by Grashof number (Gr):

$$Gr = \frac{g\beta L_B^3 \Delta T \rho^2}{\mu^2} \quad 3.57$$

where g is the gravitational acceleration, β is the thermal expansion coefficient, ΔT is the temperature difference between the peak pool temperature and solidus temperature, ρ is density of the liquid, μ is the viscosity of the liquid and L_B is a characteristic length for

the buoyancy force in the liquid pool, and is approximated by one-eighth of the pool radius.

The ratio of inertia force to gravity force was determined using the Froude number (Fr). It is a dimensionless number that expresses the significance of gravity force in flows with free surface. The Froude number was calculated using the following expression:

$$Fr \equiv \left[\frac{\text{Inertia force}}{\text{Gravity force}} \right]^{1/2} = \frac{u}{\sqrt{gH}} \quad 3.58$$

where u is liquid velocity, g is the acceleration due to gravity and H is characteristic depth of the liquid pool and is approximated by value of weld bead throat dimension. If the Froude number is much higher than unity, the inertia effect dominates the flow in the weld pool. If it is much less than unity, buoyancy or gravity force dominates the liquid metal flow.

Magnetic Reynold's number, R_m , defines the ratio of electromagnetic force to viscous force, and is expressed as:

$$R_m = \frac{\rho \mu_m I^2}{4\pi^2 \mu^2} \quad 3.59$$

Surface tension Reynolds number (Ma) is used to describe the ratio of Marangoni force to viscous force, and is calculated as:

$$Ma = \frac{\rho L_R \Delta T \left| \frac{d\gamma}{dT} \right|}{\mu^2} \quad 3.60$$

where L_R is the characteristic length and $d\gamma/dT$ is surface temperature gradient. The relative importance of the primary driving forces i.e. surface tension, electromagnetic and buoyancy forces can thus be judged by the combination of these dimensionless numbers. For example, the ratio of surface tension force to buoyancy force, $R_{S/B}$, is expressed as:

$$R_{S/B} = \frac{Ma}{Gr} \quad 3.61$$

While ratio of electromagnetic force to buoyancy force, $R_{M/B}$, is given by:

$$R_{M/B} = \frac{R_m}{Gr} \quad 3.62$$

For a GMA fillet welding, the values of Gr , Fr , R_m , Ma , $R_{S/B}$ and $R_{M/B}$ were found to be 11.9, 0.27, 3.3×10^4 , 2.9×10^4 , 2.4×10^3 and 2.8×10^3 , respectively for the welding conditions listed in case #1 in table 3-3. Since the value of Grashof number is 11.9 which is much higher than unity, the viscous force is negligible compared to buoyancy and inertia force during GMA welding. However, the value of Gr is very low compared to R_m and Ma , which means that the effect of buoyancy force is very low compared to electromagnetic and Marangoni force. The low value of Fr signifies the dominance of the gravity force over the inertia force. The values were of similar order for other welding conditions listed in table 3-3. The values of $R_{S/B}$ and $R_{M/B}$ suggest that the liquid metal flow in the weld pool is driven primarily by the Marangoni and electromagnetic forces, and to a much lesser extent, by the buoyancy force. Furthermore, the value of $R_{M/B}$ was more than double during GMA fillet welding compared to GTAW. This suggest that the electromagnetic force plays more important role during GMA fillet welding, since the arc current used in this process is much higher than that in GTAW.

3.2.4 Effect of workpiece orientations on temperature distribution, velocity fields and free surface profile

The calculated temperature and velocity field during welding of symmetrical V-shape along the horizontal, L-shaped geometry along the horizontal, downhill and uphill welding of V-shaped configuration for case # 1 (table 3-3) are shown in figures 3-9, 3-10, 3-11 and 3-12, respectively. These figures show the variation of surface profile at different transverse cross-section perpendicular to the welding directions. The region directly under the arc for symmetrical V-shape joint is shown in figure 3-9(a). This figure also shows the depression of the free surface due to the arc force. The temperature profiles in figure 3-9(b) clearly show the finger penetration characteristic of the GMA welding.

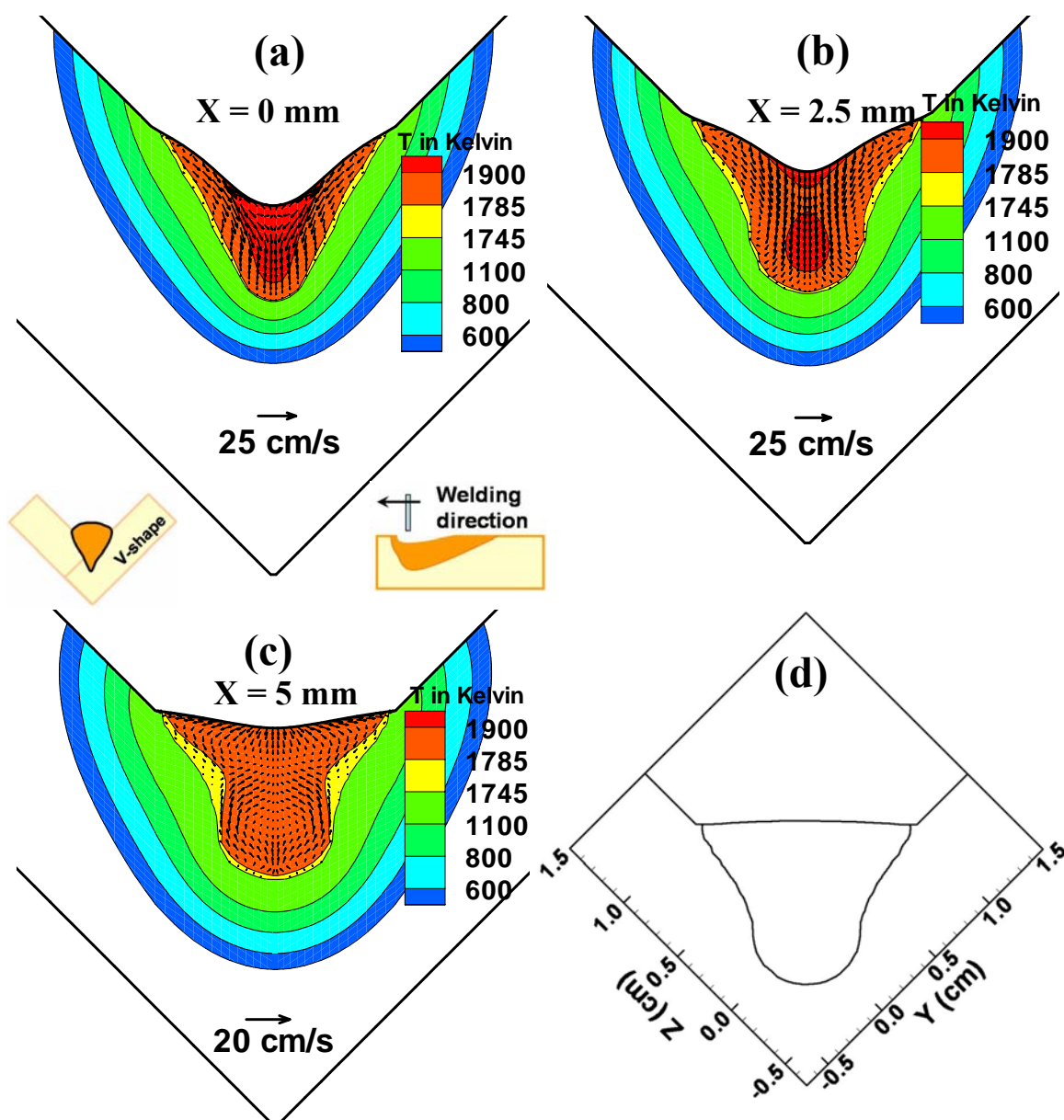


Figure 3-9: Calculated temperature field, velocity fields and solidified bead geometry during horizontal welding of symmetrical V-shape joint as shown in inset. Welding conditions are same as those given in case # 1 (table 3-3). The temperature and velocity fields at different cross sections planes perpendicular to the welding direction are shown in figures (a), (b) and (c). These figures represent the following regions: (a) directly under the arc, (b) 2.5 mm rear of the arc location, (c) 5 mm rear of the arc location and (d) the solidified reinforced weld bead geometry.

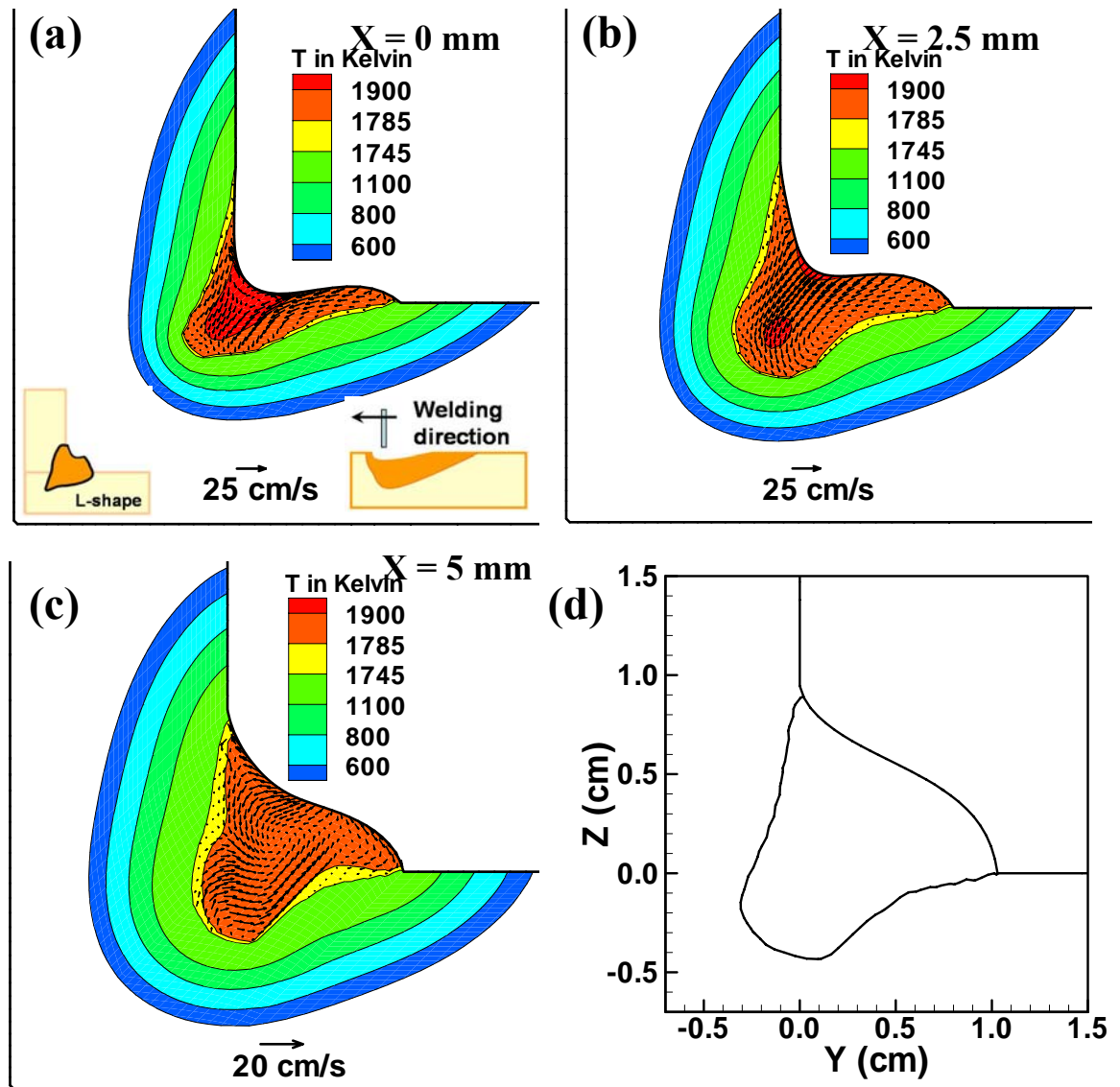


Figure 3-10: Calculated temperature field, velocity fields and solidified bead geometry during horizontal welding of L-shape joint. Welding conditions are same as those given in case # 1 (table 3-3). The temperature and velocity fields at different cross sections planes perpendicular to the welding direction are shown in figures (a), (b) and (c). These figures represent the following regions: (a) directly under the arc, (b) 2.5 mm rear of the arc location, (c) 5 mm rear of the arc location and (d) the solidified reinforced weld bead geometry.

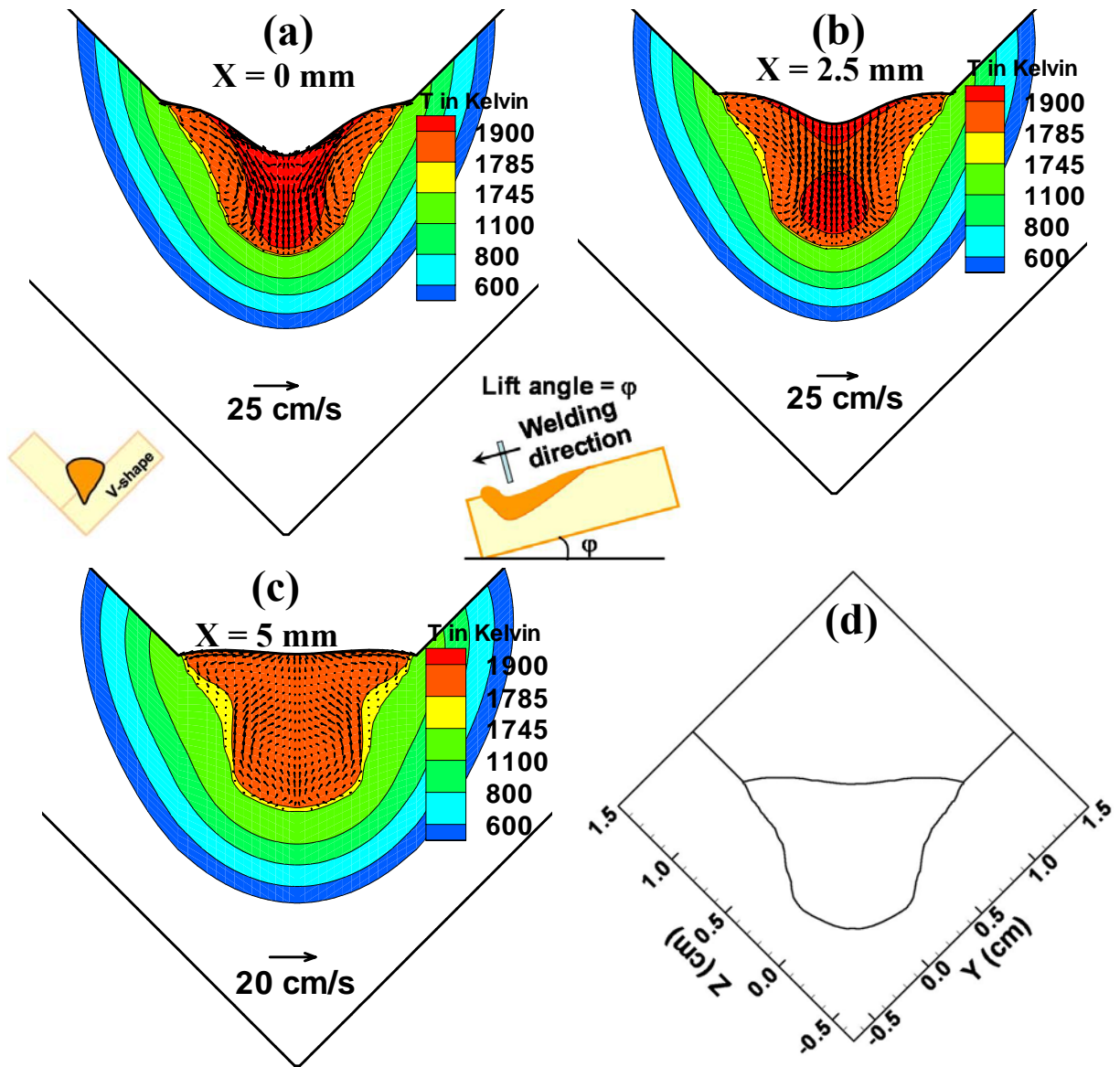


Figure 3-11: Calculated temperature field, velocity fields and solidified bead geometry during downhill welding of V-shape joint. The workpiece is lifted from behind the electrode at an angle of 10° . Welding conditions are same as those given in case # 1 (table 3-3). The temperature and velocity fields at different cross sections planes perpendicular to the welding direction are shown in figures (a), (b) and (c). These figures represent the following regions: (a) directly under the arc, (b) 2.5 mm rear of the arc location, (c) 5 mm rear of the arc location and (d) the solidified reinforced weld bead geometry.

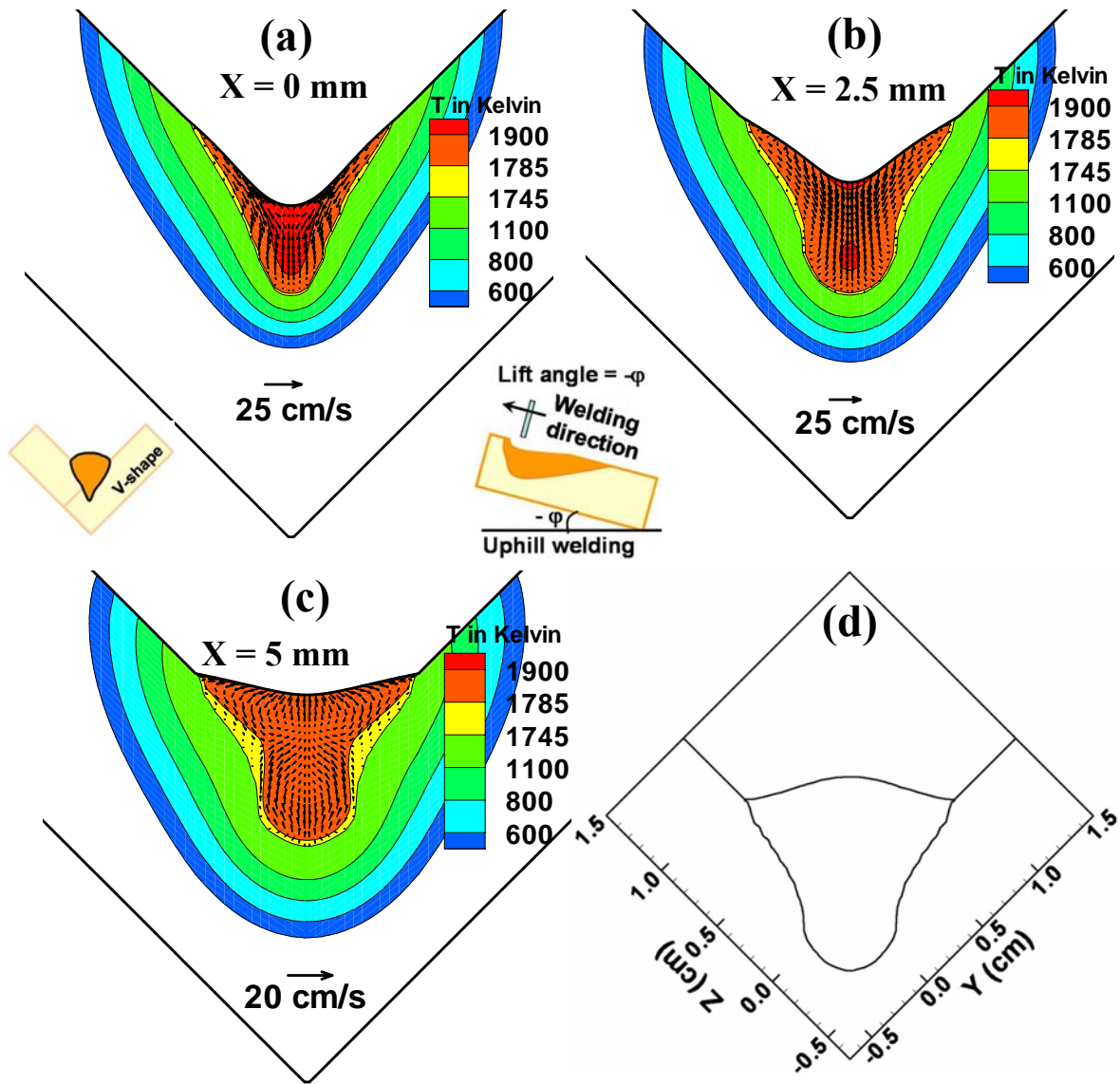


Figure 3-12: Calculated temperature field, velocity fields and solidified bead geometry during uphill welding of V-shape joint. The workpiece is lifted from ahead of the electrode at an angle of 10° . Welding conditions are same as those given in case # 1 (table 3-3). The temperature and velocity fields at different cross sections planes perpendicular to the welding direction are shown in figures (a), (b) and (c). These figures represent the following regions: (a) directly under the arc, (b) 2.5 mm rear of the arc location, (c) 5 mm rear of the arc location and (d) the solidified reinforced weld bead geometry.

The weld pool surface is severely depressed under the effect of the arc pressure, and the liquid metal flows downwards in the middle of the pool driven by the electromagnetic force. As the monitoring location moves away from the arc, the weld pool surface shows considerably less depression as would be expected from the reduction in arc pressure. Furthermore, the accumulation of the liquid metal in the rear of the weld pool is clearly visible in figure **3-9(c)**. The solidified region behind the arc is elevated owing to the filler metal addition (figure **3-9(d)**). This accumulated metal forms the weld reinforcement after solidification.

Figures **3-10**, **3-11** and **3-12** show the similar finger penetration characteristic of the GMA welding during horizontal welding of L-shaped joint; and downhill and uphill welding of V-shaped joints. However, due to effect of inclination of the geometry, the buoyancy and inertia force affects the temperature distribution and the velocity field in the workpiece as shown in figures **3-10**, **3-11** and **3-12**. Furthermore, the free surface profile differs quite remarkably in these cases (figures **3-10(d)**, **3-11(d)** and **3-12(d)**). Downhill welding affects the weld contour and penetration, as shown in figure **3-11**. The weld puddle tends to flow toward the electrode and preheats the base metal, particularly at the surface. As the angle of declination increases, the middle surface of the weld is depressed, penetration decreases and the width of weld increases.

Uphill welding affects the fusion zone and the weld surface as shown in figure **3-12**. The force of gravity causes the liquid metal to flow back and lag behind the electrode. The edges of the weld lose metal, which flows to the center. As the angle of inclination increases, reinforcement and penetration increases, and the width of the weld pool decreases. This difference in weld bead geometry may affect the strength and integrity of the welded joint [22].

Figure **3-13** shows the solidified bead profile for horizontal welding of symmetrical V-shaped joints, L-shaped joint and uphill welding of V-shaped joints welding conditions listed in case # 4 in table **3-3**. A remarkable difference in the bead geometry can be observed during the three cases. Figure **3-13(a)** shows that fillet welds made in the symmetrical (i.e. V-shape) horizontal (or, flat) position with spray transfer are usually more uniform, have equal legs and convex profiles.

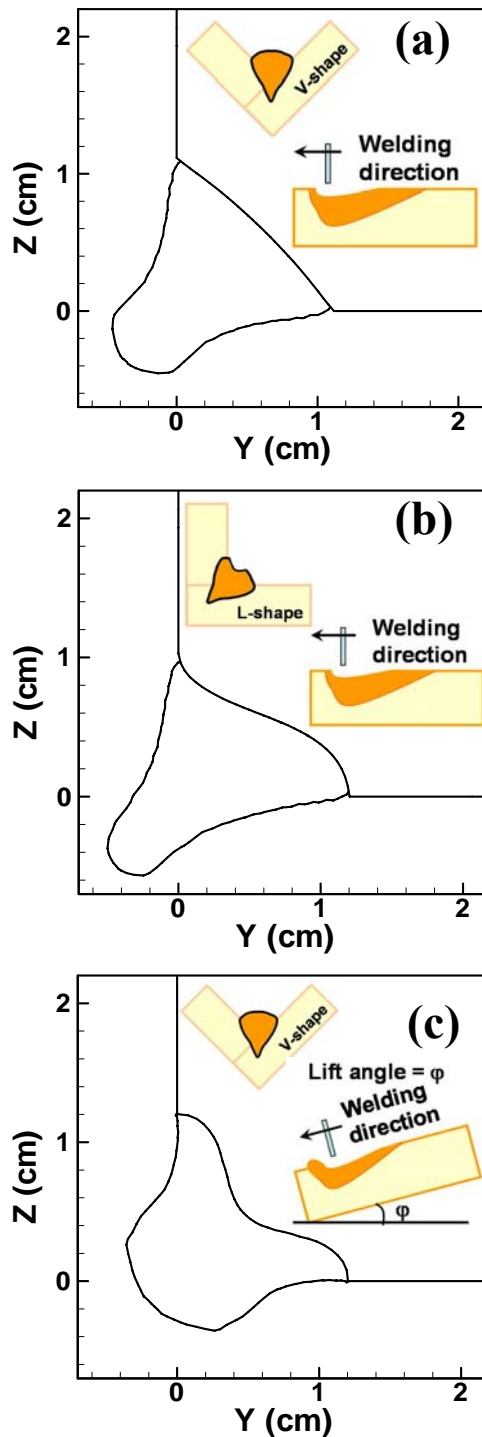


Figure 3-13: Calculated reinforced weld bead profile during (a) horizontal welding of V-shape; (b) horizontal welding of L-shape joints and (c) downhill welding of V-shape joint. During downhill welding, the workpiece was lifted from behind the electrode at an angle of 30° . Welding conditions are same as those given in case # 4 (table 3-3).

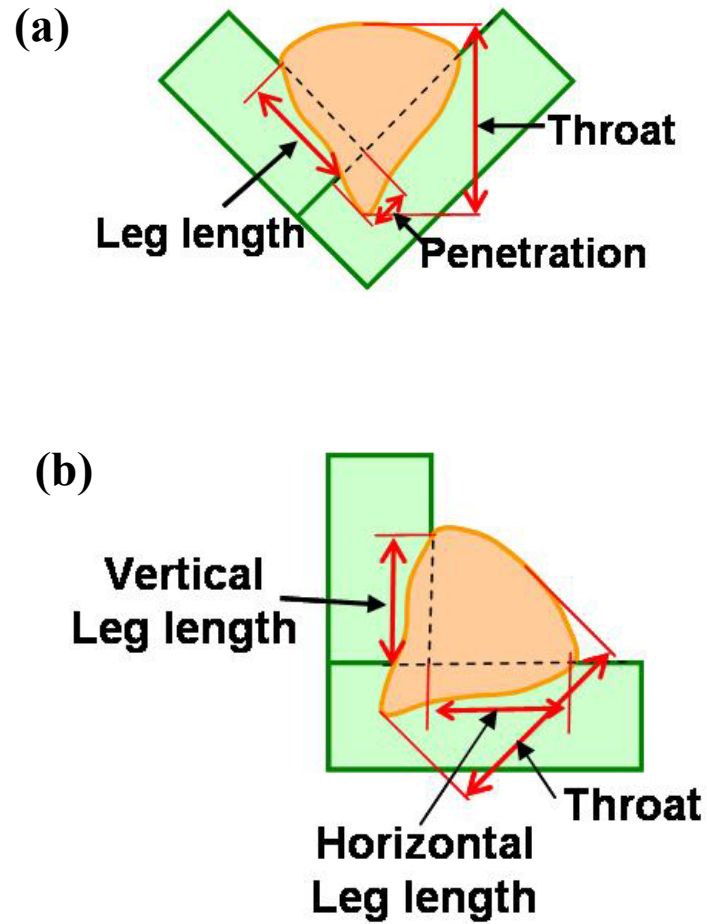


Figure 3-14: Nomenclature of weld bead geometry used to define (a) V-shape joints and (b) L-shape joints.

Figures **3-14(a)** and **3-14(b)** show the nomenclature of fillet weld bead geometry for V-shape and L-shape joints, respectively. These welds are less susceptible to undercutting than similar fillet welds made in other orientations or downhill position (figures **3-13(b)** and **3-13(c)**). Table **3-4** lists the calculated weld bead dimensions and the magnitude of maximum velocities in all the four cases. The high value of Froude number (Fr) during downhill welding signifies the dominance of the inertia force over the gravity force. In case of L-shape joint, the Fr is low, which means that the gravity plays an important role in this situation which is also evident from the free surface obtained in figure **3-13(b)**.

Table **3-4** also shows that the horizontal and vertical leg-length dimensions are higher during downhill welding compared to other welding positions. This is due to downward flow of the liquid under the gravity force which tries to force the liquid in outward direction towards the plate edges. This effect can be justified through figures **3-11(d)** and **3-13(c)**, where the free surface profile is depressed in the center. Furthermore, during uphill welding the throat dimension increases compared to horizontal or downhill welding since the molten metal starts solidifying in the central region as can be seen in figure **3-12(d)**. Similar trends were observed by Kang et. al. [41] during gas-tungsten-arc butt welding of Nickel. Their experimental data showed that uphill welding at 90° (or, parallel up welding) produces 21 % deeper penetration compared to perpendicular downhill welding (or, parallel down welding) at low welding speeds. During downhill welding, the extra mass gets accumulated ahead of the arc which leads to shallow weld pool. They also observed about 5-8 % increase in the width of the weld pool during downhill position at 3 mm/sec welding velocity. They attributed this change in weld dimensions to free surface deformation which they measured using laser profilometry. These experimental results in the literature [41] qualitatively supports the results obtained in this thesis work for more complex GMA fillet welding system.

The calculated temperature and velocity fields and surface profile at central vertical longitudinal sections parallel to the welding direction for case #1 (table **3-3**) are shown in figure **3-15**, where the weld pool boundary is represented by the 1745 K solidus isotherm. As shown all of these figures, the liquid metal motion is quite complicated due

to the combined effects of the driving forces. In the middle of the weld pool, the liquid metal is driven downwards by the electromagnetic force, and a major anticlockwise circulation loop is formed along the central longitudinal plane, i.e, $Y = 0$ plane shown in the figure 3-15. The region directly under the heat source is severely depressed under the effect of the arc pressure. As a result of the filler metal addition, the solidified weld metal forms pronounced weld reinforcement. Figure 3-15(c) shows the molten metal ahead of the arc (which is located at $X = 2.5$ cm) due to downward flow of liquid metal under the effect of inertia force. This downward flow tries to deform the weld pool surface from the center. In case of uphill welding, there is no hump of liquid metal ahead of the arc since the gravity force tries to carry all the molten metal towards rear end (figure 3-15(d)). These figures also show that away from the heat source, the weld pool surface shows considerably less depression as would be expected from the reduction in arc pressure. Also, the peak temperatures are higher at locations close to the weld center and decrease away from the heat source.

Table 3-4: Effect of different orientations of workpiece on the weld pool characteristics. Symbol u_{\max} , v_{\max} and w_{\max} represent the maximum velocity (magnitude) in x, y and z directions, respectively. The welding conditions used in calculations are listed in case # 1 in table 3-3.

	u_{\max} (mm/s)	v_{\max} (mm/s)	w_{\max} (mm/s)	Vertical leg-length (mm)	Horizontal leg-length (mm)	Throat (mm)	Fr
V-shape geometry and horizontal welding	176.3	177.9	111.4	9.8	9.8	10.8	0.27
L-shape geometry and horizontal welding	151.0	186.9	133.0	8.8	10.3	10.7	0.24
V-shape geometry and 10° uphill welding	185.2	157.8	116.3	9.5	9.5	11.7	0.28
V-shape geometry and 10° downhill welding	221.3	212.8	109.5	10.3	10.3	9.6	0.36

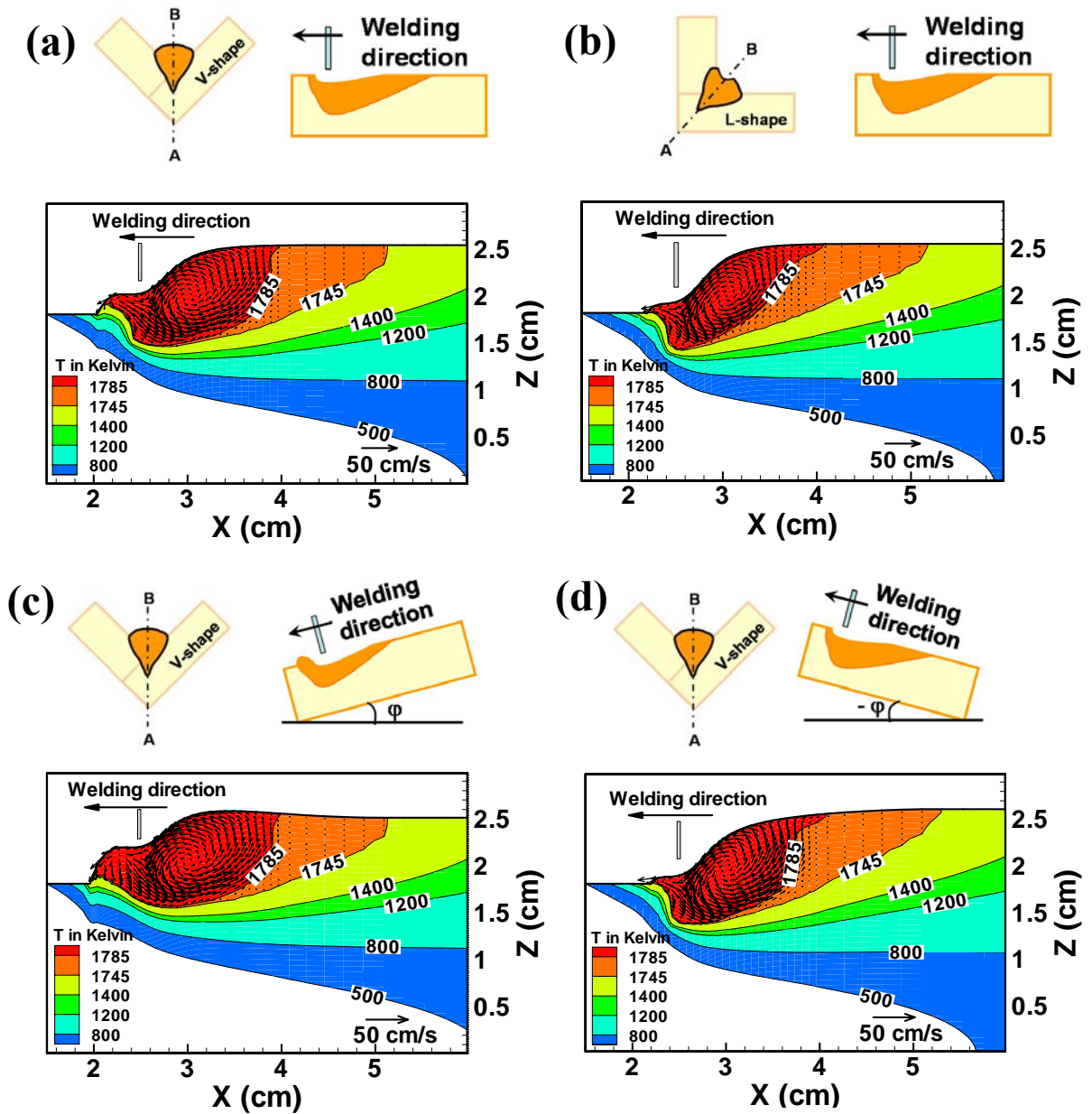


Figure 3-15: Calculated temperature and velocity vectors (shown by arrows) along central vertical longitudinal plane i.e. plane AB as shown in the inset. (a) Horizontal welding of V-shaped joint; (b) Horizontal welding of L-shaped joint; (c) Downhill welding of V-shaped joint at an angle of 10°; and (d) Uphill welding of V-shaped joint at an angle of 10°. The weld pool boundary is represented by the 1745 K isothermal line. Electrode is located at $X = 2.5$ cm. Welding conditions are the same as those in case #1 in table 3-3.

3.2.5 Effect of arc current and orientation angles on the weld pool geometry

Since the weld bead geometric characteristics affect the mechanical properties of the fillet weld, the effect of arc current and workpiece tilt angle on the weld geometry is studied. Figure 3-16 shows three important geometrical parameters of the weld bead, i.e. horizontal leg-length, vertical leg-length and throat as a function of the welding current and the workpiece tilt angle. As shown in this figure, the computed results show that the geometrical parameters increase with the arc current. For a fillet weld, the arc energy input is primarily responsible for the formation of the top part of the weld bead, whereas the volumetric heat source is largely responsible for the formation of the finger penetration. Increase in arc current, increases the heat supplied to the workpiece, downward electromagnetic force, arc pressure and the droplet frequency. Increase in all of these factors increases the weld bead dimensions.

With increase in tilt angle, the horizontal length and throat increases while the vertical leg-length decreases (figures 3-16(a), 3-16(b) and 3-16(c)). This is due to the inertia effect which tries to pull down the liquid metal in downward direction. Increase in tilt angle increases the difference between horizontal and vertical leg-lengths which may affect the final strength of the weld bead. Figure 3-16(c) shows that the computed non-dimensional throat does not vary significantly with either arc current or the tilt angle for given wire feed rate and welding speed. This behavior is expected since the dimensions of the throat depend largely on the rate of mass addition.

3.2.6 Weld thermal cycles

The temperature field obtained from the heat transfer and fluid flow calculation is at quasi-steady state, since the coordinate system is attached to the moving heat source. Therefore, the thermal cycles are calculated by converting the x distance into time using the welding speed. Figures 3-17(a) and 3-17(b) show the thermal cycles at four different locations during welding of V-shape and L-shape joints, respectively.

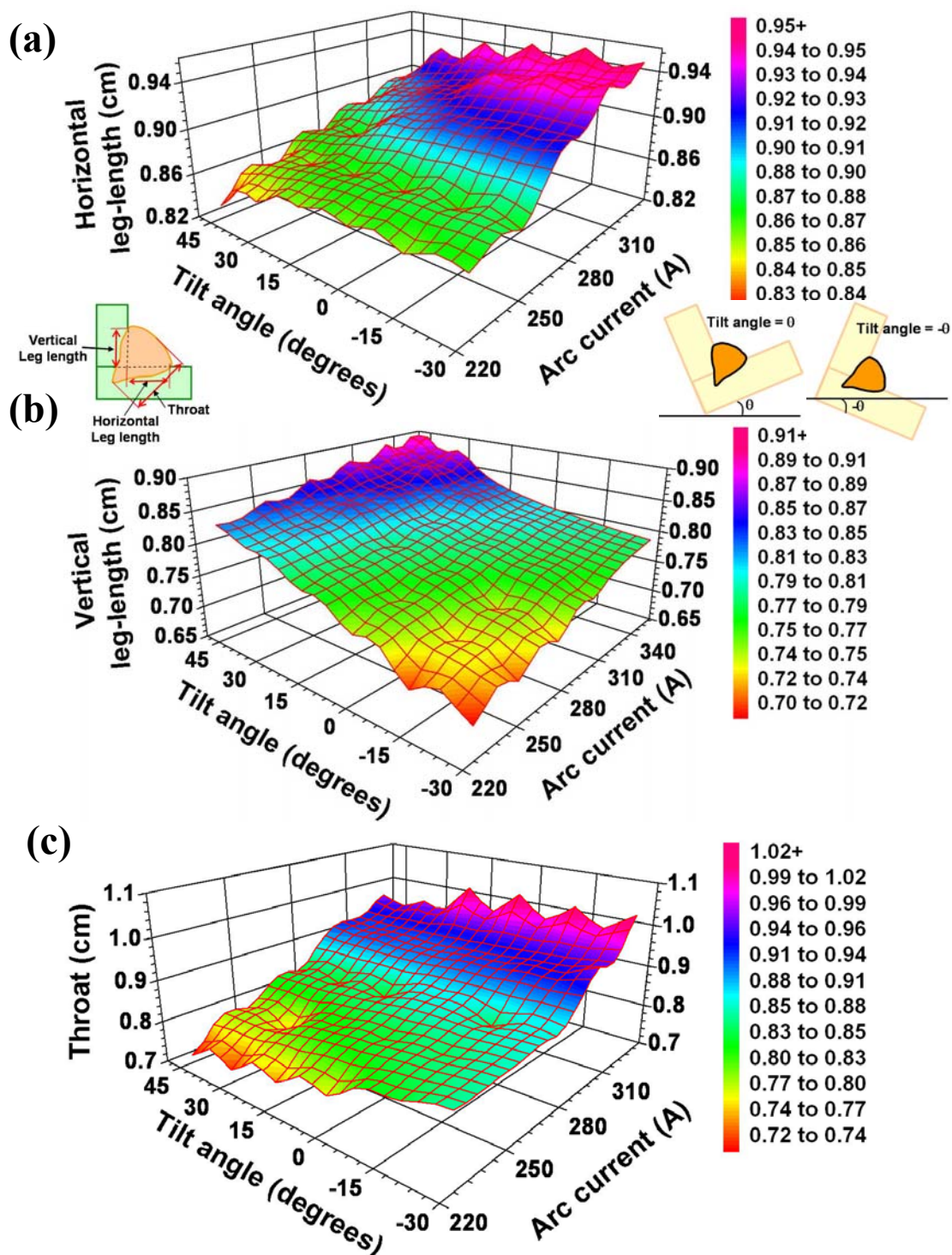


Figure 3-16: Effect of arc current and the workpiece tilt angle on (a) Horizontal leg-length; (b) Vertical leg-length; and (c) throat of the weld bead. Tilt angle = 0° refers to the V-shaped joint and 45° refers L-shape joint.

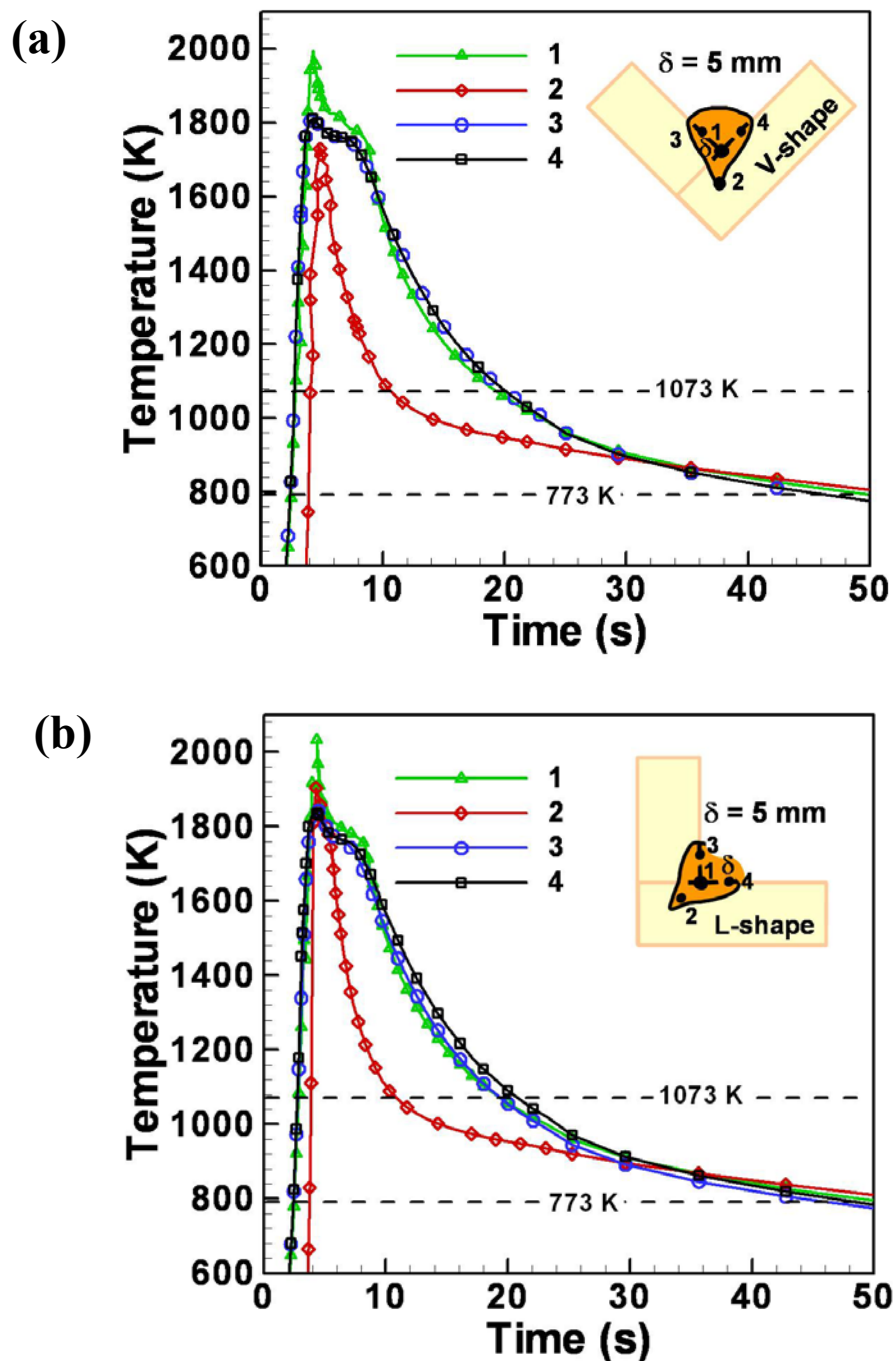


Figure 3-17: Calculated thermal cycles in the fillet weld at four different locations during horizontal welding of (a) V-shape joint; and (b) L-shape joint. Symbol δ represents the distance from the joint root to the monitoring locations as shown in the inset.

The welding conditions used in the calculations are listed in case # 1 in table 3-3. All these locations are located in the FZ. As shown in these figures, the heating rates are much higher than the cooling rates. This is due to the following two reasons. First, the isotherms in front of the heat source are compressed whereas those behind it are largely elongated due to the high welding speed. Second, the existence of the volumetric heat source also contributes to the high heating rates. As expected, the peak temperatures are higher at locations close to the weld center, and decrease as the monitoring location moves farther away. The peak temperature at location 2 in V-shape geometry is lower than in L-shape geometry. It is due to extended penetration in L-shape geometry as shown in figure 3-13. Furthermore, the thermal cycles are different for locations 3 and 4 in figure 3-17(b) due to un-symmetric weld bead geometry which affects the temperature distribution inside the workpiece. This difference in peak temperature and thermal cycles at any particular location will affect the microstructure and the residual stress inside the workpiece.

During welding of steel plates, the average cooling rate, $\dot{T}_{8/5}$, from 1073K to 773K (800 °C to 500 °C) is of importance, since it affects the final microstructure of the weld metal for most of the steels [1, 2, 42]. Figures 3-18(a) and 3-18(b) show the calculated average cooling rates at different monitoring locations for different orientations of workpiece plates (i.e. V and L configurations) and during uphill and downhill welding, respectively. As shown in these figures, the calculated average cooling rate decreases as the heat input per unit length (defined as the total power input / welding speed) increases. The effect of heat input per unit length on $\dot{T}_{8/5}$ can be explained as follows. The average cooling rate $\dot{T}_{8/5}$ is calculated as:

$$\dot{T}_{8/5} = \frac{T_{800} - T_{500}}{t_{8/5}} = \frac{300 U_w}{\Delta d_{8/5}} \quad 3.63$$

where $t_{8/5}$ is the cooling time from 1073K to 773K, U_w is the welding speed and $\Delta d_{8/5}$ is the distance between two points where a line parallel to the x direction intercepts the 1073 K and 773 K isothermal contours.

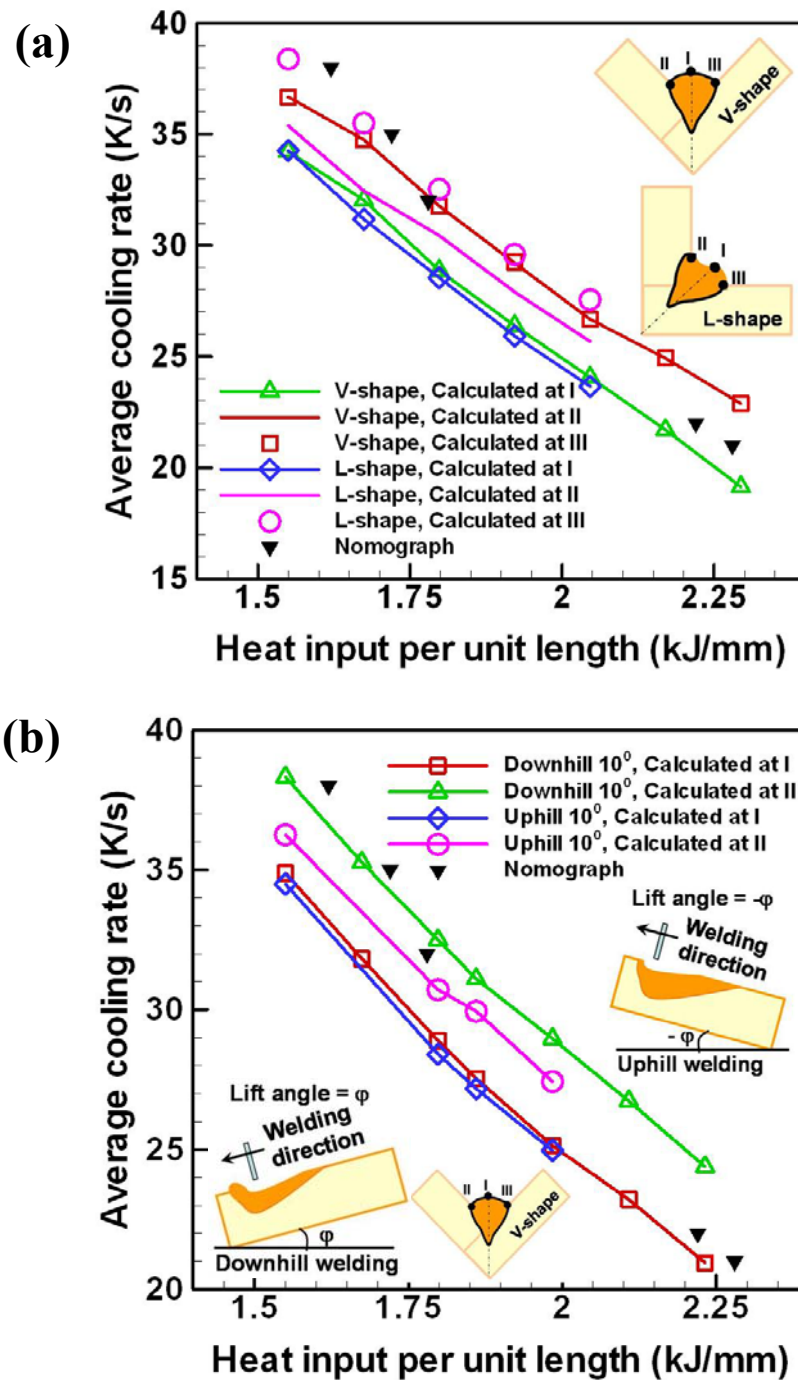


Figure 3-18: Calculated average cooling rate $\dot{T}_{8/5}$ at different monitoring locations in the fillet weld for (a) different orientations of workpiece; and (b) during downhill and uphill welding of V-shape geometry. The solid triangles represent the cooling rate estimated using the nomograph available in the literature [42].

With increase in welding speed, both the 1073 K and 773 K isothermals expands outwards. However, the distance $\Delta d_{8/5}$ does not change significantly. As a result, the cooling rate increases. Since an increase in U_w is accompanied by a reduction in the heat input per unit length, a reduction in heat input is thus accompanied by an increase in the cooling rate, as observed in figures **3-18(a)** and **3-18(b)**. On the other hand, when input power is increased while maintaining the constant welding speed, the isotherms are expanded and $\Delta d_{8/5}$ increases. Hence, the cooling rate decreases with an increase in the input power. Since both a decrease in the welding speed and an increase in the power input result in a reduction in the cooling rate, the higher the heat input per unit length, the lower the cooling rate $\dot{T}_{8/5}$.

Figures **3-18(a)** and **3-18(b)** also indicate that the average cooling rates away from the weld central line are higher than those at the central axis on the weld bead top surface. This is because the temperature is much higher under the welding torch compared to the end of weld bead joint. Figure **3-18(a)** also shows that due to unsymmetrical weld bead formation, the cooling rate are different at the two ends of the weld bead. Furthermore, the cooling rates are higher during downhill welding compared to uphill welding due to wider weld bead formation during downhill welding (figure **3-18(b)**). The cooling rate increases as we move away from the center of the weld bead. A 10-25 % increase in cooling rate can be observed between locations I and II in figures **3-18(a)** and **3-18(b)**. Furthermore, this difference in cooling rate increases with increase in heat input per unit length. They also observed that the cooling rate is much higher in case of fillet welding compared to butt welding. Svensson et al. [42] experimentally measured the cooling time for different heat input unit length during GTAW. A comparison between their measured values [42] and the calculated values for GMA fillet welding in this work shows that the cooling rates are more than 30 % higher in case of GMA fillet welding. Kihara et al. [43] also observed similar difference in the cooling rates between fillet joint and butt joint welding of high-strength steel. In the literature, a nomograph [44] is commonly used to estimate the average cooling rate $\dot{T}_{8/5}$ for various welding conditions. As shown in figures **3-18(a)** and **3-18(b)**, the calculated cooling rates at the

fusion boundary agree reasonable well with those estimated using the nomograph. This good agreement indicates the validity of the heat transfer and fluid flow calculation during GMA fillet welding. Furthermore, the heat transfer and fluid flow model is capable of providing much more information on cooling rates than the nomograph, such as the spatial variation of the cooling rate for different orientations of workpiece.

Figures **3-19(a)** and **(b)** show the effect on welding positions and orientation i.e. lift and tilt angles, respectively on $\dot{T}_{8/5}$. The value of $\dot{T}_{8/5}$ increase with increase in lift angle which means the cooling rates are much higher during downhill welding compared to uphill or flat welding positions. This may be due to downward flow present during downhill which may distribute the heat from the center towards the leading edge. The cooling rates at location II is much higher than location I since the temperature is much lower at location II. With increase in tilt angle, the cooling rate increases slightly. This may be due to more uniform and symmetrical flow with increase in tilt angle. However, there is not much effect of the tilt angle on the cooling rate as shown in figure **3-19(b)**.

Figures **3-20(a)**, **3-20(b)**, **3-20(c)** and **3-20(d)** show the comparison between calculated weld bead shape for GMA fillet welding of V-shape, L-shape joints, downhill and uphill welding. As shown in these figures, the calculated weld bead geometries agree reasonably well with the corresponding experimental results. In particular, the shape of the weld reinforcement and the finger penetration could be satisfactorily predicted by the model. On the whole, the geometric features of the fillet weld could be satisfactorily predicted by using the numerical heat transfer and fluid flow model.

3.3 Summary and Conclusions

An existing numerical heat transfer and fluid flow model of GMA fillet welding of symmetrical V-shape geometry available in our research group was modified to capture the effects of fillet joints orientations on free surface profile, temperature distribution, velocity field, weld pool shape and size and the nature of the solidified weld pool reinforcement surface.

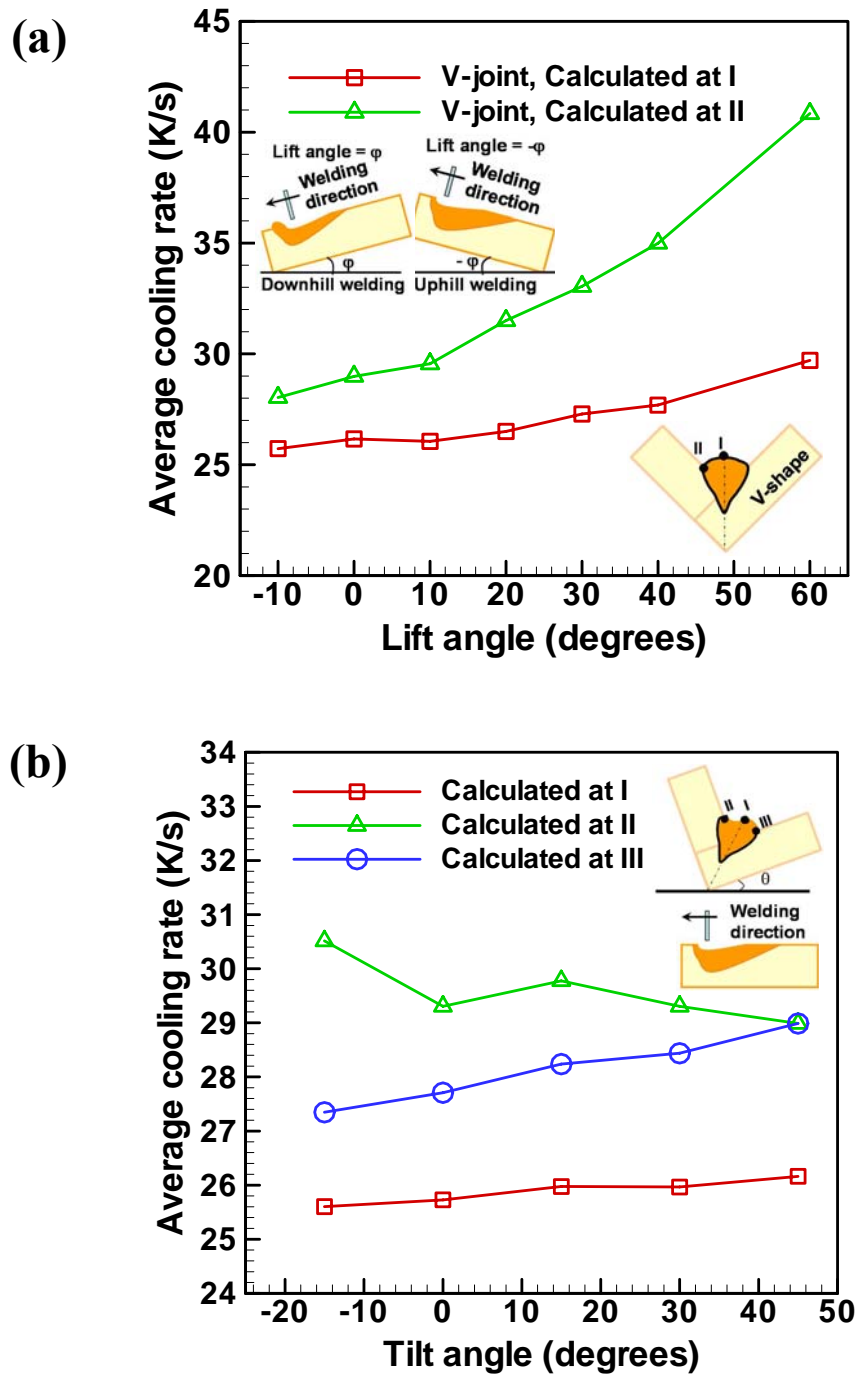


Figure 3-19: Effect of the (a) lift angle; and (b) tilt angle on the average cooling rates ($\dot{T}_{8/5}$) from 1073K to 773K at different monitoring locations during GMA fillet welding.

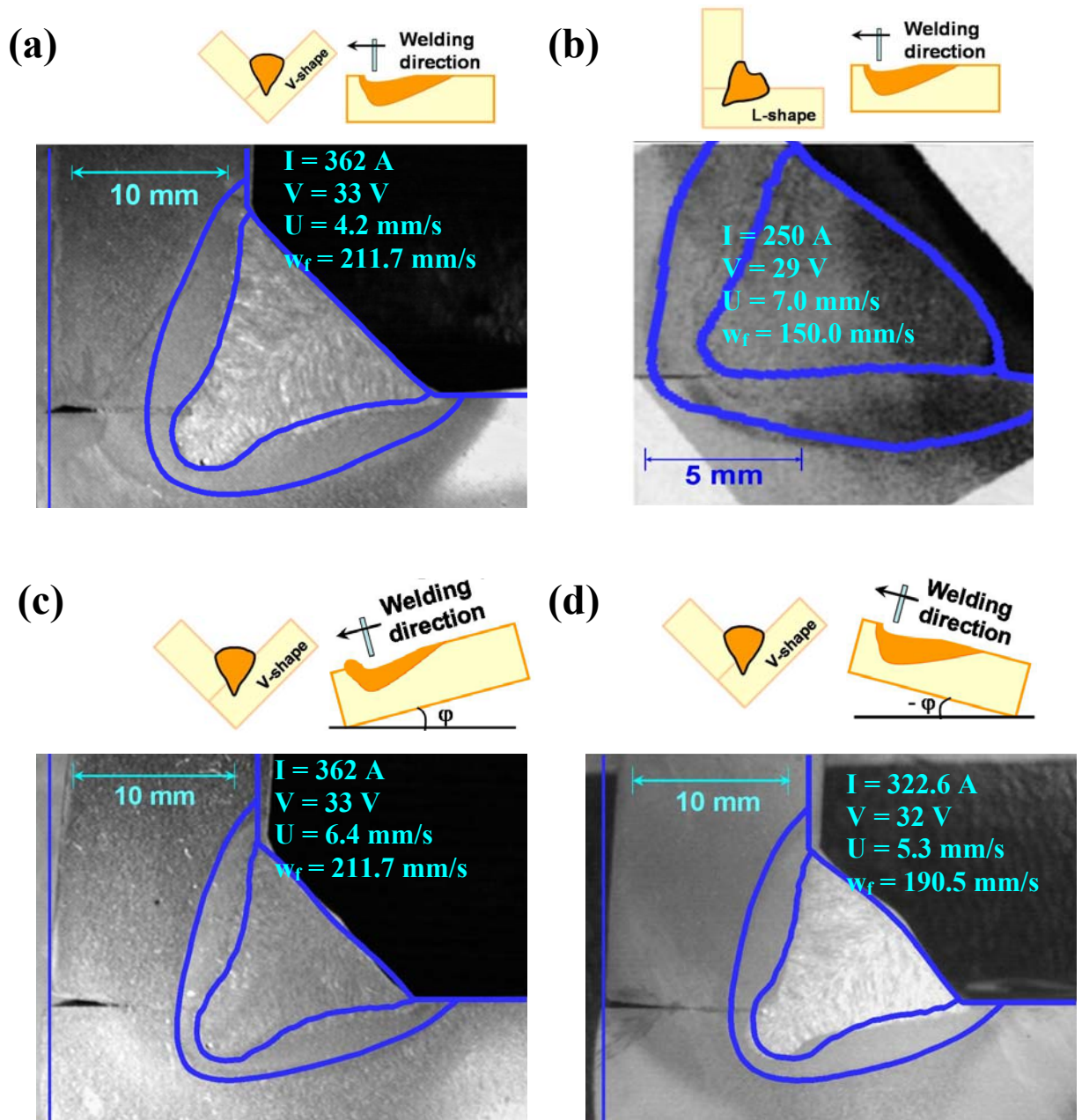


Figure 3-20: Comparison between the calculated and experimental weld geometry during GMA welding of (a) V-shape symmetric fillet joint; (b) L-shape symmetric fillet joint; (c) downhill welding at lift angle = 6° and (d) uphill welding at lift angle = -4° . The experimental micrograph in figure (b) is taken from reference [21]. Since the wire feed rate was not mentioned in the experimental conditions for this micrograph, a value of 150.0 mm/s is chosen in the simulation based on the arc current value. The inner isotherm (blue line) in all these figures represents the calculated weld pool boundary based on solidus temperature of 1745K, while outer isotherm (blue line) represents the 1073 K temperature.

The results reported in this chapter indicate a significant promise for understanding and controlling of GMA fillet welding processes based on fundamental principles of transport phenomena. The information obtained using the numerical model, such as the weld bead geometry and thermal cycles in the weldment, can be used to further understand the weld properties and structure. The following conclusions can be drawn from the results.

(1) The liquid metal convection plays a dominant role in dissipating the heat in the weld pool for all orientations of the workpiece, i.e. V and L joint configurations and horizontal, downhill and uphill welding positions. The velocities in the weld pool are found to be significantly high which affects the weld pool shape and mixing of the solutes and gases in the weld pool.

(2) The manner in which the effective viscosity and effective thermal conductivity vary in the weld pool was also analyzed using a vorticity based mixing-length turbulence model. This vorticity based turbulence model uses a variable mixing length to capture the effect of the weld pool boundary on the fluid flow in the weld pool. The results show that the enhanced viscosity is high under the arc while its value decreases in the rear part of the weld pool. The average value of enhancement factor is of the same order as reported in the literature for other welding conditions.

(3) The weld pool surface profile was calculated by minimizing the total surface energy, which includes the surface tension energy, gravity potential, and work done by arc force. The impingement of droplets on the weld pool surface was considered via a volumetric heat source. As a result, near middle of the weld pool, the predicted pool surface profile may be less displaced than that under the influence of droplet impingement. However, at the rear part of the weld pool, the predicted surface profile is expected to be reasonable, since the effect of droplet impingement in that region is small.

(4) The workpiece orientations and welding configuration affect the free surface profile significantly. During L-shape joints, the free surface profile becomes asymmetrical due to gravity which affects the strength of the weld bead. In case of uphill welding, the chances of formation of undercutting defect increases, since the fluid starts accumulating near the central welding axis. On the other hand, during downhill welding,

there are chances of formation of split beads due to depression of free surface in the center. This kind of weld bead geometry reduces the weld strength along the central symmetrical axis.

(5) The horizontal leg-length and vertical leg-length were found to increase during downhill welding while these dimensions decrease during uphill welding. The throat dimension has the opposite effect of welding position and it increases during uphill welding.

(6) The geometrical parameters such as throat, horizontal leg-length and vertical leg-length increase with the increase in arc current. It was also observed that with increase in tilt angle from -30° to 45° , the horizontal length and throat decreases while the vertical leg-length increases.

(7) The computed results show that the thermal cycles at various locations inside the workpiece vary with change in workpiece orientations or welding positions. It was found that with increase in the lift angle, the average cooling rate between 1073 K and 773 K ($\dot{T}_{8/5}$) increases for similar welding conditions. Therefore, average cooling rates for downhill welding were higher than uphill or flat welding positions. Both the calculated results and the available experimental data indicate that $\dot{T}_{8/5}$ decreases with increase in heat input per unit length. The calculated results were in good agreement with the independent experimental data available in the literature.

(8) The numerically computed fusion zone geometry, finger penetration characteristic of the GMA welds and the solidified surface profile of the weld reinforcement were in fair agreement with the experimental result.

3.4 References

1. W. Zhang, C. H. Kim and T. DebRoy, *J. Appl. Phys.* **95**, 5210 (2004).
2. W. Zhang, C. H. Kim and T. DebRoy, *J. Appl. Phys.* **95**, 5220 (2004).

3. A. Kumar, W. Zhang, C. H. Kim and T. DebRoy, *Welding in the World*, **49** (9/10), 32 (2005).
4. W. Zhang, G. G. Roy, J. W. Elmer and T. DebRoy, *J. Appl. Phys.* **93**, 3022 (2003).
5. M. C. Tsai and S. Kou, *Weld. J.*, **69**, 241s (1990).
6. K. Hong, D. C. Weckmann, A. B. Strong and W. Zheng, *Sci. Technol. Weld. Joining* **7**, 125 (2002).
7. K. Mundra, T. DebRoy, and K. Kelkar, *Numer. Heat Transfer A*, **29**, 115 (1996).
8. Z. Yang, J. W. Elmer, J. Wong, and T. DebRoy, *Weld. J.*, **79**, 97s (2000).
9. Z. Yang, S. Sista, J. W. Elmer, and T. DebRoy, *Acta Mater.*, **48**, 4813 (2000).
10. T. Hong, W. Pitscheneder and T. DebRoy, *Sci. Technol. Weld. Joining*, **3**, 33 (1998).
11. R. T. C. Choo and J. Szekely, *Weld. J.* **73**, 25 (1994).
12. J. F. Lancaster, *The Physics of Welding*, 2nd Edition, Pergamon, Oxford (1986).
13. C. S. Wu and L. Dorn, *Comput. Mater. Sci.*, **2**, 341 (1994).
14. J. W. Kim and S. J. Na, *Weld. J.*, **74**, 141s (1995).
15. Z. N. Cao and P. Dong, *J. Eng. Mater. Technol.*, Trans. ASME, **120**, 313 (1998).
16. H. G. Fan and R. Kovacevic, *J. Phys. D: Appl. Phys.*, **31**, 2929 (1998).
17. Y. Wang and H. L. Tsai, *Metall. Mater. Trans. B*, **32B**, 501 (2001).
18. C. H. Kim, W. Zhang and T. DebRoy, *J. Appl. Phys.* **94**, 2667 (2003).
19. S. Kumar and S. C. Bhaduri, *Metall. Mater. Trans. B*, **25B**, 435 (1994).
20. S.-K. Jeong and H.-S. Cho, *Proc. Instn. Mech. Engrs.* **211B**, 63 (1997).
21. S. -H. Cho and J. -W. Kim, *Sci. Technol. Weld. Joining* **6**(4), 220 (2001).
22. W. A. Bowditch and K. E. Bowditch, "Welding Technology Fundamentals", 2nd edition, The Goodheart-Willcox Company, Tinley Park, Illinois (1997).
23. V. R. Voller and C. Prakash, *Int. J. Heat Mass Transfer*, **30**, 2690 (1987).
24. A. D. Brent, V. R. Voller and K. J. Reid, *Numer. Heat Transfer A*, **13**, 297 (1988).

25. A. Kumar and T. DebRoy, *J. Appl. Phys.*, **94**, 1267 (2003).
26. S. Kou and D. K. Sun, *Metall. Trans. A*, **16A**, 203 (1985).
27. K. A. Hoffmann and S. T. Chiang, *Computational Fluid Dynamics for Engineering – Volume II*, Engineering Education System, Wichita, KS, USA (1993).
28. J. F. Thompson, Z. U. A. Warsi and C. Wayne Mastin, *Numerical Grid Generation: Fundamentals and Applications*, Elsevier Science, New York (1985).
29. K. Hong, D. C. Weckmann, A. B. Strong and W. Zheng, *Sci. Technol. Weld. Joining* **8**, 313 (2003).
30. D. C. Wilcox, *Turbulence Modeling for CFD*, DCW Industries, California (1993).
31. B. E. Launder and D. B. Spalding, *Lectures in Mathematical Models of Turbulence*, Academic Press, London (1972).
32. S. V. Patankar, *Numerical Heat Transfer and Fluid Flow*, Hemisphere Publishing, New York (1982).
33. S. Rhee and E. Kannatey-Asibu Jr., *Weld. J.*, **71**, 381s (1992).
34. L. A. Jones, T. W. Eagar and J. H. Lang, *J. Phys. D: Appl. Phys.*, **31**, 107 (1998).
35. P. Sahoo, T. DebRoy and M. J. McNallan, *Metall. Trans. B*, **19B**, 483 (1988).
36. W. Pitscheneder, T. DebRoy, K. Mundra, and R. Ebner, *Welding J.*, **75**, 71s (1996).
37. M. L. Lin and T. W. Eagar, *Metall. Trans. B*, **17B**, 601 (1986).
38. Y. S. Kim and T.W. Eagar, *Weld. J.*, **70**, 20s (1991).
39. W. H. Press, B. P. Flannery, S. A. Teukolsky and W. T. Vetterling, *Numerical Recipes in FORTRAN*, 2nd edition, Cambridge University Press, Cambridge (1992).
40. E. A. Brandes and G. B. Brook, *Smithells Metals Reference Book*, 7th Edition, Butterworth-Heinemann, Oxford (1992).
41. N. Kang, T. A. Mahank, A. K. Kulkarni and J. Singh, *J. Mater. Manuf. Proc.*, **18** (2), 549 (2003).

42. L. E. Svensson, B. Gretoft and H. K. D. H. Bhadeshia, *Scandinavian J. Metallurgy*, **15**, 97 (1986).
43. H. Kihara, H. Suzuki and H. Tamura, *Researches on Weldable High-Strength Steels*, Vol. 1, The Society of Naval Architects of Japan, Tokyo (1957).
44. K. Masubuchi, *Analysis of Welded Structures*, Pergamon, Oxford (1980).

Chapter 4

IMPROVING RELIABILITY OF MODELING HEAT TRANSFER AND FLUID FLOW IN COMPLEX GAS METAL ARC FILLET WELDS

The temperature distribution, velocity profiles, weld pool geometry, thermal cycles and cooling rate for 800°C to 500°C obtained in the preceding chapter for GMA fillet welding showed that the heat transfer and fluid flow calculations can reveal important features of welding processes and welded material that are difficult to obtain otherwise. However, these existing models suffer from a major problem. The model predictions of weld pool geometry; cooling rates etc. do not always match the corresponding experimental results which makes the outputs of these models unreliable. Why don't the model predictions always match the corresponding experimental results perfectly while they embody the phenomenological governing equations of conservation of mass, momentum and energy? The answer to this question requires a peek into the possible causes which may be the main reasons for this discrepancy. The inaccuracy in predictions may come due to following reasons:

- (a) The assumptions used in the model are not valid or are unrealistic. Any inappropriate use of such assumptions will affect the calculations and the final results.
- (b) The numerical algorithm parameters such as grid size, their distribution and the algorithm chosen for solving the partial differential equations also affect the calculation.
- (c) These numerical models require more than 22 input parameters such as arc current, voltage, welding speed, wire feed rate, arc efficiency, arc radius, arc power distribution factor, contact tube to workpiece distance (CTWD), effective thermal conductivity and effective viscosity, and material properties such as density, specific heat of the solid, specific heat of the liquid, latent heat etc.

along with numerical algorithmic parameters. Any uncertainties in the values of these variables make the calculation and the model predictions unreliable.

To know the correct reason for the discrepancies in the model predictions, we need to analyze and scrutinize these points in detail. The first reason of having unrealistic assumptions in the model does not apply to our model, since we are able to predict the trends in weld pool geometry and cooling rates satisfactorily for different welding conditions in chapter 3. Also, the predictions were in good agreement for the experimental conditions investigated in this work.

The second factor of having wrong numerical algorithm parameters is also not true for our model since it has been well tested by various members who graduated from our group [1-12]. To achieve the maximum accuracy and resolution of variables, spatially non-uniform grids with finer grids near the heat source are used in the calculation as explained in section **3.2.1**. Furthermore, the modified SIMPLE algorithm used for calculating the temperature and velocity fields has been widely accepted as one of the best algorithm for solving continuity, momentum and energy equations in steady state problems [13, 14].

Now, we are left with only the third factor which may be the reason behind these discrepancies. The input welding process parameters such as arc current, voltage, welding speed, wire feed rate and CTWD can be easily prescribed with accuracy in the model. Similarly, the material properties such as density, specific heat of the solid, specific heat of the liquid, latent heat etc. for A-36 steel are well documented in the literature and are unlikely to cause significant error. The other input variables i.e. arc efficiency, arc power distribution factor and the arc radius are related to the arc characteristic. In the literature, it has been observed that the values of arc power distribution factor and the arc radius do not change significantly with welding conditions and are more or less same for GMA welding [15-20]. However, the reported values of the arc efficiency vary significantly for apparently similar welding conditions reflecting the complexity of the GMA welding process [15, 21-23]. The two other input variables i.e. effective thermal conductivity and effective viscosity are used to take into account the momentum transport rates in the weld pool owing to the strong re-circulating velocities [1, 24-28]. In the calculations, these

effective values of thermal conductivity and viscosity capture the effects of turbulence by arbitrarily enhancing their molecular values by 10 to 100 times. Unlike the molecular values of the thermal conductivity and viscosity, the enhanced or effective values of these “transport properties” are not physical properties of the fluid and, as a result, their values cannot be obtained from the standard compilations of thermo-physical properties. The values of the effective viscosity and thermal conductivity are properties of the specific welding system and cannot be easily assigned from fundamental principles. The above discussion on values of input variables points out that out of these several input parameters, the values of arc efficiency and effective transport properties are uncertain and cannot be easily prescribed from fundamental principles. Currently there is no unified basis to accurately prescribe the values of arc efficiency, effective thermal conductivity and effective viscosity. Values of these parameters significantly affect the results of numerical heat transfer and fluid flow calculations. As a result, the model predictions do not always agree with the experimental results.

This chapter addresses the lack of reliability of model predictions by coupling the heat transfer and fluid flow model of GMA fillet welding with optimization methods to find the values of the uncertain input parameters such as arc efficiency, effective thermal conductivity and the effective viscosity. The values of these variables are obtained in this chapter as a function of various welding variables based on inverse modeling approach [29-36]. The reliability of the calculation improves with more accurate values of the uncertain input parameters. The values of these parameters were determined from a limited volume of experimentally measured weld pool penetration, throat and the leg-length data using a combination of an optimization algorithm and a numerical heat transfer and fluid flow model. The optimization algorithm minimizes the error between the predicted and the experimentally observed penetration, throat and the leg-length during the GMA welding process by considering the sensitivity of these geometric parameters to each of the uncertain parameters. The Levenberg-Marquardt (LM) and two versions of conjugate gradient method (CG) i.e., Fletcher-Reeves and Polak-Ribiere of non-linear parameter optimization [30-32, 37-39] were used to estimate these uncertain

parameters. These derivative based optimization algorithms were preferred over stochastic optimization technique like genetic algorithm (GA) due to following reasons:

(a) The derivative based techniques are faster in convergence compared to stochastic techniques [39]. Furthermore, they require very few runs of heat transfer and fluid flow models, if the initial starting values are near to the optimal values. In the literature, some ranges have been already prescribed for the values of these uncertain variables. Selection of the initial starting values of the variables in these ranges help in minimizing the computation task using derivative based optimization techniques.

(b) There exists only one unique value of each variable for a specific heat input per unit length. It eliminates any chances of having multiple optimal values of these uncertain variables. Since, Levenberg-Marquardt (LM) and conjugate gradient (CG) are two best derivative based optimization algorithms based on computation time [31, 37-39]; these algorithms are preferred to find the optimized values of uncertain variables.

In effect, the procedure identifies values of uncertain parameters for each set of welding conditions in an iterative manner starting from a set of their initial guessed values.

4.1 Mathematical Model

4.1.1 Modeling of heat transfer and fluid flow during GMA fillet welding

The heat transfer and fluid flow model takes into account the liquid metal convection in the weld pool, the complex fillet joint geometry, the deformation of the weld pool top surface, additions of the filler metal, and the heat transfer by metal droplets as explained in chapter 3. The output from the model includes temperature and velocity fields, thermal cycles, fusion zone geometry and the solidified geometry of the weld reinforcement.

4.1.2 Optimization of uncertain variables

4.1.2.1 The uncertain variables

The goal of the optimization problem was to determine how the uncertain parameters, e.g., arc efficiency, effective thermal conductivity and effective viscosity vary with heat input per unit length. For simplicity we assumed the following linear relations between these variables and heat input.

$$\eta = f_1 + f_2 \cdot P_e^* \quad 4.1$$

$$k_e = f_3 \cdot k_L + f_4 \cdot k_L \cdot P_i^* \quad 4.2$$

$$\mu_e = f_5 \cdot \mu_L + f_6 \cdot \mu_L \cdot P_i^* \quad 4.3$$

$$\text{where,} \quad P_e^* = \frac{IV / (\pi r_w^2 w_f)}{[\rho c_p (T_L - T_a) + \rho L]} \quad 4.4.a$$

$$\text{and,} \quad P_i^* = \frac{IV / (\pi r_b^2 U_w)}{[\rho c_p (T_L - T_a) + \rho L]} \quad 4.4.b$$

where η is the arc efficiency, k_e is the effective thermal conductivity, k_L is the conductivity of the liquid material, μ_e is the effective viscosity, μ_L is the viscosity of the liquid material, I is the current, V is voltage, r_w is wire radius, w_f is the wire feeding rate, ρ is the density, c_p is the specific heat, T_L is the liquidus temperature, T_a is the ambient temperature, L is the latent heat of the alloy, r_b is the arc radius, U_w is the welding speed, and f_1 , f_2 , f_3 , f_4 , f_5 and f_6 are constants. In the literature, it has been shown that arc efficiency varies linearly with heat input per unit length [6, 15, 22] but the slope of this variation depends on the welding conditions and the technique [6, 15, 22]. Recent work on butt welding showed that effective thermal conductivity and effective viscosity is also a linear function of heat input per unit length [6, 7]. Also, due to narrow range of experimental data set used in the present work, it was justified to use the linear variation of the arc efficiency, effective thermal conductivity and effective viscosity with input power. In eq. 4.1, input power was non-dimensionalized with wire feeding rate and wire radius because if any of these two parameters is large, more power will be consumed in

wire melting. Therefore, less power will go to the workpiece from the arc. In the expressions of effective thermal conductivity and effective viscosity, input power was non-dimensionalized with respect to the welding speed and the arc radius. At high welding speed or the arc radius, the input power is distributed over a large area which reduces turbulence in the weld pool and lowers the effective thermal conductivity and viscosity. The values of η , k_e and μ_e calculated from eqs. 4.1, 4.2 and 4.3 can be used for the welding experimental conditions given in table 4-1 for the GMA fillet welding in spray mode.

Table 4-1: Welding conditions used in the experiments.

No.	Contact tube to workpiece distance (CTWD) (mm)	Wire feeding rate (mm/s)	Travel speed (mm/s)	Voltage (V)	Estimated current (A)
1	22.2	169.3	4.2	31	312.0
2	22.2	211.7	6.4	31	362.0
3	22.2	169.3	6.4	33	312.0
4	22.2	211.7	4.2	33	362.0
5	28.6	169.3	6.4	31	286.8
6	28.6	169.3	4.2	33	286.8
7	28.6	211.7	4.2	31	331.4
8	28.6	211.7	6.4	33	331.4
9	25.4	190.5	5.3	29.6	322.6
10	25.4	190.5	5.3	34.4	322.6
11	25.4	190.5	7.8	32.0	322.6
12	25.4	240.8	5.3	32.0	375.6

4.1.2.2 The optimization problem

In order to calculate the values of arc efficiency, effective thermal conductivity and effective viscosity, the values of constant terms, i.e. f_1, f_2, f_3, f_4, f_5 and f_6 in eqs. **4.1**, **4.2** and **4.3** are required. To find the values of these terms, an objective function was minimized which depicts the difference between the computed and measured values. In this research work, the following objective function, $O(\mathbf{f})$, was minimized:

$$O(\mathbf{f}) = \sum_{m=1}^M (p_m^e - p_m^c)^2 + \sum_{m=1}^M (t_m^e - t_m^c)^2 + \sum_{m=1}^M (l_m^e - l_m^c)^2 \quad 4.5$$

where p_m^c, t_m^c and l_m^c were the computed penetration, actual throat and the leg length of the weld bead, respectively and p_m^e, t_m^e and l_m^e were the corresponding experimentally determined values of these three variables. The subscript m in eq. **4.5** corresponds to a specific weld in a series of M number of total welds. In eq. **4.5**, \mathbf{f} refers to a set of six uncertain non-dimensional parameters, f_1, f_2, f_3, f_4, f_5 and f_6 that are constant terms in the assumed linear functions of efficiency, η , effective thermal conductivity, k_e , and effective viscosity, μ_e , expressed by eqs. **4.1**, **4.2** and **4.3**. Evidently, $O(\mathbf{f})$ is a function of \mathbf{f} since $O(\mathbf{f})$ contains variables p_m, t_m and l_m , which are dependent on the parameters included in \mathbf{f} . Assuming that $O(\mathbf{f})$ is continuous and has a minimum value, the optimum values of the six unknowns were obtained by differentiating eq. **4.5** with respect to the six unknown parameters and equating each derivative to zero:

$$\begin{aligned} [\nabla O(\mathbf{f}^k)]_{i=1,6} &= \left(\frac{\partial O(\mathbf{f})}{\partial f_i} \right)_{i=1,6} \\ &= -2 \left[\sum_{m=1}^M \frac{(p_m^e - p_m^c)}{w_p \sigma_m^2} \frac{\partial p_m^c}{\partial f_i} + \sum_{m=1}^M \frac{(t_m^e - t_m^c)}{w_t \sigma_m^2} \frac{\partial t_m^c}{\partial f_i} + \sum_{m=1}^M \frac{(l_m^e - l_m^c)}{w_l \sigma_m^2} \frac{\partial l_m^c}{\partial f_i} \right]_{i=1,6} = 0 \end{aligned} \quad 4.6$$

where f_i represents any one of the six coefficients used in eqs. **4.1**, **4.2** and **4.3**. Eq. **4.6** contains partial derivatives of weld penetration, actual throat and leg-length with respect to all six unknown parameters. These partial derivatives are generally referred as sensitivity of the computed weld penetration, actual throat and leg-length with respect to the unknown parameters. The values of these sensitivity terms were computed

numerically by running the numerical heat transfer and fluid flow code and subsequently calculating the derivatives. For example, the sensitivity of non-dimensional penetration, p_m^c , with respect to variable 4, f_4 , was calculated from the following relation:

$$\frac{\partial p_m^c}{\partial f_4} = \frac{p_m^c(f_1, f_2, f_3, f_4 + \Delta f_4, f_5, f_6) - p_m^c(f_1, f_2, f_3, f_4, f_5, f_6)}{\Delta f_4} \quad 4.7$$

where Δf_4 is very small compared with f_4 . Eq. 4.7 depicts that each sensitivity term need two executions of the direct numerical analysis. Now, eq. 4.6 calls for the calculated values of p_m^c , t_m^c and l_m^c to be very close to the corresponding experimental values of p_m^e , t_m^e and l_m^e for all M sample welds. Since p_m^c , t_m^c and l_m^c in eq. 4.6 were obtained from the solution of the direct numerical heat and fluid flow model for a certain set of six unknown parameters, and these unknown parameters did not explicitly appear in eq. 4.6, this equation could not provide a direct solution for the desired unknown parameters. These sensitivity terms were written in a matrix form, known as sensitivity matrix, $J(\mathbf{f})$. The elements of the sensitivity matrix, i.e. sensitivity coefficients, J_{ij} , were defined as:

$$J_{ij} = \frac{\partial (p_i^c)^k}{\partial f_j} + \frac{\partial (t_i^c)^k}{\partial f_j} + \frac{\partial (l_i^c)^k}{\partial f_j} \quad \text{where, } i = 1 \text{ to } M \text{ and } j = 1 \text{ to } 6. \quad 4.8$$

where k is the iteration number.

For the estimation of these uncertain variables, Levenberg-Marquardt (LM) method and two modifications of the conjugate gradient method suggested by Fletcher-Reeves and Polak-Ribiere were used in this work. The Levenberg-Marquardt (LM) and the conjugate gradient methods differ in the calculation of step size, i.e., the increment in the uncertain parameter and the direction of descent, i.e., the relative change in the uncertain parameters [37-39]. A brief description of the main features of the calculations related to the welding problem is described below.

4.1.3 Optimization techniques

4.1.3.1 Levenberg-Marquardt method

To calculate the step size in LM method, the dependent variables p_m , t_m , and l_m was expanded using the Taylor's series to explicitly contain values of increments and unknown parameters i.e. f_1 , f_2 , f_3 , f_4 , f_5 and f_6 . The higher derivative terms in the Taylor's series were dismissed because these were very small compared to the term involving the first derivative. So, for the variable p_m^c the expansion took the following form:

$$\begin{aligned} (p_m^c)^{k+1} = & (p_m^c)^k + \frac{\partial(p_m^c)^k}{\partial f_1} \Delta f_1^k + \frac{\partial(p_m^c)^k}{\partial f_2} \Delta f_2^k + \frac{\partial(p_m^c)^k}{\partial f_3} \Delta f_3^k + \\ & \frac{\partial(p_m^c)^k}{\partial f_4} \Delta f_4^k + \frac{\partial(p_m^c)^k}{\partial f_5} \Delta f_5^k + \frac{\partial(p_m^c)^k}{\partial f_6} \Delta f_6^k \end{aligned} \quad 4.9$$

where Δf_1^k , Δf_2^k , Δf_3^k , Δf_4^k , Δf_5^k and Δf_6^k are the unknown increments in f_1 , f_2 , f_3 , f_4 , f_5 and f_6 . Superscripts k and $k+1$, represent the values at the k^{th} and $(k+1)^{\text{th}}$ iterations, respectively. All other terms on the right hand side of eq. 4.9 were considered to be known. The value of p_m^c at the end of $(k+1)^{\text{th}}$ iteration i.e. $(p_m^c)^{k+1}$, was unknown since Δf_1^k , Δf_2^k , Δf_3^k , Δf_4^k , Δf_5^k and Δf_6^k , and hence, f_1 , f_2 , f_3 , f_4 , f_5 and f_6 after $(k+1)^{\text{th}}$ iteration were unknown. It should be noted here that p_m^c was always considered to be evaluated through a direct numerical solution using a corresponding set of f_1 , f_2 , f_3 , f_4 , f_5 and f_6 and other known parameters. The terms in eq. 4.6 represents the $k+1$ iteration terms which are unknown. So these terms were rewritten as k^{th} iteration terms using eq. 4.9. Substituting eq. 4.9 in eq. 4.6 and removing the second derivative terms will convert eq. 4.6 to following form [37-39]:

$$[S] \{ \Delta f^k \} = \{ S^* \} \quad 4.10$$

with [S] as $N \times N$ matrix containing sensitivity terms, Δf^k as $N \times 1$ matrix and S^* as $N \times 1$ matrix where N represents the number of unknown variables i.e. six coefficients used in used in eqs. **4.1**, **4.2** and **4.3**. The elements of matrix [S], i.e.,

$$[S] = \begin{bmatrix} S_{11} & S_{12} & S_{13} & S_{14} & S_{15} & S_{16} \\ S_{21} & S_{22} & S_{23} & S_{24} & S_{25} & S_{26} \\ S_{31} & S_{32} & S_{33} & S_{34} & S_{35} & S_{36} \\ S_{41} & S_{42} & S_{43} & S_{44} & S_{45} & S_{46} \\ S_{51} & S_{52} & S_{53} & S_{54} & S_{55} & S_{56} \\ S_{61} & S_{62} & S_{63} & S_{64} & S_{65} & S_{66} \end{bmatrix} \quad \mathbf{4.11}$$

was written as:

$$S_{ij} = \sum_{m=1}^M \left(\frac{\partial (p_m^c)^k}{\partial f_i} \frac{\partial (p_m^c)^k}{\partial f_j} + \frac{\partial (t_m^c)^k}{\partial f_i} \frac{\partial (t_m^c)^k}{\partial f_j} + \frac{\partial (l_m^c)^k}{\partial f_i} \frac{\partial (l_m^c)^k}{\partial f_j} \right) \text{ for } i, j = 1 \text{ to } 6 \quad \mathbf{4.12}$$

The indices i and j refer to the number of unknown parameters. Furthermore,

$$\{S^*\} = \begin{Bmatrix} S_1^{ptl} \\ S_2^{ptl} \\ S_3^{ptl} \\ S_4^{ptl} \\ S_5^{ptl} \\ S_6^{ptl} \end{Bmatrix} \quad \mathbf{4.13}$$

$$S_i^{ptl} = \sum_{m=1}^M \left(\frac{\partial (p_m^c)^k}{\partial f_i} (p_m^e - (p_m^c)^k) + \frac{\partial (t_m^c)^k}{\partial f_i} (t_m^e - (t_m^c)^k) + \frac{\partial (l_m^c)^k}{\partial f_i} (l_m^e - (l_m^c)^k) \right) \quad \mathbf{4.14}$$

for $i = 1$ to 6

The unknown matrix $\{\Delta f^k\}$ in eq. **4.10** had to be modified as:

$$\{\Delta f^k\} = \begin{Bmatrix} \Delta f_1^k \\ \Delta f_2^k \\ \Delta f_3^k \\ \Delta f_4^k \\ \Delta f_5^k \\ \Delta f_6^k \end{Bmatrix} \quad \mathbf{4.15}$$

The expression in eq. 4.15 was treated as,

$$\begin{aligned}
 f_1^{k+1} &= f_1^k + \Delta f_1^k \\
 f_2^{k+1} &= f_2^k + \Delta f_2^k \\
 f_3^{k+1} &= f_3^k + \Delta f_3^k \\
 f_4^{k+1} &= f_4^k + \Delta f_4^k \\
 f_5^{k+1} &= f_5^k + \Delta f_5^k \\
 f_6^{k+1} &= f_6^k + \Delta f_6^k
 \end{aligned}
 \tag{4.16}$$

Furthermore, the sensitivity terms such as $\frac{\partial(\mathbf{p}_m^c)^k}{\partial f_i}$ or $\frac{\partial(\mathbf{t}_m^c)^k}{\partial f_i}$ or $\frac{\partial(\mathbf{l}_m^c)^k}{\partial f_i}$ (for $i = 1$

to 6) in the eq. 4.12 as well as in eq. 4.14 often tend to be very small as the values of the unknown parameters f_1, f_2, f_3, f_4, f_5 and f_6 move close to the optimum values. As the optimum combination of the unknown parameters were reached, the individual influence of a specific parameter on the dependent variables, manifested by the sensitivity terms, might become very small or zero. Subsequently, the matrix [S] may tend to become a singular matrix and the inverse problem may become ill-conditioned. The matrix [S] can be null if any column of [S] can be expressed as a linear combination of other columns. To avoid any numerical instability, eq. 4.10 was further modified following Levenburg-Marquardt method as [37-39]:

$$([S] + \lambda^k \Omega^k) \{\Delta f^k\} = \{S^*\}
 \tag{4.17}$$

where λ^k is a scalar damping co-efficient and usually taken as 0.001 and Ω^k is the diagonal matrix. The order of Ω^k was same as that of the matrix [S] and was defined as $\Omega^k = \text{diag} [S]$. Thus the product $\lambda^k \Omega^k$ in eq. 4.17 ensures that the left hand term in eq. 4.17 will remain non-zero even if the determinant of the matrix [S] was zero. The damping parameter was generally made large at the beginning of the iterations, since the problem was generally ill-conditioned in the region around the initial guess in the iterative procedure, which can be quite far from the final solution. The parameter λ^k was then gradually decreased as the iteration procedure advances to the solution of the parameter estimation problem.

Algorithm:

1. Guess initial values of unknown variables set, \mathbf{f} , i.e. the values of the six coefficients used in eqs. 4.1, 4.2 and 4.3.
2. Compute objective function, $O(\mathbf{f})$.
3. Choose a modest value for damping factor (λ), say $\lambda = 0.001$.
4. Solve for increment in unknown variables, $\Delta\mathbf{f}$.
5. Evaluate $O(\mathbf{f} + \Delta\mathbf{f})$.
6. If $O(\mathbf{f} + \Delta\mathbf{f}) \geq O(\mathbf{f})$, increase λ by a factor of 10 (or any other substantial factor) and go back to step 4.
7. If $O(\mathbf{f} + \Delta\mathbf{f}) < O(\mathbf{f})$, decrease λ by a factor of 10 (or any other substantial factor), update \mathbf{f} .
8. Exit if stopping criteria is satisfied otherwise go back to step 4.

The following stopping criteria suggested by Dennis and Schnabel [33] to stop the iterative procedure of the LM method was used in this work.

1. $O(\mathbf{f}^{k+1}) < \varepsilon_1$.
2. $\|\mathbf{f}^{k+1} - \mathbf{f}^k\| < \varepsilon_2$.

where ε_1 and ε_2 are the prescribed tolerances and $\|\cdot\|$ is the vector Euclidean norm, i.e. $\|\mathbf{x}\| = (\mathbf{x}^T \mathbf{x})^{1/2}$, where the superscript T denotes the transpose. The first criteria tests if the objective function is sufficiently small, which is going to be the neighborhood of the solution for the problem. The second stopping criteria results from the fact that changes in the vector of parameters are very small when the method has converged. The use of a stopping criteria based on small changes of the least square norm $O(\mathbf{f})$ could also be used, but with extreme caution. It may happen that the method stalls for a few iterations and then starts advancing to the point of minimum afterwards.

4.1.3.2 Conjugate gradient method

The iterative procedure of the Conjugate Gradient method for the minimization of the objective function is given by [37-39]:

$$f_i^{k+1} = f_i^k - \beta^k d_i^k \quad \text{for } i=1 \text{ to } n \quad \mathbf{4.18}$$

where β^k is the search step size; k is the number of iterations and d_i^k is the direction of descent for the i^{th} variable. The direction of descent for variable i , d_i^k , is a conjugation of the its gradient direction, $\nabla O(f^k)_i$, and its direction of the descent of the previous iteration, d_i^{k-1} and is given as [37-39]:

$$d_i^k = [\nabla O(f^k)]_i + \gamma^k d_i^{k-1} \quad \text{for } i=1 \text{ to } n \quad \mathbf{4.19}$$

where γ^k is the conjugation coefficient. Different expressions are available in the literature for the conjugate coefficient, γ^k . Fletcher and Reeves suggested γ^k as [37-39]:

$$\gamma^k = \frac{\sum_{i=1}^n [\nabla O(f^k)]_i^2}{\sum_{i=1}^n [\nabla O(f^{k-1})]_i^2} \quad \text{for } k = 1, 2, \dots; \text{ and } \gamma^0 = 0 \quad \mathbf{4.20}$$

where n is the number of unknown variables. Polak-Ribiere suggested expression for γ^k as [38, 39]:

$$\gamma^k = \frac{\sum_{i=1}^N [\nabla O(f^k)]_i [\nabla O(f_i^k) - \nabla O(f_i^{k-1})]_i}{\sum_{i=1}^N [\nabla O(f^{k-1})]_i^2} \quad \text{for } k = 1, 2, \dots; \text{ and } \gamma^0 = 0 \quad \mathbf{4.21}$$

Here, $[\nabla O(f^k)]_i$ is the gradient directions of variable i evaluated at iteration k evaluated in eq. 4.6. Either expression (eqs. 4.20 and 4.21) for the computation of the conjugation coefficient γ^k assure that the angle between the direction of descent and the negative gradient direction is less than 90° , so that the objective function is minimized. If $\gamma^k = 0$ for all iterations k , the direction of descent becomes the gradient direction in eq. 4.20 and the steepest-descent method is obtained. The search step size, β^k , was obtained as the one which minimizes the objective function. Substituting the values of Taylor series expansion of the unknown parameters at iteration $k+1$ (i.e. eq. 4.18 in eq. 4.5), and minimizing with respect to β^k , we get [37-39]:

$$\beta^k = \frac{\sum_{m=1}^M \left\{ \frac{(p_m^c - p_m^e)}{w_p \sigma_m^2} \left[\sum_{i=1}^N \left(\frac{\partial p_m^c}{\partial f_i^k} \right) d_i^k \right] + \frac{(t_m^c - t_m^e)}{w_t \sigma_m^2} \left[\sum_{i=1}^N \left(\frac{\partial t_m^c}{\partial f_i^k} \right) d_i^k \right] + \frac{(l_m^c - l_m^e)}{w_l \sigma_m^2} \left[\sum_{i=1}^N \left(\frac{\partial l_m^c}{\partial f_i^k} \right) d_i^k \right] \right\}}{\sum_{m=1}^M \left[\sum_{i=1}^N \left(\frac{\partial p_m^c}{\partial f_i^k} \right) d_i^k + \sum_{i=1}^N \left(\frac{\partial t_m^c}{\partial f_i^k} \right) d_i^k + \sum_{i=1}^N \left(\frac{\partial l_m^c}{\partial f_i^k} \right) d_i^k \right]^2} \quad 4.22$$

After computing the sensitivity terms, the gradient direction, the conjugation coefficient and the search step size, the iterative procedure given by eq. 4.18 was implemented until a stopping criterion is satisfied.

Algorithm:

1. Calculate the objective function, $O(\mathbf{f})$ for the initial guesses of unknown variables, \mathbf{f} , i.e. the values of the six coefficients used in eqs. 4.1, 4.2 and 4.3.
2. Check the stopping criteria. Continue if not satisfied.
3. Compute the sensitivity matrix, $J(\mathbf{f})$.
4. Compute the gradient direction, $\nabla O(\mathbf{f}^k)_i$.
5. Evaluate the conjugate coefficient, γ^k .
6. Compute the direction of descent, d_i^k .
7. Compute the search step size, β^k .
8. Compute the new estimates for the unknown variables, \mathbf{f}^{k+1} .
9. Increase the iteration no. and return to step 1.

4.2 Results and Discussion

The effects of variation of effective thermal conductivity and arc efficiency on the non-dimensional weld geometry i.e. leg-length, throat and penetration are shown in figures 4-1(a) to 4-1(c) for case #1 listed in table 4-1. The non-dimensional values of the leg-length, throat and penetration shown in these figures are obtained by dividing the numerically computed values with the corresponding experimentally obtained values. The increase in k_e leads to higher heat conduction rate inside the weld pool and, consequently, results in lower temperature gradient.

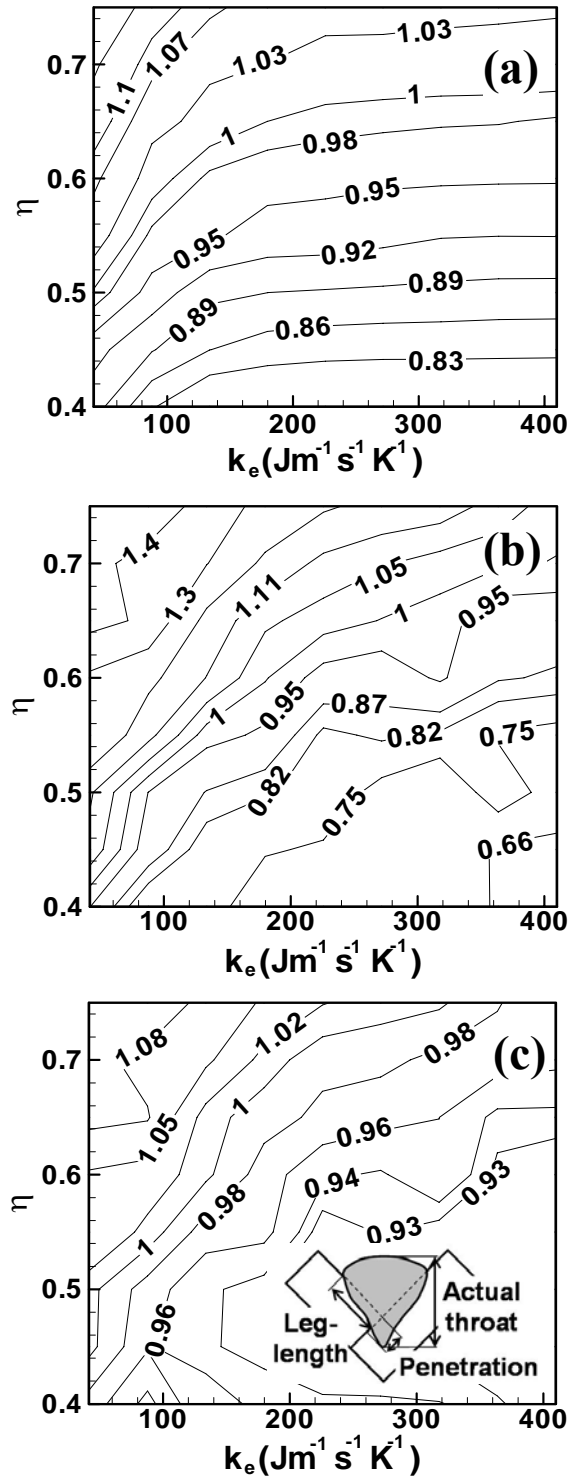


Figure 4-1: Contour plot of (a) non-dimensional leg-length, (b) non-dimensional penetration (c) and non-dimensional throat for various values of arc efficiency (η) and effective thermal conductivity (k_e) for case #1 listed in table 4-1.

Since most of the heat flows downward, the value of the leg-length decreases with increase in k_e for a fixed value of arc efficiency as shown in figure 4-1(a). However, when the arc efficiency is increased, from 0.40 to 0.75, about 25 % increase in the non-dimensional leg-length is achieved because the leg-length depends mainly on the heat input from the arc. In contrast to leg-length, penetration is significantly affected by the heat transfer due to impinging metal droplets. The sensible heat of droplets is distributed mainly to a region directly under the arc and it affects penetration. The enhanced thermal conductivity improves heat transfer rate. The more efficient distribution of a given amount of heat from the droplets in all directions leads to smaller penetration as shown in figure 4-1 (b). This figure also shows that the penetration increases with increase in heat input as expected. Figure 4-1 (c) shows that the computed non-dimensional throat does not vary significantly with either the arc efficiency or the effective thermal conductivity for a given wire feed rate and welding speed. This behavior is also expected, since the size of the throat is affected by the rate of mass addition. Furthermore, weld pool dimensions decrease with increase in the value of effective viscosity for a fixed value of arc efficiency due to retardation in convective flow. The trends shown in figures 4-1 (a), 4-1 (b) and 4-1 (c) were also true for other values of current, voltage, wire feed rate, CTWD and welding speed investigated.

Figures 4-1(a), 4-1(b) and 4-1(c) show that there are several independent combinations of η and k_e that would result in good agreement between the computed and the experimental values of leg-length, penetration or throat. However, there is no guarantee that the same combination of η and k_e would lead to satisfactory prediction of all weld dimensions given by $p_m^* = t_m^* = l_m^* = 1$. An optimum set of values of arc efficiency (η), effective thermal conductivity (k_e) and effective viscosity (μ_e) are required to correctly predict the weld bead geometry and improve reliability of the results obtained using numerical heat transfer and fluid flow models. Figure 4-2 shows the non-dimensional penetration, actual throat and leg-length obtained by using the values of arc efficiency as 0.54, $k_e = 209.0 \text{ J m}^{-1} \text{ s}^{-1} \text{ K}^{-1}$ and $\mu_e = 0.12 \text{ kg m}^{-1} \text{ s}^{-1}$ as suggested in the literature [1, 2, 25]. The non-dimensional penetration value obtained using these values are higher than 1.0 for most of the cases.

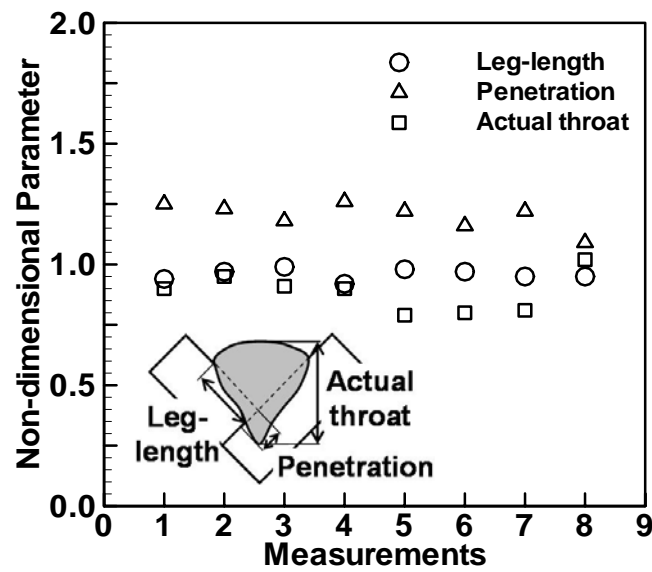


Figure 4-2: Computed values of non-dimensional actual throat, penetration and leg-length using $\eta = 0.59$, $k_e = 209.0 \text{ J m}^{-1} \text{ s}^{-1} \text{ K}^{-1}$ and $\mu_e = 0.12 \text{ kg m}^{-1} \text{ s}^{-1}$ for 1 to 8 measurement cases listed in table 4-1. The non-dimensional values of penetration, actual throat and leg-length are obtained by dividing their computed values with the corresponding experimentally measured values.

Therefore, the suggested combination of μ_e and k_e will not lead to optimum prediction of geometry for the weld conditions studied here and a set of optimized values of η , μ_e and k_e is needed.

4.2.1 Validation of the model

The following tasks were undertaken to examine the effectiveness of the optimization scheme:

- (a) The heat transfer and fluid flow calculations were done with a set of assumed values of η , μ_e and k_e of 0.6, 0.064 kg/m-s and 80.0 J/m-s-K, respectively, to calculate leg-length, penetration and actual throat for the welding conditions pertinent to cases # 1, # 3, # 7 and # 8 in table 4-1. These cases were selected because of the similarity of the welding conditions so that same values of arc efficiency, effective thermal conductivity and effective viscosity are appropriate for all the four cases.
- (b) In order to check if the optimization model is capable of determining the correct values of uncertain welding parameters, the computed values of leg-length, penetration and actual throat calculated in step (a) for the four cases were used as known geometric parameters. The model should be able to predict the same values of η , μ_e and k_e as assumed in step (a). To start the calculations, a set of initial values of these parameters were deliberately chosen to be different from the values used in step (a). The starting values of $\eta = 0.75$, $\mu_e = 0.0512$ kg/m-s and $k_e = 63.0$ J/m-s-K were used to search for the optimized values of these three quantities.
- (c) The objective function was then calculated using equation (7) and the computed values of leg-length, penetration and actual throat obtained in step (a). This computed objective function was minimized by adjusting values of η , μ_e and k_e using the optimization methods discussed in this paper. The obtained optimized

values of η , μ_e and k_e were compared with those used in step (a) and presented in table 4-2.

Table 4-2: Estimates of the exact parameters (i.e. $\eta = 0.6$, $k_e = 80.0$ J/m-s-K, $\mu_e = 0.064$ kg/m-s) during validation of model by using Levenberg-Marquardt (LM) and two versions of conjugate gradient method (CG), i.e., Fletcher- Reeves and Polak- Ribiere using initial assumed values of $\eta = 0.75$, $k_e = 63.0$ J/m-s-K and $\mu_e = 0.0512$ kg/m-s.

Technique	Parameters	Error, i.e., $\sigma = 0.0$ mm		Error, i.e., $\sigma = 0.2$ mm	
		Estimates	Confidence interval	Estimates	Confidence interval
Levenberg-	η	0.602	-	0.610	$0.591 \leq \eta \leq 0.629$
Marquardt	k_e (J/m-s-K)	82.011	-	82.602	$78.684 \leq k_e \leq 86.524$
(LM)	μ_e (kg/m-s)	0.063	-	0.064	$0.059 \leq \mu_e \leq 0.069$
Fletcher-	η	0.601	-	0.609	$0.595 \leq \eta \leq 0.623$
Reeves CG	k_e (J/m-s-K)	81.259	-	80.159	$77.218 \leq k_e \leq 83.098$
	μ_e (kg/m-s)	0.063	-	9.934	$0.060 \leq \mu_e \leq 0.068$
Polak-	η	0.602	-	0.611	$0.598 \leq \eta \leq 0.624$
Ribiere CG	k_e (J/m-s-K)	81.268	-	80.241	$76.912 \leq k_e \leq 83.572$

All the three optimization techniques gave converged solutions within 7 iterations as evidenced by the low values of the objective function smaller than 10^{-6} m². Table 4-2 shows that almost exact values of all three parameters are obtained from all the optimization techniques. Thus, the optimization techniques can provide correct values of η , μ_e and k_e when the weld dimensions are known.

In reality, weld dimensions may vary from run to run for the same welding conditions because of random measurement errors. To simulate this variation and examine how the random errors in the measurements would affect the optimization

process, random errors were introduced in the values of leg-length, penetration and actual throat obtained from step (a) by adding appropriate error terms to the weld dimensions in following manner [38]:

$$p = p_{ex} + \omega_1\sigma \quad \mathbf{4.23.a}$$

$$t = t_{ex} + \omega_2\sigma \quad \mathbf{4.23.b}$$

$$l = l_{ex} + \omega_3\sigma \quad \mathbf{4.23.c}$$

where subscript 'ex' means exact dimension obtained in step (a), σ is the standard deviation in these dimensions and ω_1 , ω_2 and ω_3 are random variables with normal distribution, zero mean and unitary standard deviation. It may be noted from eq. **4.23** that the same magnitude of errors were added to penetration, leg-length and actual throat since the measurement errors were experimentally found to be roughly equal. The value of σ was taken as 0.2 mm based on analysis of experimental data and Box-Miller method [38] was used to generate the three random numbers, ω_1 , ω_2 and ω_3 . The values of penetration, actual throat and leg-length obtained from eq. **4.23** represent the region where the actual values of these variables will lie for a known value of the variance and probability (or confidence limit). For the 95 % confidence level [38], ω_1 , ω_2 and ω_3 lie between -1.96 to +1.96. Consequently, the values of penetration, leg-length and actual throat lie between their values calculated in step (a) $\pm 1.96\sigma$ with a probability of 0.95. The results in table **4-2** indicate that when the weld dimensions contain random errors, accurate estimates of η , μ_e and k_e can be obtained by all three gradient based methods using starting values of $\eta = 0.75$, $\mu_e = 0.0512$ kg/m-s and $k_e = 63.0$ J/m-s-K. As the errors introduced in eq. **4.23** are Gaussian in distribution, the accuracy of the calculated values of η , μ_e and k_e can be checked by calculating the standard deviation of their values. The confidence intervals of η , μ_e and k_e obtained from the covariance matrix and given in table **4-2** show that the original values of these parameters lie in the range predicted by the proposed model for the 95% confidence level. These results show that the proposed model is able to capture the values of η , μ_e and k_e accurately when the measurements of geometrical dimensions contain random errors.

4.2.2 Optimized values of effective thermal conductivity, viscosity and arc efficiency

Figure 4-3 depicts the variation in the objective function (i.e. $O(\mathbf{f})$) with number of iterations. The objective function decays rapidly in the first 4 iterations in the Levenberg-Marquardt (LM) method and both versions of the conjugate gradient (CG) method. After that, the objective function becomes almost constant for several iterations and then starts fluctuating. Figure 4-3 shows that the Fletcher and Reeves's CG method gives somewhat better convergence of the objective function compared to the other two methods. In the Fletcher and Reeves's CG method, the minimum value of the objective function obtained is 0.22 after 13 iterations while LM and Polak-Ribiere's CG method produced the value as 0.27 and 0.26 in 13 and 14 iterations, respectively. Therefore, the final optimized values of arc efficiency, effective thermal conductivity and effective viscosity are calculated using Fletcher and Reeves's CG method.

Figures 4-4(a) and 4-4(b) show the variation in the values of non-dimensional weld dimensions, arc efficiency, enhancement factor for thermal conductivity, $\left(f_k^e = \frac{k_e}{k_L} \right)$, and viscosity, $\left(f_\mu^e = \frac{\mu_e}{\mu_L} \right)$ with iterations for case #2 in table 4-1. Figure 4-4(a) shows that non-dimensional weld geometrical parameters are initially very large due to the large value of the assumed arc efficiency. However, as the calculation progresses, the weld dimensions decrease and tend to attain the target value of one. The decreasing trend of the values of the weld dimensions is somewhat similar to that of arc efficiency. These trends are consistent with the fact that arc efficiency has a major impact on weld pool dimensions.

Figures 4-4(a) and 4-4(b) show that enhancement factor for thermal conductivity and viscosity increases as the calculation progresses and the computed weld pool dimensions tend to agree progressively better with the corresponding experimental values. The optimal value of these unknown parameters can be expressed as:

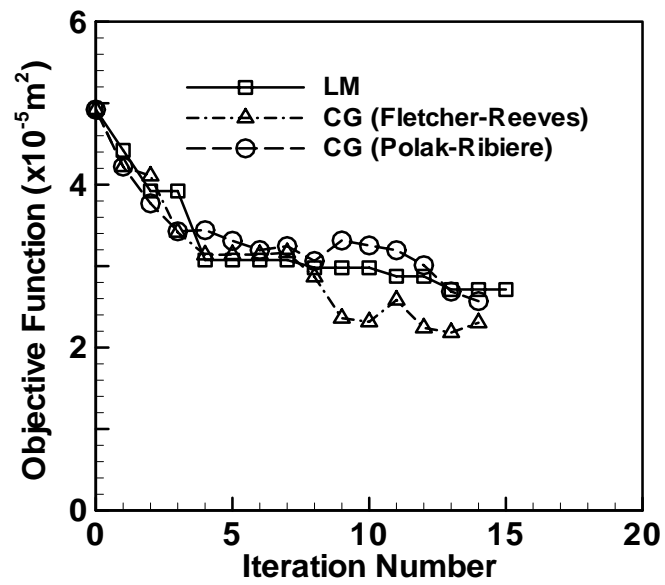


Figure 4-3: Computed values of the objective function, $O(f)$, using LM method and the two versions of CG method as a function of iteration number.

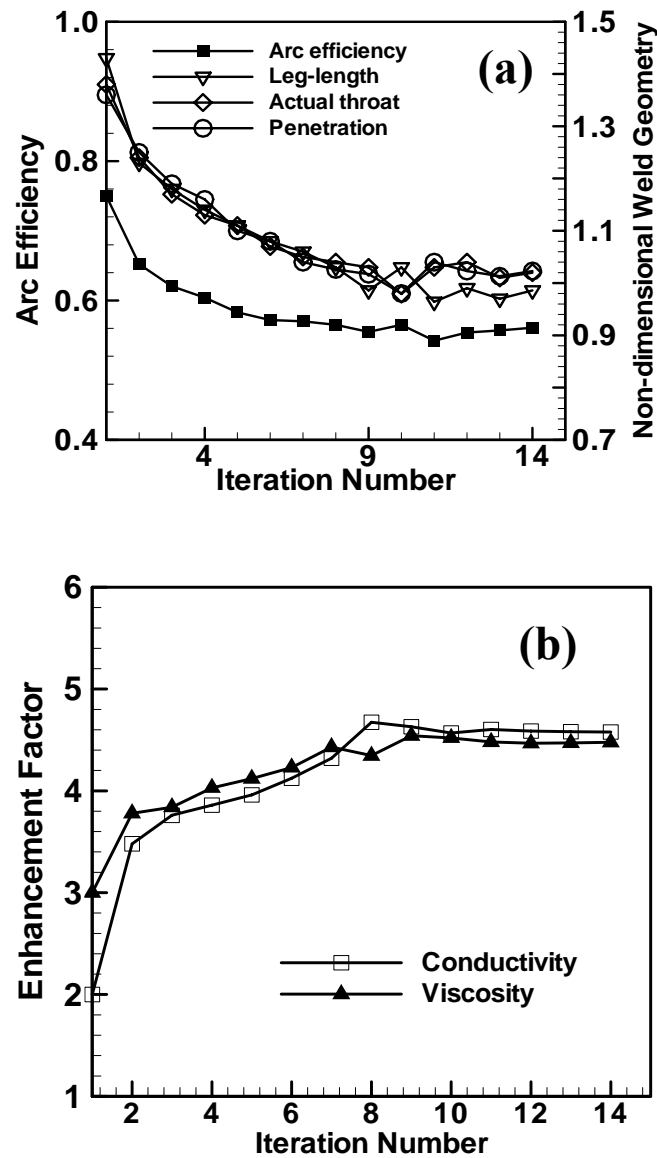


Figure 4-4: Optimized values of (a) arc efficiency (represented on left side vertical axis) and non-dimensional weld dimensions (represented on right side vertical axis) (b) enhancement factor of thermal conductivity (i.e. $f_k^e = \frac{k_e}{k_L}$) and viscosity (i.e. $f_\mu^e = \frac{\mu_e}{\mu_L}$); by using Fletcher-Reeves CG method for case #2 of table 4-1.

$$\eta = 0.31 + 4.65 \times 10^{-6} \frac{IV}{w_f} \quad 4.24$$

$$k_e = 41.80 + 3.17 \times 10^{-5} \frac{IV}{U_w} \quad (\text{W/m} \cdot \text{K}) \quad 4.25$$

$$\mu_e = 0.016 + 1.05 \times 10^{-8} \frac{IV}{U_w} \quad (\text{kg/m} \cdot \text{s}) \quad 4.26$$

where I is the current (A), V is voltage (V), w_f is the wire feeding speed (m/s) and U_w is the welding speed (m/s). The values of η , k_e and μ_e calculated from eqs. 4.24, 4.25 and 4.26 can be used for the experimental conditions given in table 4-1 for the GMA welding in spray mode. Eq. 4.24 defines the value of arc efficiency for any specific arc current, voltage and wire feed rate. This expression can be rewritten in the following form:

$$\eta = 0.50 + 4.65 \times 10^{-6} \left(\frac{IV}{w_f} - \frac{I^{\text{ref}} V^{\text{ref}}}{w_f^{\text{ref}}} \right) \quad 4.27$$

where, I^{ref} , V^{ref} and w_f^{ref} are the reference values of arc current, voltage and wire feeding speed, respectively. The reference values of these variables are chosen as the general starting values of these variables for GMA welding in spray mode. The values of I^{ref} , V^{ref} and w_f^{ref} correspond to 250 A, 25 V and 0.15 m/s, respectively. The value of arc efficiency obtained using eq. 4.27 is in the range of 0.50 to 0.65 for GMA welding. In case of GMA welding, since 12-14 % of total input heat is also carried by the droplets to the workpiece [1, 20, 40, 41], the net efficiency becomes 0.62 to 0.79. Various researchers [15, 21-23] have experimentally measured the value of net arc efficiency and found that it lie between 0.65 to 0.85 for GMA welding. However, they did not specify the droplet transfer mode during their experimental conditions. The calculated values of arc efficiency also lie in the same range as reported in the literature.

Figure 4-5 and table 4-3 show that the arc efficiency increases slightly with the increase in input power and decrease in the wire feeding rate (case #3 and case #8 of table 4-1). Approximately, 8 % increase in the value of arc efficiency is observed with decrease in the value of wire feed rate from 211.7 mm/s to 169.3 mm/s for almost same heat input/length (case #3 and case #8 of Table 4-1). This behavior is consistent with the

fact that with decrease in wire feed rate, less power is consumed in melting the wire and more heat is available to the workpiece for the same heat input rate.

Table 4-3 also shows that there can be 50% variation in the value of the effective thermal conductivity depending on heat input rate. Eqs. 4.25 and 4.26 show that effective thermal conductivity and effective viscosity increase with increase in the heat input per unit length. The increase in heat input rate enhances mixing in the weld pool and increases the effective thermal conductivity and viscosity. The optimized values indicate enhancement factors (i.e. $f_k^e = \frac{k_e}{k_L}$) for thermal conductivity and viscosity (i.e. $f_\mu^e = \frac{\mu_e}{\mu_L}$) to be in the range of 5 to 9. This behavior is consistent with the presence of turbulent flow in the weld pool during GMA welding as reported in the literature [1, 2, 24-28, 42]. Hong et al. [25-28] suggested an enhancement factor between 12 to 15 for thermal conductivity and a factor more than 6 for the viscosity for GTA welding using 150 A current and 25 V based on peak temperature analysis in the weld pool and k- ϵ turbulence model calculations. Choo and Szekely [24] suggested an enhancement factor of 8 for thermal conductivity and a factor of 30 for the viscosity at a current of 100 A by matching the calculated weld pool geometry with the experimentally determined geometry. They also verified the weld pool shape and values of enhancement factors using the k- ϵ turbulence model. The values available in the literature [1, 6-10, 24-28] are specific to the welding procedure and the specific welding conditions. Because of the scarcity of data, the available literature cannot be used as a basis for the selection of enhanced transport parameters for any specific welding conditions. The computed values of μ_e and k_e for various heat inputs indicate that the rates of transport of momentum and heat are considerably higher than that for laminar flow. The relation between the two variables is governed by the turbulent Prandtl number (Pr) which is defined as:

$$Pr = \frac{\mu_T c_p}{k_T} \quad 4.28$$

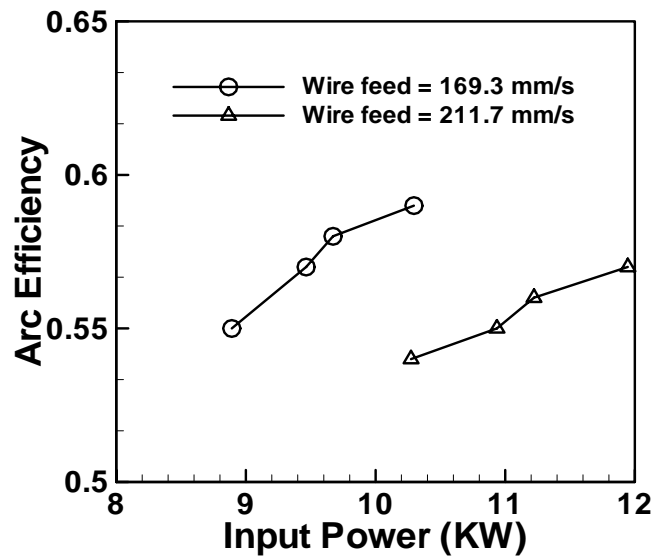


Figure 4-5: Computed values of arc efficiency using estimated values of unknown parameters for different welding conditions listed in table 4-1.

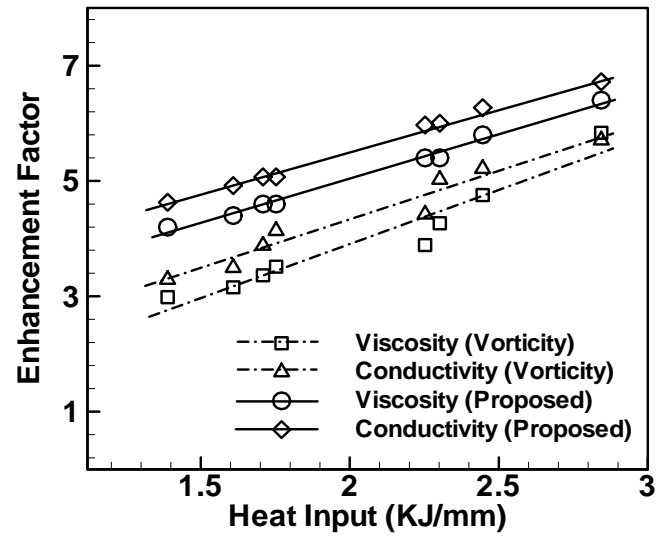


Figure 4-6: Computed values of enhancement factor for thermal conductivity and viscosity using estimated values of unknown parameters by using proposed model and vorticity based turbulence model for different welding conditions listed in table 4-1.

where $\mu_e = \mu_L + \mu_T$ and $k_e = k_L + k_T$, μ_T and k_T are the turbulent viscosity and turbulent conductivity to account for the fluctuating fluid movement and resulting enhanced transport of heat and mass within the weld pool and c_p is the specific heat of the liquid. The value of Pr available in the literature [42] for a fully developed turbulent flow in molten alloys and steels are 0.9 and 0.2, respectively. The optimized values of μ_T and k_T obtained from Fletcher and Reeves CG method results in Prandtl numbers between 0.2 to 0.3. These values of the Prandtl number lie between laminar and fully turbulent flow which suggests that the flow in GMAW fillet weld is neither laminar nor fully turbulent in traditional sense for the welding conditions given in table 4-1. The structure of the flow in the weld pool is consistent with the need for enhanced values of transport properties for the heat transfer and fluid flow calculations.

Table 4-3: Comparison of optimized values of arc efficiency, η , effective thermal conductivity, k_e , and effective viscosity, μ_e , obtained using Fletcher and Reeves CG method for the first eight welds listed in table 4-1.

No.	Heat input/length (kJ/mm)	η	k_e (J/m-s-K)	μ_e (kg/m-s)	Prandtl number
1	2.30	0.58	112.9	0.04	0.29
2	1.75	0.56	96.1	0.03	0.24
3	1.61	0.59	92.0	0.03	0.23
4	2.84	0.57	133.8	0.04	0.24
5	1.39	0.55	87.8	0.03	0.28
6	2.25	0.57	112.9	0.04	0.29
7	2.45	0.54	121.2	0.04	0.26
8	1.71	0.55	96.1	0.03	0.24

Vorticity based mixing length turbulence model [43, 44] has been used extensively for the calculation of effective viscosity and effective thermal conductivity. Using this model, the average value of the enhancement factor for viscosity in the weld pool was found to be 4.26 for the welding conditions indicated by weld #1 in table 4-1.

The corresponding enhancement factor obtained from eq. 4.26 is 5.24. This shows a reasonably good agreement between the values of enhancement factor in viscosity by using vorticity based mixing length turbulence model and the proposed eq. 4.26.

Using the effective viscosity of 4.26 and $Pr (= 0.29)$ obtained from the numerical heat transfer and fluid flow model for weld #1 in table 4-1, the enhancement factor for thermal conductivity was calculated. Figure 4-6 shows the calculated enhancement factors (i.e. $f_k^e = \frac{k_e}{k_L}$) for thermal conductivity and viscosity (i.e. $f_\mu^e = \frac{\mu_e}{\mu_L}$) as a function of heat input by using vorticity based turbulence model and the proposed eqs. 4.25 and 4.26. The calculated enhancement factors for thermal conductivity and viscosity by using vorticity based turbulence also increase with increase in the heat input per unit length as obtained by eqs. 4.25 and 4.26. Figures 4-7(a), 4-7(b) and 4-7(c) depict comparison between the computed and the experimentally obtained weld pool dimensions using the optimized values of arc efficiency, effective thermal conductivity and effective viscosity obtained from eqs. 4.24 to 4.26 for the welding conditions listed in table 4-1. These figures show satisfactory agreement between the computed and the experimentally obtained weld geometry for various welding conditions. The reliability of numerical heat transfer and fluid flow calculations can be significantly enhanced by using the optimized values of uncertain welding parameters from a limited volume of measured weld dimensions.

4.3 Summary and Conclusions

The reliability of numerical heat transfer and fluid flow calculations was improved by developing a comprehensive model that embodies a heat transfer and fluid flow sub-model and an algorithm for searching and optimizing the values of uncertain process variables from a limited volume of experimental data. The model was used to estimate the values of three uncertain input parameters, arc efficiency (η), effective thermal conductivity (k_e) and viscosity (μ_e) as a function of welding conditions.

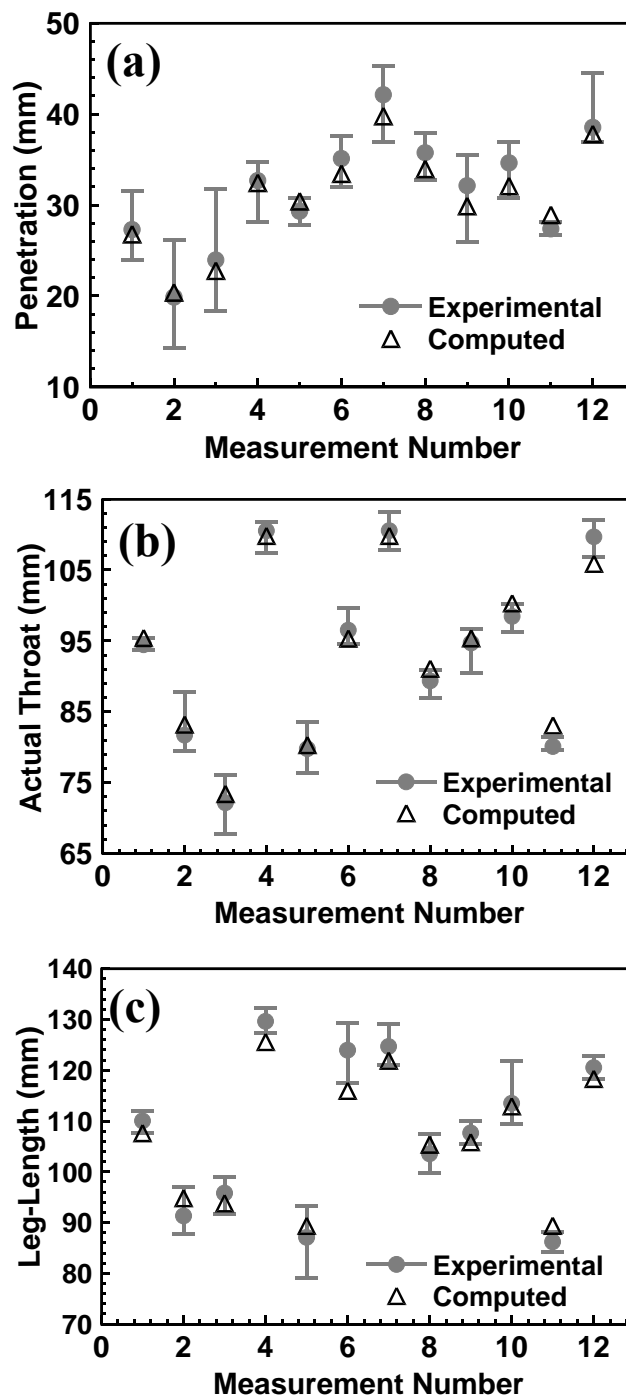


Figure 4-7: Comparison between the computed and the experimental values of (a) penetration (b) actual throat and (c) leg-length obtained using the optimized value of arc efficiency, effective thermal conductivity and effective viscosity for all the conditions listed in table 4-1.

The optimized values of arc efficiency, effective thermal conductivity and effective viscosity were found to depend on the welding conditions. The enhancement factors for thermal conductivity and viscosity were in the range of 5 to 9 for the welding conditions used in this study. The average values of the enhancement factors for thermal conductivity and viscosity calculated using vorticity based mixing length turbulence model agreed well with the values predicted by the proposed model. This chapter also showed that the values of the uncertain welding parameters can be determined using this method even when the measurements contain random errors.

4.4 References

1. W. Zhang, C. H. Kim and T. DebRoy, *J. Appl. Phys.* **95**, 5210 (2004).
2. W. Zhang, C. H. Kim and T. DebRoy, *J. Appl. Phys.* **95**, 5220 (2004).
3. K. Mundra, T. DebRoy and K. Kelkar, *Numer. Heat Transfer A*, **29**, 115 (1996).
4. W. Zhang, G. G. Roy, J. W. Elmer and T. DebRoy, *J. Appl. Phys.* **93**, 3022 (2003).
5. K. Mundra, J. M. Blackburn and T. DebRoy, *Sci. Technol. Weld. Joining*, **2**, 174 (1997).
6. A. De and T. DebRoy, *J. Phys. D: Appl. Phys.* **37**, 140 (2004).
7. A. De and T. DebRoy, *J. Appl. Phys.* **95**, 5230 (2004).
8. S. Mishra and T. DebRoy, *J. Phys. Appl. Phys.* **38**, 2977 (2005).
9. S. Mishra and T. DebRoy, *J. Appl. Phys.* **98** (4): Article No. 044902 (2005).
10. X. He, P. W. Fuerschbach and T. DebRoy, *J. Phys. D: Appl. Phys.*, **36**, 1388 (2003).
11. X. He, T. DebRoy and P. W. Fuerschbach, *J. Appl. Phys.*, **94**, 6949 (2003).
12. Z. Yang, J. W. Elmer, J. Wong and T. DebRoy, *Welding J.*, **79**, 97s (2000).

13. S. V. Patankar, *Numerical Heat Transfer and Fluid Flow*, Hemisphere Publishing, New York (1982).
14. K. A. Hoffmann and S. T. Chiang, *Computational Fluid Dynamics for Engineering – Volume II*, Engineering Education System, Wichita, KS, USA (1993).
15. J. F. Lancaster, *The Physics of Welding*, 2nd Edition, Pergamon, Oxford (1986).
16. M. L. Lin and T. W. Eagar, *Metall. Trans. B*, **17B**, 601 (1986).
17. Y. S. Kim and T.W. Eagar, *Weld. J.*, **70**, 20s (1991).
18. M. C. Tsai and S. Kou, *Weld. J.*, **69**, 241s (1990).
19. Y. Wang and H. L. Tsai, *Metall. Mater. Trans. B*, **32B**, 501 (2001).
20. C. H. Kim, W. Zhang and T. DebRoy, *J. Appl. Phys.* **94**, 2667 (2003).
21. R. W. Messler, *Principles of Welding*, John Wiley and Sons, NY, (1999).
22. N. Christensen, V. de L. Davies and K. Gjermundsen, *Brit. Weld. J.*, **12**, 54 (1965).
23. S. Kou, *Welding Metallurgy*, John Wiley and Sons, New Jersey (2003).
24. R. T. C. Choo and J. Szekely, *Weld. J.* **73**, 25 (1994).
25. K. Hong, D. C. Weckmann, A. B. Strong and W. Zheng, *Sci. Technol. Weld. Joining* **7**, 125 (2002).
26. P. G. Jonsson, J. Szekely, R. T. C. Choo and T. P. Quinn, *Model. Simul. Mater. Sci. Eng.* **2**, 995 (1994).
27. K. Hong, D. C. Weckman, A. B. Strong and E. Pardo, *Proceedings of the First Int. Conference on Transport Phenomena in Processing*, Hawaii ed. by Secuk I. Guceri, Technomic Pub. p. 626 (1992).
28. K. Hong, D. C. Weckmann, A. B. Strong and W. Zheng, *Sci. Technol. Weld. Joining* **8**, 313 (2003).
29. J. V. Beck, B. Blackwell and C. R. St. Clair, “*Inverse Heat conduction: ill-posed problems*” Wiley International, NY (1985).

30. J. V. Beck and K. J. Arnold, "*Parameter estimation in engineering and science*", John Wiley and Sons, NY (1977).
31. M. N. Ozisik and H. R. B. Orlande, "*Inverse heat transfer: fundamentals and applications*", Taylor and Francis, NY (2000)
32. Y. Bard, "*Nonlinear parameter estimation*", Academic Press, NY (1974).
33. J. Dennis and R. Schnabel, "*Numerical methods for unconstrained optimizations and non-linear equations*", Prentice Hall (1983).
34. O. M. Alifanov, "*Inverse heat transfer problems*", Springer-Verlag, NY (1994).
35. R. W. Fonda and S. G. Lambrakos, *Sci. Technol. Weld. Joining*, **7**(3), 177 (2002).
36. V. A. Karkhin, V. V. Plochikhine and H. W. Bergmann, *Sci. Technol. Weld. Joining*, **7**(4) 224 (2002).
37. R. Fletcher and C. M. Reeves, *Computer J.*, **7**, 149 (1964).
38. W. H. Press, B. P. Flannery, S. A. Teukolsky and W. T. Vetterling, *Numerical Recipes*, Cambridge University Press, Cambridge (1988).
39. J. Nocedal and S. J. Wright, "*Numerical optimization*", Springer-Verlag, NY (1999).
40. S. Rhee and E. Kannatey-Asibu Jr., *Weld. J.*, **71**, 381s (1992).
41. L. A. Jones, T. W. Eagar and J. H. Lang, *J. Phys. D: Appl. Phys.*, **31**, 107 (1998).
42. J. Szekely, *Fluid Flow Phenomena in Material Processing*, Academic Press, NY (1979).
43. D. C. Wilcox, *Turbulence Modeling for CFD*, DCW Industries, California (1993).
44. B. E. Launder and D. B. Spalding, *Lectures in Mathematical Models of Turbulence*, Academic Press, London (1972).

Chapter 5

A NEURAL NETWORK MODEL OF HEAT AND FLUID FLOW IN GAS METAL ARC FILLET WELDING

Since the geometry, composition and structure of welds are affected by the welding variables, these output variables are often adjusted by trial and error to achieve defect free, structurally sound and reliable welds. However this approach is time consuming, expensive, and does not always provide optimum welds. In the past few decades, systematic correlations between welding variables and weld characteristics have been attempted by statistical regression analysis [1], artificial neural network [1-13] and phenomenological modeling [14-25]. In principle, regression analysis can relate weld pool geometry with welding variables using a large volume of experimental data. However, this approach is difficult for gas-metal-arc (GMA) fillet welding due to complex interaction of various physical processes where each variable affects the weld pool dimensions, cooling rate and other parameters in a complex manner [17-20]. In recent years, numerical models of heat transfer and fluid flow in fusion welding have provided significant quantitative insight about both the welding processes as well as the welded materials. The computed temperature and velocity fields, cooling rates, weld pool geometry for various concentrations of surface active elements, concentrations of oxygen, nitrogen and hydrogen, and formation of defects have been studied quantitatively using numerical models. Although these models are recognized as powerful tools for research, they are not extensively used in the welding industry because the models are highly complex, require specialized training to develop and test, and consume a large amount of computer time to run.

The neural network models are capable of relating input variables like welding process parameters and material properties with weld characteristics such as the weld geometry [1-5] and properties. The previous efforts to model GMA fillet welding process using neural network were based on training the network with experimental data. Since

the volume of experimental data required to train a neural network depends on the number of input and output variables, most previous efforts considered only few input parameters to keep the necessary volume of experimental data tractable [1-4]. For example, Kim et al. [1], Smartt and Johnson [2], Cook et al. [3] and Li et al [4] developed the neural network models of GMA welding process which considered the effects of process parameters like welding speed, arc voltage and arc current as inputs. Since the weld pool geometry depends on other welding variables as well as various material properties, the effects of many of the welding variables and material properties cannot be determined from the available neural networks. Furthermore, the output variables considered in the previous neural networks were also limited. For example, the existing neural network models do not provide any information about some of the important parameters such as the cooling rate or peak temperature. A review of previous work [1-4] indicates that what is needed is a framework for rapid calculation of weld pool geometry, cooling rate and peak temperature in the weld pool for GMA welding of various materials. A neural network trained with the results of a numerical heat transfer and fluid flow model can correlate various output variables such as the weld pool geometry, cooling rate, liquid velocities and peak temperatures with all the major welding variables and material properties. Furthermore, such correlations satisfy the phenomenological laws. Recently, Dr. Mishra [5] at Penn State University developed a neural network model of GTA butt welding using the results of heat transfer and fluid flow model to train the network. He used the steepest gradient method along with genetic algorithm to find the optimal weights of the network. The steepest gradient method requires prescribed values of the learning rate and the momentum term for the calculation of step size (or change in weights at each iteration). The convergence and the efficiency of finding the optimal solution of this algorithm depend on the values of these variables. In the literature [27-29], it has been shown that steepest gradient algorithm works very poorly compared to other advanced second order derivative based techniques like conjugate gradient descent, quasi-Newton, and Levenberg-Marquardt which do not require any prescription of learning rate and the momentum term. The conjugate gradient algorithms require only a little more storage than the steepest gradient method, so they are often a

good choice for networks with a large number of weights. It is the recommended technique for any network with a large number of weights (more than a few hundred) and/or multiple output units. For smaller networks, either Quasi-Newton or Levenberg-Marquardt may be better. Levenberg-Marquardt method is generally preferred for low-residual regression problems. Due to advantages of conjugate gradient method over other derivative based technique, a hybrid optimization scheme involving the conjugate gradient (CG) method and a genetic algorithm (GA) was used in this doctoral work to calculate the weights of the neural network. The neural network produced by the hybrid optimization model produced better results than the networks based on the CG method alone.

5.1 Mathematical Model

5.1.1 Heat Transfer and Fluid Flow Model of GMA Fillet Welding to Generate Database

The datasets for training, validation and testing of the neural net were generated by using a well-tested heat transfer and fluid flow model that solves the equations of conservation of mass, momentum and energy in three dimensions. The thermo-fluid model takes into account the complex fillet joint shape, the deformation of the weld pool top surface, heat transfer by the hot metal droplets and the addition of the filler metal from the consumable electrode as discussed in chapter 3.

5.1.2 Neural Network Model

All the 22 input variables and their range of values used to develop the neural network are listed in table 5-1. While most of these variables are easily understood, the following comments may be of interest to the readers. The input variables such as the arc efficiency, arc power distribution factor and the arc radius determine how heat is

absorbed at various locations from the arc [21]. The droplet efficiency [15-18] is defined as the ratio of the total sensible heat input owing to metal droplets (Q_d) over the total heat input (IV), i.e., $\eta_d = Q_d / (IV)$ where I is arc current (Amp) and V is the voltage (V). Since temperature independent thermophysical properties of the solid alloy are used in the model, a question arises as to how to select their values. Since the heat flow in the solid region near the weld pool affect both the size and shape of the weld pool as well as the temperature field in the entire work piece, it is appropriate to use thermophysical properties at a temperature closer to the melting point than to the ambient temperature. The effective thermal conductivity and viscosity are used to represent enhanced heat and momentum transfer within the weld pool because of the fluctuating components of velocities in a strong recirculating flow confined in a small weld pool. These variables represent system properties and their values, determined by reverse modeling, are available in the literature [17-20] for GMA fillet welding for various heat input values. The effect of surface active elements have not been rigorously studied in the development of the neural network to simplify calculations. Therefore the results are valid for low concentrations of surface active elements.

All the important output variables from the model included in the neural network are listed in table 5-2. The three output variables describing the weld cross-section are penetration, leg-length and throat. In addition, the length of the weld pool is also considered as an output of the neural network as shown in table 5-2. Other outputs of the neural network model include the peak temperature in the weld pool, maximum velocity in the weld pool and the cooling time between 800 °C and 500 °C. The cooling time was calculated on the workpiece surface along the welding direction.

Figure 5-1 shows the structure of each neural network that contains an input layer, a hidden layer and an output layer. The input layer comprises of all the 22 input variables which are connected to neurons in the hidden layer through the weights assigned for each link. The number of neurons in the hidden layer is found by optimizing the network. In mathematical terms, we describe the output from a neuron, y , at each node (represented by circles in figure 5-1) as follows [27-29]:

Table 5-1: The range of input variables used in the generation of training, validation and testing datasets.

Variables	Minimum	Maximum	Mean
Arc current (Amp)	200.0	410.0	326.3
Arc voltage (V)	25.0	42.0	33.8
Welding speed (mm/s)	4.2	8.5	6.4
Wire feeding rate (mm/s)	120.0	290.0	199.6
Arc efficiency	0.4	0.7	0.5
Arc radius (mm)	4.0	6.5	5.1
Arc distribution factor	0.5	3	1.4
Droplet efficiency	0.1	0.2	0.13
CTWD (mm)	17.5	30.0	23.4
Wire radius (mm)	0.5	0.9	0.7
Effective thermal conductivity (J/m-sec-K)	83.6	543.4	298.5
Effective viscosity (Kg/m-sec)	2.0×10^{-2}	21.0×10^{-2}	7.9×10^{-2}
Density (Kg/m ³)	7000.0	8500.0	7742.1
Solidus temperature (K)	1690.0	1790.0	1741.7
Liquidus temperature (K)	1745.0	1815.0	1784.6
Enthalpy of solid at melting point (kJ/Kg)	731.5	1149.5	1002.4
Enthalpy of liquid at melting point (kJ/Kg)	1045.0	1463.0	1280.2
Specific heat of solid (J/Kg-K)	543.4	794.2	677.0
Specific heat of liquid (J/Kg-K)	689.7	919.6	789.7
Thermal conductivity of solid (J/m-sec-K)	14.6	40.5	26.9
Coefficient of thermal expansion (1/K)	0.0	1.7×10^{-5}	9.1×10^{-6}
$d\gamma/dT$ of alloy without any surface active element (N/m-K)	-5.5×10^{-4}	-2.5×10^{-4}	-4.2×10^{-4}

$$y = f \left(\sum_{i=0}^N w_i x_i \right) \quad 5.1$$

where $x_1, x_2, x_3, \dots, x_N$ are the input signals to the neuron and $w_1, w_2, w_3, \dots, w_N$ are the synaptic weights that embody the non-linear relationships between the input and the output variables.

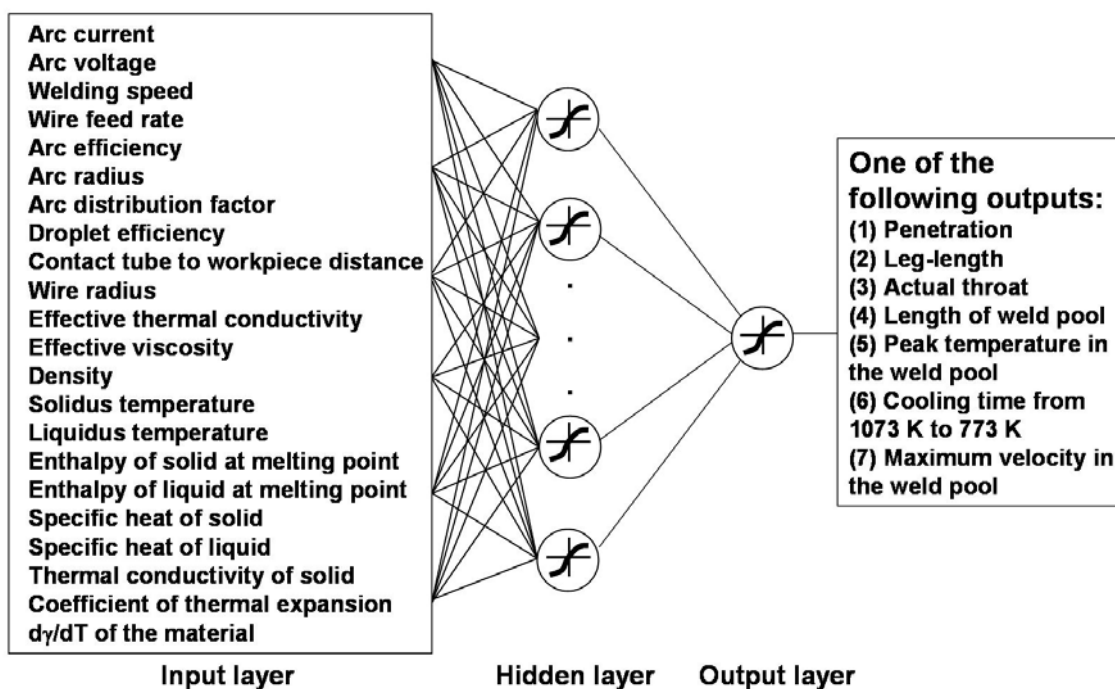


Figure 5-1: The architecture of the neural net model used in this work. The input layer comprises of 22 variables, which is connected to a hidden layer. The output of the network is either penetration, leg-length, throat, weld pool length, cooling time between 800 °C to 500 °C, maximum velocity or peak temperature in the weld pool.

Table 5-2: Root mean square error for different output variables

Output Variable	Training	Validation	Testing
Leg-length (mm)	0.01	0.02	0.14
Actual throat (mm)	0.02	0.18	0.29
Penetration (mm)	0.02	0.08	0.11
Length of the weld pool (mm)	0.16	0.18	0.19
Peak temperature in the weld pool (K)	4.27	4.58	4.82
Cooling time between 800 °C to 500 °C (s)	0.04	0.06	0.06
Maximum velocity in the weld pool (mm/s)	2.27	2.53	1.85

The combination of a fixed input, $x_0 = 1$, and an extra input weight, w_0 , accounts for the *bias* input. The activation function, denoted by f , captures the non-linear interaction of various welding variables such as the arc current, voltage, wire feed rate, welding speed and material properties on the weld geometry, cooling rate and peak temperature in the weld pool during GMA fillet welding. The following hyperbolic tangent function (which is a symmetric *sigmoid* function) is used as the activation function:

$$y = \tanh \left(a \sum_{i=0}^N w_i x_i \right) \quad 5.2$$

where a is the *slope parameter* of the sigmoid function. By varying the parameter a , we can obtain sigmoid functions of different slopes [27-29]. Increase in the value of a increases the slope of the activation function and vice versa. A very high value of the slope makes the curve close to a step function while a low value retards the convergence rate. Based on the findings of previous works, a value of 1.5 was used to achieve rapid convergence [29, 30]. Furthermore, the use of the tanh function in eq. 5.2 as the activation function helps in keeping the problem reasonably well-conditioned. An attractive feature of the hyperbolic tangent function is that its derivative, given by $f' = 1 - f^2$, does not increase computational volume significantly [27-29].

To find the weights, \mathbf{w} , a modified backpropagation algorithm [31] is used for the training of these neural networks [27-29]. The algorithm tries to minimize the objective function, O , i.e. the least square error between the predicted and the target outputs and is given by:

$$\text{Objective function} = O = \frac{1}{2} \sum_p (d_o^{(p)} - y_o^{(p)})^2 \quad \mathbf{5.3}$$

where p represents the number of training datasets and o represents the number of output nodes, which is one in this work. The desired outputs of the network such as weld penetration, leg-length, throat, cooling rate and peak temperature is dependent on input welding conditions, material properties and the network parameters such as the weights. The working procedure of backpropagation algorithm is as follows:

The backpropagation training consists of two passes of computation, a forward pass and a backward pass [27-31]. In the forward pass an input vector (i.e. set of welding variables) is applied to the sensory nodes of the network. The signals from the input layer propagate to the units in the first layer and each unit produces an output according to eq. 5.2. The outputs of these units are propagated to units in subsequent layers and this process continuous until the signals reach the output layer where the actual response of the network (i.e. weld geometry parameters like penetration, throat, leg-length and cooling time etc.) to the input vector is obtained. During the forward pass the synaptic weights of the network are fixed. During the backward pass, on the other hand, the synaptic weights are all adjusted in accordance with an error signal, which is propagated backward through the network. The basic idea is that the objective function (given by eq. 5.3), which is an error between the desired solution and the predicted values has a particular surface over the weight space and therefore an iterative process such as the CG method can be used for its minimization. In short, the basic backpropagation algorithm looks as follows [27-29, 31]:

1. Normalize the input and output variables values
2. Decide the number of hidden layers and the nodes in the network
3. Initialize the weights in the network
4. Presentation of training data and validation data to the network

5. Calculate the objective function or the error in the network
6. Backpropagate the error and update the weights accordingly

The above steps are explained below in detail.

Normalize the input and output variables values: The values of the input and output variables vary significantly. The vastly different scales of inputs and bias values lead to ill-conditioning of the problem [27-29]. While large inputs cause ill-conditioning by leading to very small weights, large outputs do so by leading to very large weights [27-29]. To eliminate the ill-conditioning problem, the data was normalized using the following formula [29]:

$$x' = 2 \left(\frac{x - x_{\min}}{x_{\max} - x_{\min}} \right) - 1 \quad 5.4$$

where x is the original value of the variable, x' is the normalized value, while x_{\min} and x_{\max} represent the minimum and maximum values of the variable in whole dataset. Eq. 5.4 normalizes the data in the range of -1 to 1. The range of values of all input and output parameters from -1 to +1 implies that the standard deviation cannot exceed 1, while its symmetry about zero means that the mean will typically be relatively small. Furthermore, its maximum derivative is also 1.5, so that backpropagated errors will be neither magnified nor attenuated more than necessary [29].

Decide the number of hidden layers and the nodes in the network: The number of hidden layers in a neural network depends on the type of the problem and the relationships between the input and the output variables. Theoretically, any continuous variation of output with respect to input can be represented by a single hidden layer [39, 40]. Two hidden layers are needed when the relationship between the input and the output variables are discontinuous [39, 40]. The use of more than optimal number of hidden layers in the network may result in undesirable overfitting of the data [27-30, 39, 40]. A single hidden layer was used since the outputs are continuous in nature in the GMA fillet welding. For a single hidden layer network, the number of weights is given by the following:

$$\text{Number of weights in the network} = (n_i + 1) * n_h + (n_h + 1) * n_o \quad 5.5$$

where n_i is the number of input variables, i.e. 22 in the present work, n_h is the number of nodes in the hidden layer and n_o is the number of output variables, i.e. 1. Since the number of weights increase with the increase in the number of nodes, an optimal number of nodes is required.

Initialize the weights in the network: In the backpropagation algorithm, the magnitude of the error propagated backward through the network is proportional to the value of the weights. If all the weights are the same, the back propagated errors will be the same, and consequently all of the weights will be updated by the same amount [27-29]. To avoid this symmetry problem, the initial weights of the network were selected randomly. Furthermore, to avoid the premature saturation of the network, the initial values of the weights were distributed inside a small range of values, i.e. in the interval [-0.5 to 0.5]. When the weights are small, the neurons operate in the *linear regions* of the activation function and consequently the activation function does not saturate.

Presentation of training data and validation data to the network: A large database is required for training, validation and testing of the neural net. The number of training dataset should be more than number of weights connecting different nodes. A database was generated based on design of experiments technique and is explained later in this chapter.

Calculate the objective function or the error in the network: At each iteration, the error in the network or the objective function is calculated using eq. 5.3. Our aim is to find a set of optimized weights in the network which lead to lowest error between the predicted and the actual values of the output variables. To minimize the error in the network, it is passed in the backward direction and the weights are updated accordingly using backpropagation algorithm as explained in the next step.

Backpropagate the error and update the weights accordingly: The basic or the original back-propagation algorithm adjusts the weights in the steepest descent direction (negative of the gradient) [27-29, 31]. This is the direction in which the error decreases most rapidly. Since this algorithm requires a learning rate parameter to determine the extent to which the weights change in an iteration, i.e., the step sizes, its performance depends on the choice of the value of the learning rate [27-29, 31]. A slight modification of the

backpropagation algorithm includes a momentum term. The momentum term ensures that the previous changes in the weights are considered in determining the current direction of changes of weights. Although, there is some guidance for the selection of these parameters, they are more oriented towards specific problems like pattern recognition and their performance varies with the type of problem [27-29, 31]. Due to difficulty in the selection of the learning rate parameter and momentum term, the original backpropagation algorithm was modified by replacing the steepest gradient method with the conjugate gradient (CG) method for optimizing the weights [31] as explained in the next section.

5.1.3 Modified Backpropagation Algorithm

In the conjugate gradient method [17, 18, 20, 27, 31] the weights are updated after each iteration based on the objective function (or, error) calculated using eq. 5.3 for the entire training data set. To calculate the optimal weights, the objective function is minimized. The weights at each iteration are modified by calculating the step size or change in weights and the search direction which can lead to global minimal value of the objective function. The step size is calculated at each iteration by using the Brent's algorithm [27-29, 31] whereas the search direction is calculated by conjugating the previous direction with the current gradient of the objective function. The Brent's iterative line search algorithm [19, 24] utilizes the parabolic interpolation and Golden section search method [27-29, 31] to locate the line minima. At the first iteration, since there is no previous direction, the search is performed in the direction of the steepest descent. The directions of search at next iterations are calculated by conjugating the previous direction with the current gradient. These conjugate directions are actually calculated on the assumption that the error surface is quadratic [27-29]. However, if the algorithm discovers that the current line search direction is not downhill, it simply calculates the line of steepest descent and restarts the search in that direction. Once a point close to a minimum is found, the quadratic assumption holds true and the minimum can be located very quickly using Golden section search method [27-29, 31]. The steps

involved in the calculation are as follows [22, 23, 28, 31]. A line search is performed to determine the optimal distance to move along the current search direction. If we let p_k denote the direction vector at iteration k of the algorithm then the weights in the network are updated using the following rule [27-29, 31]:

$$\mathbf{w}^{k+1} = \mathbf{w}^k + \Delta \mathbf{w}^k = \mathbf{w}^k - \eta^k \left(\frac{\partial O}{\partial \mathbf{w}} \right)_0 = \mathbf{w}^k + \eta^k p^k \quad 5.6$$

where η^k is the learning rate or search step size calculated at iteration, k , by using Brent's method [32, 33]. For the first iteration, the initial direction, p^0 , is the same as the steepest descent direction (negative of the gradient):

$$p^0 = -g^0 = - \left(\frac{\partial O}{\partial \mathbf{w}} \right)_0 \quad 5.7$$

where g is the gradient of error with respect to the weight of the link connecting any two consecutive layers. Then the next search direction is determined so that it is conjugate to previous search directions. The general procedure for determining the new search direction is to combine the new steepest descent direction with the previous search direction [22, 23]:

$$p^k = -g^k + \beta^k p^{k-1} \quad 5.8$$

The various versions of conjugate gradient are distinguished by the manner in which the constant β^k is computed. For the Polak-Ribière update, the constant β^k is computed by [17, 18, 20, 22, 23, 32] the following relation:

$$\beta^k = \frac{\left(\Delta g^{k-1} \right)^T g^k}{\left(g^{k-1} \right)^T g^{k-1}} \quad 5.9$$

where T refers to transpose of the matrix, i.e., rows changed to columns. This is the product of the previous change in the gradient with the current gradient divided by the norm squared of the previous gradient. The gradient between the hidden node, h , and the output node, o , is given by [27-29, 31]:

$$\mathbf{g} = \mathbf{g}_{oh} = \frac{\partial O}{\partial \mathbf{w}_{oh}} = -\sum_p \delta_o^{(p)} \mathbf{y}_h^{(p)} \quad \mathbf{5.10}$$

$$\delta_o^{(p)} = (\mathbf{d}_o^{(p)} - \mathbf{y}_o^{(p)}) f'(\mathbf{x}_o^{(p)}) \quad \mathbf{5.11}$$

where $\mathbf{y}_h^{(p)}$ and $\mathbf{y}_o^{(p)}$ represent the output at hidden and output nodes, respectively and $\mathbf{x}_o^{(p)}$ is the input. For the input-to-hidden connections, the gradient between hidden node, h , and input node, i , is given by [27-29, 31]:

$$\mathbf{g}_{hi} = \frac{\partial O}{\partial \mathbf{w}_{hi}} = -\sum_p \delta_h^{(p)} \mathbf{y}_i^{(p)} \quad \mathbf{5.12}$$

$$\delta_h^{(p)} = f'(\mathbf{x}_h^{(p)}) \sum_o \delta_o^{(p)} \mathbf{w}_{oh} \quad \mathbf{5.13}$$

The value of output nodes, o , is one in eqs. **5.10**, **5.11** and **5.13**, since only one output is produced by each of the neural nets. In the gradient descent algorithms, calculations are started at some point on the error function defined over the weights, and an attempt is made to move to the global minimum of the function. The gradient based methods can easily get trapped in local minima. Stochastic optimization techniques are capable of finding the global minima and avoiding local minima [34]. Therefore, a genetic algorithm [34] is used along with the conjugate gradient method to find the optimal global weights in the present work.

A parent centric recombination (PCX) operator based generalized generation gap (G3) GA model [24, 35-38] was used in this work. The PCX operator is a steady-state, elitist, scalable and computationally fast population-alteration model [35]. This model was chosen because it has been shown to have a faster convergence rate on standard test functions as compared to other evolutionary algorithms and classical optimization algorithms including other real-parameter GAs with the unimodal normal distribution crossover (UNDX) and the simplex crossover (SPX) operators, the correlated self-adaptive evolution strategy, the covariance matrix adaptation evolution strategy (CMA-ES), the differential evolution technique, and the quasi-Newton method [35]. Detailed description of this model is available in the literature [24, 35-38] and is not included here.

The various terms used to describe GA are explained in table 5-3. The steps involved in calculating the optimal values of weights using genetic algorithm are as follows:

1. A population is a collection of many individuals and each individual represents a set of randomly chosen values of all the weights. A parent refers to an individual in the current population. The best parent is the individual that has the best fitness, i.e., gives the minimum value of the objective function, defined by eq. 5.3, in the entire population. The best parent and two other randomly selected parents are chosen from the population.
2. From the three chosen parents, two offsprings or new individuals are generated using a recombination scheme. PCX based G3 models are known to converge rapidly when three parents and two offsprings are selected. A recombination scheme is a process for creating new individuals from the parents. The recombination scheme (step 2) used in the present model is based on parent centric recombination (PCX) operator [24, 34-38].
3. Two new parents are randomly chosen from the current population of the individuals.
4. A subpopulation of four individuals that includes the two randomly chosen parents in step 3 and two new offsprings generated in step 2 is formed.
5. The two best solutions, i.e., the solutions having the least values of the objective function, are chosen from the subpopulation of four members created in step 4. These two individuals replace the two parents randomly chosen in step 3.

The calculations are repeated from step one again until convergence is achieved as shown in figure 5-2. The recombination scheme (step 2) used in the present model is based on parent centric recombination (PCX) operator. A brief description of this operator, tailored to the present problem is as follows:

First three parents, i.e., $(w_1^0, w_2^0, w_3^0, \dots, w_n^0)$, $(w_1^1, w_2^1, w_3^1, \dots, w_n^1)$, $(w_1^2, w_2^2, w_3^2, \dots, w_n^2)$, are randomly selected from the current population. Here the subscripts represent the number of weight in the network, while the superscripts denote the parent identification number.

Table 5-3: Terminology used in genetic algorithm

Biological terms	Equivalent neural network variables and representation in genetic algorithm
Genes: Units containing hereditary information	In the form of weights of the network variables, w_1, w_2, \dots, w_n . E.g. $w_1 = -0.10; w_2 = 0.17; w_n = 0.26$
Chromosome/ individual: A number of genes folded together	A set of values of weights taken together i.e. $(-0.10, 0.17, \dots, 0.26)$
Population: Collection of many chromosomes/ individuals	Collection of multiple sets of weights: $(-0.10, 0.17, \dots, 0.26),$ $(0.15, 0.27, \dots, 0.24),$ $(0.33, -0.14, \dots, 0.43)$
Parents: Chromosomes/ individuals participating for creating new individuals (or offsprings)	Parents: E.g. $(-0.10, 0.17, \dots, 0.26),$ $(0.15, 0.27, \dots, 0.24)$
Fitness value: Value of fitness function determines if a chromosomes/ individual survives or dies	Objective function or fitness function: Calculated for each set of input variables using eq. 5.3.

Then the centroid, $\bar{g} = \left(\frac{w_1^0 + w_1^1 + w_1^2}{3}, \frac{w_2^0 + w_2^1 + w_2^2}{3}, \frac{w_3^0 + w_3^1 + w_3^2}{3}, \dots, \frac{w_n^0 + w_n^1 + w_n^2}{3} \right)$,

of the three chosen parents is computed. To create an offspring, one of the parents, say $\bar{x}^{(p)} = (w_1^0, w_2^0, w_3^0, \dots, w_n^0)$, is chosen randomly. The direction vector, $\vec{d}^{(p)} = \bar{x}^{(p)} - \bar{g}$ is next calculated from the selected parents to the mean vector or centroid. Thereafter, from each of the other two parents, i.e., $(w_1^1, w_2^1, w_3^1, \dots, w_n^1)$, and $(w_1^2, w_2^2, w_3^2, \dots, w_n^2)$, perpendicular distances, D_i , to the direction vector, $\vec{d}^{(p)}$, are computed and their average, \bar{D} , is found. Finally, the offspring, i.e., $\bar{y} = (w'_1, w'_2, w'_3, \dots, w'_n)$, is created as follows [24, 34-38]:

$$\bar{y} = \bar{x}^{(p)} + z_c \left| \vec{d}^{(p)} \right| + \sum_{i=1, i \neq p}^n z_i \bar{D} \vec{h}^{(i)} \quad 5.14$$

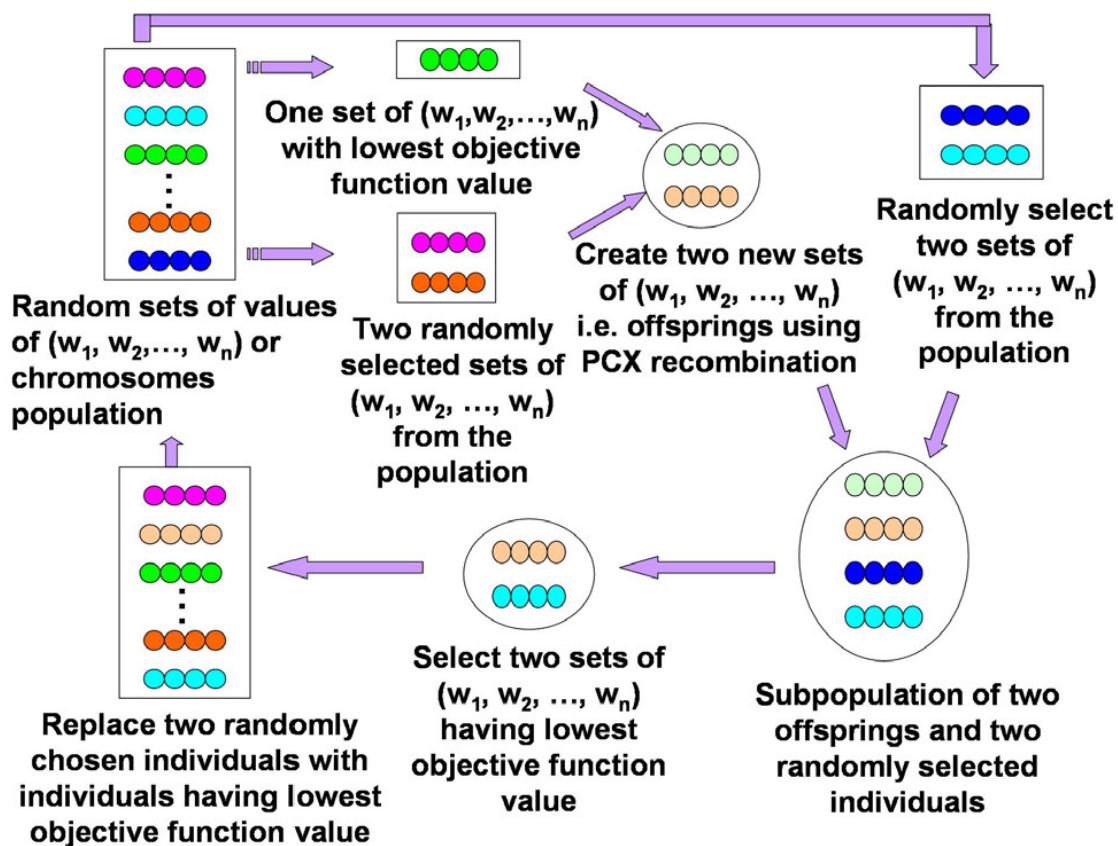


Figure 5-2: The working principle of the genetic algorithm based on Generalized Generation Gap (G3) model and using parent centric recombination (PCX) operator.

where $\bar{h}^{(i)}$ are the orthonormal bases that span the subspace perpendicular to $\bar{d}^{(p)}$, and z_ζ and z_η are randomly calculated zero-mean normally distributed variables.

5.2 Database Generation Based on Design of Experiments

A database for training of the neural nets was generated based on design of experiments to capture the effects of all the welding parameters and material properties [41]. The original $L_{81}(3^{40})$ orthogonal array contains 81 rows and 40 columns of variables each having 3 levels of values for capturing the interaction among all 40 variables [41]. However, in case of GMA fillet welding, we have 22 input variables. In $L_{81}(3^{40})$ array, only 22 columns are used and the remaining 18 remain vacant. Since only three levels of weld process parameters are not capable to capturing the complex interaction among variables, the array is modified to $L_{81}(9^6 \times 3^{16})$ based on linear graph theory [41]. The columns in $L_{81}(3^{40})$ orthogonal array have 2 degrees of freedom [41]. Since, any variable in modified $L_{81}(9^6 \times 3^{16})$ array with 9 levels requires 8 degrees of freedom [41], it was necessary to determine the appropriate four columns from the $L_{81}(3^{40})$ orthogonal array to which to assign this variable. The procedure for converting the standard orthogonal array to a multi-level $L_{81}(9^6 \times 3^{16})$ array includes the following steps:

Step 1: Establish the standard $L_{81}(3^{40})$ orthogonal array

Step 2: Choose a suitable linear graph. For example, a linear graph joining four columns in the $L_{81}(3^{40})$ orthogonal array is shown in figure 5-3(a). Based on this graph, four columns, i.e. column no. 6, 18, 28 and 35 were selected from the standard $L_{81}(3^{40})$ orthogonal array as shown in table 5-4.

Step 3: The linear graph was modified with different combinations of 1's, 2's and 3's from columns 6, 18 and 28 without having to consider the 35th column as shown in table 5-5. In this table only few rows of the array are shown to save the space.

Step 4: Columns 6, 18, 28 and 35 in the original $L_{81}(3^{40})$ orthogonal array were replaced with the modified nine level column.

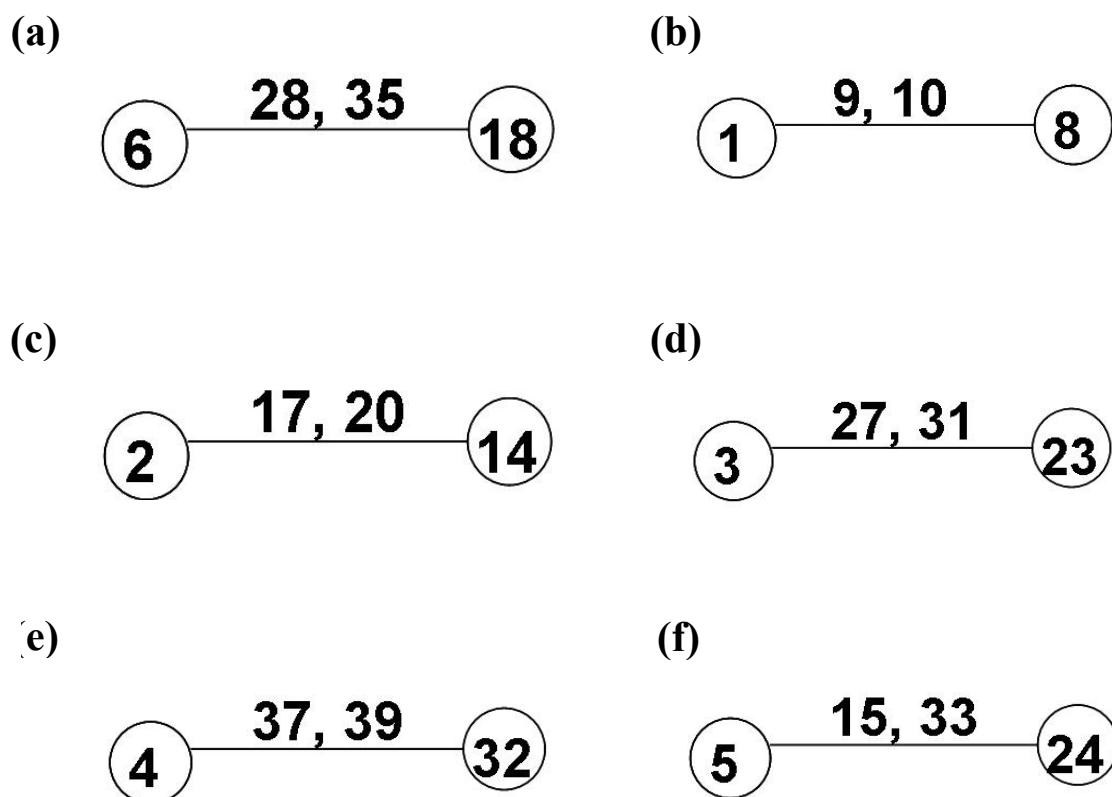


Figure 5-3: Linear graphs of the $L_{81}(3^{40})$ orthogonal array for columns (a) 6, 18, 28 and 35, (b) 1, 8, 9 and 10, (c) 2, 14, 17 and 20, (d) 3, 23, 27 and 31, (e) 4, 32, 37 and 39, (f) 5, 15, 24 and 33, to capture the interaction among variables. The numbers in these figures represents the column numbers of the original $L_{81}(3^{40})$ orthogonal array. The columns of the orthogonal array correspond to the different variables whose effects are being analyzed.

Table 5-4: Columns of $L_{81} (3^{40})$ orthogonal array selected based on linear graph shown in figure 4(a).

Case \ Column	6	18	28	Modified	35
1	1	1	1	1	1
2	1	2	2	2	2
3	1	3	3	3	3
4	2	1	2	4	3
5	2	2	3	5	1
6	2	3	1	6	2
7	3	1	3	7	2
8	3	2	1	8	3
9	3	3	2	9	1

Table 5-5: First nine rows of the modified multi-level $L_{81} (9^6 \times 3^{16})$ orthogonal array

Variable	1	2	3	4	5	6	7	8	9	10	11	12	13	14	15	16	17	18	19	20	21	22
<i>Case 1</i>	1	1	1	1	1	1	1	1	1	1	1	1	1	1	1	1	1	1	1	1	1	1
<i>Case 2</i>	1	2	2	2	2	2	1	1	1	1	2	2	2	2	2	2	2	2	2	2	2	2
<i>Case 3</i>	1	3	3	3	3	3	1	1	1	1	3	3	3	3	3	3	3	3	3	3	3	3
<i>Case 4</i>	2	1	2	3	4	4	2	2	2	2	1	1	1	1	2	2	2	2	3	3	3	3
<i>Case 5</i>	2	2	3	1	5	5	2	2	2	2	2	2	2	2	3	3	3	3	1	1	1	1
<i>Case 6</i>	2	3	1	2	6	6	2	2	2	2	3	3	3	3	1	1	1	1	2	2	2	2
<i>Case 7</i>	3	1	3	2	7	7	3	3	3	3	1	1	1	1	3	3	3	3	2	2	2	2
<i>Case 8</i>	3	2	1	3	8	8	3	3	3	3	2	2	2	2	1	1	1	1	3	3	3	3
<i>Case 9</i>	3	3	2	1	9	9	3	3	3	3	3	3	3	3	2	2	2	2	1	1	1	1

The process was repeated with other linear graphs shown in figure 5-3 to achieve six columns each with 9 levels of values in the original orthogonal array. First few rows of the resulting multi-level $L_{81} (9^6 \times 3^{16})$ array are shown in table 5-5. In the modified array, six most important variables, current, voltage, welding speed, wire feed rate, effective thermal conductivity and effective viscosity, are assigned 9 levels and remaining 16 variables are assigned three values each. Rest of the variables such as the efficiency, arc radius, arc power distribution factor, contact tube to workpiece distance (CTWD) and material properties such as density, specific heat of the solid, specific heat of the liquid, latent heat etc. are kept at three levels. This procedure increases the degrees of freedom and helps to capture the effect of the variables, which have large influence on the weld geometry and cooling rate.

Two $L_{81} (9^6 \times 3^{16})$ arrays for each of the Fe 1005, Fe 1045 and A36 steels were used. For each steel, we used two different nine levels of values of current, voltage, welding speed, wire feed rate, effective thermal conductivity and effective viscosity to capture the interactions. Similarly, material properties and other parameters like arc efficiency, arc radius, arc power distribution factor, and contact tube to workpiece distance are different in each array. Therefore we have 18 levels of all the input variables in the form of 6 $L_{81} (9^6 \times 3^{16})$ arrays, or 486 datasets for training. For validation and testing of the neural net, additional 50 and 25 different datasets were generated using three dimensional heat transfer and fluid flow model. These datasets for validation and testing were generated randomly by selecting the values of variables, which are different from the training dataset. The ranges of all the 22 input variables used for the generation of datasets are shown in the table 5-1. The different levels or values of the variables are decided based on their sensitivity on weld geometry. In the database, the variables like arc current, arc voltage, welding speed, wire feed rate, effective thermal conductivity and effective viscosity which have major influence on weld geometry are taken at many levels compared to other remaining variables as shown in figure 5-4. The material properties in the database were selected around their corresponding values for Fe1005 steel, Fe 1045 steel and A-36 steel.

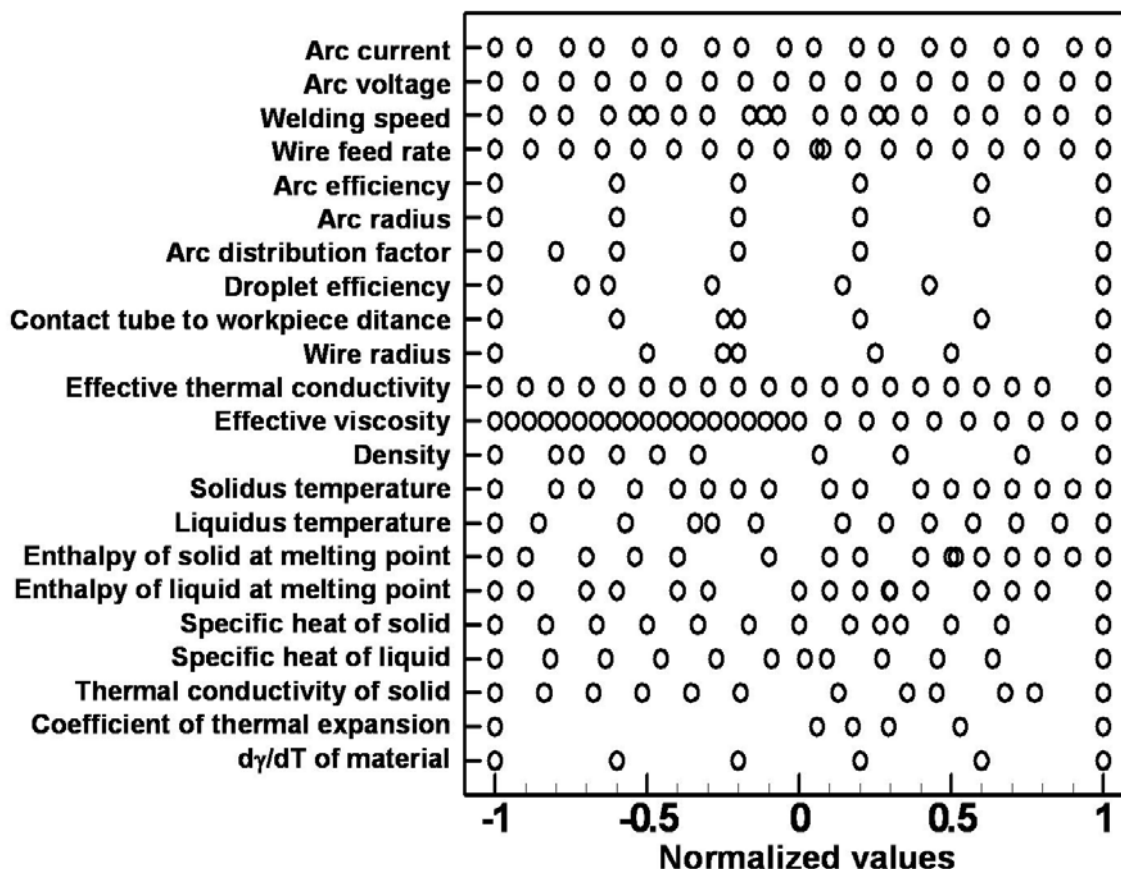


Figure 5-4: The range of input variables in the database used for training, validation and testing of the network. The normalized value of the variables was obtained using eq. 5.4 and corresponding minimum and maximum value listed in table 5-1. Various combinations of these 22 input variables were generated using the modified L_{81} ($9^6 \times 3^{16}$) array in the database.

5.3 Results and Discussion

The calculation starts with the selection of number of nodes in the hidden layer. The total number of weights in the network is calculated based on the number of nodes in the hidden layer. The weights are then initialized randomly in the interval $[-0.5, 0.5]$ as described in the previous section. In the next step, a modified backpropagation algorithm is used to minimize the error on the training dataset. The weights calculated by the CG method are stored as one possible set of weights. This process is repeated 10 times with different randomly selected initial weights for fixed values of nodes in the hidden layer. All of these ten sets of weight are provided as input to the GA. The final aim of the GA is to find the weights in the network through a systematic global search that will give the least error between the neural net prediction and heat transfer and fluid flow calculations. The flowchart of the calculation scheme is presented in figure 5-5. The convergence is based on the error in training and validation data. When the error during validation starts increasing, the calculation is stopped to avoid over-fitting even if the error with training dataset decreases with iteration.

The number of nodes in the hidden layer were varied to get an optimum number of nodes that resulted in minimum mean square error (MSE) as shown in figure 5-6. The mean square error (MSE) error is defined as follows:

$$\text{MSE} = \frac{2 \cdot E}{p} = \frac{1}{p} \sum_p (d_o^{(p)} - y_o^{(p)})^2 \quad 5.15$$

where E is objective function represented by eq. 5.3.

Figure 5-6(a) shows that $\log(\text{MSE})$ decreases almost linearly with increase in the number of hidden nodes. The results are shown for penetration as the output variable. Other output variables also showed the same trend. These runs were conducted using the CG method with ten different randomly selected initial sets of weights in the neural net to avoid any local optimal solution. Figure 5-6(b) also shows a similar trend for the variation in $\log(\text{MSE})$ for leg-length. The $\log(\text{MSE})$ for penetration and leg-length becomes almost constant for more than 19 hidden nodes in the network.

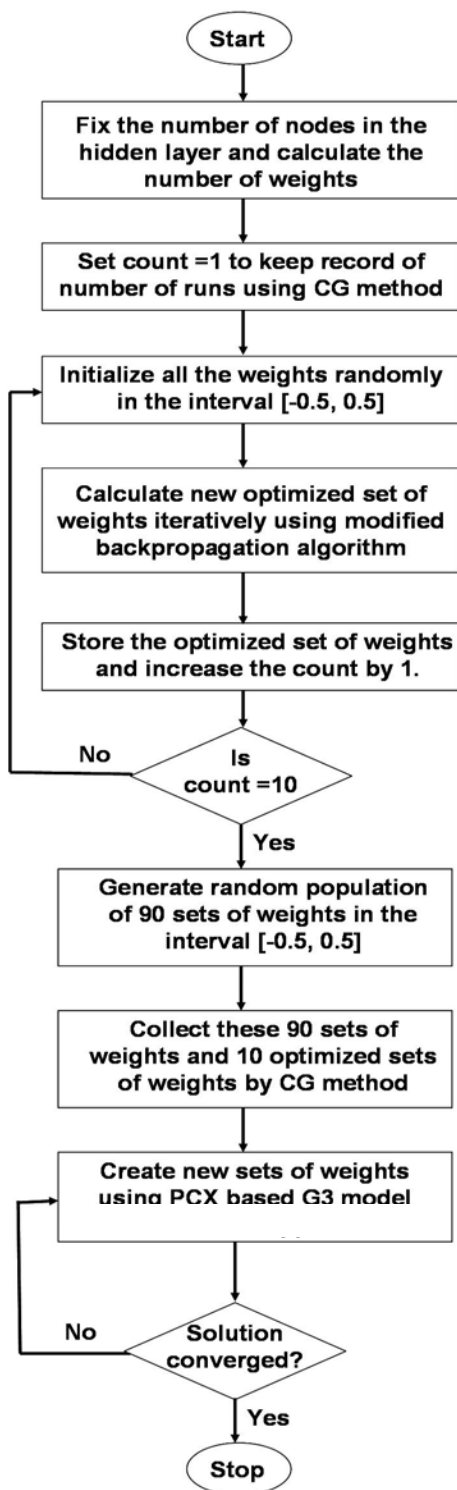


Figure 5-5: Flow chart of the modified backpropagation algorithm using hybrid optimization model after coupling of generalized generation gap (G3) genetic algorithm with the conjugate gradient method.

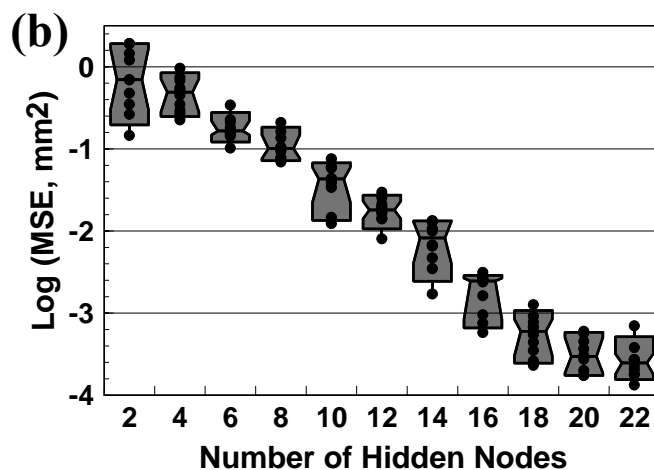
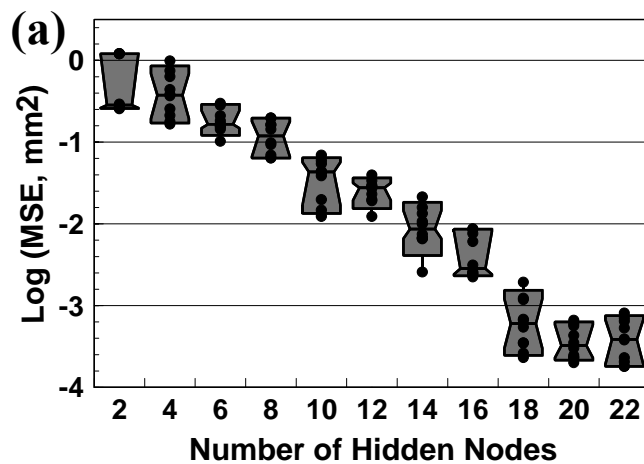


Figure 5-6: Variation of $\log(\text{MSE})$ for (a) penetration; and (b) leg-length with number of hidden nodes for training data by using the CG optimization method after 50000 iterations. The box whisker plot shows the variation and the mean of the $\log(\text{MSE})$ for different number of hidden nodes. In the box plot, the shaded region shows the lower quartile, median and upper quartile. The dots represent the $\log(\text{MSE})$ obtained in ten different runs which were taken to examine the effect of initial weights on the final converged solution. 75% of the data lies inside the shaded box.

Figure 5-7 shows that most of the runs for 19 hidden nodes attained very small value of error within 15000 iterations. However, the convergence rate depended on the choice of the initial set of weights. This is the main difficulty in using the CG method alone to find the optimal weights. In order to solve this problem and obtain globally optimized weights, the weights obtained by using CG method for ten different runs were included in the input to a genetic algorithm based optimization model. Since, the GA requires a population of at least 100 individuals (or different sets of weights) [24, 34, 35] to start the calculations, rest of the 90 sets of weights were generated randomly in the interval [-0.5, 0.5].

Figures 5-8(a) and 5-8(b) show the log(MSE) for penetration and leg-length, respectively, using best optimized set of weights for various numbers of hidden nodes with the hybrid optimization scheme. For the first 19 hidden nodes, the error decreased continuously with the increase in the number of nodes and then started increasing slightly with the increase in nodes. The lower value of MSE may also be due to over-fitting of the network. The performance of the network was tested using the validation and testing datasets. The network was trained using only the training data. The validation data were randomly generated independent of the training data. During training if the network learns the effect of input variables on the output, the MSE on the validation set improves with the iterations. However, if the network minimizes the MSE on the training data by overfitting, the MSE on the validation dataset will increase. This behavior indicates that the interactions between different input variables of the training dataset are accurately modeled only for the training data but not for all possible values of input variables. This behavior also means that the performance of the network may vary significantly for training, validation and testing datasets. To avoid overtraining (or, overfitting), the training was stopped after some iterations when the performance of the network for the validation data was optimal. The testing data was used to check the overall performance of the network.

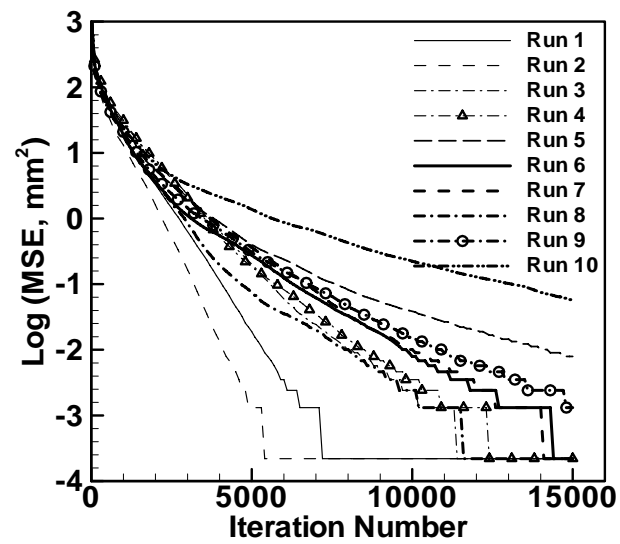


Figure 5-7: Variation of $\log(\text{MSE})$ for penetration training data with number of iterations for 19 hidden nodes by using the CG optimization method.

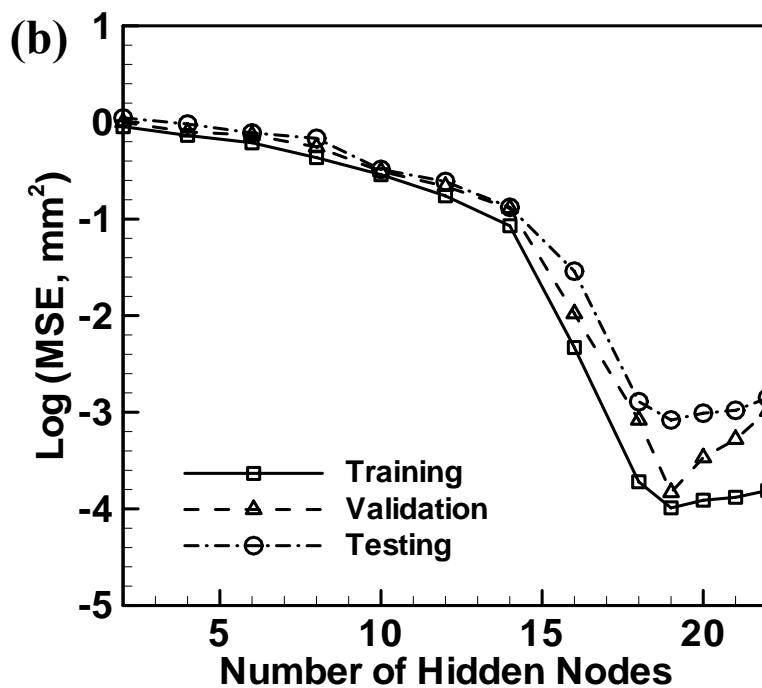
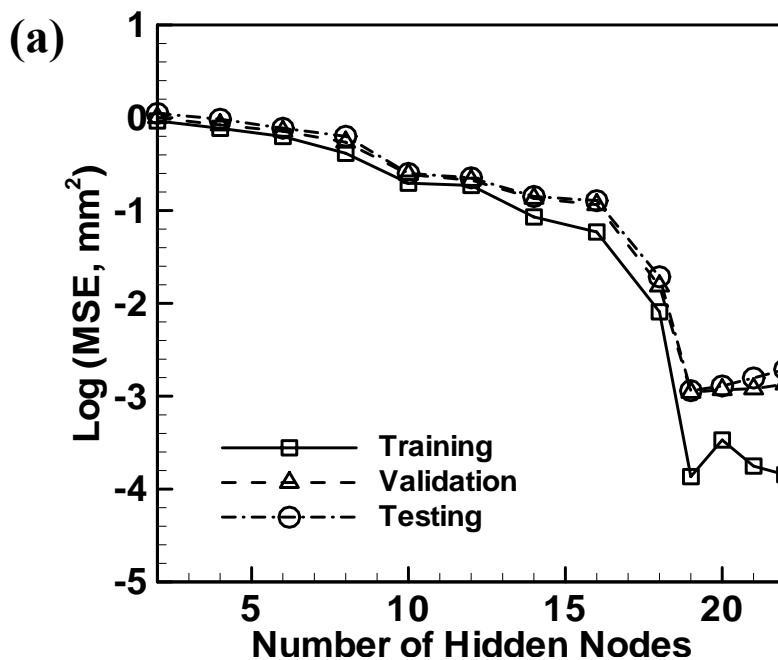


Figure 5-8: Variation of log of mean square error (MSE) in (a) penetration and (b) leg-length for training, validation and testing data by using the hybrid optimization scheme after 50,000 iterations. Figure shows that the 19 nodes in the hidden layer provide less error on all the three datasets.

Figure 5-8(a) shows that 19 hidden nodes provide the lowest value of $\log(\text{MSE})$ for penetration for the training, validation and testing data. Similarly, the minimum value of $\log(\text{MSE})$ for leg-length was found for 19 hidden nodes as shown in figure 5-8(b). Since a neural network with 19 hidden nodes showed low errors for all other output variables, 19 hidden nodes were selected for all the variables for simplicity.

Figure 5-9 shows the variation of $\log(\text{MSE})$ in penetration and leg-length with iterations using hybrid method for 19 nodes in the hidden layer. Initially, the error for both training and validation data decreases with iterations. However, once the network gets the optimal weights, the error almost become constant. The calculation was stopped when the error for validation data started increasing with change in weights or iterations. Furthermore, the number of iterations depended on the output variables and was not same for all variables. For example, for leg-length and penetration, the calculations were stopped after 42000 and 48000 iterations, respectively based on the results in figure 5-9. Table 5-2 shows the root mean square error for all the output variables. The root-mean-square (RMS) errors in the training data for penetration, leg-length, and peak temperature in the weld pool were 0.02 mm, 0.01 mm and 4.27 K, respectively. These RMS errors were quite small compared to the magnitude of these output variables. The RMS errors in training data for other outputs were also very small. However, the RMS errors were higher for both the validation and testing data. The leg-length showed good match for all the three datasets. This is due to the fact that leg-length depends mainly on the heat input and is not significantly influenced by the impingement of droplets [17-19]. Furthermore, the RMS error for penetration was large because its calculation involves complex interactions between various welding process parameters like arc current, welding speed and wire feed rate. The RMS error on testing data was generally higher because the testing data was selected near the extreme range of input variables with the exception of maximum velocity for which the errors in the testing data are smaller.

To further check the accuracy of the predicted result by the neural net, the relative errors were calculated as follows:

$$(\text{Relative \% error})_i = 100 \times \left(\frac{d_i - y_i}{d_i} \right) \quad 5.16$$

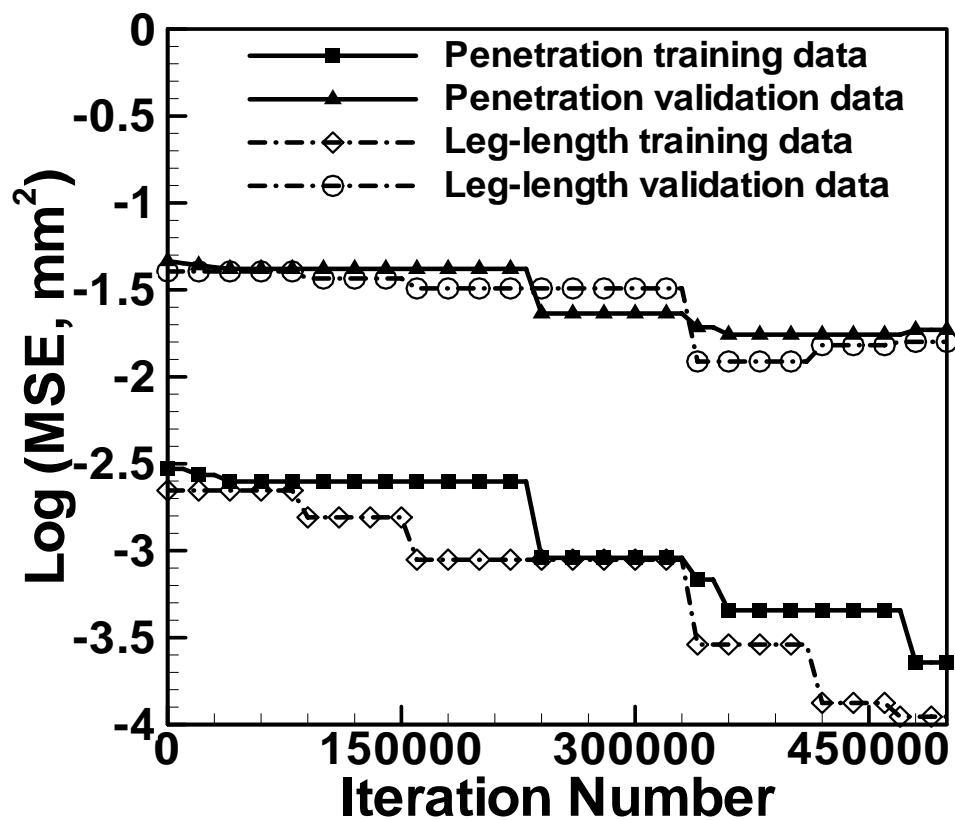


Figure 5-9: Variation of averaged log of mean square error (MSE) in penetration and leg-length for all the 100 individual members in the population by using the hybrid optimization method for 19 nodes in the hidden layer. The calculation was stopped when the error on the validation data started increasing.

where, d_i is the desired value of the penetration for the i^{th} data point while y_i is calculated value of the penetration by neural net for the same dataset. The results are presented in typical frequency versus relative % error for penetration in figure 5-10. This error has classical Gaussian distribution nature with center around zero. Furthermore, more than 90% of data has error less than 0.8 % on training dataset. This low percentage error indicates the accuracy of the neural network models.

Various runs were conducted using the hybrid optimization method with different randomly selected initial sets of weights in the population to obtain the optimized values of all weights. The hybrid method provided either smaller or same error than the CG method. The computations took approximately 6 hours for 19 hidden nodes on a 3.06 GHz Intel P4 CPU with 512 Mb PC2700 DDR-SDRAM memory. Figure 5-11 compares the relative % error for training, validation and testing data for different best sets of optimal weights obtained using CG method alone, GA method alone and the hybrid method involving CG and GA. The results show that the best set of weights obtained using hybrid method provides less error than the best sets obtained using CG method or GA method alone. The GA method gives worse performance compared to CG and hybrid method since it does not take any account of any information of the gradient or the variation of the objective function with weights. The relative % errors on training data using CG method in runs 4, 6, and 8 were low. However, all of these runs resulted in a large relative % error on validation and testing data (figures 5-11(b) and 5-11(c)). The use of CG method or GA method to determine the weights produced sub-optimal solutions. By using the optimal weights produced by the hybrid method, the average relative % errors in training data, validation data and testing data were 0.5%, 2.4% and 3.8%, respectively for the predicted value of the penetration. Table 5-6 shows that the average relative % errors in training data for other output variables were less than 0.5 % except for maximum velocity which had a maximum error of 0.7%. Computed values of penetration, actual throat, leg-length, length of weld pool, peak temperature, cooling time and maximum velocity in the weld pool from the neural network model were compared with their corresponding values obtained from the heat transfer and fluid flow model to examine the accuracy of the neural network.

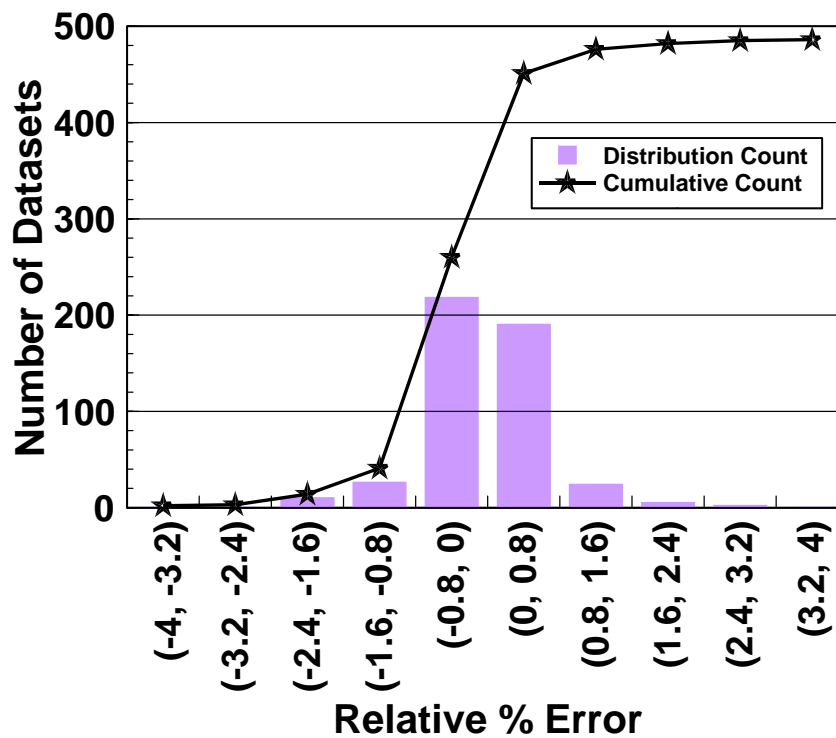


Figure 5-10: Frequency plot showing the number of training datasets of penetration lying in different ranges of relative % error. This plots shows that the relative % error follows the Gaussian distribution with center around zero. Also, more than 90% of data has error with in -0.8 % to 0.8 % on training dataset.

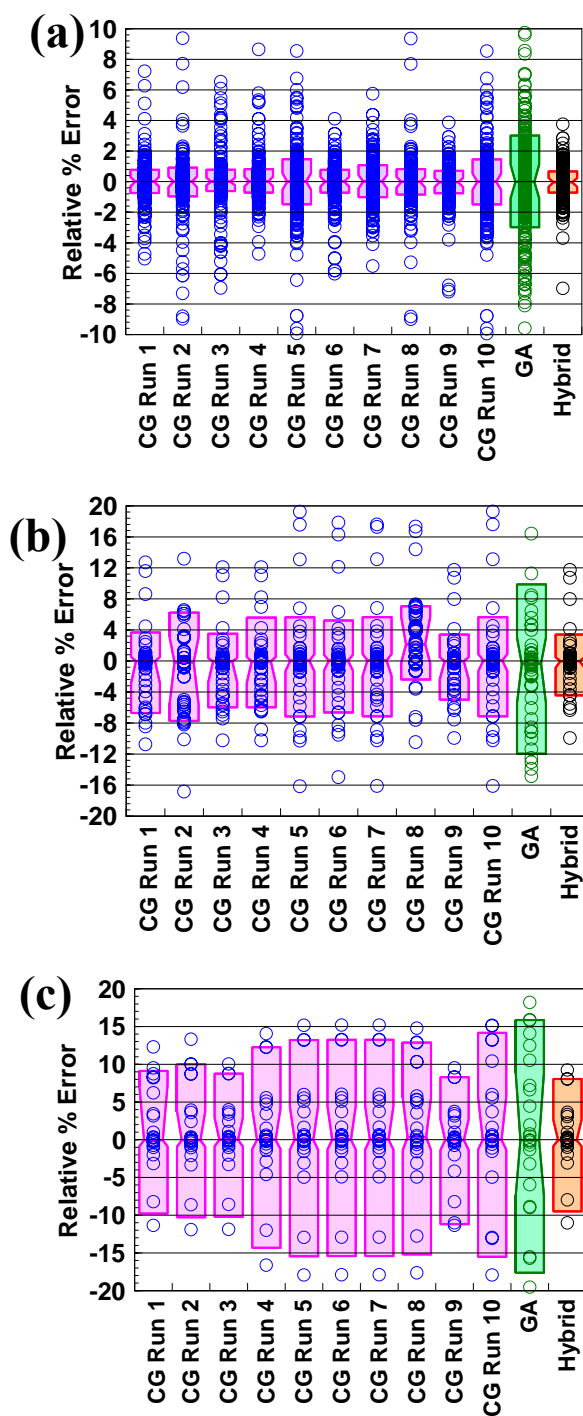


Figure 5-11: Comparison of relative % error in penetration for (a) training data, (b) validation data, (c) testing data, calculated by taking ten different runs of CG method, GA method and the hybrid optimization method. These box-whisker plots show that the hybrid optimization method always produced less error than the CG method or GA method alone. The dots represent the relative % error in the data and 75% of the data points lie inside the shaded box.

Figure 5-12 shows all the output data obtained using different sets of welding variables used during the training, validation and testing of the network. All the neural nets of GMA fillet weld comprised only one hidden layer containing 19 nodes for each of the seven output variables, i.e. penetration, actual throat, leg-length, length of weld pool, peak temperature, cooling time and maximum velocity in the weld pool. Figure 5-12 shows the predicted values of outputs from the neural network and the corresponding values calculated using heat transfer and fluid flow model. The plots show that all points lie on or very close to the diagonal line and the results obtained from the neural network agree well with the values calculated using heat transfer and fluid flow model. Table 5-6 shows the average absolute value of the relative % error in all the output variables for training, validation and testing data. The maximum average value of the relative % error in all outputs was 1.1, 2.4 and 6.0 in training, validation and testing data, respectively. The results indicate that the neural network can be used for simulations with predetermined good accuracy.

Table 5-6: Average absolute value of the relative % error for different output variables

Output Variable	Training	Validation	Testing
Leg-length	0.1	0.1	1.2
Actual throat	0.1	1.0	1.8
Penetration	0.5	2.4	3.8
Length of the weld pool	0.4	0.4	0.5
Peak temperature in the weld pool	0.1	0.2	0.2
Cooling time between 800 °C to 500 °C	0.2	0.2	0.7
Maximum velocity in the weld pool	0.7	0.8	0.8

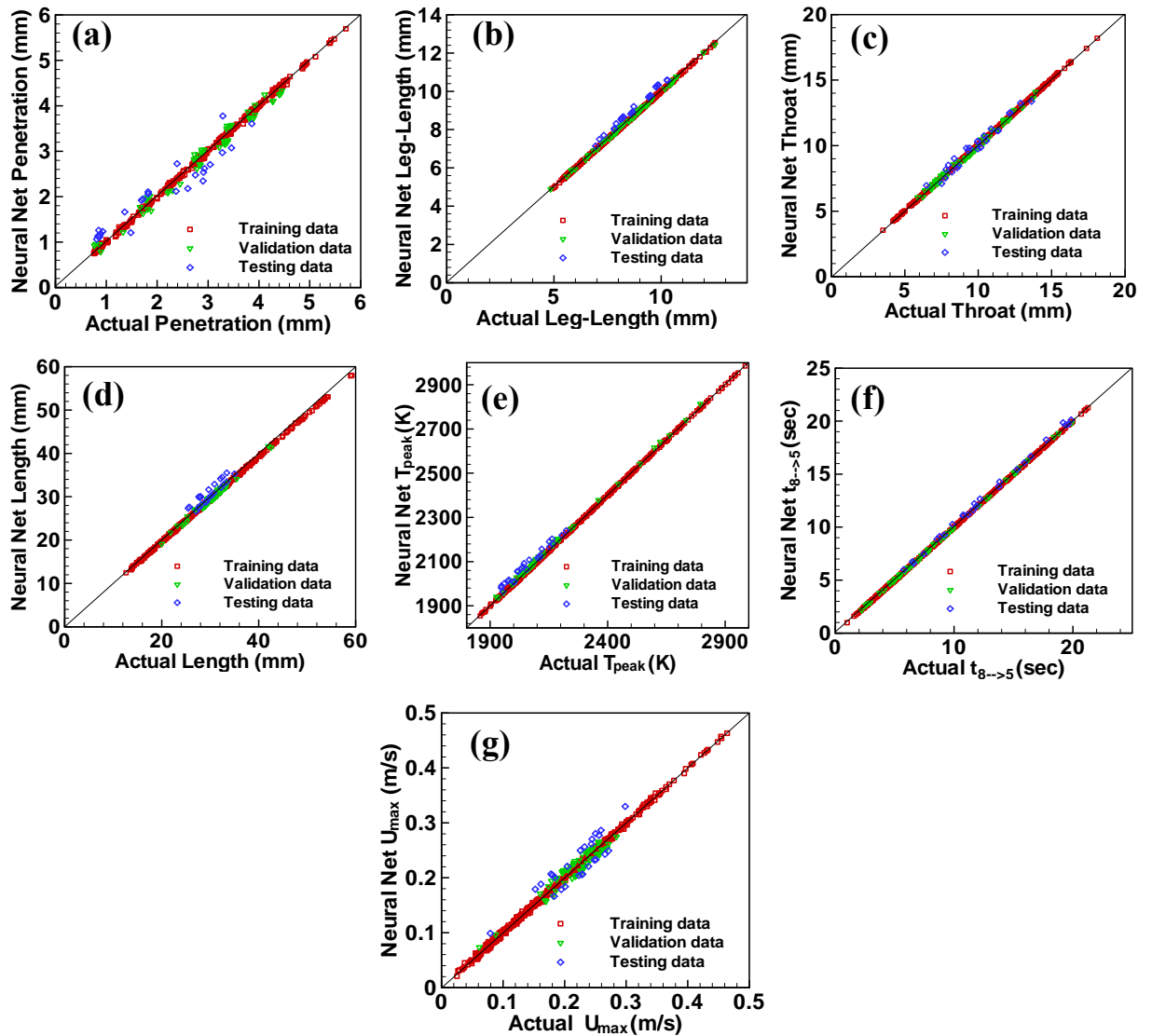


Figure 5-12: Comparison of output variables, i.e. (a) penetration, (b) leg-length, (c) throat, (d) length of weld pool, (e) peak temperature in the weld pool, (f) cooling time between 800°C to 500°C , (g) maximum velocity (U_{\max}) in the weld pool, calculated by heat transfer and fluid flow model (x-axis) with corresponding values predicted by neural network model of GMA fillet weld. The diagonal lines in each plot show that ideally all the points should lie on this line. The training data, validation data and test data comprises of 486, 50 and 25 datasets, respectively.

5.4 Summary and Conclusions

A set of multiple feed forward neural networks was developed for GMAW fillet welding to calculate penetration, leg-length, throat, weld pool length, cooling time between 800 °C to 500 °C, maximum velocity and peak temperature in the weld pool. These neural net models used 22 input variables including welding process parameters and material properties. A hybrid optimization scheme involving a conjugate gradient and a genetic algorithm for finding global optimal weights resulted in low errors in training, validation and testing data. The results obtained using the hybrid scheme were better than the CG method or GA method alone. For each output variable, a separate neural network model was developed. This approach provided superior results and greater flexibility than one neural net for all the output variables. These neural net models can replace output of complex heat transfer and fluid flow model with significant computational economy.

5.5 References

1. I. S. Kim, S. H. Lee, and P. K. D. V. Yarlagadda, *Sci. Technol. Weld Joining*, **8** (5), 347 (2003).
2. H. B. Smartt and J. A. Johnson, *Proceedings of the Artificial Neural Networks in Engineering (ANNIE'91)*, St. Louis, MO, 10 to 13 November 1991, C. H. Dagli, S. R. T. Kumara, Y. C. Shin, Eds., ASME, New York, p.711 (1991).
3. G. E. Cook, K. Andersen, G. Karsai, and K. Ramaswamy, *IEEE Transactions on Industry Applications*, **26**, 824 (1990).
4. X. Li, S. W. Simpson, and M. Rados, *Sci. Technol. Weld. Joining*, **5** (2), 71 (2000).
5. S. Mishra, 'Tailoring Weld Geometry and Composition in Fusion Welding Through Convective Mass Transfer Calculations', Doctoral Thesis, The Pennsylvania State University (2006).
6. J. M. Vitek, Y. S. Iskander, and E. M. Oblow, *Welding J.*, **79** (2), 33 (2000).

7. S. H. Lalam, H. K. D. H. Bhadeshia and D. J. C. MacKay, *Sci. Technol. Weld. Joining*, **5** (3), 135 (2000).
8. E. A. Metzbower, J. J. DeLoach, S. H. Lalam and H. K. D. H. Bhadeshia, *Sci. Technol. Weld. Joining*, **6** (2), 116 (2001).
9. I. S. Kim, Y. J. Jeong, C. W. Lee, and P. K. D. V. Yarlagadda, *International Journal of Advanced Manufacturing Technology*, **22** (9-10), 713 (2003).
10. D. S. Nagesh, and G. L. Datta, *J. Mater. Process. Technol*, **123** (2), 303 (2002).
11. K. H. Christensen, T. Sorensen, and J. K. Kristensen, *Sci. Technol. Weld. Joining*, **10** (1), 32 (2005).
12. A. De, J. Jantre, and P. K. Ghosh, *Sci. Technol. Weld. Joining*, **9** (3), 253 (2004).
13. C. S. Wu, T. Polte, and D. Rehfeldt, *Sci. Technol. Weld. Joining*, **5** (5), 324 (2000).
14. C. H. Kim, W. Zhang, and T. DebRoy, *J. Appl. Phys.*, **94**, 2667 (2003).
15. W. Zhang, C. H. Kim, and T. DebRoy, *J. Appl. Phys.*, **95**, 5210 (2004).
16. W. Zhang, C. H. Kim, and T. DebRoy, *J. Appl. Phys.*, **95**, 5220 (2004).
17. A. Kumar and T. DebRoy: *Int. J. Heat Mass Tran.*, **47**, 5793 (2004).
18. A. Kumar, W. Zhang, and T. DebRoy: *J. Phys.D: Appl. Phys.*, **38**, 119 (2005).
19. A. Kumar and T. DebRoy: *J. Phys.D: Appl. Phys.*, **38**, 127 (2005).
41. A. Kumar, W. Zhang, C. H. Kim, and T. DebRoy, *Mathematical Modelling of Weld Phenomena 7*, Graz, Austria, Oct 2004, ed. H. Cerjak, H.K.D.H. Bhadeshia, E. Kozeschnik, pp. 1 (2005).
20. A. Kumar and T. DebRoy, *J. Appl. Phys.*, **94**(2), 1267 (2003).
21. A. De and T. DebRoy, *Welding Journal*, **84** (7), 101 (2005).
22. A. De and T. DebRoy, *J. Phys.D: Appl. Phys.*, **37**, 140 (2004).
23. A. Kumar and T. DebRoy, *Metall. Mat. Trans. A.*, **36A**, 2725 (2005).
24. S. Kumar and S. C. Bhaduri, *Metall. Trans. B*, **25** 435 (1994).
25. S.V. Patankar, '*Numerical Heat Transfer and Fluid Flow*', Hemisphere, NY (1980).
26. S. Haykin, '*Neural Network: A Comprehensive foundation*', 2nd ed., Prentice Hall Pub., NJ

27. M. T. Hagan, '*Neural Network Design*', 1st ed., PWS Pub., Boston.
28. T. Masters, '*Practical neural network recipes in C++*', Academic Press, Boston.
29. Barry L. Kalman and Stan C. Kwasny, '*Proceedings of the International Joint Conference on Neural Networks*', **4**, 578 (1992).
30. C. Charalambus, '*IEE Proceedings-G*', **139**, 301 (1992).
31. W. H. Press, B. P. Flannery, S. A. Teukolsky, and W. T. Vetterling, '*Numerical Recipes in C*', 2nd ed., Cambridge University Press, Cambridge.
32. Richard P. Brent, '*Algorithms for Minimization Without Derivatives*', Prentice-Hall, NJ (1993).
33. D.E. Goldberg, '*Genetic Algorithm in Search, Optimization and Machine Learning*', Addison-Wesley, MA (1989).
34. K. Deb, A. Anand, and D. Joshi, '*Evolutionary Computation*', **10**, 371 (2002).
35. A. Kumar, S. Mishra, J. W. Elmer, and T. DebRoy, '*Metall. Mat. Trans. A.*', **36**, 15 (2005).
36. S. Mishra and T. DebRoy, '*J. Phys.D: Appl. Phys.*', **38**, 2977 (2005).
37. S. Mishra and T. DebRoy, '*J. Appl. Phys.*', **98(4)**, Art. No. 044902 (2005).
38. R. P. Lippman, '*IEEE ASAP magazine*', 4 (1987).
39. J. Makhoul, A. El-Jaroudi, and R. Schwartz, '*International Joint Conference on Neural Nets*', Vol. 1, pp. 455 (1989).
40. G. S. Peace, '*Taguchi Methods: A Hands-on-Approach*', Addison-Wesley, MA (1993).

Chapter 6

TAILORING FILLET WELD GEOMETRY USING GENETIC ALGORITHM AND A NEURAL NETWORK

As explained in earlier chapters, the phenomenological models of heat transfer and fluid flow [1-16], microstructure [4, 8] and thermal stress calculation [17-19] of various fusion welding processes such as the gas tungsten arc welding [1-10], gas metal arc (GMA) welding [11-13] and laser welding [14,16] have been developed to better understand physical processes in welding. Furthermore, these models have been used extensively to calculate the weld geometry [1-10], weld metal phase composition [4, 8], grain sizes [5, 6], cooling rate [4, 11-13], inclusion structure [7] and the residual stresses [17-19] in the workpiece. Although, these powerful models have provided significant insight about the effect of various welding variables, their applications have been rather limited [20-22] for several reasons. First, the models are comprehensive and require significant amount of computer time. Second, they are designed to calculate temperature and velocity fields for a given set of welding variables, i.e. they are unidirectional in nature. In other words, they cannot predict the welding variables needed to achieve a target weld geometry [20-23] or other weld attributes. Finally, the GMA welding system is highly complex and involves non-linear interaction of several welding variables [11-16, 24]. As a result, a particular weld attribute such as the geometry can be obtained via multiple paths, i.e., through the use of various sets of welding variables. What is very much needed, and not currently available, is for the models to have a capability to offer various choices of welding variable combinations, each capable of producing a target weld attribute. Traditional reverse models cannot produce multiple solutions and, in most instances, cannot confirm to any phenomenological laws.

To systematically tailor a weld attribute such as weld geometry based on scientific principles, the model should satisfy the following three criteria.

- (1) The model should be capable of capturing all the major complex physical processes occurring during the gas metal arc (GMA) fillet welding.
- (2) The model must have a bi-directional capability i.e. it should be able to find the combination of welding variables to achieve desired weld attribute as well as predict the weld geometry for given input welding conditions.
- (3) The model must be able to determine various welding variable sets needed to attain a target weld geometry within a reasonable time.

Since multiple paths can lead to a target weld geometry, the classical gradient-based search and optimization methods [20-22] that produce a single optimum solution cannot be used. These methods use a point-by-point approach, where one relatively imperfect solution in each iteration is modified to a different more appropriate solution [25, 26]. Therefore, a combination of one of these classical optimization methods with the phenomenological model can provide only a single local optimum solution in situations where multiple solutions exist. In contrast, genetic algorithms (GA) mimic nature's evolutionary principles to derive its search towards a population of optimal solutions [25-28]. In the context of welding, a GA can systematically search for multiple combinations of welding variable sets that comply with the phenomenological laws of welding physics and improve with iterations [20-22].

In the initial stage of this work, a bi-directional phenomenological model of GMA fillet welding was developed by coupling a genetic algorithm based optimization method with three-dimensional heat transfer and fluid flow model [20]. Since this model requires the multiple runs of heat transfer and fluid flow model, the computation time was very large. A parallel computing facility was developed in our research lab at Penn State by connecting three CPUs together in a network to reduce the computation time. This model was then run on three processors simultaneously. It was found that this approach can predict multiple combinations of welding variables to achieve a target geometry. However, this model [20] is not suitable for practical applications, since it requires several days of computer calculations. Since it is very hard to maintain such a sophisticated computing facility in a manufacturing industry, the heat transfer and fluid flow model coupled with genetic algorithm can only be used for research purposes.

Unless a model can do calculations in a reasonable time, it is unlikely to find widespread practical applications.

To reduce the computation time, a new approach was developed in which heat transfer and fluid flow model was replaced with an efficient neural network model of GMA fillet welding. In gas-metal-arc (GMA) welding, the effect of welding variables on the weld geometry is non-linear and highly complex. The results presented in Chapter 5 show that a set of neural network models trained with the results of a numerical heat transfer and fluid flow model can correlate various output variables such as the weld pool geometry, cooling rate, liquid velocities and peak temperatures with all the major welding variables and material properties. These neural network models are able to predict the outputs for different welding conditions rapidly [29-31]. The good prediction of outputs for given input welding conditions within a fraction of a second, justifies the use of well trained and rigorously tested neural network models [29-31] in place of heat transfer and fluid model in this work. Furthermore, these neural network models satisfy the basic scientific phenomenological laws expressed in the equations of conservation of mass, momentum and energy.

In this chapter, the multiple sets of welding variables that are capable of producing a target weld geometry are calculated in a realistic time frame by coupling a genetic algorithm with a neural network model of gas-metal-arc fillet welding that has been trained with the results of a well tested heat transfer and fluid flow model.

6.1 Mathematical Model

The main computational engine used here is a neural network model [29] which is trained and validated using the results of well-tested heat transfer and fluid flow model [11-16]. The neural network model includes all the welding variables and material properties as input and provides weld dimensions, peak temperatures, maximum velocities and the cooling rates between 800 °C to 500 °C. This network has 22 input parameters which are connected to output layer through a hidden layer of 19 nodes as

shown in figure 5-1. A hyperbolic tangent function (which is a symmetric *sigmoid* function) is used as the activation function to include non-linear behavior of different variables. A back-propagation algorithm [29, 32-34] was used to update the synaptic weights of the neural network. The algorithm used a hybrid method involving a genetic algorithm and a conjugate gradient technique to reduce the least square error, E, between the actual outputs (d) and predicted values (y) [29]:

$$E = \frac{1}{2} \sum_p (d_o^{(p)} - y_o^{(p)})^2 \quad 6.1$$

where p represents the number of training datasets and o represents the number of output nodes, which is one in this work. The hybrid algorithm reduces the training time as the conjugate gradient method takes advantage of gradient information to calculate the optimal solution, whereas the genetic algorithm helps to avoid local minima [29]. The resulting neural network is computationally more efficient than a phenomenological heat transfer and fluid flow model. Furthermore, the results from the neural network model match with the corresponding results from the heat and fluid flow model.

The genetic algorithm based search for multiple sets of welding variables to achieve a target weld geometry starts with many initial sets of randomly chosen values of the four most important welding variables, i.e., current, voltage, welding speed and the wire feed rate. A systematic global search is next undertaken to find multiple sets of values of these four welding variables that lead to least error between the calculated and the target weld dimensions, i.e., penetration, throat and the leg-length. The neural network model calculates the values of these weld dimensions for each set of input welding variables. The chosen values of welding variables do not always produce the desired weld dimensions and the resulting mismatch between the computed and the desired weld dimensions is expressed by the following objective function, O(f):

$$O(f) = \left(\frac{p^c}{p^t} - 1 \right)^2 + \left(\frac{t^c}{t^t} - 1 \right)^2 + \left(\frac{l^c}{l^t} - 1 \right)^2 \quad 6.2$$

where p^c, t^c and l^c are the computed penetration, throat and the leg-length of the weld bead, respectively and p^t, t^t and l^t are the corresponding target or desired values of these three parameters. The objective function, $O(f)$, depends on four main welding variables, i.e., current, I , voltage, V , welding speed, U , and the wire feed rate, w_f .

$$O(\mathbf{f}) = O(f_1, f_2, f_3, f_4) = O\left(\frac{I}{I_r}, \frac{V}{V_r}, \frac{U}{U_r}, \frac{w_f}{(w_f)_r}\right) \quad \mathbf{6.3}$$

In eq. **6.3**, the reference values, I_r, V_r, U_r and $(w_f)_r$ represent the order of magnitude of the welding variables. Note that eq. **6.3** is made non-dimensional to preserve the importance of all four welding variables by making their non-dimensional values comparable in magnitude. The GA produces new individuals, or sets of welding conditions, with iterations based on the evolutionary principles [20-22, 26-28].

6.1.1 Genetic algorithm

Genetic algorithms work with a set of "individuals" - a population, where each individual is a solution of a given problem. The initial population defines the possible solutions of the optimization problem, i.e., sets of welding variables that completely define a weld such as current, voltage, welding speed, contact tube to workpiece distance and wire feed rate. There are two popular ways of representing the variables in the population in GA: binary and real numbers. Generally binary representation of variables converges slowly compared to the real representations. In addition, since the binary genetic algorithm has its precision limited by the binary representation of variables, using real numbers allows representation to the machine precision. The real coded genetic algorithm also has the advantage of requiring less storage than the binary GA because a single floating point number represents a variable instead of many integers having values 0 and 1. The other important advantage of using real coded GA is its accuracy and precision in representing the variables in continuous search space. Table **6-1** provides the explanation of various terminology used in GA related to welding.

Table 6-1: Terminology used in genetic algorithm.

Biological terms	Equivalent welding variables and representation in genetic algorithm
Genes: Units containing hereditary information	In the form of non-dimensional variables, f_1, f_2, f_3 and f_4 . E.g. $f_1 = 1.10$; $f_2 = 0.70$; $f_3 = 0.56$, $f_4 = -0.34$.
Chromosome/ individual: A number of genes folded together	A set of input variable values taken together i.e. (1.10, 0.70, 0.56, -0.34)
Population: Collection of many chromosomes/ individuals	Collection of multiple sets: (1.10, 0.70, 0.56, -0.34), (0.90, 0.54, 1.65, 0.27), (1.23, 1.65, -0.75, 1.45)
Parents: Chromosomes/ individuals participating for creating new individuals (or offsprings)	Parents: E.g. (1.10, 0.70, 0.56, -0.34), (1.23, 1.65, -0.75, 1.45)
Objective function value: Value of objective function determines if a chromosomes/ individual survives or dies	Objective function: Calculated for each set of input variables using eq. 6.2.

6.1.2 PCX operator based genetic algorithm

The genetic algorithm (GA) used in the present study is a parent centric recombination (PCX) operator based generalized generation gap (G3) model [20-22, 27-29]. The generic parent-centric recombination operator (PCX) is an elite-preserving model [27] which means it uses the best individual in the population for generating the new members. This model was chosen because it has been shown to have a faster convergence rate on standard test functions as compared to other evolutionary algorithms and classical optimization algorithms including other real-parameter GAs with the unimodal normal distribution crossover (UNDX) and the simplex crossover (SPX) operators, the correlated self-adaptive evolution strategy, the covariance matrix

adaptation evolution strategy (CMA-ES), the differential evolution technique, and the quasi-Newton method [27]. The original G3 model applied by Deb et al. [20] and Mishra and DebRoy [21, 22] for different welding applications has very high selectivity due to elitist nature of the PCX operator in which the new individuals at every iteration are created using the best parent and two randomly chosen members. The selection of best parent to generate new individuals tends to draw the whole population of solutions towards one side of the parameter space which is more closer to the best solution. This elitist nature of the algorithm to follow the best solution restricts the proper exploration of the solution space. In order to maintain diversity in the population, a modified version of the generalized generation gap (G3) model is used in this work. In this work, we have used three randomly chosen parents to create new individuals in place of best parent and two randomly chosen individuals in the original algorithm. The steps involved in the calculations are as follows:

6. A population is a collection of many individuals and each individual represents a set of randomly chosen values of the four non-dimensionalized welding variables. A parent refers to an individual in the current population. The best parent is the individual that has the best fitness, i.e., gives the minimum value of the objective function, defined by eq. 6.2, in the entire population. Three parents are chosen randomly from the population of solutions.
7. From the three randomly chosen parents, two offsprings or new individuals are generated using a recombination scheme. PCX based G3 models are known to converge rapidly when three parents and two offsprings are selected [27]. A recombination scheme is a process for creating new individuals from the parents.
8. Two new parents are randomly chosen from the current population of the individuals.
9. A subpopulation of four individuals that includes the two randomly chosen parents in step 3 and two new offsprings generated in step 2 is formed.
10. The two best solutions, i.e., the solutions having the least values of the objective function, are chosen from the subpopulation of four members created in step 4. These two individuals replace the two parents randomly chosen in step 3.
11. The calculations are repeated from step one again until convergence is achieved.

The above steps, as applied to the present problem, are shown in figure 5-2. Figure 6-1 illustrates the working of the model to find the window of welding parameters to achieve a target weld geometry. The recombination scheme (step 2) used in the present model is based on parent centric recombination (PCX) operator [20-22, 27, 28]. A brief description of this operator, as applied to the present problem is presented below:

First three parents, i.e., $(f_1^0, f_2^0, f_3^0, f_4^0)$, $(f_1^1, f_2^1, f_3^1, f_4^1)$, $(f_1^2, f_2^2, f_3^2, f_4^2)$ are randomly selected from the current population. Here the subscripts represent the four variables or the welding parameters, while the superscripts denote the parent identification number.

The mean vector or centroid, $\bar{g} = \left(\frac{f_1^0 + f_1^1 + f_1^2}{3}, \frac{f_2^0 + f_2^1 + f_2^2}{3}, \frac{f_3^0 + f_3^1 + f_3^2}{3}, \frac{f_4^0 + f_4^1 + f_4^2}{3} \right)$, of

the three chosen parents is computed. To create an offspring, one of the parents, say $\bar{x}^{(p)} = (f_1^0, f_2^0, f_3^0, f_4^0)$, is chosen randomly. The direction vector, $\bar{d}^{(p)} = \bar{x}^{(p)} - \bar{g}$ is next calculated from the selected parents to the mean vector or centroid. Thereafter, from each of the other two parents, i.e., $(f_1^1, f_2^1, f_3^1, f_4^1)$, and $(f_1^2, f_2^2, f_3^2, f_4^2)$ perpendicular distances, D_i , to the direction vector, $\bar{d}^{(p)}$, are computed and their average, \bar{D} , is found. Finally, the offspring i.e., $\bar{y} = (f_1', f_2', f_3', f_4')$, is created as follows:

$$\bar{y} = \bar{x}^{(p)} + w_\zeta \left| \bar{d}^{(p)} \right| + \sum_{i=1, i \neq p}^4 w_\eta \bar{D} \bar{h}^{(i)} \quad \mathbf{6.4}$$

where $\bar{h}^{(i)}$ are the orthonormal bases that span the subspace perpendicular to $\bar{d}^{(p)}$, and w_ζ and w_η are randomly calculated zero-mean normally distributed variables. The values of the variables that characterize the offspring, $\bar{y} = (f_1', f_2', f_3', f_4')$, are calculated as follows:

$$f_1' = f_1^0 + f_{11} + f_{12} \quad \mathbf{6.5.a}$$

$$f_2' = f_2^0 + f_{21} + f_{22} \quad \mathbf{6.5.b}$$

$$f_3' = f_3^0 + f_{31} + f_{32} \quad \mathbf{6.5.c}$$

$$f_4' = f_4^0 + f_{41} + f_{42} \quad \mathbf{6.5.d}$$

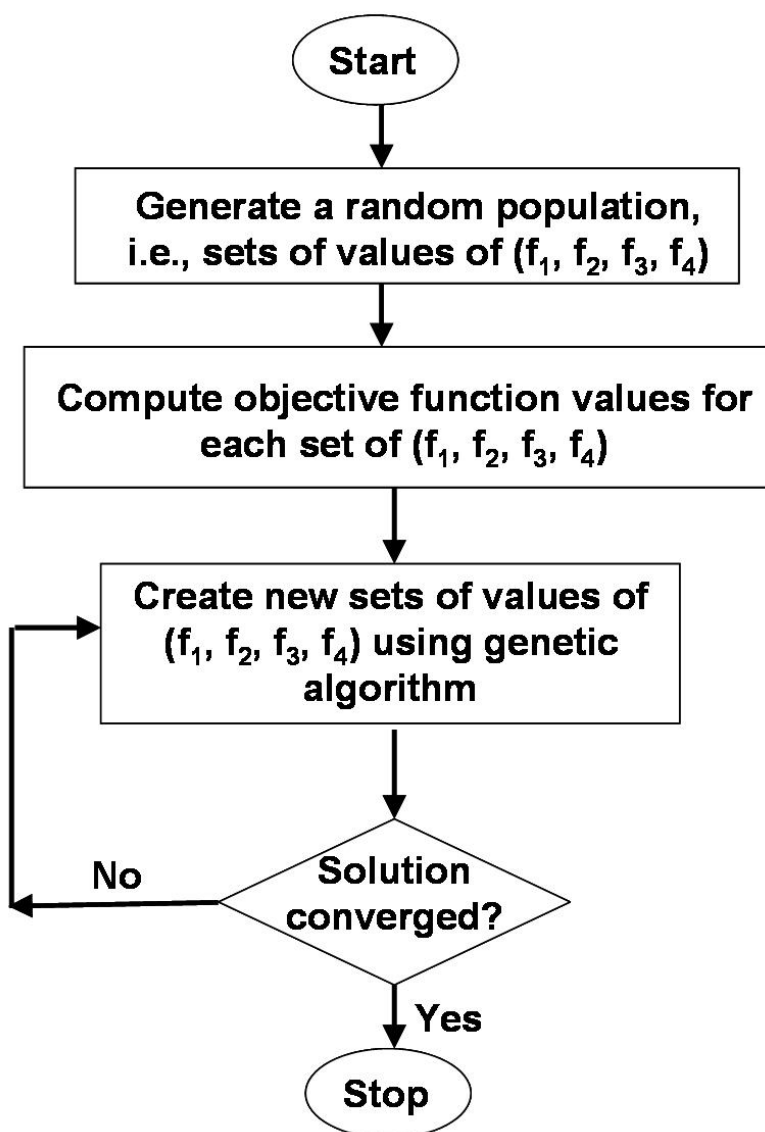


Figure 6-1: Flow chart of the proposed model after coupling of generalized generation gap (G3) genetic algorithm with neural network model.

$$f_{11} = w_{\zeta} \left(\frac{2f_1^0 - f_1^1 - f_1^2}{3} \right) \quad \mathbf{6.6.a}$$

$$f_{21} = w_{\zeta} \left(\frac{2f_2^0 - f_2^1 - f_2^2}{3} \right) \quad \mathbf{6.6.b}$$

$$f_{31} = w_{\zeta} \left(\frac{2f_3^0 - f_3^1 - f_3^2}{3} \right) \quad \mathbf{6.6.c}$$

$$f_{41} = w_{\zeta} \left(\frac{2f_4^0 - f_4^1 - f_4^2}{3} \right) \quad \mathbf{6.6.d}$$

$$f_{12} = w_{\eta} \left(\frac{a_2 + b_2}{2} \right) \left[1 - \left(\frac{2f_1^0 - f_1^1 - f_1^2}{3d} \right)^2 \right] \quad \mathbf{6.6.e}$$

$$f_{22} = w_{\eta} \left(\frac{a_2 + b_2}{2} \right) \left[1 - \left(\frac{2f_2^0 - f_2^1 - f_2^2}{3d} \right)^2 \right] \quad \mathbf{6.6.f}$$

$$f_{32} = w_{\eta} \left(\frac{a_2 + b_2}{2} \right) \left[1 - \left(\frac{2f_3^0 - f_3^1 - f_3^2}{3d} \right)^2 \right] \quad \mathbf{6.6.g}$$

$$f_{42} = w_{\eta} \left(\frac{a_2 + b_2}{2} \right) \left[1 - \left(\frac{2f_4^0 - f_4^1 - f_4^2}{3d} \right)^2 \right] \quad \mathbf{6.6.h}$$

The various unknown variables used in eqs. **6.6.a** to **6.6.h** can be represented in simplified form as follows:

$$d = \sqrt{\left(\frac{2f_1^0 - f_1^1 - f_1^2}{3} \right)^2 + \left(\frac{2f_2^0 - f_2^1 - f_2^2}{3} \right)^2 + \left(\frac{2f_3^0 - f_3^1 - f_3^2}{3} \right)^2 + \left(\frac{2f_4^0 - f_4^1 - f_4^2}{3} \right)^2} \quad \mathbf{6.7.a}$$

$$a_2 = e_1 \times \sqrt{1 - (a_1)^2} \quad \mathbf{6.7.b}$$

$$b_2 = e_2 \times \sqrt{1 - (b_1)^2} \quad \mathbf{6.7.c}$$

$$a_1 = \sum_{i=1}^{i=4} \frac{(f_i^1 - f_i^0) \left(\frac{2f_i^0 - f_i^1 - f_i^2}{3} \right)}{d \times e_1} \quad \mathbf{6.7.d}$$

$$e_1 = \sqrt{(f_1^1 - f_1^0)^2 + (f_2^1 - f_2^0)^2 + (f_3^1 - f_3^0)^2 + (f_4^1 - f_4^0)^2} \quad \mathbf{6.7.e}$$

$$b_1 = \sum_{i=1}^4 \frac{(f_i^2 - f_i^0) \left(\frac{2f_i^0 - f_i^1 - f_i^2}{3} \right)}{d \times e_2} \quad \mathbf{6.7.f}$$

$$e_2 = \sqrt{(f_1^2 - f_1^0)^2 + (f_2^2 - f_2^0)^2 + (f_3^2 - f_3^0)^2 + (f_4^2 - f_4^0)^2} \quad \mathbf{6.7.g}$$

6.2 Results and Discussion

As discussed in chapter 5, the neural network was trained and validated with results from a well tested three-dimensional numerical heat transfer and fluid flow model. A large database of outputs for different welding conditions was generated based on design of experiments (DOE) [29] to capture the correlations between the welding variables and the weld attributes. Separate feed forward neural networks were developed, one each for predicting penetration, leg-length and throat of GMA fillet weld in spray mode to achieve high accuracies in the calculation of penetration, leg-length and throat. The neural network model provided correct values of penetration, actual throat and leg-length for various combinations of welding variables I, V, U and w_f as shown in figure 6-2. The figure also shows that a given set of weld dimensions can be obtained using various alternative sets of input power, welding speed and wire feed rate. Since GA can provide a population of solutions, the neural network model must be combined with an appropriate GA to tailor weld attributes.

6.2.1 Sensitivity analysis to study the dependency of welding variables

Insight into the estimated values of welding variables can be obtained by examining the values of correlation coefficients obtained from sensitivity matrix, S , whose elements are given by:

$$S_{ij} = \frac{\partial(p^c)^k}{\partial f_i} \frac{\partial(p^c)^k}{\partial f_j} + \frac{\partial(t^c)^k}{\partial f_i} \frac{\partial(t^c)^k}{\partial f_j} + \frac{\partial(l^c)^k}{\partial f_i} \frac{\partial(l^c)^k}{\partial f_j} \quad \mathbf{6.8}$$

for $i, j = 1$ to 4 (i.e. number of welding variables)

The coefficients of correlation matrix, C , are then computed from the sensitivity matrix, using the following relation:

$$C_{ij} = \frac{S_{ij}}{\sqrt{S_{ii}S_{jj}}} \quad 6.9$$

The C_{ij} represents the correlation coefficient between the i^{th} and j^{th} variables. The values of correlation coefficients are listed in table 6-2. When an off-diagonal element of correlation matrix, C (i.e. C_{ij} where $i \neq j$) is close to ± 1 , then the matrix is called ill-conditioned which leads to larger confidence intervals (or large standard deviations in the values of the estimated parameters). In such cases, the estimated values of uncertain parameters are linearly dependent and may be expressed in terms of each other, which means that the parameters have similar influence on the objective function. By examining the correlation coefficients, it can be concluded that the estimated values of the welding variables are correlated. These correlation coefficients indicate a large correlation (C_{21}) between arc current (I) and voltage (V) while welding speed and wire feed rate have very low correlations with I and V as indicated by the values of C_{31} , C_{41} , C_{32} and C_{42} . However, the welding speed and wire feed rate are strongly correlated to each other as shown by the coefficient C_{43} in table 6-2. A positive value of the correlation coefficient between two variables signify similar trend on the output variable and means that the increase in one variable will be compensated by reduction in the value of other variable.

Table 6-2: The coefficients of correlation matrix obtained using eqs. 6.8 and 6.9. The magnitude and the sign of the coefficients provide information about the inter-dependency of the estimated welding variables values.

j i		1	2	3	4
		Arc current	Arc voltage	Welding speed	Wire feed rate
1	Arc current	1.00	0.94	-0.55	0.23
2	Arc voltage	0.94	1.00	-0.44	0.24
3	Welding speed	-0.55	-0.44	1.00	-0.89
4	Wire feed rate	0.23	0.24	-0.89	1.00

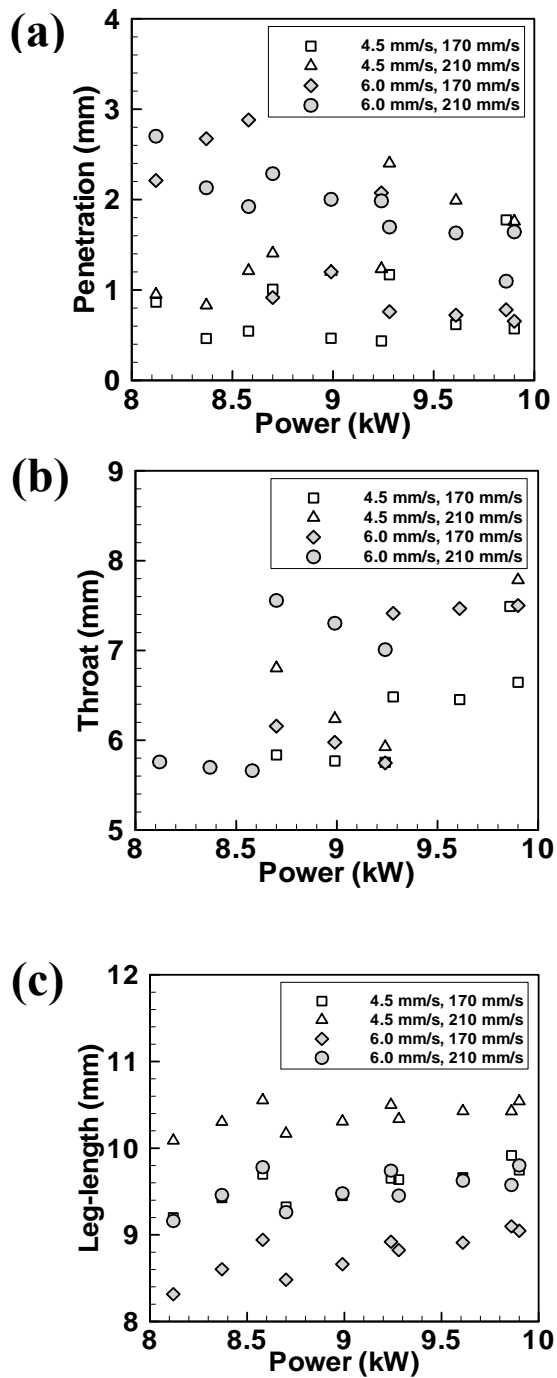


Figure 6-2: Weld bead geometric parameters as a function of input power: (a) penetration, (b) throat, and (c) leg-length. The values indicated in the legends represent the welding speed and wire feed rate, respectively.

6.2.2 Combinations of welding variables obtained by using bi-directional model to achieve desired weld geometry

The model was tested by finding different sets of welding variables i.e. arc current, voltage, welding speed and wire feed rate, which could provide a specified weld geometry. The computational task involved following three steps.

- (1) Initially, a target weld geometry was specified by prescribing the values of penetration, throat and leg-length.
- (2) Then, the model was run to obtain multiple combinations of arc current, voltage, welding speed and wire feed rate, each of which could produce the specified target weld geometry.
- (3) Finally, the results obtained from the model were verified. These three steps are explained in detail in the next section.

To start the calculation, a target geometry was specified by prescribing three weld dimensions, i.e., penetration, throat and leg-length. To test the model, these three weld dimensions from an actual welding experiment were specified as a target geometry. If the model works correctly, the various combinations of welding variables obtained from the model must include a set of welding variables that are fairly close to the set of variables used in the experiment. It should be noted that the ability of the model to produce this solution is only a necessary, but not sufficient, component of the model verification. Since the model produced multiple combinations of welding variables, other combinations obtained from the model had to be verified by comparing the calculated weld geometry with the target experimentally obtained geometry.

In the next step (i.e. second step), a population of 200 individuals was defined to start the operation of GA. Each individual in the population defined a set of randomly chosen welding variables such as current (I), voltage (V), welding speed (U) and wire feed rate (w_f). Figure 6-3(a) depicts the initial values of the individuals, i.e., sets of I, V, U and w_f of each individual solution with I and V plotted as their product in the form of input arc power. Values of the welding variables I, V, U and w_f were chosen randomly in the range of 250A-400A, 27-35 V, 3.5-7.0 mm/s and 150-250 mm/s, respectively. These ranges of welding variables cover all the combinations of welding variables used during

GMA welding in spray mode. The values of the welding variables in such large ranges also helped in maintaining diversity in the solutions. These welding variable sets were then improved iteratively using a combination of GA and the neural network. With the progress in the calculations, the average objective function values decreased with iterations. An individual with a low objective function indicates correct combinations of current, voltage, welding speed, and wire feed rate that can result in the target weld geometry. Figure **6-3(b)** shows the computed values of the objective functions for all the individuals depicted in figure **6-3(a)**. This figure shows that for many sets of welding variables, the values of the objective function, $O(f)$, were fairly low. The low value of the objective function for all of these combinations indicates that each of these welding variable sets could produce a weld geometry that would be close to the target geometry.

Figure **6-4** shows that the objective function decreased rapidly with iterations for the best individual compared to the average value of the objective function of the whole population. This behavior is consistent with the fact that as GA tries to explore the solution space, it produces new sets of welding parameters that may have high values of objective function. Figure **6-5(a)** indicates several individuals with objective function values lower than 0.01 corresponding to the 1000th generation or iteration. With the increase in number of iterations the diversity of population decreases and the solution starts crowding in different regions. Figures **6-5(b)** and **6-5(c)** show the individual solutions with objective function values less than 1×10^{-4} and 1×10^{-5} at generations 3000 and 6000, respectively. The calculation is continued until 5 % individuals in the population have the value of objective function less than 1.0×10^{-6} . The chosen value of the objective function (fitness) ensured sufficient accuracy within the practical limits of the experimental errors. The calculated combinations of the welding variables are presented in table **6-3**. The calculations required less than one minute in a PC with 3.2 GHz Intel P4 CPU and 1024 Mb PC2700 DDR-SDRAM memory. It is useful to recall that several days of computational time was required on multiple processors by an earlier model developed by Kumar and DebRoy [20] that used a numerical heat transfer and fluid flow model. This time saved by using a neural network justifies its use as a forward model in place of a heat transfer and fluid flow model.

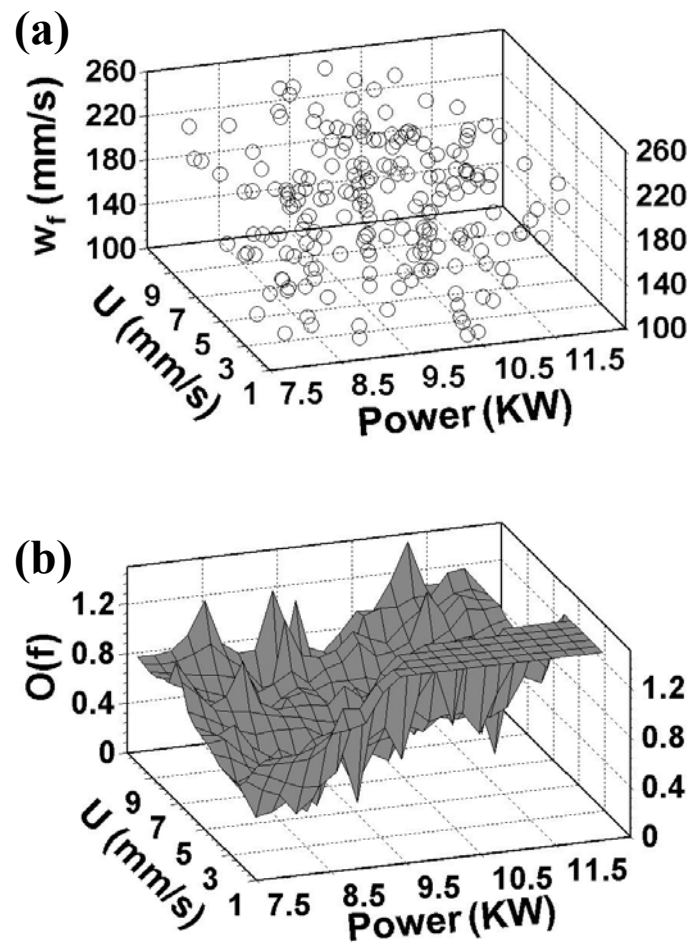


Figure 6-3: Initial values of individual welding variable sets and their objective functions. (a) A large space of variables was searched to find optimum solutions as shown by two hundred randomly selected initial welding variable sets. (b) The low values of the objective functions of several individuals in the initial population indicate the possibility of existence of multiple optimal solutions.

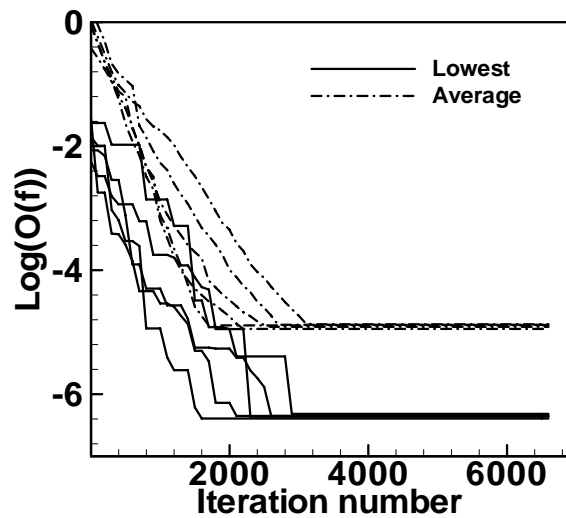


Figure 6-4: Variation of the minimum value and the average value of the objective function in whole population with iterations for 5 different randomly selected initial populations. The low value of the objective function shows that the converged solution is independent on initial selection of values of individuals in the population.

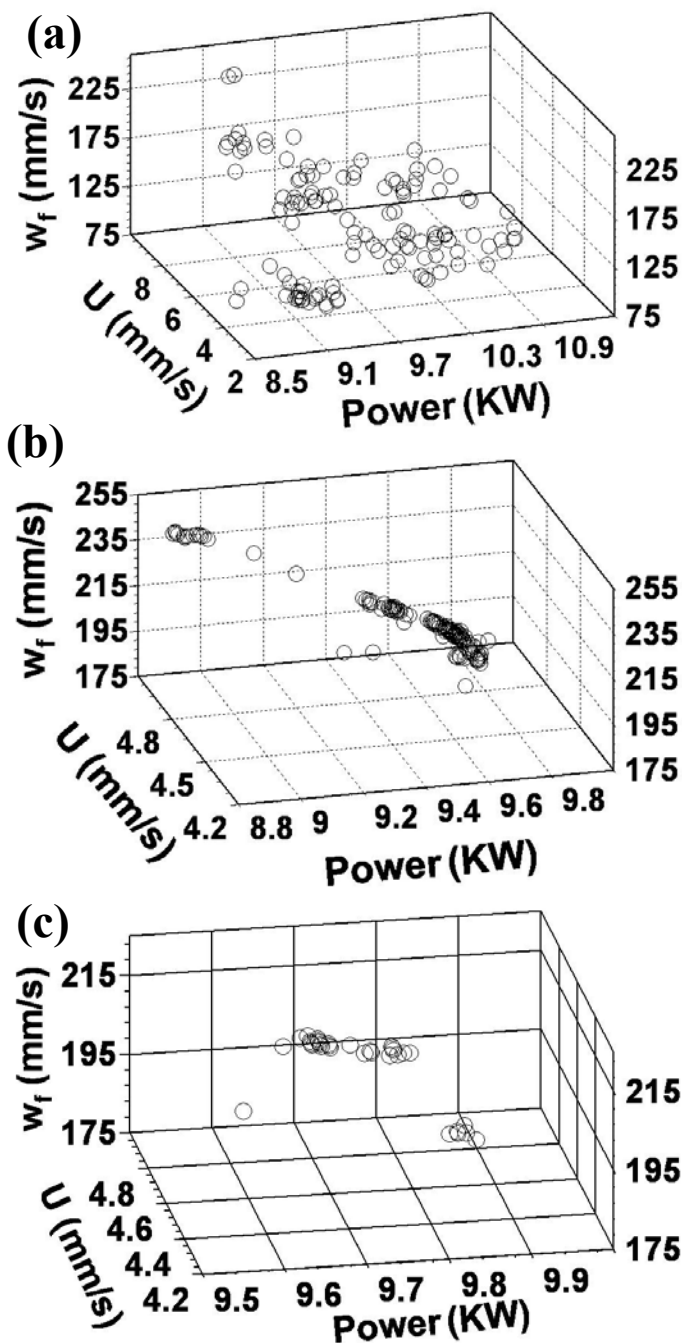


Figure 6-5: Several fairly diverse welding variable sets could produce low values of the objective function indicating the existence of alternate paths to obtain the target weld geometry. The plots show the welding variable sets that produced low values of the objective function, $O(f)$ with iterations. (a) individuals after 1000 iterations with $O(f)$ less than 1×10^{-2} , (b) individuals after 3000 iterations with $O(f)$ less than 1×10^{-4} , and (c) individuals after 6000 iterations with $O(f)$ less than 1×10^{-5} .

The third step involved verification of the obtained combinations of welding variables. Since the target geometry was produced by conducting an experiment, an initial test is to check if the multiple sets of welding variables produced by the model include a set of welding variables that is very close to, if not same as, that used to produce the weld. Solution (a) in table 6-3 involves welding parameters that are very close, within less than 1%, to those used to produce the experimental weld. This table also includes values of other variable sets, i.e., current, voltage, welding speed and wire feed rate, computed by the model to produce the desired values of leg length, penetration and throat. Each solution, i.e., a set of current, voltage, welding speed and wire feed rate was used to calculate weld geometric parameters.

Table 6-3: The various combinations of welding parameters, i.e., arc current (I), arc voltage (V), welding speed (U) and wire feed rate (w_f) obtained using neural network model to achieve the following target weld dimensions: penetration = 1.6 mm, leg-length = 10.5 mm and throat = 7.2 mm. The target weld geometry was obtained experimentally using the following welding variables: I = 286.8 A, V= 33.0 V, U = 4.2 mm/s and w_f = 169.3 mm/s.

Individual Solutions	I (Amp)	V (Volt)	U (mm/s)	w_f (mm/s)	Penetration (mm)	Leg-length (mm)	Throat (mm)
(a)	285.1	33.1	4.2	172.4	1.7	10.5	7.2
(b)	293.3	32.6	4.3	211.0	1.6	10.6	7.1
(c)	298.3	31.3	4.5	216.2	1.6	10.5	7.2
(d)	290.8	33.5	4.6	210.0	1.6	10.5	7.2
(e)	324.7	29.5	5.2	231.0	1.5	10.3	7.4
(f)	303.3	30.6	4.6	210.5	1.6	10.3	7.3
(g)	294.1	31.4	4.9	227.0	1.6	10.5	7.2
(h)	294.7	31.0	5.0	231.0	1.6	10.5	7.2

The accuracy of these individual solutions was examined by calculating weld geometry for each welding variable sets (a) through (h) in table 6-3 and comparing the computed weld dimensions with that obtained experimentally. The comparison, shown in figures 6-6(a) through 6-6(h) between the computed and the experimental weld

dimensions show that the individual welding variable sets resulted in correct predictions of the weld shape and size as measured by penetration, throat and leg-length in each case. Figure 6-6 and table 6-3 show that for each set of computed welding conditions, the corresponding geometric parameters agreed well with the desired experimentally obtained weld geometry.

A similar exercise was also undertaken where a hypothetical weld geometry represented by a leg length of 12 mm, penetration of 3.7 mm and throat of 10 mm was produced by a 301.6A current, 34.6 V voltage, 3.4 mm/s welding speed and 228.6 mm/s wire feed rate. Table 6-4 lists all other combinations of welding variables i.e. solutions (b) to (g) that can also produce this geometry. The values of the welding variables differ considerably from each other. For example, the current and the welding speed vary among solutions by 33% and 100 %, respectively. All these differences in the important welding variables indicate significant diversity in the paths, all of which lead to the same set of target weld dimensions. Furthermore, different combinations of welding variables listed in tables 6-3 and 6-4 suggest that the variation in welding conditions also depend on the specified weld geometry due to non-linear behavior of various welding variables.

Table 6-4: The various combinations of welding parameters, i.e., arc current (I), arc voltage (V), welding speed (U) and wire feed rate (w_f) obtained using neural network model to achieve the following target weld dimensions: penetration = 3.7 mm, leg-length = 12.0 mm and throat = 10.0 mm. The target weld geometry was obtained using the welding conditions listed in (a).

Individual Solutions	I (Amp)	V (Volt)	U (mm/s)	w_f (mm/s)	Penetration (mm)	Leg-length (mm)	Throat (mm)
(a)	301.6	34.6	3.4	228.6	3.7	12.0	10.0
(b)	306.2	34.6	3.6	236.6	3.7	12.0	10.0
(c)	300.3	34.6	3.3	225.9	3.7	12.0	10.0
(d)	311.0	35.3	4.5	270.8	3.7	12.0	10.0
(e)	417.5	37.5	6.7	234.0	3.6	10.6	10.1
(f)	290.8	35.4	4.1	260.2	3.7	12.0	10.0
(g)	314.1	33.5	3.8	239.0	3.7	11.83	10.0

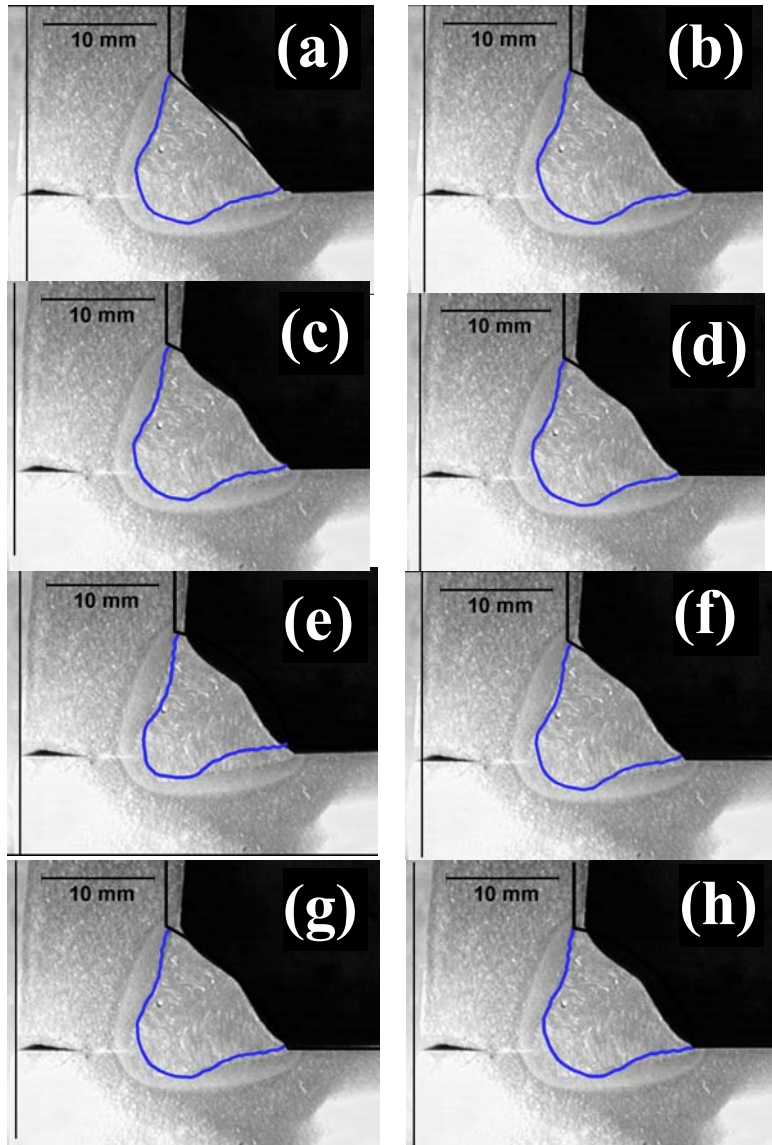


Figure 6-6: Comparisons between the calculated and the desired weld bead geometry for different optimum combinations of welding parameters. The results show that a target geometry can be obtained via multiple paths. The blue line represents the calculated weld pool boundary.

The rapid computational methodology involving a neural network and a genetic algorithm described here enables realistic tailoring of GMA fillet weld geometry. The model computes practical choices of alternative paths involving multiple combinations of welding variables to achieve a desired weld geometry in less than a minute in a commonly available PC. It is hoped that the methodology will serve as basis for formulating, testing and implementing realistic computational tools for tailoring weld attributes to achieve defect free, structurally sound, and reliable welds.

6.3 Summary and Conclusions

Unlike conventional heat transfer and fluid flow models that can predict weld geometry for a particular set of welding conditions, a new model has been developed that can calculate alternative welding conditions needed to obtain a target weld geometry. The model developed is significantly different from traditional reverse models that provide only one set of welding conditions necessary for obtaining a target weld geometry. In reality, a particular weld geometry can be obtained by using various combinations of welding variables and the new model can calculate these alternative pathways. The model combines a neural network model of heat and fluid flow with a real number based genetic algorithm to calculate alternative welding conditions needed to obtain a target weld geometry for GMA fillet welding. The use of a neural network model in place of a heat transfer and fluid flow model significantly increased computational efficiency and provided multiple solutions within one minute in a commonly available computer.

The model was used to determine multiple sets of welding variables, i.e., combinations of welding current, voltage, speed and wire feeding rate to obtain a specified weld pool geometry. It was found that a specific weld geometry was attainable via multiple pathways involving various sets of welding variables. Furthermore, these sets of welding variables involved significantly different values of current, voltage, welding speed and wire feed rate. Good agreement between the model predictions and the experimental data of leg length, penetration and throat for various welding conditions

show that this approach is promising for practical shop floor applications to achieve the desired weld joint by different paths. The different combinations of welding variables provides the flexibility to the engineers to select the best optimal set of welding conditions based on the machine set up and the cost analysis. The cost analysis will involve the consideration of input power cost, price of wire feed material, labor charges and other surcharges to select the best combination of welding variable with low manufacturing cost. Although the work reported here focuses on tailoring weld geometry, the results provide hope that science based tailoring of structure and properties of weldments may also become attainable in the future.

6.4 References

1. S. A. David and T. DebRoy, *Science* **257**, 497 (1992).
2. T. DebRoy and S. A. David, *Rev. Mod. Phys.* **67** (1), 85 (1995).
3. A. Kumar and T. DebRoy, *J. of Appl. Phys.* **94** (2), 1267 (2003).
4. W. Zhang, J. W. Elmer and T. DebRoy, *Scrip. Mater.* **46**(10), 753 (2002).
5. S. Mishra and T. DebRoy *J. Phys. D: Appl. Phys.* **37**, 2191 (2004).
6. S. Mishra and T. DebRoy, *Acta Mater.* **52**(5), 1183 (2003).
7. T. Hong and T. DebRoy, *Metallurgical and Materials Transactions B* **34**, 267 (2003).
8. A. De and T. DebRoy, *J. Appl. Phys.* **95**(9), 5230 (2004).
9. A. De and T. DebRoy, *J. Phys. D: Appl. Phys.* **37**, 140 (2004).
10. A. De and T. DebRoy *Welding J.* **84** (7), 101 (2005).
11. C. H. Kim, W. Zhang and T. DebRoy, *J. Appl. Phys.* **94**, 2667 (2003).
12. W. Zhang, C. H. Kim and T. DebRoy, *J. Appl. Phys.* **95**, 5210 (2004).
13. W. Zhang, C. H. Kim and T. DebRoy, *J. Appl. Phys.* **95**, 5220 (2004).
14. X. He, P. Fuerschbach and T. DebRoy, *J. Appl. Phys.* **96**(8), 4547 (2004).
15. X. He, P. Fuerschbach and T. DebRoy, *J. Phys. D: Appl. Phys.* **36**, 1388 (2004).
16. H. Zhao and T. DebRoy, *J. Appl. Phys.* **93**(12), 10089 (2003).

17. P. Michaleris and A. DeBiccari, *Welding J.* **76**(4), 172 (1997).
18. O. A. Vanli and P. Michaleris, *J. Ship Prod.* **17**, 226 (2001)
19. L. E. Lindgren, *J. Therm. Stresses* **24**, 141 (2001).
20. A. Kumar and T. DebRoy, *Metall. and Mat. Trans. A*, **36A**, 2725 (2005).
21. S. Mishra and T. DebRoy, *J. Phys. D: Appl. Phys.* **38**, 2977 (2005).
22. S. Mishra and T. DebRoy, *J. Appl. Phys.* **98**, article no.: 044902 (2005).
23. P. W. Fuerschbach and G. R. Eisler, *Sci. Tech. Weld. Joining* **7**(4), 241 (2002).
24. H. B. Smartt and C. J. Einerson, *Welding J.* **72** (5), 217 (1993).
25. D. E. Goldberg, *Genetic Algorithm in Search, Optimization and Machine Learning*, Addison-Wesley, MA (1989).
26. K. Deb, *Multi-objective optimization using evolutionary algorithms*, Wiley, New York (2001).
27. K. Deb, A. Anand and D. Joshi, *Evolut. Comp.* **10**, 371 (2002).
28. A. Kumar, S. Mishra, J. W. Elmer and T. DebRoy, *Metall. Mat. Trans. A* **36**, 15 (2005).
29. A. Kumar and T. DebRoy, *Sci. Tech. Weld. Joining* **11**, 106 (2006).
30. J. M. Vitek, Y. S. Iskander and E. M. Oblow, *Welding J.* **79** (2), 33 (2000).
31. H. K. D. H. Bhadeshia *ISIJ International* **39** (10): 966 (1999).
32. S. Haykin, *Neural Network: A Comprehensive foundation*, Prentice Hall Pub., NJ (199).
33. T. Masters, *Practical neural network recipes in C++*, Academic Press, Boston (1993).
34. M. T. Hagan, *Neural Network Design*, PWS Pub., Boston (1996).

Chapter 7

A UNIFIED MODEL TO PREVENT HUMPING DEFECTS IN GAS TUNGSTEN ARC WELDING

Productivity enhancement in the manufacturing of fabricated parts is often achieved by increasing welding speed and power. During arc welding, a continuous increase in the welding speed and current often results in a weld defect with bead-like appearance known as humping [1-9]. Various experimental investigations have been undertaken to understand and prevent humping. In addition, several theoretical models were proposed based on capillary instability [1, 6], force balance and scaling analysis [7-9]. The previous work on humping can be classified into three groups. First, efforts have been made to experimentally determine the onset of humping [2, 3] during gas tungsten arc (GTA) welding. These results have provided improved understanding of the effects of various variables on humping. Second, some of the previous modeling work [1, 6] used Rayleigh's theory of instability of liquid metal cylinders to understand humping during welding. These efforts ignored important physical processes such as arc shear force on the weld pool surface, gravity effect and surface tension of the liquid metal and, therefore, the results are preliminary. Finally, force balance [7-9] and non-dimensional scaling analysis [8, 9] were used to calculate conditions for humping. The non-dimensional parameter based calculations are accurate only within an order of magnitude. They are not designed to explain the effects of all important welding variables and cannot precisely calculate the onset of humping. No comprehensive unified theoretical model exists today that can predict the formation of humping defects considering the effects of important welding variables such as the arc current, voltage, welding speed, nature of the shielding gas, electrode geometry, torch angle and ambient pressure.

During GTA welding, a surface wave forms owing to the flow of shielding gas on the weld pool surface driven by a balance between molten metal's inertia, surface tension and gravity forces [10-12]. The elevation and the velocity of the wave depend on various

parameters such as the surface tension of liquid metal, densities of liquid metal and shielding gas, weld pool size and the relative velocity between the shielding gas and the liquid metal. Any phenomenological model for understanding humping must take into account the effects of all the welding variables on the stability of the surface waves. An unstable surface wave can carry packets of liquid metals toward the solidifying region of the weld pool and contribute to humping.

In this thesis work, a comprehensive mathematical model was developed and tested extensively to quantitatively understand the welding conditions that result in humping defects. The model is based on Kelvin-Helmholtz hydrodynamic instability [10-12] of waves on the surface of the weld pool. The model predicts humping when the elevation of the surface wave increases with time. Since the original Kelvin-Helmholtz model uses semi-infinite thickness of both the layers, a modified version is used here to take into account the finite depths of weld pools and specific thicknesses of the shielding gas layer depending on welding conditions. The velocity of surface wave was determined by solving the potential flow equations with appropriate boundary conditions. The model indicates that the velocity of the surface wave is affected by the surface tension of the liquid metal, densities of liquid metal and shielding gas, weld pool size and the velocities of plasma and liquid metal on the weld pool surface. The weld pool size and liquid metal velocity were calculated by solving the equations of conservation of mass, momentum and energy in three dimensions with appropriate boundary conditions [13-21]. The shielding gas velocity was calculated from an analytical relation of jet flow over a flat surface [22]. The computed results indicate how the values of arc current, welding speed, electrode tip angle, electrode type, nature of the shielding gas, ambient pressure, inclination of the torch and the external magnetic field affect humping formation in GTA steel welds. The computed welding conditions for the formation of humping were compared with the corresponding independent experimental results available in the literature for various GTA welding conditions. Recommendations are made to prevent humping under extreme welding conditions when high welding speed and current are needed to sustain productivity goals.

7.1 Mathematical Model

7.1.1 Humping model based on Kelvin-Helmholtz hydrodynamic instability

The following simplifying assumptions are made.

(a) The motion of the surface waves along the direction of welding is considered in the model.

(b) The liquid is assumed to be incompressible and inviscous for the calculation of the surface wave velocity for simplicity.

(c) The shielding gas flow is assumed to be steady and specified by a constant horizontal velocity.

On the weld pool surface, the wave propagation is represented by the following wave equation:

$$\frac{\partial^2 \eta}{\partial x^2} = \frac{1}{c^2} \frac{\partial^2 \eta}{\partial t^2} \quad 7.1$$

where η is local elevation that depends on position along welding direction, x and time, t , and c is the velocity of the wave opposite to the welding direction x . The general solution of wave equation (i.e. eq. 7.1) is given by the following expression [10]:

$$\eta = ae^{ik(x-ct)} \quad 7.2$$

where a is the amplitude and k is the wave number. The wave speed, c , can be expressed in general form as follows:

$$c = \alpha + i\beta \quad 7.3$$

where α and β are the real and the imaginary parts of the wave speed, respectively. After substituting the expression for c in eq. 7.2, we get:

$$\eta = ae^{ik(x-\{\alpha+i\beta\}t)} = ae^{ik(x-\alpha t)}e^{-k\beta t} \quad 7.4$$

Eq. 7.4 shows that if β , is positive, the value of elevation, η , will increase with time and the interface between the liquid metal and shielding gas will become unstable. It should be noted that η cannot be determined from eq. 7.4 unless the values of α and β that characterize the wave velocity are known. In order to determine the stability of the surface wave, its velocity given by eq. 7.3 needs to be calculated. This task is accomplished by solving the velocity potentials in the gas and the liquid phases from the following two Laplace equations [10-12]:

$$\frac{\partial^2 \Phi_l}{\partial x^2} + \frac{\partial^2 \Phi_l}{\partial z^2} = 0 \quad 7.5.a$$

$$\frac{\partial^2 \Phi_g}{\partial x^2} + \frac{\partial^2 \Phi_g}{\partial z^2} = 0 \quad 7.5.b$$

where x is the direction opposite to the welding direction, z is the vertical direction, and Φ_l and Φ_g are the velocity potentials in the liquid metal and shielding gas, respectively. These velocity potentials (i.e. Φ_l and Φ_g) are the functions of wave speed, c , and need to be calculated using appropriate boundary conditions. It should be noted that we need four sets of boundary conditions in each layer to solve the velocity potentials defined by equations Eqs 7.5.a and 7.5.b. The first set of boundary conditions can be written using the known velocities of the liquid metal (U_l) and shielding gas (U_g) as follows:

$$\frac{\partial \Phi_l}{\partial x} = U_l \quad 7.6.a$$

$$\frac{\partial \Phi_g}{\partial x} = U_g \quad 7.6.b$$

The liquid metal velocity, U_l , was calculated from three-dimensional heat transfer and fluid flow calculations while the shielding gas velocity, U_g , was calculated using the analytical expressions as explained in the next section. The velocities of the liquid and gas at the surface depend on the location on the surface. The calculations were performed with maximum velocities on the weld pool surface to ensure consideration of the location most susceptible to humping. The second set of boundary conditions can be written by linking the velocity potentials with the local elevation position function through the following expression [10-12]:

$$\frac{D\eta}{Dt} = \left(\frac{\partial \Phi_l}{\partial z} \right)_{z=\eta} = \left(\frac{\partial \Phi_g}{\partial z} \right)_{z=\eta} \quad 7.7$$

where $\frac{D}{Dt} = \frac{\partial}{\partial t} + U \frac{\partial}{\partial x}$. Eq. 7.7 represents the fact that the substantial derivative of the surface position function of the wave, η , is equal to the normal velocity of the fluids at the interface since the fluid particles at the interface move with the surface wave. After expanding $\left(\frac{\partial \Phi_l}{\partial z} \right)_{z=\eta}$ and $\left(\frac{\partial \Phi_g}{\partial z} \right)_{z=\eta}$ using Taylor's theorem and neglecting the higher order terms, the following expressions are obtained for both the liquid and gas layers [10-12]:

$$\frac{\partial \eta}{\partial t} + U_l \frac{\partial \eta}{\partial x} = \left(\frac{\partial \Phi_l}{\partial z} \right)_{z=0} \quad 7.8.a$$

$$\frac{\partial \eta}{\partial t} + U_g \frac{\partial \eta}{\partial x} = \left(\frac{\partial \Phi_g}{\partial z} \right)_{z=0} \quad 7.8.b$$

where $z = 0$ is the interface between the shielding gas layer and liquid metal as shown in figure 7-1. The first and second terms on the left hand side in eqs. 7.8.a and 7.8.b represent the local rate of change in elevation of surface wave at a given point and convective term due to change in η as a result of flow of the fluids. The third set of boundary conditions is written based on the assumption made earlier that there is no net flow across the shielding gas and liquid metal layer along the vertical direction as follows:

$$\left(\frac{\partial \Phi_l}{\partial z} \right)_{z=-h_l} = 0 \quad 7.9.a$$

$$\left(\frac{\partial \Phi_g}{\partial z} \right)_{z=h_g} = 0 \quad 7.9.b$$

where h_l is the depth of the weld pool and h_g is the height of the shielding gas layer as shown in figure 7-1.

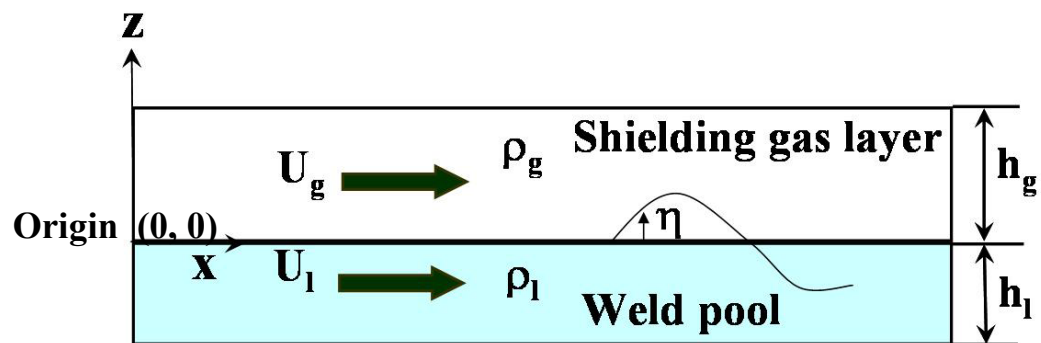


Figure 7-1: The waves generated at the interface of shielding gas layer and liquid metal in the weld pool due to shear across the interface.

The fourth and the final set of boundary conditions is written based on pressure and energy balance using the unsteady Bernoulli's theorem to keep the pressure continuous at the interface. These boundary conditions in each layer are [10-12]:

$$P_1 + \rho_1 \left[\frac{\partial \Phi_1}{\partial t} + \frac{1}{2} \left\{ \left(\frac{\partial \Phi_1}{\partial x} \right)^2 + \left(\frac{\partial \Phi_1}{\partial z} \right)^2 \right\} + g\eta \right] = \text{constant} \quad \mathbf{7.10.a}$$

$$P_g + \rho_g \left[\frac{\partial \Phi_g}{\partial t} + \frac{1}{2} \left\{ \left(\frac{\partial \Phi_g}{\partial x} \right)^2 + \left(\frac{\partial \Phi_g}{\partial z} \right)^2 \right\} + g\eta \right] = \text{constant} \quad \mathbf{7.10.b}$$

where ρ_1 and ρ_g are the densities of liquid metal and shielding gas, respectively, P_1 and P_g are the pressures in lower liquid and upper gaseous layers, respectively and g is the acceleration due to gravity. The first, second, third and the fourth terms on the left hand side of eqs. **7.10.a** and **7.10.b** represent the pressure, unsteady velocity potential, kinetic energy and potential energy terms, respectively [10]. The effect of surface tension was calculated by considering a force balance on the free liquid pool surface as shown in figure 7-2. The pressure difference along the interface was calculated by considering the force balance in a direction perpendicular to arc segment PQ of length ds shown in figure 7-2, as follows [10-12]:

$$-P_g ds + P_1 ds + \gamma d\theta = 0 \quad \mathbf{7.11}$$

where γ is the surface tension of the liquid metal in the weld pool and $d\theta$ is included angle between the tangential forces acting on arc segment PQ. Furthermore, the pressure difference is related to the radius of curvature, r , by following relation [10-12]:

$$P_g - P_1 = \gamma \frac{d\theta}{ds} = \frac{\gamma}{r} \quad \mathbf{7.12}$$

The curvature $1/r$ of surface wave profile, η is given by [10-12]:

$$\frac{1}{r} = \frac{\partial^2 \eta / \partial x^2}{\left[1 + (\partial \eta / \partial x)^2 \right]^{3/2}} \approx \frac{\partial^2 \eta}{\partial x^2} \quad \mathbf{7.13}$$

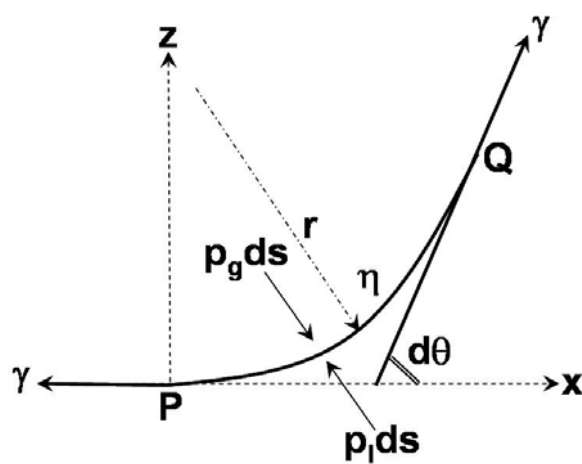


Figure 7-2: Segment of a free surface under the action of surface tension.

Eq. 7.13 is valid for small slopes and can be substituted in eq. 7.12 to obtain the following equation:

$$P_g - P_l = \gamma \frac{\partial^2 \eta}{\partial x^2} \quad 7.14$$

After subtracting eq. 7.10.a from eq. 7.10.b and neglecting the non-linear velocity terms, for small amplitude waves, we get:

$$P_g - P_l + \rho_g \left[\frac{\partial \Phi_g}{\partial t} + g\eta \right] - \rho_l \left[\frac{\partial \Phi_l}{\partial t} + g\eta \right] = 0 \quad 7.15$$

After substituting the value of pressure difference at the interface (i.e. eq. 7.12) in the above expression, we get:

$$\gamma \frac{\partial^2 \eta}{\partial x^2} + \rho_g \left[\frac{\partial \Phi_g}{\partial t} + g\eta \right] - \rho_l \left[\frac{\partial \Phi_l}{\partial t} + g\eta \right] = 0 \quad 7.16$$

For the lower liquid metal layer and the upper gaseous layers, the velocity potentials, Φ_l and Φ_g , which satisfy the eqs. 7.5.a, 7.5.b, 7.6.a, 7.6.b, 7.9.a and 7.9.b can be written as:

$$\Phi_l = U_l x + B_1 e^{ik(x-ct)} c \cosh[k(z+h_l)] \quad 7.17.a$$

$$\Phi_g = U_g x + B_2 e^{ik(x-ct)} c \cosh[k(z-h_g)] \quad 7.17.b$$

where, B_1 and B_2 are constants whose value will be calculated based on the remaining boundary conditions given by eqs. 7.8.a, 7.8.b, and 7.16. After substituting the values of velocity potentials, Φ_l , Φ_g and η from eqs. 7.17.a, 7.17.b, and 7.2, in eq. 7.8.a and 7.8.b, and rearranging the terms, we get [10, 12]:

$$B_1 = -\frac{iak(c - U_l) \cos ec(h_l k)}{k} \quad 7.18.a$$

$$B_2 = \frac{ika(c - U_g) \cos ec(h_g k)}{k} \quad 7.18.b$$

After substituting the values of Φ_l , Φ_g and η in eq. 7.16, we get:

$$e^{ik(x-ct)}\gamma ak^2 - \rho_1 \left(iB_1 ce^{ik(x-ct)}k \cosh(k(h_1 + z)) - iB_1 e^{ik(x-ct)}kU_1 \cosh(k(h_1 + z)) - e^{ik(x-ct)}ga \right) + \rho_g \left(iB_2 ce^{ik(x-ct)}k \cosh(k(z - h_g)) - iB_2 e^{ik(x-ct)}kU_g \cosh(k(z - h_g)) - e^{ik(x-ct)}ga \right) = 0 \quad 7.19$$

Dividing eq. 7.19 by the term $e^{ik(x-ct)}$ and putting $z = 0$ at the interface, we get:

$$\gamma ak^2 - \rho_1 \left(iB_1 ck \cosh(kh_1) - iB_1 kU_1 \cosh(kh_1) - ga \right) + \rho_g \left(iB_2 ck \cosh(kh_g) - iB_2 kU_g \cosh(kh_g) - ga \right) = 0 \quad 7.20$$

Substituting the values of B_1 and B_2 in eq. 7.20 and rearranging the terms:

$$-ka \left(\rho_1 \coth(h_1 k) + \rho_g \coth(h_g k) \right) c^2 + 2ka \left(U_1 \rho_1 \coth(h_1 k) + U_g \rho_g \coth(h_g k) \right) c + \gamma ak^2 + ga(\rho_1 - \rho_g) - ka \left(U_1^2 \rho_1 \coth(h_1 k) + U_g^2 \rho_g \coth(h_g k) \right) = 0 \quad 7.21$$

After canceling the amplitude 'a' from all the terms in eq. 7.21, we get following relation for wave speed.

$$k\rho_1 (U_1 - c)^2 \coth(h_1 k) + k\rho_g (U_g - c)^2 \coth(h_g k) = \gamma k^2 + g(\rho_1 - \rho_g) \quad 7.22$$

The eq. 7.22 describes the dependency of various variables on surface wave velocity. Eq. 7.22 provides the velocity of surface wave traveling opposite to the welding direction. which is given by:

$$c = \alpha + i\beta = \frac{-B + \sqrt{B^2 - 4AC}}{2A} \quad 7.23.a$$

where,

$$A = -k \left(\rho_1 \coth(h_1 k) + \rho_g \coth(h_g k) \right) \quad 7.23.b$$

$$B = 2k \left(U_1 \rho_1 \coth(h_1 k) + U_g \rho_g \coth(h_g k) \right) \quad 7.23.c$$

$$C = \gamma k^2 + g(\rho_1 - \rho_g) - k \left(U_1^2 \rho_1 \coth(h_1 k) + U_g^2 \rho_g \coth(h_g k) \right) \quad 7.23.d$$

A three-dimensional heat transfer and fluid flow model described in next section was used to calculate the length, L_p , the depth, h_1 , and the surface velocity, U_1 , of the weld pool. The wave number, k , is $2\pi/L$ where L is the length scale which is taken as the length of the weld pool, L_p :

$$k = \frac{2\pi}{L_p} \quad 7.24$$

Eq. 7.23.a shows that the velocity of the wave can be real or complex depending on the value of term $(B^2 - 4AC)$. If this term is negative, and consequently, β is positive, the instability will grow in the weld pool because value of elevation, η , will increase with time as indicated in eq. 7.4.

7.1.2 Three-dimensional heat transfer and fluid flow model

The equations of conservation of mass, momentum and energy are solved numerically in three-dimensional Cartesian coordinate system [13-21]. The governing equations are discretized using the control volume approach based on the power law scheme [23]. At each time step, the discretized equations are solved using the widely used SIMPLE algorithm [23]. Fine non-uniform grids with finer grid spacing near the heat source were used to achieve high computational accuracy. A typical grid system contained $101 \times 61 \times 41$ grid points in a 8 cm long, 5 cm wide and 2 cm deep computational domain. The minimum grid spacing along the x, y and z directions were about 200, 200 and 125 μm , respectively.

The surface tension of the molten steel (γ) in the weld pool was calculated by using the following expression [24]:

$$\gamma = 1.943 - 4.3 \times 10^{-4}(T - 1809) - 1.3 \times 10^{-8} RT \cdot \ln \left[1 + 0.00318 a_s e^{(1.66 \times 10^6 / RT)} \right] \quad 7.25$$

where T is the average of liquidus temperature and peak temperature of the liquid metal in the weld pool in K, R is the universal gas constant and a_s is the activity of the sulfur in steel. Eq. 7.25 represents the relationships between the surface tension, composition and temperature and was obtained by Sahoo *et. al.* [24] based on Gibbs and Langmuir adsorption isotherm and thermodynamic calculations. The material properties used in the heat transfer and fluid flow calculations are listed in table 7-1. The liquid metal velocity, U_l , is taken as the peak velocity present on the weld pool surface. The arc voltage (V)

required for the calculation of input power at any current level for constant arc length was calculated by using the following volt-ampere characteristic expression:

$$V=A + B \times I + C/I \quad 7.26$$

where A, B and C are the constants whose values are available in the literature [25, 26] and listed in table 7-2.

Table 7-1: Data used for the calculation of weld pool geometry and the velocity of the liquid metal by three dimensional heat transfer and fluid flow model [14, 18].

Name	Value
Liquidus temperature (K)	1802
Solidus temperature (K)	1779
Density of liquid metal (kg m ⁻³)	7.87 × 10 ³
Viscosity of liquid (kg m ⁻¹ s ⁻¹)	6.3 × 10 ⁻³
Thermal conductivity of solid (J m ⁻¹ s ⁻¹ K ⁻¹)	36.4
Thermal conductivity of liquid (J m ⁻¹ s ⁻¹ K ⁻¹)	36.4
Specific heat of the solid (J kg ⁻¹ K ⁻¹)	754
Specific heat of the liquid (J kg ⁻¹ K ⁻¹)	754
Latent heat of melting (J kg ⁻¹)	2.7 × 10 ⁵
Temperature coefficient of surface tension (N m ⁻¹ K ⁻¹)	-0.47 × 10 ⁻³

Table 7-2: Constants for arc characteristic used in the calculation of arc voltage [25, 26]

Arc length (mm)	A	B	C
1.0	7.2	0.007	170
2.0	6.7	0.010	175
8.0	10.0	0.015	160
16.0	14.0	0.007	160

7.1.3 Average velocity and other arc parameters

During GTA welding, the Lorentz force creates a pressure difference between the anode (work piece) and the cathode (electrode). Due to high current density near the electrode compared to the work piece surface, the static pressure at the cathode was higher than the anode. This pressure difference produces a jet of plasma towards the anode. In GTAW, the arc pressure is caused by the momentum transfer of the impinging plasma jet on the weld pool and is a major factor in producing surface depressions and weld defects [8, 9]. The dependence of arc pressure (p_{arc}) on the arc velocity (V_{arc}) could be expressed as follows [25, 27]:

$$p_{arc} = \frac{1}{2} \rho_g V_{arc}^2 \quad 7.27$$

The arc velocity depends on the welding current, arc length, electrode shape and the shielding gas composition and was calculated using the expressions proposed by Chang et al. [22]. The current density distribution required for the calculation of arc velocity was assumed to be Gaussian and could be described by the following function [28, 29]:

$$J = \frac{3I}{\pi r_j^2} \exp\left(-\frac{3r^2}{r_j^2}\right) \quad 7.28$$

where J is the current density, I is current, r is the radial distance from the arc location and r_j is the effective radius of the arc. Using eq. 7.28, the maximum and average current density could be written as [25, 27]:

$$J_{max} = \frac{3I}{\pi r_j^2} \quad 7.29$$

$$J_{avg} = \frac{I}{\pi r_j^2} = \frac{1}{3} (J)_{max} \quad 7.30$$

Lin and Eager [27] suggested that current density is proportional to arc velocity based on the following relation:

$$p_{arc} = \frac{1}{2} \rho_g V_{arc}^2 = \frac{\mu_o J^2 r_j^2}{4} \quad 7.31$$

where μ_0 is the magnetic permeability of free space. Using eqs.7.29, 7.30 and 7.31, we can write:

$$U_g = (V_{\text{arc}})_{\text{avg}} = \frac{1}{3}(V_{\text{arc}})_{\text{max}} \quad 7.32$$

where $(V_{\text{arc}})_{\text{max}}$ is the maximum value of arc velocity (i.e. at $r = 0$) along the arc axis.

At high arc pressures, the weld pool surface gets deformed and the distance between the electrode and the work piece increases [30]. Therefore, the following expression of effective arc length (l_{eff}) was used to calculate the maximum arc velocity [8]:

$$l_{\text{eff}} = \text{arc length} + 0.5 \times \text{depth of weld pool} = l_a + 0.5 \times h_l \quad 7.33$$

7.2 Results and Discussion

7.2.1 Sensitivity of different variables on humping

The effects of various welding variables on the parameters that affect humping are listed in table 7-3. It can be seen from this table that almost all of the welding variables affect the depth and length of the weld pool, liquid metal velocity in the weld pool, surface tension of liquid metal and the velocity of the arc jet. The values of these variables also affect the velocity of the surface wave given by eq. 7.23.a which includes the effects of surface tension, shear force, pressure gradient and gravity.

Figure 7-3 shows the effects of ignoring either the gravity or the surface tension effect on the humping formation based on the value of (B^2-4AC) . The values of A, B, and C are calculated from eqs. 7.23.b to 7.23.d and the data indicated in the caption of figure 7-3. If the effect of the gravity in the instability criteria given by eqs.7.23.a to 7.23.d is neglected, then (B^2-4AC) term is positive only for smaller weld pool length and the model will predict humping even for the safe welding conditions. The results indicate

that the gravitational force has a significant stabilizing effect that cannot be ignored. On the other hand, if the surface tension effect is neglected, the weld pool is unstable under all welding conditions. The results presented later shows that the consideration of both the surface tension and gravity effects are necessary to accurately predict humping.

Table 7-3: Effect of various welding variables on the parameters required to predict the humping defects

Welding variable	Parameters affected
Arc current	Depth of weld pool, velocity of liquid metal, length of the pool, surface tension of the liquid metal, velocity of arc plasma
Arc length	Depth of weld pool, velocity of liquid metal, length of the pool, surface tension of the liquid metal, velocity of arc plasma, height of shielding gas layer
Nature of the shielding gas	Depth of weld pool, velocity of liquid metal, length of the pool, surface tension of the liquid metal, velocity of arc plasma, density of the gas
Nozzle to work piece distance	Height of shielding gas layer
Electrode tip angle	Depth of weld pool, velocity of liquid metal, length of the pool, surface tension of the liquid metal, velocity of arc plasma
Ambient pressure	Depth of weld pool, velocity of liquid metal, length of the pool, surface tension of the liquid metal, velocity of arc plasma
Electrode inclination angle	Depth of weld pool, velocity of liquid metal, length of the pool, surface tension of the liquid metal, velocity of arc plasma

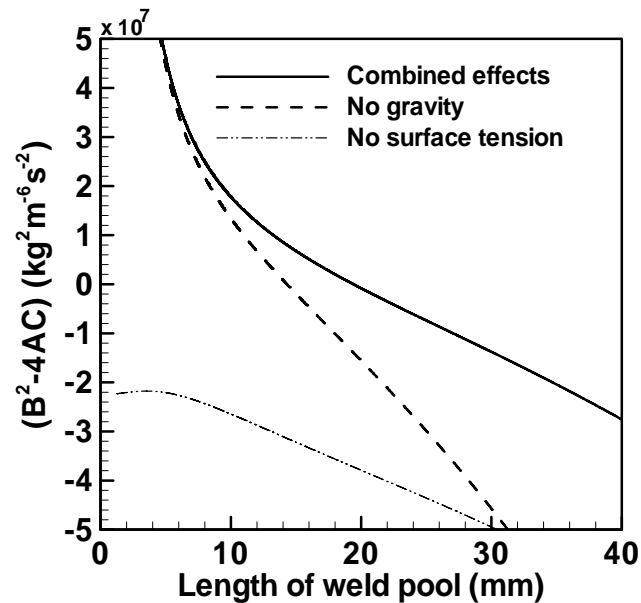


Figure 7-3: Effects of gravity and surface tension forces on the (B^2-4AC) term calculated by using eqs. 7.23.a, 7.23.b, 7.23.c, 7.23.d and 7.24. The negative value of (B^2-4AC) term signifies the instability of surface wave or the initiation of humping in the weld pool. Values of different variables used in the calculation are: $h_l = 1.5$ mm, $h_g = 7.5$ mm, $U_l = 0.7$ m/s, $U_g = 210.0$ m/s, $\rho_l = 7200$ kg/m³, $\rho_g = 0.018$ kg/m³ and $\gamma = 1.8$ N/m. These values are selected because they represent the same order of the values in GTA welding with Ar-shielding gas at 300 A, 11 mm/s welding speed and arc length = 2.4 mm.

Figures 7-4(a) and 7-4(b) show the sensitivity of various variables such as U_g , ρ_g , L_p , U_l , h_g , h_l , ρ_l and γ , on the value of the (B^2-4AC) term. Higher values of U_g , ρ_g and L_p , decrease the value of (B^2-4AC) , making the weld pool more susceptible to humping due to higher drag force as shown in figure 7-4(a). Figure 7-4(b) shows that the liquid weld metal with high surface tension (i.e. low percentage of sulfur and relatively lower temperature) is more stable than a liquid metal with low surface tension. The increase in γ enhances the resistive power of the liquid metal against the drag force. Furthermore, the prominent effect of increase of γ on humping can be observed from the steep slope of (B^2-4AC) versus γ plot in figure 7-4(b). On the other hand, the increase in the values of h_g , h_l , U_l and ρ_l have significantly mild effect on the value of (B^2-4AC) term as can be seen from the relatively low slopes of plots in figure 7-4(b). The relatively mild effect of U_l on the value of (B^2-4AC) term justifies the use of the peak surface velocity in the calculations.

7.2.2 Effect of arc current and welding speed

The length of weld pool and the arc velocity significantly affect humping. The effective arc radius used for the calculation of the depth and length of the weld pool from heat transfer and fluid flow calculations are listed in table 7-4. The properties of shielding gas used for calculating the arc velocity are given in table 7-5 for different welding conditions. For each combination of arc current and welding speed, values of U_l , U_g , ρ_l , ρ_g , h_l , h_g , L_p and γ were substituted in eq. 7.23.a to calculate the value of (B^2-4AC) . The calculated line in figure 7-5 represents zero value of the (B^2-4AC) . The region above this line has a negative value of (B^2-4AC) , as a result, humping defects appear for those welding conditions. With the increase in arc current, both the temperature in the weld pool and the arc velocity increase. The high arc velocity increases the viscous drag force on the weld pool surface and decreases the $(B^2 - 4AC)$ term. The higher current also increases the temperature in the weld pool which decreases the surface tension of the liquid metal.

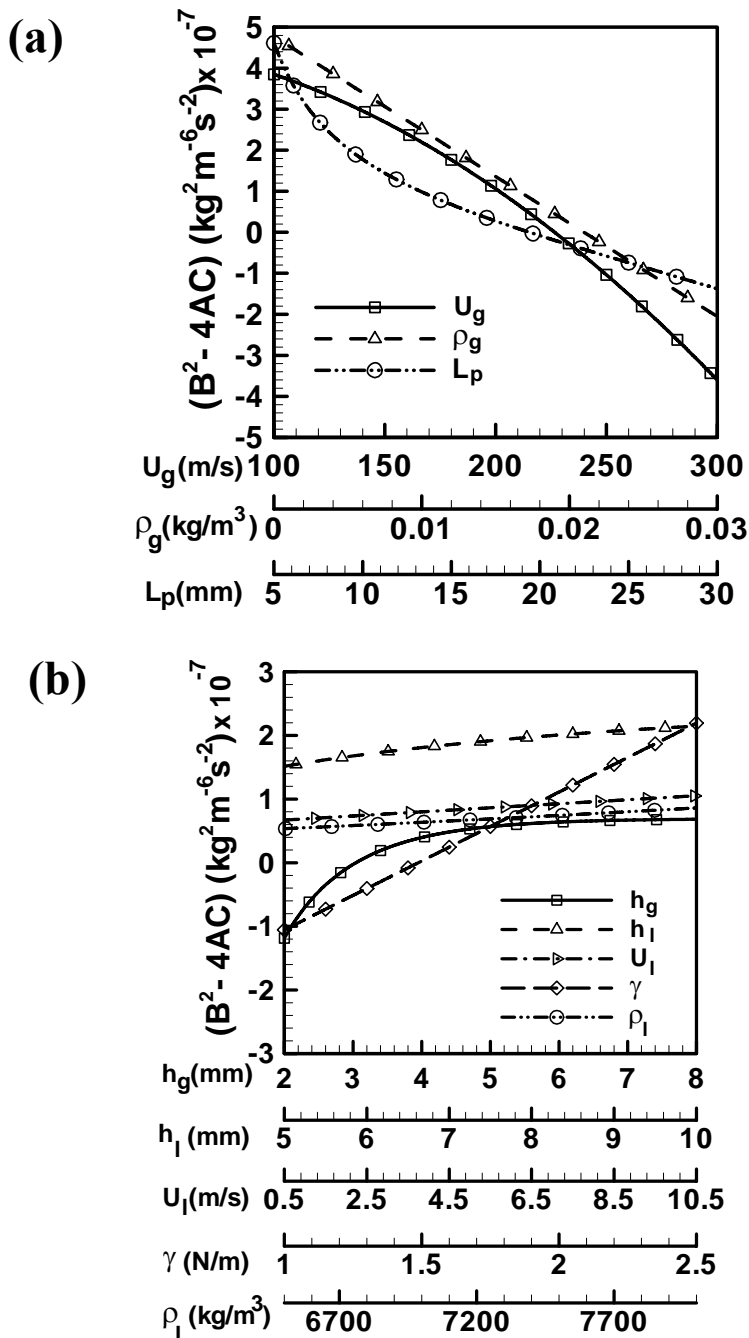


Figure 7-4: Sensitivity of (a) U_g , ρ_g and L_p ; and (b) h_g , h_l , U_l , γ and ρ_l on $(B^2 - 4AC)$ term given by eqs. 7.23.a, 7.23.b, 7.23.c and 7.23.d. The negative value of $(B^2 - 4AC)$ term signifies the instability of surface wave or the initiation of humping in the weld pool.

Table 7-4: Values of effective arc radius, r_j for current density distribution, and effective arc radius for heat flux distribution, r_q , in mm for different welding conditions [25, 27, 31-35] used in the heat transfer and fluid flow calculations and arc velocity calculation [22]. The variables I and l_a in the table represent arc current (A) and arc length (m), respectively.

Welding conditions	Values
Argon shielding gas, 1 atm. pressure, 90° electrode tip angle	$r_j = 1.085 \times I^{0.2892}$ $r_q = 7.543 \times I^{0.2645} l_a^{0.3214}$
Argon shielding gas, 1 atm. pressure, 18° electrode tip angle	$r_j = 1.017 \times I^{0.2892}$ $r_q = 6.786 \times I^{0.2645} l_a^{0.3214}$
Argon shielding gas, 32 mm Hg pressure, 25° electrode tip angle	$r_j = 1.067 \times I^{0.2892}$ $r_q = 7.466 \times I^{0.2645} l_a^{0.3214}$
Helium shielding gas, 1 atm. pressure, 90° electrode tip angle	$r_j = 1.391 \times I^{0.2892}$ $r_q = 9.666 \times I^{0.2645} l_a^{0.3214}$

Table 7-5: Properties of shielding gas [22, 25, 33, 35] required for arc velocity calculation using the expression proposed by Chang et al. [22].

Ambient pressure	Properties	Value
At 1 atmospheric pressure (i.e. 760 mm Hg pressure)	Density of argon gas	0.018 kg/m^3
	Viscosity of argon gas	$2.32 \times 10^{-4} \text{ kg.m}^{-1}\text{sec}^{-1}$
	Cathode radius	$1.191 \times 10^{-3} \text{ m}$
	Density of helium gas	0.0018 kg/m^3
At 32 mm Hg pressure	Viscosity of helium gas	$2.32 \times 10^{-4} \text{ kg.m}^{-1}\text{sec}^{-1}$
	Density of argon gas	0.0018 kg/m^3
	Viscosity of argon gas	$1.90 \times 10^{-4} \text{ kg.m}^{-1}\text{sec}^{-1}$

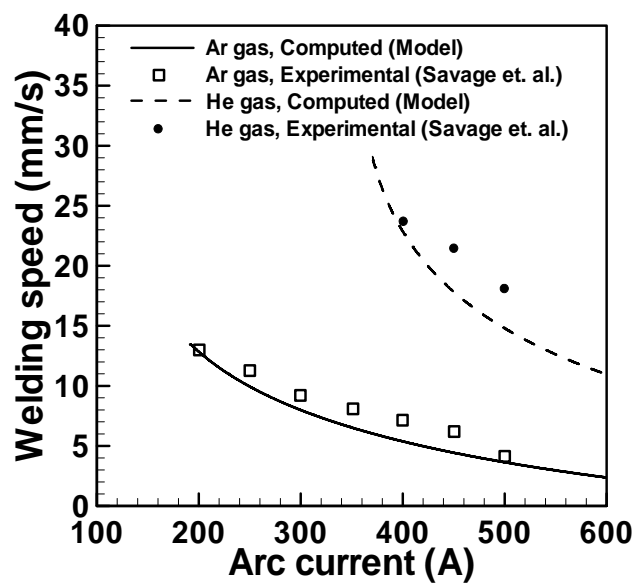


Figure 7-5: The variation of critical welding speed with arc current for argon and helium as shielding gases. The welding conditions used in the calculation are: 2.4 mm arc length, 90° electrode tip angle, 3.2 mm thick tungsten electrode and the 1 atm ambient pressure. The welding speed higher than the critical speed will produce humping.

Figure 7-5 shows that humping may occur due to decreased surface tension and increased drag force at high currents even at low welding speeds. The variations of relative velocity (i.e. the difference between arc velocity and liquid velocity), weld pool depth, length and the surface tension of liquid metal with arc current are shown in figures 7-6(a), 7-6(b), 7-6(c) and 7-6(d) for two different values of welding speed. With increase in arc current, the relative velocity between arc plasma and liquid metal increases which makes the weld pool interface unstable. Furthermore, with increase in welding speed, the relative velocity also increases. This trend justifies the fact that with increase in arc current and welding speed, there are high chances of humping defects. The weld pool depth is more at low welding speed due to more heat input per unit length for fix value of arc current as shown in figure 7-6(b). With increase in arc current, the temperature in the weld pool also increases, which lower down the surface tension as shown in figure 7-6(d). The welding speed has more prominent effect on relative velocity and weld pool depth compared to weld pool length and surface tension as can be seen from figures 7-6(a), 7-6(b), 7-6(c) and 7-6(d).

When the current is kept constant, the depth of the weld pool decreases with the increase in the welding speed. The lower weld pool depth decreases the effective arc length and increases the arc velocity. Thus, the higher welding velocity increases the drag force and makes humping more likely as shown in figure 7-5. Calculations were done for the conditions similar to those chosen by Savage et al. [2] in their experiments. In particular, argon shielding gas, the electrode to work piece distance of 2.4 mm, electrode thickness 3.2 mm and vertex angle 90° were considered. Humping would occur if the welding speed is higher than the critical speed in figure 7-5 for the welding conditions considered as can be observed from both experimental data and the calculations. Table 7-6 also shows a good agreement in predicting humping for different set of experiments conducted by Mendez et al. [8]. Good agreement between the calculated and the experimentally obtained critical speed limits [2, 8] shows that the model can satisfactorily predict humping for a wide variety of welding conditions.

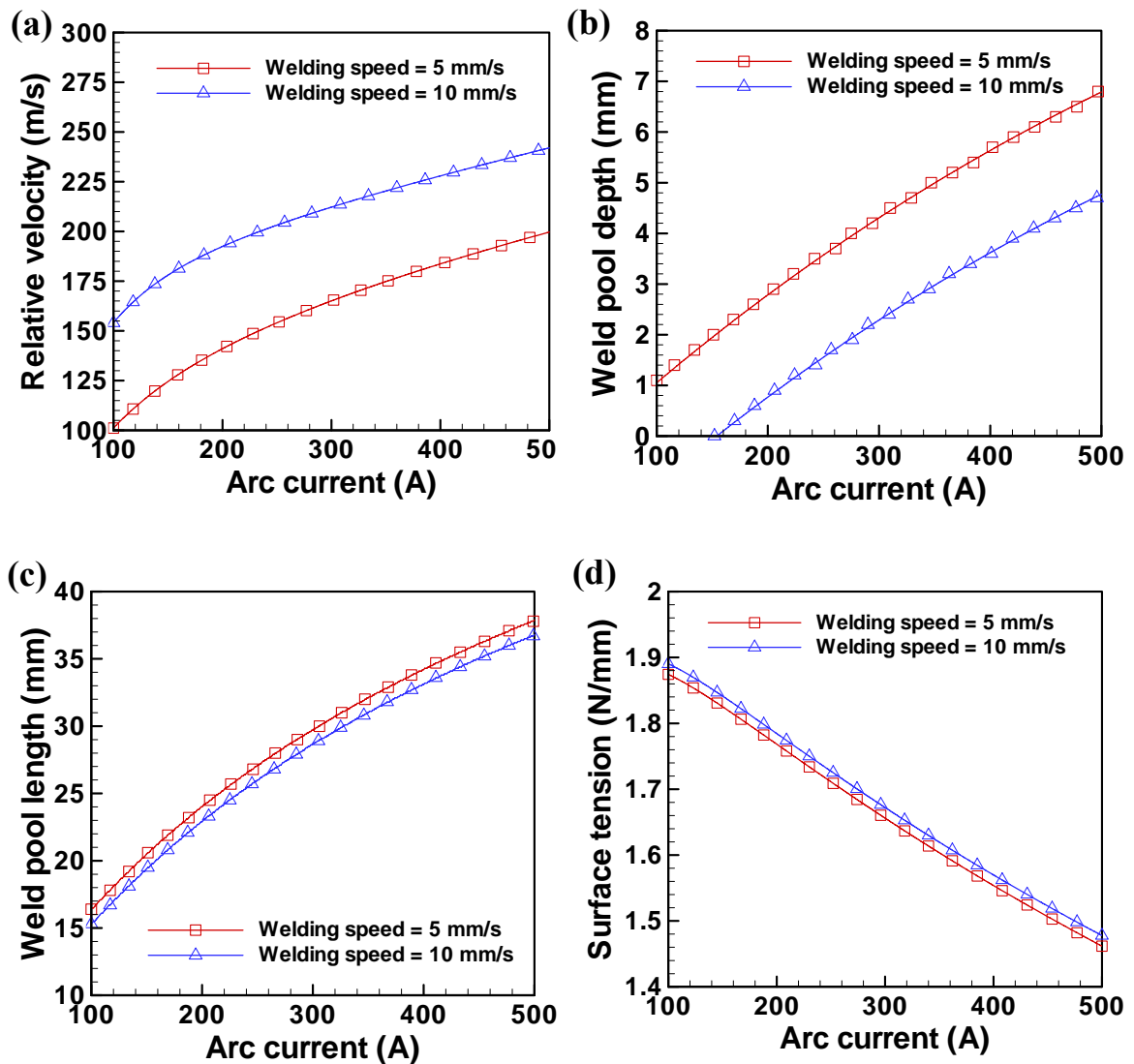


Figure 7-6: Variations of (a) relative velocity (i.e. the difference between arc velocity and liquid velocity); (b) weld pool depth; (c) length and (d) the surface tension of liquid metal with arc current. The welding speed has more prominent effect on relative velocity and weld pool depth compared to weld pool length and surface tension of the liquid metal.

Table 7-6: Welding conditions of Mendez and Eager [8] used for the prediction of humping by the proposed model.

Arc current (A)	Welding speed (mm/s)	Arc length (mm)	Sulfur content (ppm)	Humping
274	11.6	7.3	6	No
334	14.1	7.5	6	No
500	10.6	9.4	6	No
500	15.0	8.5	6	No
500	10.6	9.2	230	Yes
500	15.0	8.2	230	Yes

7.2.3 Effect of shielding gas

Since the nature of the shielding gas affects arc shape [25, 27, 31, 32], it also influences the current density distribution. The arc shape influences the pressure difference between the cathode and the anode and therefore, the arc pressure. According to Lin and Eager [27], the spread of the plasma or the effective current radius is proportional to η^2/ρ , where η is the viscosity and ρ is the density of the gas. Since, the density and viscosity of Helium was about 1/10th and twice, respectively those of Argon, at high temperatures [27, 33], the He arc is broader than that of Argon. Furthermore, high thermal conductivity of helium compared to argon leads to more uniform heat distribution in the arc. Savage et al. [2] also reported that Argon arc was brighter and more cylindrical than Helium arc. The variation of dynamic viscosity of argon, helium and the mixtures of these two gases with temperature [25, 33] are given in figure 7-7. The density and viscosity of Helium used in the calculations are listed in table 7-5. The arc velocity is lower in He than in Ar due to low density and high viscosity of Helium. As a result, the drag force of He on the liquid metal is lower than that of Ar. The critical welding speed for humping was higher by a factor of 3 in Helium than in Argon for the

same values of arc current and voltage as shown in figure 7-5. Comparisons of the results for He and Ar show that in He humping does not occur at low arc currents even at high welding speeds. Use of Ar makes welds more susceptible to humping. The computed critical welding speed for humping shows good agreement with the corresponding experimental values reported in the literature [2].

The Richardson number (Ri) was calculated to for various combinations of arc current and welding speed as shown in figure 7-8. It was calculated using the following expression:

$$Ri = \frac{g(\rho_l - \rho_g)h_g}{\rho_g U_g^2} = \frac{\text{Buoyancy force}}{\text{Inertia force}}$$

where U_g is arc velocity, h_g is the height of shielding gas layer; ρ_l and ρ_g are the densities of liquid metal and shielding gas, respectively. It is a dimensionless number that expresses the ratio of potential to kinetic energy or the buoyancy force to inertia force. If the Richardson number is much less than unity, buoyancy is unimportant in the flow. If it is much greater than unity, buoyancy is dominant (in the sense that there is insufficient kinetic energy to homogenize the fluids). If the Richardson number is of order unity, then the flow is likely to be buoyancy-driven. It was found in this work that if the value of Richardson number (Ri) is less than 0.8, then there are high chances of humping defects to occur. The low value of Ri favors humping. However, calculation of Ri will only give order of magnitude values and they can not identify the welding conditions precisely.

7.2.4 Effect of the electrode tip angle

Several researchers [24, 26, 31, 32, 34, 35] have shown that the electrode tip angle significantly affects arc behavior. Tsai and Eager [31] found that the arc radius increased by approximately 15 % when current increased from 100 Amp to 200 Amp in Ar-plasma with a 75° tip angle and 5.5 mm arc length. Yamauchi and Taka [32] have shown that the effect of electrode tip angle on arc pressure was more pronounced at high current levels.

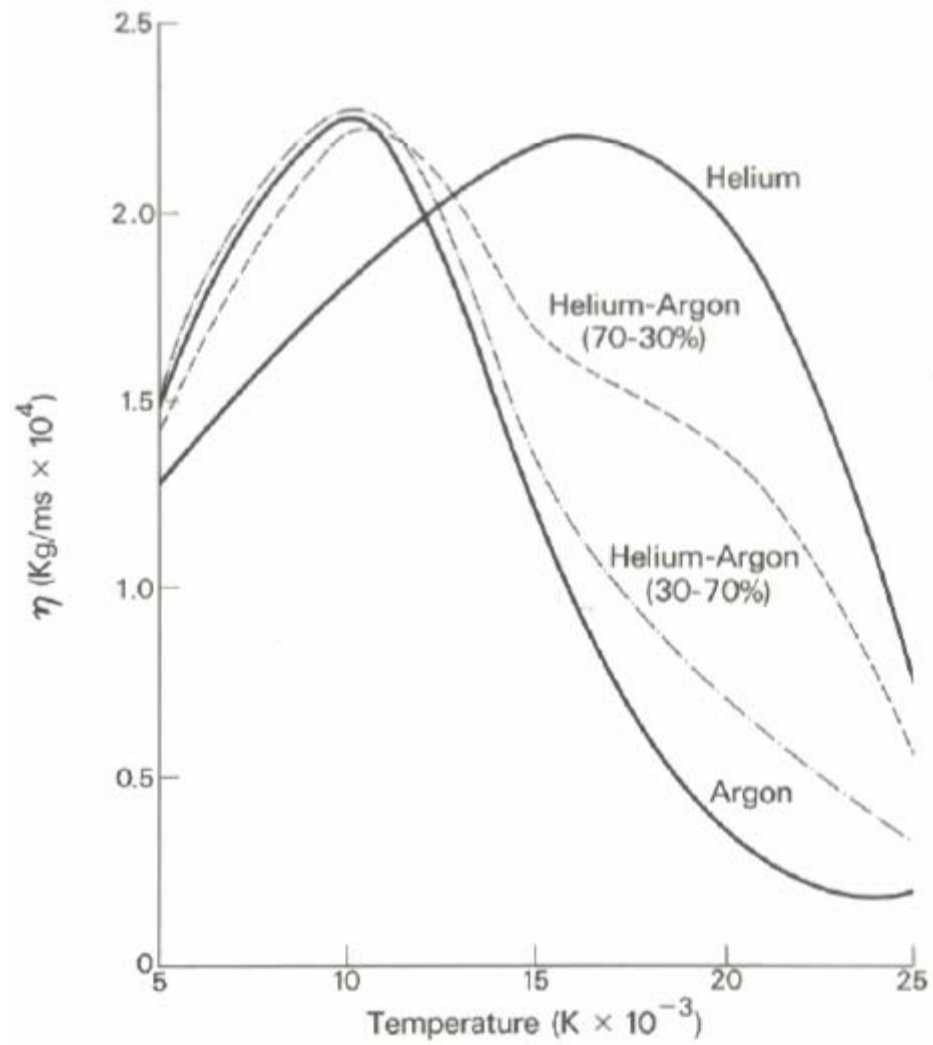


Figure 7-7: Dynamic viscosity of the helium, argon and their mixture at 1 atm. pressure [25, 33].

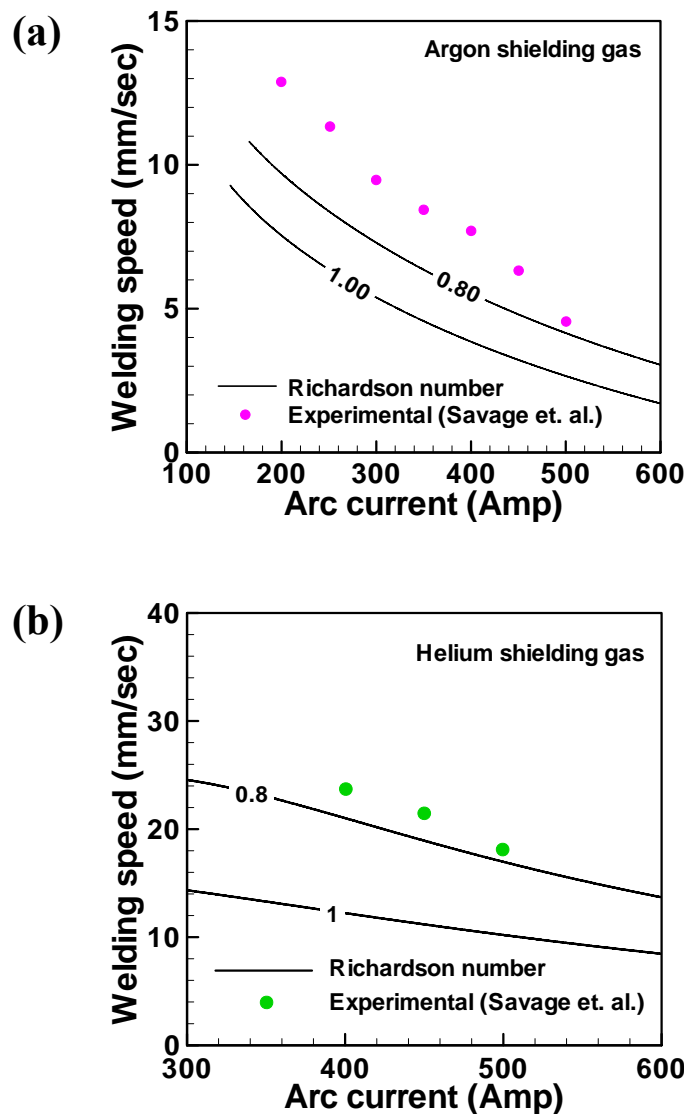


Figure 7-8: Variation of Richardson number with arc current and welding speed for (a) argon and (b) helium shielding gases. If Richardson number (R_i) is less than 0.8, then there are chances of humping defects to occur.

Lin and Eager [27] observed that the arc pressure increased when electrodes with sharper tip angles were used. With increase in arc pressure for sharper tip electrodes (e.g., 18° tip), the peak current density and arc velocity also increases. As a result, the drag force on the liquid metal increases which makes humping more likely as shown in figure 7-9. The experimental values of critical welding speed for humping reported by Savage et al. [2] and Yamamoto and Shimada [3] for 18° , 25° and 90° electrode tip angle show a good agreement with the corresponding computed values. Therefore, electrodes with large tip angle can be used to achieve high welding speed and prevent humping.

7.2.5 Effect of the electrode shape

Yamauchi and Taka [32] showed that the use of hollow electrode in place of solid electrode reduced the arc force. They [32] found that the arc root formed symmetrically inside the hole for a typical 5 mm diameter tungsten electrode with a 3 mm central hole. They suggested that the average arc velocity reduced by about 15 % compared to solid electrode based on the measurement of arc force by Yamauchi and Taka [32]. The decrease in the arc velocity reduced the drag force on the liquid metal and increased the computed critical welding speed for humping by about 50 % as shown in figure 7-10. The computed results are consistent with the fact that the hollow electrodes reduce the arc pressure [36], and therefore, they may be used to achieve high fabrication rate and prevent humping under welding conditions where humping may occur when solid electrodes are used.

7.2.6 Effect of external magnetic field

An external magnetic field applied transverse to welding direction will deflect the arc due to electromagnetic force. Depending on the direction of the field, a transverse magnetic field will deflect the arc either in the welding direction or opposite to it [25, 37, 38] as shown in figure 7-11.

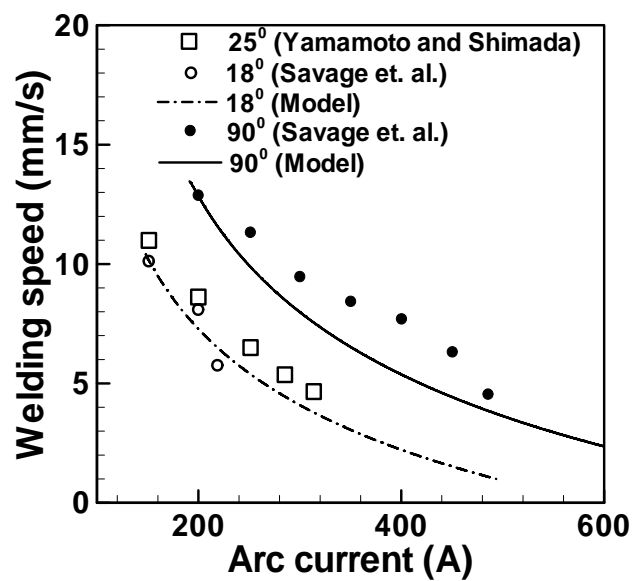


Figure 7-9: The effect of the electrode tip angle on humping. The welding conditions used in the calculations are: 2.4 mm arc length, 3.2 mm diameter tungsten electrode, argon shielding gas and 1 atm. ambient pressure. The results show that the electrodes with smaller tip angle produces humping at lower welding speed than those with larger tip angles.

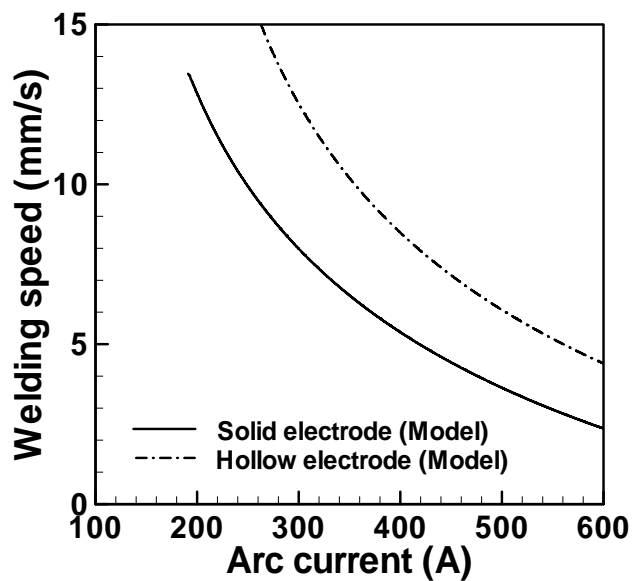


Figure 7-10: The effect of the hollow and solid electrodes on the critical welding speed to initiate humping. The welding conditions used in the calculation are: 2.4 mm arc length, 90° electrode tip angle, argon shielding gas and 1 atm. ambient pressure. The results show that solid electrodes produce humping at lower welding speed than hollow electrodes.

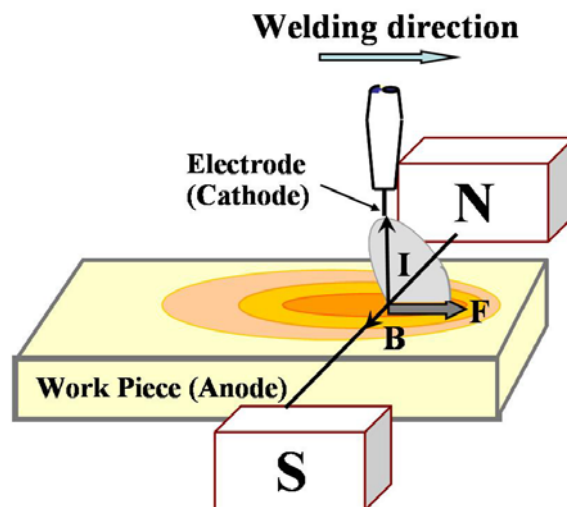


Figure 7-11: The effect of the externally applied transverse magnetic field on arc deflection based on Fleming's left hand rule. The arc is deflected in the welding direction when the north pole is on the left side of the moving electrode. If the north and south poles are interchanged, the arc will be deflected in the reverse direction.

The deflection of arc increases the effective arc length and arc radius. The increase in arc length decreases the arc velocity and drag force on the weld pool surface. The extent of the arc deflection (δ) depends linearly on the magnitude of the externally applied magnetic field and the effective arc length (l_{eff}) as represented by the following equation [24, 37, 38]:

$$\delta = K_1 B_x l_{\text{eff}} \quad 7.34$$

where K_1 is a constant and B_x is the externally applied magnetic field in Tesla. The value of constant, K_1 , was obtained to be 100.0 Tesla^{-1} by fitting the above equation with the experimental results reported in the literature [37] for Ar-shielding gas. However, the value of the constant, K_1 , may vary with the welding conditions like welding current, shielding gas composition and the ambient pressure. The modified effective arc length (l_{eff}) could be calculated by using the value of arc deflection (δ) as follows:

$$l_{\text{eff}} = \sqrt{\delta^2 + (\text{arc length} + 0.5 \times \text{depth of weld pool})^2} \quad 7.35$$

The higher effective arc length decreased the magnitude of the drag force created by the flow of the plasma on the liquid metal in the weld pool. The reduction in drag force with increase in the magnitude of the external magnetic field reduced the chances of humping in the weld and increased the critical welding speed by 10-15 % for magnetic field of 0.003 Tesla as shown in figure 7-12. Furthermore, the critical welding speed increases by more than 75 % when the arc length increases from 2.4 mm to 3.0 mm as shown in figure 7-13. The computed results show that the longer arc length and an appropriate transverse external magnetic field during welding would provide a higher operating welding speed without any humping.

7.2.7 Effect of the ambient pressure

Higher ambient pressure increases the current density in the arc column [3, 25, 39, 40]. Matsunawa and Nishiguchi [39] observed that the arc column becomes narrower and brighter at high pressures and more diffused and rounded at low pressures. Yamamoto

and Shimada [3, 40] observed that the arc pressure at 32 mm Hg reached about one tenth of that at atmospheric pressure. Based on these observations, the effective arc radius for current and heat distribution at 32 mm Hg pressure were assumed to be 10 % more than their values at the atmospheric pressure. The effective arc radius is required for both heat transfer and fluid flow calculations as well as the arc velocity estimation. The expressions used in the calculations of arc radius are presented in table 7-4 and the properties of shielding gas are given in table 7-5. For each combination of arc current and welding speed, values of liquid metal velocity in the weld pool, U_l , shielding gas velocity, U_g , density of liquid metal, ρ_l , density of shielding gas, ρ_g , depth of weld pool, h_l , shielding gas layer height, h_g , length of weld pool, L_p and surface tension of liquid metal, γ , were substituted in equations (16.b), (16.c) and (16.d) to calculate the value of (B^2-4AC) . The calculated line in figure 7-14 represents zero value of the (B^2-4AC) . The region below this line has positive value of (B^2-4AC) and is free of humping defects. At 32 mm of Hg ambient pressure, the shielding gas density is low which leads to low drag force and welds free of humping as shown in figure 7-14. Comparison of figures 7-4 and 7-14 show that by reducing the ambient pressure, critical welding speed can be increased by more than 200 %. The computed critical welding speed for humping showed good agreement with the corresponding experimental values reported by Yamamoto and Shimada [3] indicating accuracy of the model.

7.2.8 Effect of torch angle

To capture the effect of the torch angle (inclination) in the model, the effective arc length was modified by assuming an asymmetric weld pool surface shown in figure 7-15. Since the front of the weld pool is depressed significantly more than the trailing region [41], the trailing region is assumed to make a 45° angle with the horizontal plane along the welding direction as shown in figure 7-15.

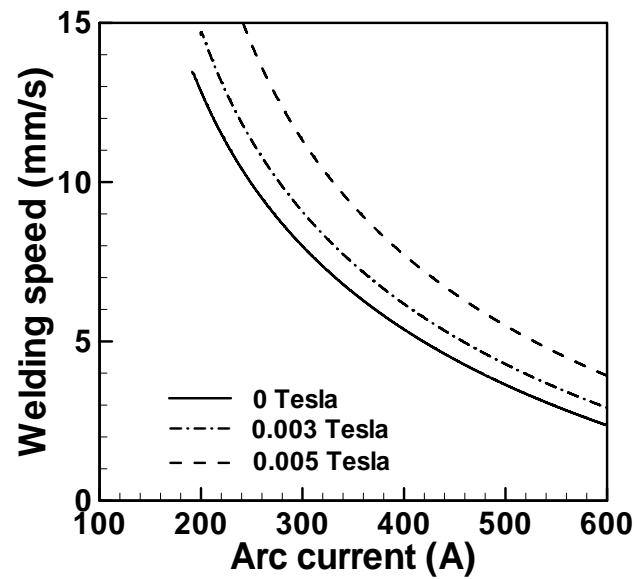


Figure 7-12: The effect of the externally applied transverse magnetic field on the critical welding speed to initiate humping in the weld. The welding conditions used in the calculation are: 2.4 mm arc length, 90° electrode tip angle, argon shielding gas and 1 atm. ambient pressure. The results show that the critical welding speed increases with the increase in externally applied transverse magnetic field.

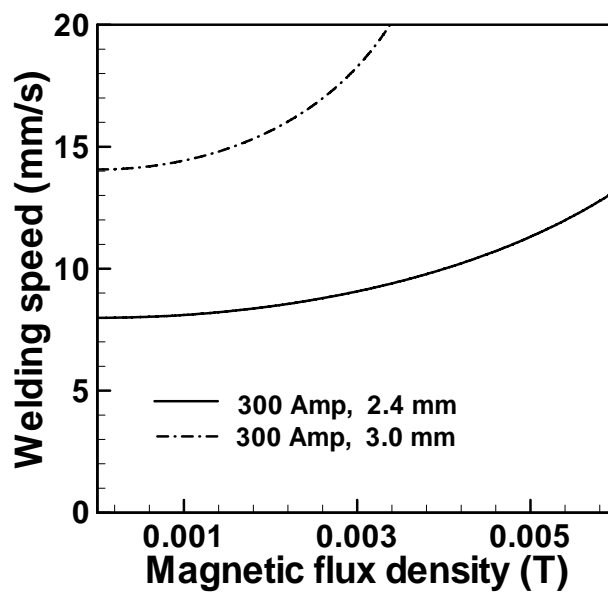


Figure 7-13: The variation of critical welding speed with externally applied transverse magnetic field for different arc lengths. The welding conditions used in the calculation are: 300 A arc current, 90° electrode tip angle, argon shielding gas and the 1 atm. ambient pressure. The results show that the critical welding speed increases with the increase in externally applied transverse magnetic field and the arc length.

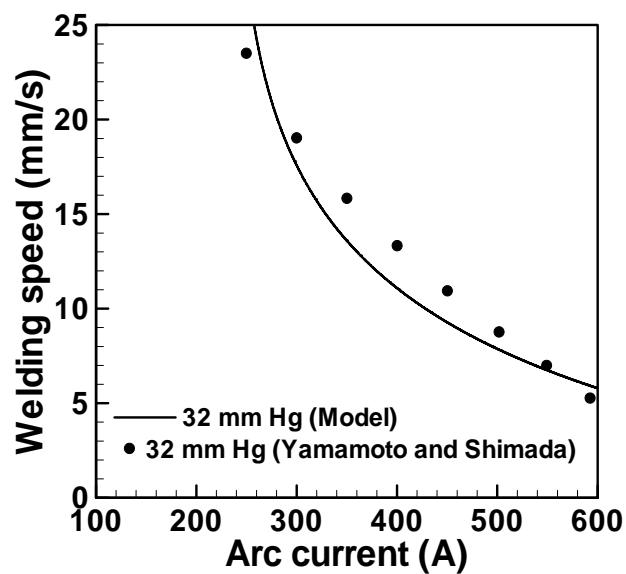


Figure 7-14: The variation of critical welding speed with arc current at low pressure for vertical torch position. The welding conditions used in the calculation are 2.4 mm arc length, 25° electrode tip angle, 3.2 mm diameter tungsten electrode, argon shielding gas and 32 mm of Hg ambient pressure. Higher values of critical welding speed were achieved at low ambient pressures.

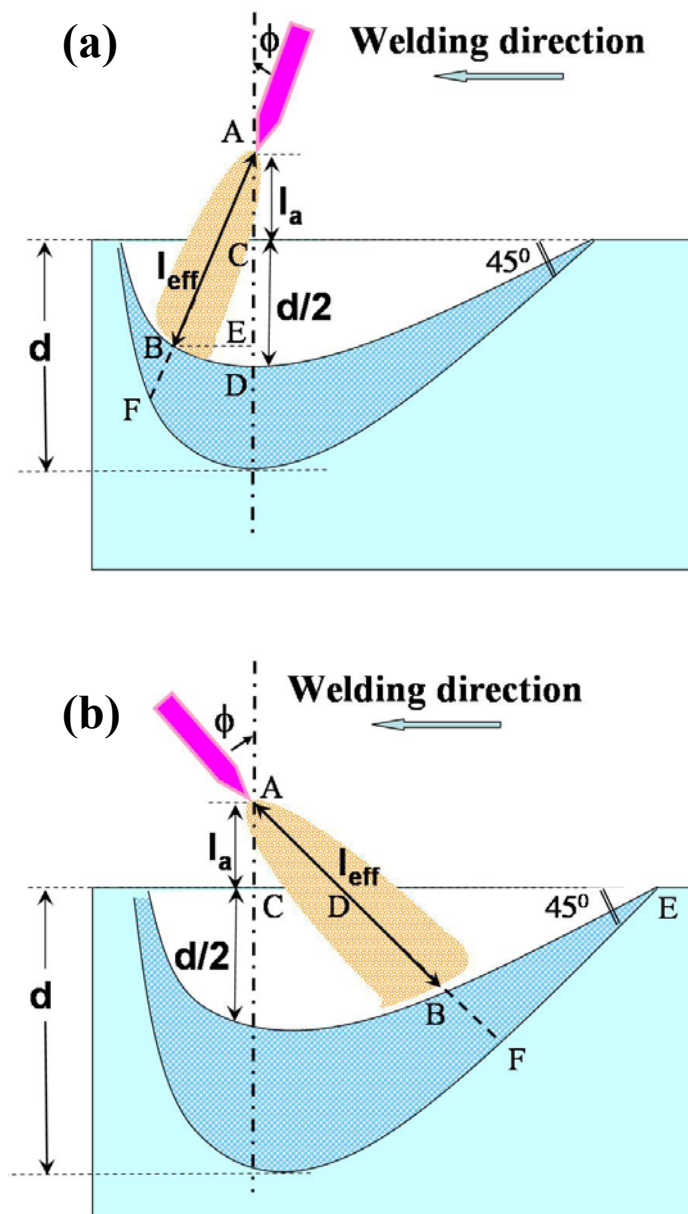


Figure 7-15: The effect of torch inclination on the effective arc length. Figure (a) shows the welding torch in push position while figure (b) shows the pull position.

Based on the above assumption, the effective arc length was calculated using the geometry of the system shown in figure 7-15 (a) for different torch angles. For inclined torch practice, the torch can have two orientations, pull and push as shown in figure 7-15. A drag or pull technique provides more penetration and a narrower bead compared to a push technique where the arc is directed ahead of the weld bead. For the push configuration $\phi > 0$ and the effective arc length was calculated using the following expression:

$$l_{\text{eff}} = \left(\frac{l_a + 0.5 \times \text{depth of weld pool}}{\cos(\phi)} \right) \quad \text{for } \phi \geq 0 \quad 7.36$$

The presence of cosine of the inclination angle in the denominator increases the arc length and the arc radius on the weld pool surface. With increase in arc radius, the peak heat intensity decreases which leads to a wider and shallower pool. The effective arc length for the pull technique when the arc was directed behind the weld bead, i.e., for $\phi < 0$, was calculated based on the geometry. The effective arc length for pull technique (i.e. negative ϕ) shown in figure 7-15 (b) was calculated from the following expression:

$$l_{\text{eff}} = \frac{l_a}{\cos(\phi)} + 0.5 \left(\frac{\sin(\pi/4) \times \text{depth of weld pool} - l_a \tan(\phi)}{\sin(\phi + \pi/4)} \right) \quad 7.37$$

for $\phi < 0$

Figure 7-16 shows the variation of weld pool depth with torch inclination angle, ϕ . A reasonable agreement with the experimental results for different torch angles [42] suggested that the above expressions of effective arc length could be used in the model. The depth and length of the weld pool was larger during pull technique compared to push technique for similar welding conditions. The calculations were done using a three dimensional heat transfer and fluid flow model with modification for the electromagnetic force calculation [28, 42] at different torch angles. This behavior matched very well with the effect of inclination of torch observed experimentally [41].

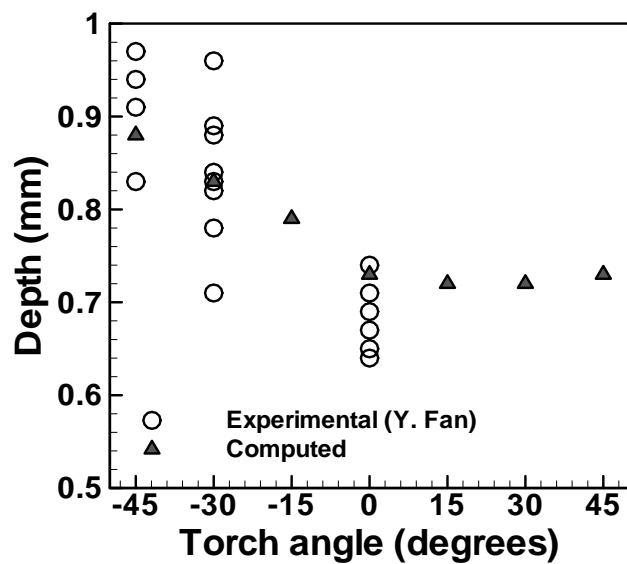


Figure 7-16: The variation of weld pool depth with inclination of torch for 67.0 A arc current, 9.0 V arc voltage and 4.0 mm/s welding speed. The positive torch angle means that the welding torch is in push position while the negative angle means that torch is used in pull position.

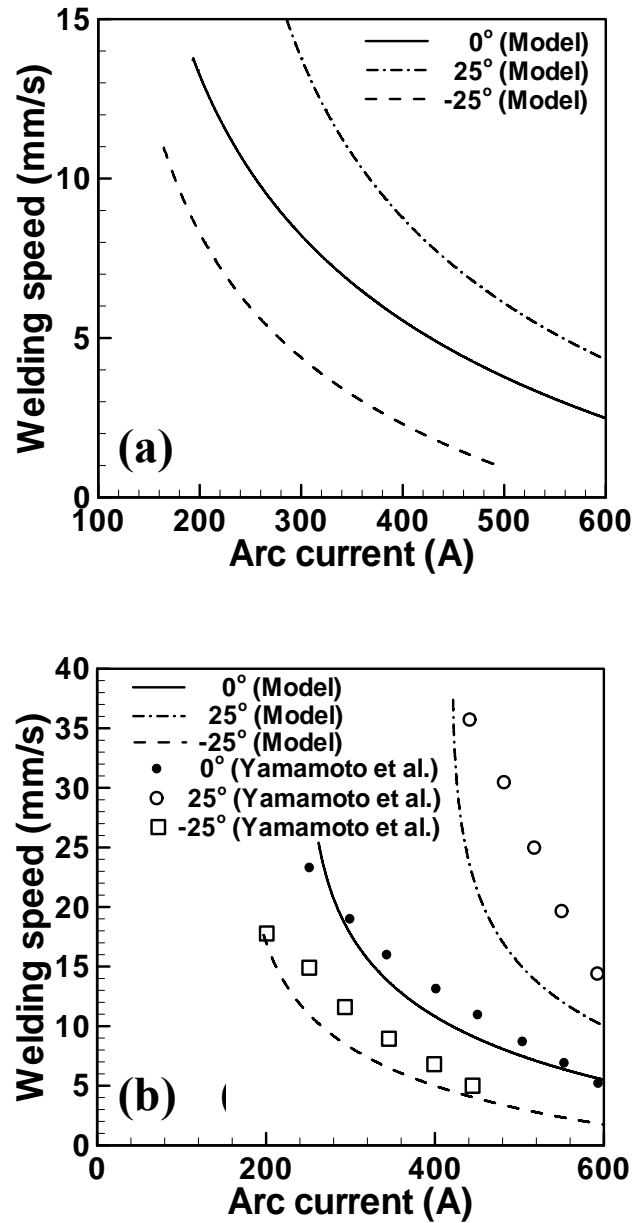


Figure 7-17: The variation of critical welding speed with arc current for the initiation of humping defects in the weld for different torch angles at (a) atmospheric pressure and (b) at 32 mm Hg pressure. Higher values of critical welding speed were achieved when the welding torch was in the push configuration i.e., when the arc strikes ahead of the torch axis.

Figure 7-17 shows that the critical welding speed for humping defects increases with inclination of arc ahead of weld bead i.e. during push technique. For 25° inclination, the computed critical welding speed increased by about 60 %. This behavior was due to the decrease in both arc velocity and arc pressure on the weld pool surface with increase in the effective arc length. The inclination of torch in the negative direction (i.e. in pull or drag technique) reduced the critical welding speed and generated humping even at lower speed as shown in figure 7-17 (a). Recently, Nguyen et al. [43] observed that the critical welding speed during gas-metal arc welding in spray mode increases when torch is directed ahead of the weld bead. Lancaster [25] also recommended the use of welding torch in push position to avoid humping. The computed results also showed a similar behavior.

Yamamoto and Shimada [3] also showed the effect of the inclination of torch on the critical welding speed at low ambient pressure. They found that at low ambient pressure, the inclination of torch in push direction increased the critical welding speed and vice-versa. The computed critical welding speed, shown in figure 7-17(b), for different torch inclination angles and 32 mm Hg ambient pressure, showed good agreement with the corresponding experimental values reported by Yamamoto and Shimada [3] indicating the accuracy of the calculations.

7.3 Summary and Conclusions

A phenomenological model based on the stability of waves on the weld pool surface due to relative motion between the plasma and the liquid weld metal was developed to examine the conditions for the formation of humping defects. Good agreement was obtained between the model predictions for humping and independent experimental results from various sources for a wide variety of welding conditions. This model can estimate the critical welding conditions for humping considering the values of arc current, welding speed, nature of the shielding gas, electrode geometry, ambient

pressure, torch angle and external magnetic field during gas tungsten arc (GTA) welding. The following conclusions can be drawn from the results.

1. Increase in welding speed above certain critical speed leads to initiation of humping defects.
2. The value of the critical speed varies with the welding conditions. The critical welding speed decreases with increase in arc current.
3. The nature of the shielding gas affects humping. Chances of humping are lower in He than in Ar. The use of He increases the critical welding speed by more than three times.
4. Blunt electrodes with large tip angles help in preventing humping. More than 50 % increase in critical welding speed was obtained with electrode having 90° tip angle compared to 18° tip angle.
5. Application of external magnetic field in transverse direction that deflects arc in the welding direction helps in avoiding humping.
6. Low ambient pressure reduces the occurrence of humping
7. The inclination of torch away from the welding direction i.e. in push position suppresses humping while the torch is pull position favors humping. The critical welding speed increases by more than 200 % in push position compared to pull position.

These results show that the adjustment of welding variables can prevent humping. Even when high welding speed and current are needed to sustain productivity goals, several steps can be taken to prevent humping. These include selection of hollow electrodes, imposition of appropriate external magnetic field, inclination of the torch, careful selection of shielding gas and, where practical, reduced pressure.

7.4 References

1. B. J. Bradstreet, *Welding J.* **47**(7), 314 (1968).
2. W. F. Savage, E. F. Nippes and K. Agusa, *Welding J.* **58** (7), 212 (1979).

3. T. Yamamoto and W. Shimada, in *International Symposium in Welding*, Osaka, Japan (1975).
4. M. Beck, P. Berger, F. Dausinger and H. Hugel, in *Proceedings of 8th International Symposium on Gas Flow and Chemical Lasers*, Madrid, Spain (1991).
5. K. C. Mills, B. J. Keene, *International Materials Reviews*, **35**(4), 185 (1990).
6. U. Gratzke, P. D. Kapadia, J. Dowden, J. Kroos and G. Simon, *J. Phys. D: Appl. Phys.* **25**, 1640 (1992).
7. N. Yamauchi and T. Taka, *International Institute of Welding*, document no.: 212-437-78 (1978).
8. P. F. Mendez and T. W. Eagar, *Welding J.* **82**(10), 296 (2003).
9. P. F. Mendez, K. L. Niece and T. W. Eagar, in *Proceedings of the International Conference on Joining of Advanced and Specialty Materials II, Materials Solutions '99, Cincinnati, OH*, pp: 151 (2000).
10. P. K. Kundu and I. M. Cohen, *Fluid Mechanics*, Elsevier Academic Press, San Diego (2004).
11. L. M. Thomson, *Theoretical Hydrodynamics*, Macmillan, New York (1968).
12. P. G. Drazin and W. H. Reid, *Hydrodynamic Stability*, Cambridge University Press, Cambridge (2004).
13. K. Mundra, T. DebRoy and K. M. Kelkar, *Numer. Heat Trans. A* **29**, 115 (1996).
14. W. Zhang, G. G. Roy, J. W. Elmer and T. DebRoy, *J. Appl. Phys.* **93**(5), 3022 (2003).
15. A. De and T. DebRoy, *J. Appl. Phys.* **95**(9), 5230 (2004).
16. A. De and T. DebRoy, *J. Phys. D: Appl. Phys.* **37**, 140 (2004).
17. A. De and T. DebRoy, *Welding J.* **84** (7), 101 (2005).
18. S. Mishra and T. DebRoy, *Journal of Physics D* **38**: 2977 (2005).
19. V. R. Voller and C. Prakash, *Inter. J. Heat Mass Trans.* **30** (8), 1709 (1987).
20. A. D. Brent, V. R. Voller and K. J. Reid, *Num. Heat Trans.* **13**, 297 (1988).
21. K. Mundra, J. M. Blackburn and T. DebRoy, *Science and Technology of Welding and Joining* **2**, 174 (1997).
22. C. W. Chang, T. W. Eagar and J. Szekely, *Arc Physics and Weld Pool Behavior*, The Welding Institute, Cambridge, England, pp: 381 (1980).

23. S. V. Patankar, *Numerical Heat Transfer and Fluid Flow*, McGraw-Hill, New York (1988).
24. P. Sahoo, T. DebRoy and M. J. McNallan, *Metallurgical Transaction B* **19B**, 483 (1988).
25. J. F. Lancaster, *The Physics of the Welding*, Pergamon, Oxford (1986).
26. K. Goldman, *Physics of the Welding Arc*, Institute of welding, London (1966).
27. M. L. Lin and T. W. Eagar, *Welding J.* **64**(6), 163 (1985).
28. A. Kumar and T. DebRoy, *J. Appl. Phys.* **94** (2), 1267 (2003).
29. S. Kou and D. K. Sun, *Metall. Trans. A* **16A**, 203 (1985).
30. S. I. Rokhlin and A. C. Guu, *Welding J.* **72**(8), 381 (1993).
31. N. S. Tsai and T. W. Eagar, *Metall. Trans. B* **16**(12), 841 (1985).
32. N. Yamauchi and T. Taka, *International Institute of Welding*, document no.: 212-452-79 (1979).
33. M. Monval. *International Institute of Welding*, document no.: 212-264-73 (1973).
34. M. Goodarzi, R. T. C. Choo and J. M. Toguri, *J. Phys. D: Appl. Phys.* **30**, 2744 (1997).
35. R. T. C. Choo, J. Szekely and R. C. Westhoff, *Welding J.* **69**(9), 346 (1990)
36. G. G. Chernyshov and V. L. Kovtun, *Welding Prod.* **32**(2), 23 (1985).
37. Y. H. Kang and S. J. Na, *Welding J.* **81**(1), 8 (2002).
38. I. M. Kovalev, *Welding Prod.* **12**(10), 9 (1965).
39. A. Matsunawa and K. Nishiguchi, *Arc Physics and Weld Pool Behavior*, The welding Institute, Cambridge (1979).
40. T. Yamamoto and W. Shimada, *International Institute of Welding*, document no.: 212-157-68 (1968).
41. *Welding Handbook*. 2004. American Welding Society, Miami, Florida.
42. Y. Fan, *M.S. Thesis*, The Pennsylvania State University, PA (2003).
43. T. C. Nguyen, D. C. Weckman, D. A. Johnson and H. W. Kerr, *Science and Technology of Welding and Joining* **10**(4), 447 (2005).

Chapter 8

CONCLUDING REMARKS

8.1 Summary

The existing transport phenomena based models of welding can not be used for tailoring weld attributes. The work reported in this thesis seeks to propose and verify a methodology for tailoring weld attributes based on fundamental principles of transport phenomena and an advanced real number based genetic algorithm. The overall work involved the following components.

1. Recently, a heat transfer and fluid model of GMAW was developed in our research group to calculate the bead profile for V-shape fillet joints during welding in flat position. However, different fillet joints orientations such as L-joints are more commonly manufactured in the industry. Furthermore, the welding is performed on the structures in uphill and downhill position which affects the weld pool convective flow and hence the weld bead profile. Therefore, the capability of the existing numerical heat transfer and fluid flow model of gas metal arc fillet welding available in our research group was improved to study the effect of joint orientations and welding positions on temperature distribution, velocity profiles, free-surface, thermal cycles and the cooling rates.

2. Since any uncertainty in the values of some of the input parameters such as arc efficiency, effective thermal conductivity and effective viscosity of the liquid metal affects the outputs of the heat transfer and fluid flow calculation, the values of these parameters were found using inverse modeling approach. In this approach, a derivative based optimization algorithm was coupled with a heat transfer and fluid flow model to find the uncertain input parameters based on the phenomenological governing equations using a limited volume of experimental data.

3. The numerical heat transfer and fluid flow model of GMA fillet welding are computationally very intensive and takes about 40 minutes of computation time for each run. In order to obtain alternative combinations of welding variables to attain desired weld attributes, the heat transfer and fluid flow model need to be coupled with a genetic algorithm (GA) based optimization model. It was expected that this approach may take more than 200 hours of computation time if the heat transfer and fluid flow model is used as the main computational engine to calculate the weld geometry since it requires multiple runs of the heat transfer and fluid flow calculations. In order to reduce the computation time, a neural network was trained with the pre-calculated results of temperature and velocity fields for various welding conditions obtained using the heat transfer and fluid flow model. These neural network models consider same input variables as the heat transfer and fluid flow model and provide weld dimensions, peak temperatures, maximum velocities and the cooling rates between 800 to 500 °C as outputs. The neural network takes only a fraction of second for predicting the weld bead geometry compared to the heat transfer and fluid flow model which requires around 40 minutes.

4. In the industries, the desired weld attributes such as the weld geometry and structure are commonly produced by empirically adjusting the welding variables. However, this approach does not always produce optimum welds due to non-linear behavior between various welding variables. In this research work, a bi-directional model was developed which can predict the input welding conditions to achieve the target weld geometry based on scientific principles. This approach is based on coupling a genetic algorithm based optimization model with neural network model. This model was able to predict alternate combinations of input welding conditions such as arc current, voltage, wire feed rate and welding speed to achieve welds with desired geometry.

5. In real world, the welding productivity is often achieved by increasing welding speed and the arc current and keeping heat input per unit length constant. However, in many cases, the high welding speed or the arc current can lead to humping defects which affect the quality and integrity of the weld. In this thesis work, a comprehensive mathematical model was developed to quantitatively understand the welding conditions

that result in humping defects. This model was able to quantitatively predict the welding conditions that may lead to humping defects by considering the effect of arc current, welding speed, electrode tip angle, electrode type, nature of the shielding gas, ambient pressure, inclination of the torch and the external magnetic field in GTA steel welds. The computed results were in good agreement with the independent experimental results from various sources for a wide variety of welding conditions.

8.2 Conclusions

This thesis research work aims to alter the current status in the modeling of fusion welding by proposing and proving a new methodology to tailor weld geometry based on scientific principles. The methodology involved the improvement in the reliability of outputs of transport phenomena based models by finding the uncertain input parameters such as arc efficiency. Furthermore, the use of neural network models in this work provided significant saving of computation time since the model takes few seconds compared to more than two week time taken when the heat transfer and fluid flow model was used. This model is implemented on gas-metal-arc (GMA) welding which is one of the most widely used welding processes in the industry. The following are some of the important conclusions of this thesis research.

(a) The results from the modified heat transfer and fluid flow of GMA fillet welding show that the weld pool surface profile changes with workpiece orientations and welding positions. During the uphill and downhill welding, there are chances of undercut and formation of split bead defects, respectively. The velocities in the weld pool were found to be of the order of 150 mm/s which are much higher than those calculated for GTA welding. Furthermore, liquid metal convection in the weld pool affects the weld pool shape and mixing of the solutes and gases. The computed results show that the average cooling rates between 1073 K and 773 K ($\dot{T}_{8/5}$) at various locations inside the workpiece vary with change in workpiece orientations or welding positions. It was found that with increase in the lift angle, the $\dot{T}_{8/5}$ increases for similar welding conditions.

Therefore, average cooling rates for downhill welding were higher than uphill or flat welding positions. Furthermore, the $\dot{T}_{8/5}$ decreases with increase in heat input per unit length. The computed results were in good agreement with the corresponding experimental results available in the literature.

(b) The reliability of outputs of the numerical heat transfer and fluid flow calculations was improved by finding optimized values of several uncertain input parameters such as arc efficiency. The optimized values of these uncertain input parameters determined as a function of heat input were within the ranges of their values reported in the literature. The good agreement between the computed and the corresponding experimental weld bead geometry for various welding conditions indicates the effectiveness of the approach used in this thesis work.

(c) When the details of temperature distribution and velocity fields are not of interest, the neural network models can be used to calculate various outputs such as weld geometric parameters i.e. leg-length, throat and penetration, cooling rate, peak temperature and maximum velocity in the weld pool with significant computational economy. A hybrid optimization scheme involving conjugate gradient method and genetic algorithm was used to train these neural networks using the results of heat transfer and fluid flow model. The hybrid optimization scheme was able to produce better neural networks compared to any individual algorithm. The database for training of neural network was generated by running the heat transfer and fluid flow model. The use of modified orthogonal arrays helped in reducing the size of database required to train the network by capturing the effects of all the welding parameters and material properties based on the principles of design of experiments. The results provided by the neural networks agreed well with the corresponding results obtained from the heat transfer and fluid flow model, indicating the accuracy of its predictions.

(d) Weld attributes can be tailored by combining a neural network model with an advanced real number based genetic algorithm. This bi-directional methodology developed by combining the neural networks with a genetic algorithm was able to predict the multiple combinations of welding variables to achieve a specific weld geometry. The model developed in this work is significantly different from traditional inverse models

that provide only single solution (i.e. one set of welding conditions) necessary for obtaining a target weld geometry. The use of a neural network model in place of transport phenomena based model provided significant saving in the computational time by providing the multiple solutions within few seconds. This doctoral thesis work outlines a completely new direction of exceptional promise for tailoring the weld geometry based on scientific principles in place of trial and error method commonly used in the welding industry.

(e) A phenomenological model was developed to examine the welding conditions for the formation of humping defects. The calculated results for the formation of humping defects were in good agreement with the independent experimental results from various sources. The model for understanding of humping defects considers the effect of various welding variables on humping defects by taking the various outputs of heat transfer and fluid flow model as an input in this model. It was found that the increase in welding speed above certain critical speed leads to initiation of humping defects. The value of the critical speed varies with the welding conditions. The results showed that the humping defects can be avoided even at high welding speed and arc current by using hollow electrodes, or applying appropriate external magnetic field, or tilting the torch, or selecting the shielding gas with low molecular weight. This model quantitatively predicts the values of various welding conditions which can be used to avoid humping defects which was not possible with earlier existing models. For example, this model suggests that the use of helium as shielding gas in place of argon can increase the critical welding speed by more than three times.

The ability of the model to correctly predict multiple combinations of welding variable that can lead to the target weld dimensions provides the choices to the engineers to achieve a given weld attribute through different routes. This work also proves that by combining the various computational tools with transport phenomena based models, a useful phenomenological framework can be created to transform welding from art to science. Although the work reported here focuses on finding welding conditions to achieve desired weld geometry, the results provide hope that this methodology can be used further for tailoring the structure and properties of weldments.

8.3 Future Work

During this doctoral thesis research, various areas were identified that requires further investigation.

First, in Chapter 3, the existing model of GMA fillet welding was modified to capture the effect of workpiece orientations and welding directions. Due to complexity of this welding system, several assumptions were made in the model to simplify the computational task. In the future, some of the simplifying assumptions used in the present research can be relaxed and address more realistic situations. (a) The electromagnetic force calculations were based on analytical relations which involved various assumptions for simplification. A more comprehensive numerical calculation can be incorporated in the model to accurately calculate the electromagnetic force. This will involve the calculation of current density, magnetic flux fields and the resulting electromagnetic force field in three dimensions in the entire workpiece. The current density and the magnetic field at any point inside the workpiece can be obtained by solving the Laplace potential equation and by using the Biot-Savart law, respectively. (b) The additional heat carried by the droplets in the model is considered by using a volumetric heat source in the weld pool. This approach is only valid for spray mode droplet transfer and may not be applicable for globular and short-circuit transfer modes. Therefore, appropriate calculations of the additional heat transported by droplets under different modes will be a useful undertaking. It will involve the transient calculation of heat transfer and fluid flow in the arc plasma and the workpiece. A coupled simultaneous solution of the energy equation and the Navier-Stokes equations will be required in both the regions to capture the effect of other droplet transfer mechanisms.

Second, in chapter 6, a bi-directional phenomenological model was developed by coupling the genetic algorithm with a neural network which was trained using the results of a well-tested heat transfer and fluid flow model. This model was used to calculate input welding conditions to achieve the desired weld geometry. To increase its practical application, this approach can be further extended to tailor other weld attributes such as microstructure and the stresses in the workpiece by incorporating their phenomenological

models. The microstructure calculation can be performed by using the non-isothermal Johnson-Mehl-Avrami (JMA) equation which represents the kinetics of phase transformation. For desired microstructure calculations, the objective function can be formed as a function of phase fractions in place of weld dimensions used in the present work.

Third, in Chapter 7, a comprehensive model for predicting the humping defects was developed and tested for GTA butt welding. In the future, this model can be extended to predict and prevent the humping defects during other welding processes such as GMAW and laser welding.

It is hoped that the aforementioned areas be addressed in the future to provide a better capability for welding engineers to tailor the defect free weld joints with desired attributes using the transport phenomena based models.

Appendix A

NEURAL NET MODEL OF GAS METAL ARC FILLET WELDING

The neural network model of gas metal arc fillet welding includes all the welding variables and material properties as input and provides weld dimensions, peak temperatures, maximum velocities and the cooling rates between 800 to 500 °C as output. A separate neural net is used for each of the output variables, i.e. penetration, actual throat, leg-length, length of weld pool, peak temperature, cooling rate and peak velocity in the weld pool. It comprises of one hidden layer which contains 19 nodes. The following hyperbolic tangent function (which is a symmetric sigmoid function) is used as the activation function:

$$y = \tanh\left(a \sum_{i=0}^N w_i x_i\right) \quad \text{A.1}$$

where a is the slope parameter of the sigmoid function whose value was taken as 1.5 in this model.

To run the program under windows environment, the users need to have java installed on their computer. To run the program, just double click on “Fillet_Neural” which is a MS-DOS batch file to get the following “Welcome window” as shown in figure A-1. To start the calculation, please click on the “start button” located below the address information in figure A-1. On clicking the “start button”, the following window appears (shown in figure A-2). The materials properties, such as the thermal conductivity, specific heat, and density, can be defined in the edit windows. The default values of material properties for alloys Fe1005, Fe1045 and A-36 steels have been specified in the model. The material properties for a particular material can be selected from the pull-down menu box. However, the user can also specify other values of these variables in the following “Material window.”

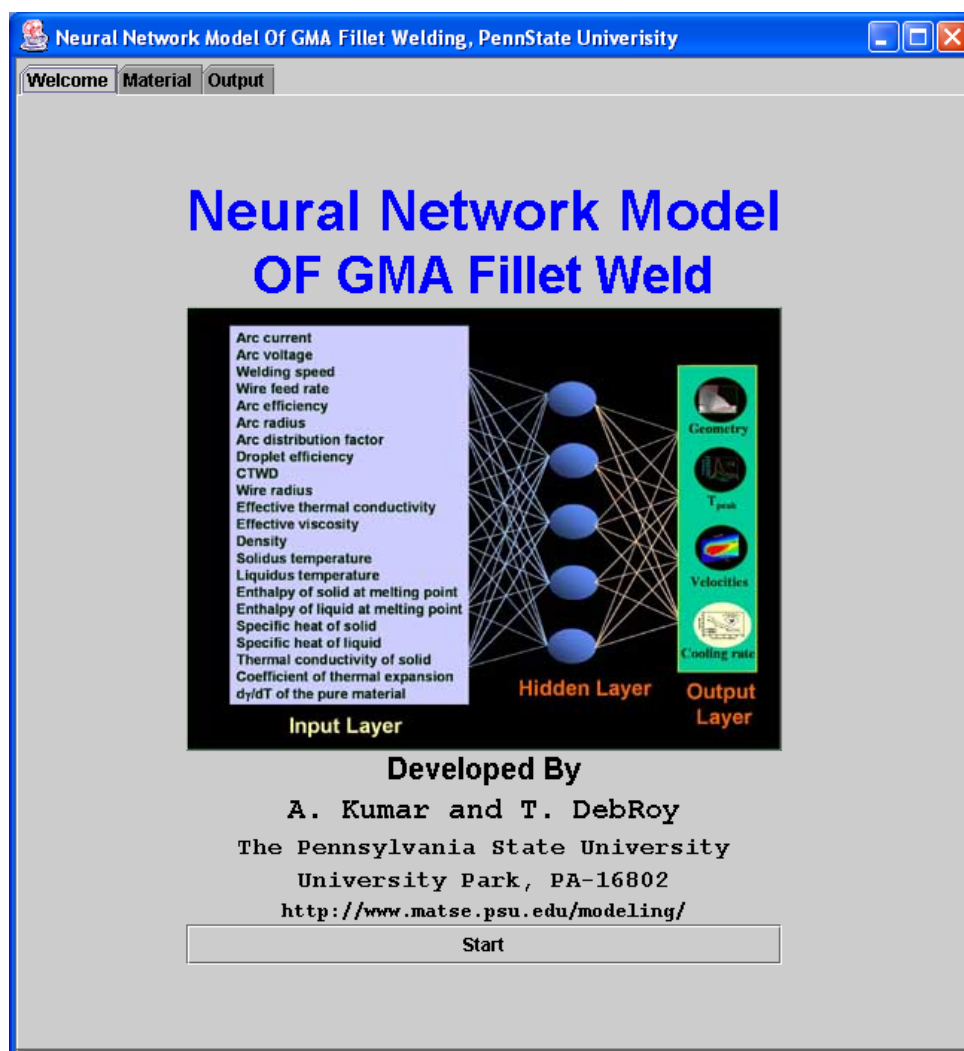


Figure A-1: “Welcome window” obtained on clicking the MS-DOS batch file.

Input Welding Conditions		
Input Variables	Default Values	Input Values
Arc current (Amp.)	286.7811	<input type="text"/>
Arc Voltage (Volt)	31.0	<input type="text"/>
Welding speed (cm/s)	0.635	<input type="text"/>
Wire feed rate (cm/s)	16.93	<input type="text"/>
Arc efficiency	0.54	<input type="text"/>
Arc radius (cm)	0.5	<input type="text"/>
Arc distribution factor	0.5	<input type="text"/>
Droplet efficiency	0.12173	<input type="text"/>
CTWD (cm)	2.86	<input type="text"/>
Wire radius (cm)	0.06604	<input type="text"/>

Select Material A36 steel

Material Properties	User Input
Effective thermal cond. (cal/cm-s-K)	<input type="text" value="0.35"/>
Effective viscosity (gm/cm-s)	<input type="text" value="0.3"/>
Density (gm/cm ³)	<input type="text" value="7.8"/>
Solidus temp. (K)	<input type="text" value="1745.0"/>
Liquidus temp. (K)	<input type="text" value="1785.0"/>
Enthalpy solid at melting point (cal/gm)	<input type="text" value="250.76"/>
Enthalpy liquid at melting point (cal/gm)	<input type="text" value="314.76"/>
Sp. heat solid (cal/gm-K)	<input type="text" value="0.168"/>
Sp. heat liquid (cal/gm-K)	<input type="text" value="0.193"/>
Thermal conductivity solid (cal/cm-sec-K)	<input type="text" value="0.05"/>
Coeff. of thermal exp.(1/K)	<input type="text" value="1.0e-5"/>
d(gamma)/dT of material (dynes/cm-K)	<input type="text" value="-0.35"/>

Figure A-2: The “material window” obtained after clicking the start button. The welding process parameters and other welding conditions along with material properties need to be typed at appropriate places in the applet.

To start the calculations, click the “Calculate” button and the program will show the calculated values of the penetration, leg-length, actual throat, peak temperature, maximum value of the root-mean-square velocity and the cooling time for 800°C to 500°C along the weld center line on next output screen as shown in figure A-3 . User can also go backwards and change the inputs by clicking on material panel shown on upper left corner.

The codes can be accessed with appropriate prior arrangement with my advisor Professor T. DebRoy of The Pennsylvania State University at debroy@psu.edu.

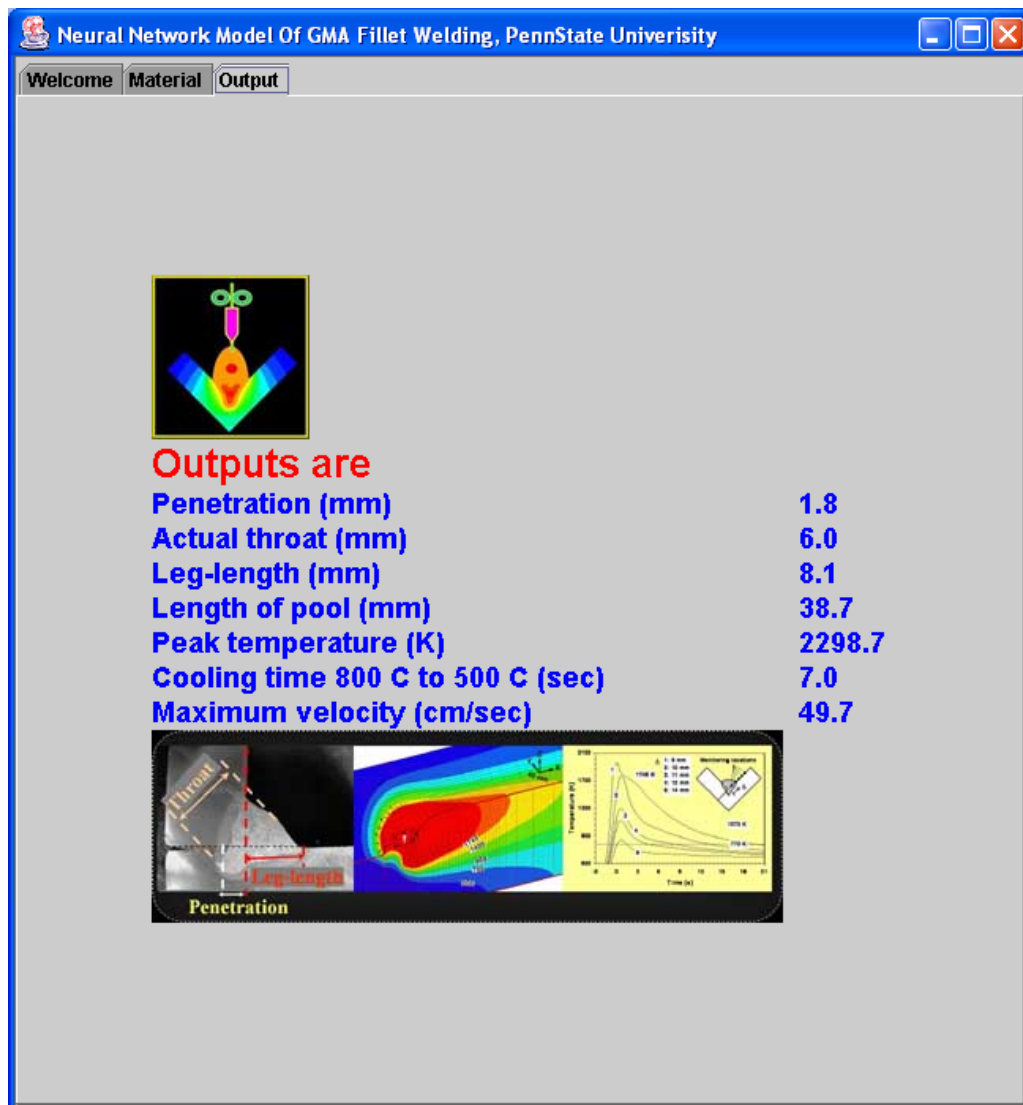


Figure A-3: This screen shows the calculated values of the penetration, leg-length, actual throat, peak temperature, maximum velocity and the cooling time for 800°C to 500°C along the weld center line for given welding conditions.

VITA

Amit Kumar

Amit Kumar was born in Dankaur (Uttar Pradesh), India, on January 2, 1978. In August 1997, he enrolled in the Department of Mechanical Engineering, Saradar Vallabhbhai National Institute of Technology (SVNIT), Surat, India where he was awarded the degree of Bachelor of Engineering in July 2001. In the fall of 2002, he joined the Pennsylvania State University to pursue doctoral study in Materials Science and Engineering with minor in High-Performance Computing under the guidance of Professor T. DebRoy. The author is a member of American Welding Society (AWS) and American Society of Metals (ASM-International). A list of the author's publications in various referred journals during his Ph.D. study at Penn State is as follows.

1. A. Kumar and T. DebRoy, *Science and Technology of Welding and Joining*, **11**, 106-119 (2006).
2. A. Kumar and T. DebRoy, *Metallurgical and Materials Transaction A*, **36A**, 2725-2735 (2005).
3. A. Kumar, W. Zhang and T. DebRoy, *Journal of Physics D: Applied Physics*, **38**, 119-126 (2005).
4. A. Kumar and T. DebRoy, *Journal of Physics D: Applied Physics*, **38**, 127-134 (2005).
5. A. Kumar, S. Mishra, J. W. Elmer and T. DebRoy, *Metallurgical and Materials Transaction A*, **36A**, 15-22 (2005).
6. A. Kumar, W. Zhang, C. H. Kim and T. DebRoy, *Welding in the World*, **49** (9/10), 32-48 (2005).
7. A. Kumar and T. DebRoy, *International Journal of Heat and Mass Transfer*, **47**, 5793-5806 (2004).
8. A. Kumar and T. DebRoy, *Journal of Applied Physics*, **94**, 1267-1277 (2003).
9. A. Kumar and T. DebRoy, "Tailoring Fillet Weld Geometry using a Genetic Algorithm and a Neural Network Trained with Convective Heat Flow Calculations", *Welding Journal* (submitted).
10. A. Kumar and T. DebRoy, "Toward a Unified Model to Prevent Humping Defects in Gas Tungsten Arc Welding", *Welding Journal* (submitted).